DESIGN OF A CONTROL MOMENT GYROSCOPE WITH OUTER ROTOR BLDC MOTOR

A THESIS SUBMITTED TO
THE GRADUATE SCHOOL OF NATURAL AND APPLIED SCIENCES
OF
MIDDLE EAST TECHNICAL UNIVERSITY

BY

BERK İNCE

IN PARTIAL FULFILLMENT OF THE REQUIREMENTS
FOR
THE DEGREE OF MASTER OF SCIENCE
IN
ELECTRICAL AND ELECTRONICS ENGINEERING

SEPTEMBER 2019

Approval of the thesis:

DESIGN OF A CONTROL MOMENT GYROSCOPE WITH OUTER ROTOR BLDC MOTOR

submitted by **BERK İNCE** in partial fulfillment of the requirements for the degree of **Master of Science in Electrical and Electronics Engineering Department, Middle East Technical University** by,

Prof. Dr. Halil Kalıpçılar
Dean, Graduate School of **Natural and Applied Sciences** _____

Prof. Dr. İlkay Ulusoy
Head of Department, **Electrical and Electronics Eng.** _____

Prof. Dr. H.Bülent Ertan
Supervisor, **Electrical and Electronics Eng., METU** _____

Examining Committee Members:

Assist. Prof. Dr. Ozan Keysan
Electrical and Electronics Engineering, METU _____

Prof. Dr. H.Bülent Ertan
Electrical and Electronics Eng., METU _____

Assist. Prof. Dr. Emine Bostancı
Electrical and Electronics Engineering, METU _____

Assist. Prof. Dr. Özgür Bayer
Mechanical Engineering, METU _____

Prof. Dr. Timur Aydemir
Electrical and Electronics Engineering, Gazi University _____

Date: 30.09.2019

I hereby declare that all information in this document has been obtained and presented in accordance with academic rules and ethical conduct. I also declare that, as required by these rules and conduct, I have fully cited and referenced all material and results that are not original to this work.

Name, Surname: Berk İnce

Signature:

ABSTRACT

DESIGN OF A CONTROL MOMENT GYROSCOPE WITH OUTER ROTOR BLDC MOTOR

İnce, Berk
Master of Science, Electrical and Electronics Engineering
Supervisor: Prof. Dr. H.Bülent Ertan

September 2019, 201 pages

The aim of this thesis is to design a control moment gyroscope (CMG) with outer rotor BLDC motor for medium size satellites. CMG is a device that provides high output torque to the satellite in order to maneuvering satellites rapidly. CMG is the most efficient actuator in terms of output torque capacity when it is compared with other type actuators such as the reaction wheel.

The first step of the designing CMG is to determine CMG design specifications. The mass and volume specifications of the designed CMG are selected to be the same as the previous satellite actuator (reaction wheel) that was used in the previous satellite program Satellite maneuvering calculations on x and y axes are covered for four different maneuvering cases to determine the required CMG output torque capacity. Operating temperature, operating voltage, and maximum gimbal angle excursion are other specifications to be considered in the design process of the CMG in this thesis. In addition, the effect of the four different maximum gimbal angle excursions on the CMG design is investigated.

The designed CMG consists of the wheel, BLDC motor, and gimbal structure. The wheel that provides the required inertia is designed to generate CMG output torque. During the wheel design, mass and volume reduction calculations are done and yield

stress and safety factor constraints of the wheel are considered. To drive the wheel of CMG, the outer rotor BLDC motors are designed. The designed motor satisfies electrical loading and magnetic loading constraints and the mass of the motor is selected as low as possible. Step motor for gimbal angle control, step motor driver and gear system are selected for gimbal structure to overcome the required torque of the gimbal system. The thermal simulation model of the designed CMG is created to analyze thermal performance of the CMG. In the end, the design results of CMG are shown. In this thesis, it is shown that although mass and volume are the same for these two actuators, the output torque capacity of the designed CMG is higher than the previous reaction wheel.

Keywords: Control Moment Gyroscope (CMG), Spacecraft Thermal Control Systems, Outer Rotor Permanent Magnet BLDC Motor Design, CMG Output Torque Calculations, Flywheel Design

ÖZ

ROTORU DIŞARDA FIRÇASIZ DA MOTORA SAHİP KONTROL MOMENT JİROSKOBUNUN TASARIMI

İnce, Berk
Yüksek Lisans, Elektrik ve Elektronik Mühendisliği
Tez Danışmanı: Prof. Dr. H.Bülent Ertan

Eylül 2019, 201 sayfa

Bu tez çalışmasının amacı orta büyüklükteki uydular için rotoru dışarda fırçasız DA motora sahip kontrol moment jiroskobu (KMJ) tasarlamaktır. Kontrol moment jiroskobu, uydunun hızlı manevra yapabilmesi için uyduya yüksek tork sağlayan bir eyleyicidir. KMJ, uydularda kullanılan diğer eyleyecilerle karşılaştırıldığında çıkış tork kapasitesi en verimli olan eyleyicidir.

KMJ tasarımındaki ilk adım KMJ'nin tasarım kriterlerini belirlemektir. KMJ kütle ve hacim kriteri daha önceki uyduda kullanılan tepki tekeri ile eşit olarak seçilmiştir. KMJ'nin çıkış tork kapasitesini belirlemek için, uydunun x ve y eksenlerindeki manevra hesaplamaları dört farklı durum için incelenmiştir. Ayrıca KMJ'nin çalışma sıcaklığı, çalışma gerilimi ve azami yalpa açısı bu tezde dikkate alınan diğer kriterlerdir. Bunlara ek olarak, dört farklı azami yalpa açısının KMJ tasarımındaki etkisi araştırılmıştır.

Tasarlanan KMJ tekerlekten, fırçasız DA motordan ve yalpa sisteminden oluşmaktadır. KMJ'nin çıkış torkunu üretmek için gerekli ataleti sağlayan tekerlek tasarımı yapılmıştır. Tekerlek tasarımı sırasında, kütle ve hacim azaltma çalışmaları yapılmış ve tekerin sünme gerilimi ve güvenlik faktörü dikkate alınmıştır. KMJ'nin tekerini döndürmek için, rotoru dışarda fırçasız DA motor tasarlanmıştır. Bu motor

belirlenen elektriksel ve manyetik kısıtları sağlarken, motorun kütlesi de olabildiğince düşük seçilmiştir. Yalpa sisteminin gerekli torkunu sağlamak için, kademeli motor, kademeli motorun sürücüsü ve dişli sistemi yalpa yapısı için seçilmiştir. KMJ'nin termal performansını analiz etmek için termal benzetim modeli oluşturulmuştur. Son olarak KMJ'nin tasarım sonuçları paylaşılmıştır. Bu tez çalışmasında, tasarlanan KMJ'nin kütle ve hacmi bir önceki uyduda kullanılan tepki tekerinin kütlesiyle ve hacmiyle eşit olmasına rağmen, KMJ'nin daha yüksek tork kapasitesine sahip olduğu gösterilmiştir.

Anahtar Kelimeler: Kontrol Moment Jiroskobu (KMJ), Uzay Araçlarının Termal Kontrol Sistemleri,Rotoru Dışarda Sabit Mıknatıslı Fırçasız DA Motor Tasarımı, KMJ Çıkış Torku Hesaplamaları, Tekerlek Tasarımı

To my family and my friends

ACKNOWLEDGEMENTS

I would like to express appreciation to my supervisor Prof. Dr. H.Bülent Ertan for his guidance and almost infinite patience. He always insists me to finish this thesis when I feel hopeless.

I would like to thank specially to executives of Tübitak Space Technologies Research Institute who support me economically and psychologically.

Very special thanks are addressed to members of Attitude Orbit Control System in Tübitak Uzay Dr. Çağatay Yavuzyılmaz and Yusuf Acar for their support about determining CMG requirements, creating mathematical models, and simulation of CMG.

I would like to express my deepest thanks to İ. Sedat Gülle who created designed CMG model mechanically.

I would like to give credits to my parents Ali, Ayşen and my elder brother Utku for their vision, support, and unrequited love. They always encourage me to follow rationalism and science.

The final and greatest thanks go to my dearest love Funda İpek who supports me in any conditions. Her love and encouragement are the first and fundamental motivation source for me during the whole study.

TABLE OF CONTENTS

LIST OF TABLES

TABLES

LIST OF FIGURES

FIGURES

CHAPTER 1

INTRODUCTION

1.1. Scope of the Thesis

In aerospace applications, there are many actuators which perform various function in satellites such as hold-down release mechanism of solar array, solar array drive mechanism, antenna release mechanism, antenna tracking system and satellite maneuvering. Antenna and solar array should be at stowed position before launch since satellite should be fit into the rocket. After separation, antenna and solar array change their position from stowed to deployed by using hold-down release mechanism. Solar array tracks sun by using solar array drive mechanism in order to obtain and use maximum sun power. Antenna tracking actuator is another significant actuator to provide straight broadcast performance.

One of the most valuable actuators in satellites is satellite maneuvering actuator since rapid rotational maneuverability and agility indicate the ability of satellite. Efficient satellites should have strong Attitude and Orbit Control System (AOCS). Stronger AOCS can provide fast multi-target pointing and tracking capabilities [1]. For instance, if the earth observation satellite is more agile, it can take numerous images from the earth at different angle position to acquire high resolution images and also return of data speed is faster.

This study will focus on the design of Control Moment Gyroscopes (CMG), which is one of the most efficient satellite maneuvering actuator types. Dynamic CMG equations, spacecraft thermal control systems, determination of CMG specifications CMG output torque calculations, proper wheel design, BLDC motor design, and selection of step motor and step motor driver for gimbal structure are studied.

1.2. Outline of the Thesis

There are eight more chapters except for this chapter in this thesis. Each chapter focuses on different topics deeply.

In Chapter 2, different types of satellite actuators are compared and space coordinate system are defined separately. Classification of control moment gyroscope is studied briefly, and output torque equations are derived for pyramidal configuration.

Chapter 3 includes the results of the mathematical models for different output torque and for different sizes of the satellites. Required maneuvering duration is calculated for different maneuvering angle on x,y, and z directions.

In Chapter 4, spacecraft thermal control system is explained in detail. In order to understand the relationship space environment and CMG, fundamentals of heat transfers and thermal control components are described briefly. Finally, thermal qualification level of CMG is determined.

In Chapter 5, CMG design specifications are determined in terms of mechanically, thermally, maneuvering duration and electrically. Based on these specifications, the required output torque that satisfies these requirements is calculated for different maximum gimbal angle excursions. Required moment of the inertia is calculated for these different cases.

Chapter 6 is assigned to calculate dimensions of the wheel that provide sufficient inertia to satellite for different maximum gimbal angle excursions. The wheel is designed for different outer radii and design results are shared in this chapter.

In Chapter 7, the design procedure of BLDC motors is covered. Firstly, the required output torque of BLDC motor that rotates and accelerates the wheel in a specified time is determined. After that, different types of BLDC motor are discussed. Finally, BLDC motor equations are derived, and several BLDC motors are designed and obtained by changing the ratio of inner diameter to length of motor for different maximum gimbal angle excursions.

Chapter 8 explains gimbal structure of CMG. It consists of stepper motor, stepper motor driver and gear structure. Proper stepper motor and stepper motor are selected. This stepper motor changes the angle of the rotating wheel. CMG output torque is generated by this change. Angle between the first position and the last position of the wheel is called as gimbal angle. Gear ratio calculations that increases output torque of stepper motor are also covered in this section.

Chapter 9 concludes the thesis by sharing and discussing the design results of CMG. At the end of the chapter, future work is stated.

1.3. Literature Overview

In literature, there are several findings and results that are related to CMG design, spacecraft thermal control methods, wheel design, BLDC motor design and motor topologies.

In [2] and [3], control techniques for the aerospace system are studied in detail. Firstly, satellites are classified in terms of mass. The attitude control system is explained briefly. CMG for a small satellite is studied. Agility and slew rate requirement is determined and analyzed. Low-cost miniature CMG is designed and tested. The total mass of designed SGCMG is 200 g and the output torque of CMG is 52.25 mNm. In conclusion, designed CMG is compared with a reaction wheel that is used for the same satellite. In [4], control moment gyroscope is designed for small satellites. Dynamic CMG equations are derived. Iterative design is applied for CMG subparts such as flywheel, flywheel motor, bearings, and gimbal motor. In addition, mass budget of CMG is also analyzed.

In [5], control moment gyroscope is compared reaction wheel in terms of dimensional approach, market study, power consumption per torque, the agility of the satellite and market evolution. As a result, although reaction wheel mechanical design is less difficult than CMG design, CMGs have more torque at a fraction of the power. In [6], double gimbal axis control moment gyroscope is studied and CMG is modeled by using Lagrange’s equations and adaptive feedback control law is developed.

In [7], axial flux and radial flux brushless DC motor topologies are compared for control moment gyroscope applications. Conventional radial flux motor and axial flux motor are designed in this study. Motor designs are analyzed for 10000 rpm and output torque of the motors are 32 mNm for steady-state operation and 50 mNm for acceleration output torque. Sinusoidal and square wave excitations are applied to each type of motor. As a result, sinusoidal excited axial flux motor has more advantages than conventional radial flux motor in terms of mass, efficiency, torque/mass, and torque/volume. In [8], outer rotor radial flux BLDC motor is studied and designed. Speed of motor is 10000 rpm and motor output torque are 32 mNm for steady-state operation and 50 mNm for acceleration. Design results of outer rotor radial flux motors are compared with axial flux motor. In conclusion, outer rotor radial flux BLDC motor has more advantages than axial flux motor in terms of mass, efficiency, torque/mass, and torque/volume. Motor design in this thesis is based on [8].

In [9], kinematic problems of CMG is investigated. Singularity problem is described and steering law for control moment gyroscope in spacecraft attitude control is explained in detail.

In [10], spacecraft thermal control system is explained in detail. This study is a fundamental source of the thermal design for spacecraft and equipment such as CMG studied in this thesis. Passive and active thermal components, qualification requirements for spacecraft and equipment are explained in detail.

In [11], mathematical model and output torque calculations of CMG for a small satellite is investigated. The relationship between the satellite and CMG is studied. Examples of satellite attitude control and simulations results are shown for different maneuvering. Imaging sequence during satellite operation is explained and finally, designed CMG is tested.

1.4. Thesis Organization

The aim of the thesis is to design a control moment gyroscope (CMG) for space applications. CMG is a device that provides high output torque to the satellite in order to maneuvering satellite rapidly. CMG is the most efficient actuator in terms of output torque capacity when it is compared with the output torque capacity of the reaction wheel that is used in previous Turkish satellites. The mass and the volume of the designed CMG are selected the same as the previous actuator (reaction wheel) that was used in the previous satellite program. In this thesis, it will be shown that although mass and volume are the same for these two actuators, the output torque capacity of the designed CMG is higher than the previous reaction wheel.

The starting point of the designing CMG is to determine CMG design specifications. The specifications are obtained from satellite system design and they are related to the mission of the satellite. Firstly, maximum satellite maneuvering durations are specified, and the required torque capacity of CMG is defined. Secondly, reserved mass and volume of CMG in the satellite are assigned. Thirdly, the operating voltage of CMG is determined, and it depends on the solar array and battery characteristics of the satellite. Then, power loss and operating temperature of the CMG are limited by the satellite thermal control system. In addition, maximum gimbal angle excursion is defined by Attitude and Orbit Control System (AOCS). In conclusion, in order to satisfy CMG design specifications, parts of CMG that are the wheel, BLDC motor, and gimbal structure are investigated in this thesis. It is also noted that parts of CMG (see Figure 9.1) are designed for different maximum gimbal angle excursion to understand the effect of the gimbal angle on CMG design.

The wheel must provide the required inertia to the system in order to create CMG output torque. The most important consideration of the wheel design is to obtain the lowest mass and volume since the total mass and volume of CMG should satisfy CMG design specification and it is also very crucial for space application to decrease launch

cost. During wheel design calculations, yield stress limitation of the wheel material and safety factor of the wheel in space application are considered.

The BLDC motor is designed to accelerate and rotate the wheel at a constant speed. Thanks to this rotation, angular momentum is created on the wheel. Therefore, BLDC motor must provide acceleration and steady-state torque requirements of the wheel. In this thesis, the mass and the volume of the BLDC motor must be as low as possible due to CMG design specifications. Furthermore, it must satisfy electrical loading, magnetic loading and manufacturability constraints and it must be compatible with bus voltage of the satellite. In conclusion, BLDC motor is designed by satisfying design constraints mentioned above. During the design procedure, different motors that have different ratio of inner diameter to length are investigated to obtain the most efficient motor for in terms of the mass and the volume for the CMG application considered.

The gimbal structure must be built to change the rotation angle of the wheel. Thanks to the gimbal structure, the direction of the angular momentum vector is changed dramatically, and a huge CMG output torque is obtained by changing the rotation angle of the wheel. The most critical design constraint of the gimbal structure is a gyro torque acting back to the gimbal structure. Therefore, the gimbal structure must overcome gyro torque during the space mission of the satellite. It consists of a step motor, step motor driver and gear system. Proper step motor and step motor driver are selected, and gear system is designed to overcome gyro torque acting back to the gimbal system.

The design results of the parts of CMG are investigated for different maximum gimbal angle excursion and the results are discussed. In conclusion, the most suitable gimbal angle is selected and CMG design results that have the lowest mass and volume wheel and BLDC motor are presented. It is not sufficient for given motor design to provide the desired torque. It must be able to perform within specified conditions satisfying thermal requirements. For this reason, thermal analysis of the designed CMG in the

thermal-vacuum chamber is performed as well as in clean-room conditions. The thermal performance results are presented in CHAPTER 9. Finally, CMG is compared with the actuator used in a similar satellite and it is shown that the torque capacity of CMG is much higher than the reaction wheel previously used, although the mass and volume of these two actuators are the same. The summary of the thesis organization is shown in Figure 1.1.

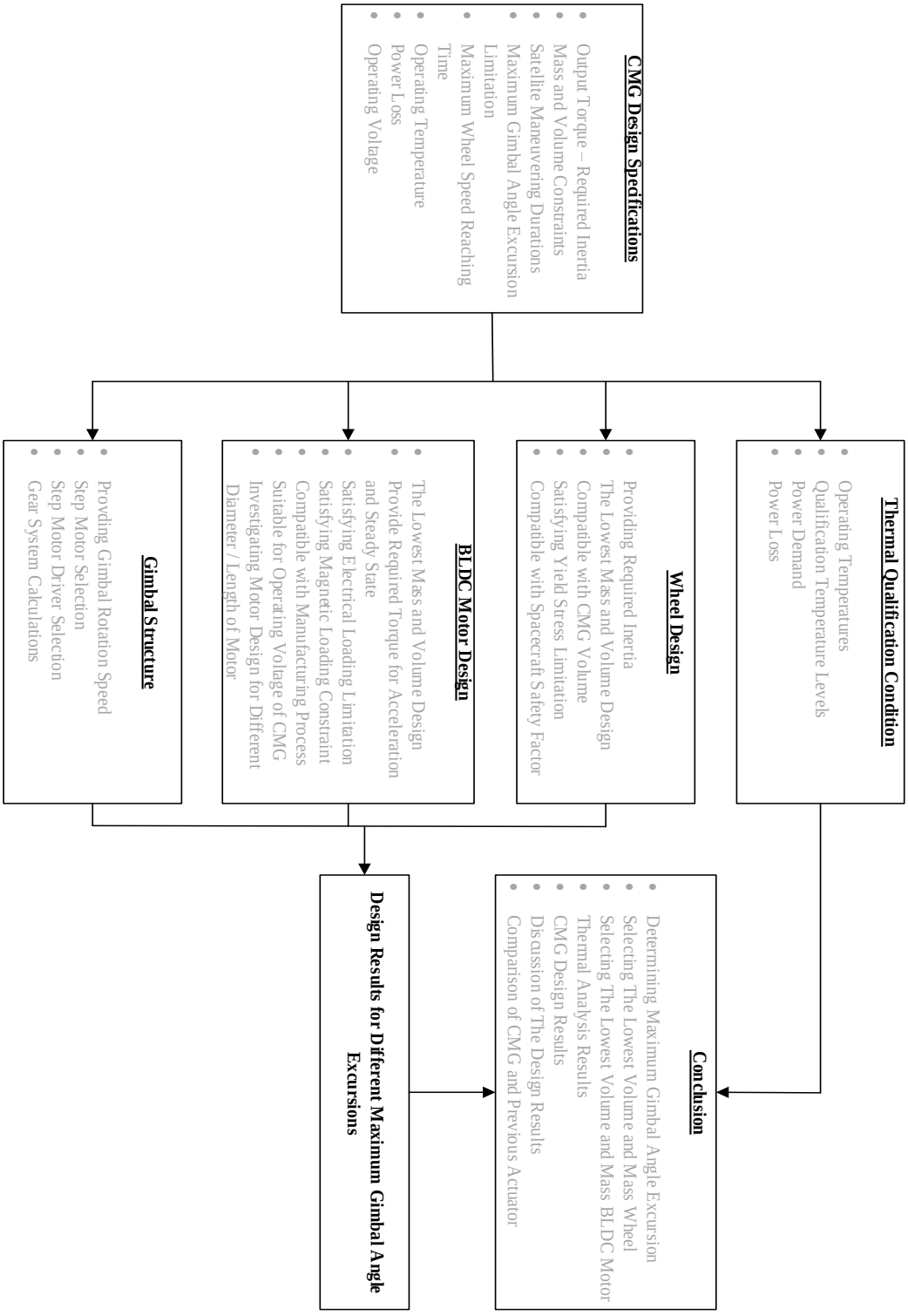

Figure 1.1 Summary of Thesis Organization

CHAPTER 2

SATELLITE ACTUATORS' BACKGROUND AND DYNAMIC CMG EQUATIONS

2.1. Satellite Actuators

For satellite maneuvering, there are three different actuators which are used in spacecraft; momentum wheels (MW), reaction wheels (RW) and control moment gyroscope (CMG). A satellite that has momentum wheels and reaction wheels are not agile satellites since they cannot provide high output torque. However, control moment gyroscope can provide high output torque and it can increase the agility of satellite. For instance, Table 2.1 compares CMG and RW in terms of mass, torque capacity and slew rate. CMG torque capacity (52mNm) is higher than RW torque capacity (20 mNm).On the other hand, mass of RW (4 kg) is four times higher than CMG (1 kg). Therefore, the slew rate of the satellite which has CMGs is faster than the satellite which has RWs. In addition, CMGs can generate output torque from 135 Nm to 4067 Nm, whereas the maximum torque capacity of the reaction wheel is around 1.35 Nm.[1] Therefore, from small satellites to large satellites, the trend of satellite maneuvering actuators are shifted from MW and RW to CMG. In addition, the classification of satellites is shown in Table 2.2.

Table 2.1 *Example of Comparison of RW and CMG [2]*

Actuator	**CMG**	**RW**
Satellite Inertia (kg.m^2)	[2.5, 2.5, 2.5]	[2.5, 2.5, 2.5]
Satellite Mass (kg)	50	50
Torque (mNm)	52.25	20
Actuator Mass (kg)	1	4
Slew Rate (º / s)	3	1.85

Table 2.2. *Satellite Classification*

Satellite Size	**Weight**
Small	100kg – 500 kg
Medium	500kg – 1000 kg
Large	> 1000 kg

The main idea of satellite maneuvering actuators is momentum exchange principle (conservation of momentum). Momentum wheel and reaction wheel is driven by only one DC motor and output torque is obtained by changing the speed of the wheel. Output torque is in the same direction as the wheel rotation shown in Figure 2.2. Since torque is obtained by changing wheel speed, there is a saturation problem in reaction wheel due to the maximum speed limitation of wheel and DC motor. In other words, although satellite requires torque for maneuvering, sufficient torque is not created and acceleration is not provided when the wheel reaches its maximum speed. However, control moment gyroscope has wheel and gimbal and generally wheel speed is constant (6000rpm to 10000 rpm) [7]. The wheel is mounted on gimbal shown in Figure 2.1 and gimbal changes the direction of the wheel when the wheel is rotating.

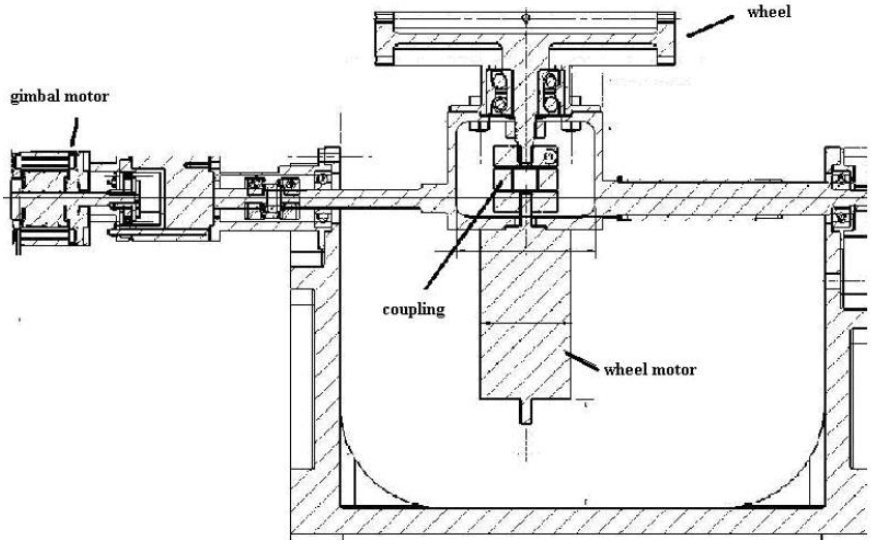

Figure 2.1 The Example of CMG [7]

Output torque is obtained by rotation of gimbal. Rotation axis of the gimbal and rotation of wheel spin are perpendicular to each other, and output torque direction shown in Figure 2.3 is perpendicular to these two rotation directions. Therefore, sufficient torque can be created continuously by rotating the gimbal. Another advantage of CMG is mass and volume. Especially for large satellites, CMG torque per unit volume and torque per unit mass are higher than RW torque per unit volume and torque per unit mass. These physicals advantages are very crucial for space applications in terms of launch cost and positioning equipment in spacecraft.

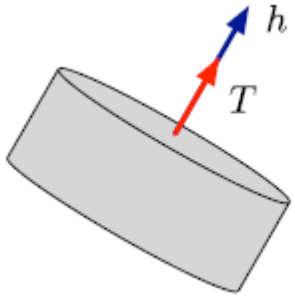

Figure 2.2. Basic Torque Diagram of Reaction Wheel [5]

Reaction wheel torque equations are given by [5]

$$h_{satellite} = I_{satellite}\ w_{satellite} \tag{2.1}$$

$$T = \frac{dh}{dt} = I\ \frac{dw}{dt} \tag{2.2}$$

$$T = -T_{satellite}\ = I\frac{dw_{satellite}}{dt} \tag{2.3}$$

Where,

h: *Angular momentum of the wheel*

$h_{satellite}$: *Angular momentum of the satellite*

I: *Inertia of the wheel*

$I_{satellite}$: *Inertia of the satellite*

w: *Angular speed of the wheel*

$w_{satellite}$*: Angular speed of the satellite*

T: *Output torque of RW*

$T_{satellite}$***:*** *Affected torque of the satellite*

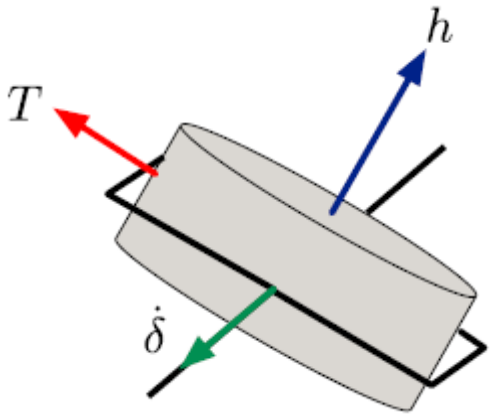

Figure 2.3 Basic Torque Diagram of CMG [5]

CMG torque equations are given by [5]

$$h = Iw \tag{2.4}$$

$$\dot{\delta} = w_{gimbal} \tag{2.5}$$

$$T = \dot{\delta}\ x\ h = w_{gimbal}\ I\ w \tag{2.6}$$

w_{gimbal}*: angular speed of the gimbal*

$\dot{\delta}$: *The derivative of gimbal angle that it is equal to the angular speed of the gimbal*

Current CMGs are designed with conventional radial flux DC motor. Nowadays, Axial flux DC motor usually uses for wheel motor since axial flux DC motor has higher performance than conventional radial flux DC motor in terms of mass, volume, torque/mass, torque/volume, efficiency and inertia contribution [7]. In this thesis, the control moment gyroscope with outer rotor radial flux DC motor is designed. Outer rotor radial flux DC motor has a little bit more performance characteristics than axial

flux DC motor in terms of torque/mass, torque/volume, efficiency inertia contribution [8] since the rotor is placed at the outer surface of the motor. Structures of radial flux and axial flux DC motor is shown in Figure 2.4.

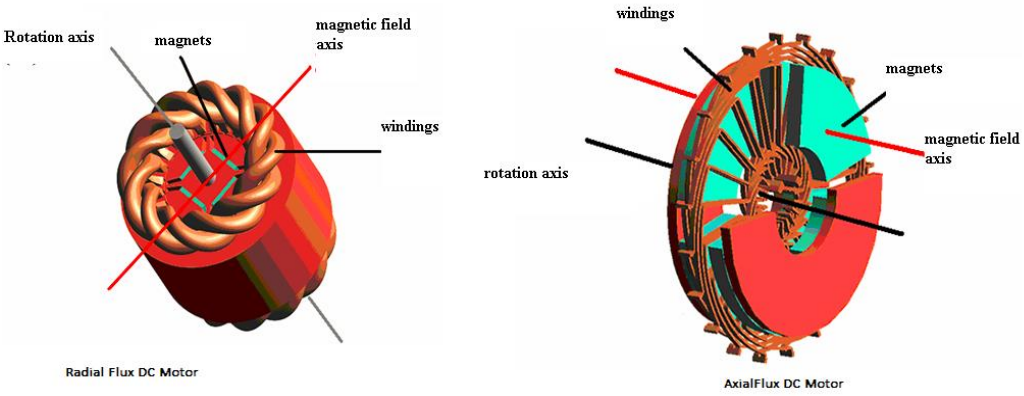

Figure 2.4 Structures of Radial and Axial Flux DC Motor [7]

2.2. Background

2.2.1. Coordinate Definition

X-axis

X-direction indicates the flight direction of the satellite. X-direction is named as *"Roll"* in literature. If the rotation axis of the satellite is x-axis, it is called "Roll axis maneuvering". Roll maneuvering agility of satellite is important since thanks to rapid roll axis maneuvering capability, satellites can acquire many images from a different place on earth. In addition, minus x-direction is called *"Wake "*and plus x-direction is called *"Ram"*.

Y-axis

Y-direction indicates normal of the orbit. Y-direction is named as *"Pitch"* in literature. If the rotation axis of the satellite is y-axis, it is called "Pitch axis maneuvering". Pitch axis maneuvering agility of satellites is important since thanks to rapid pitch axis maneuvering capability, satellites can acquire a lot of different perspective images

from the same place on earth. The example of pitch axis maneuvering and taking images from earth representation is shown in Figure 2.5.

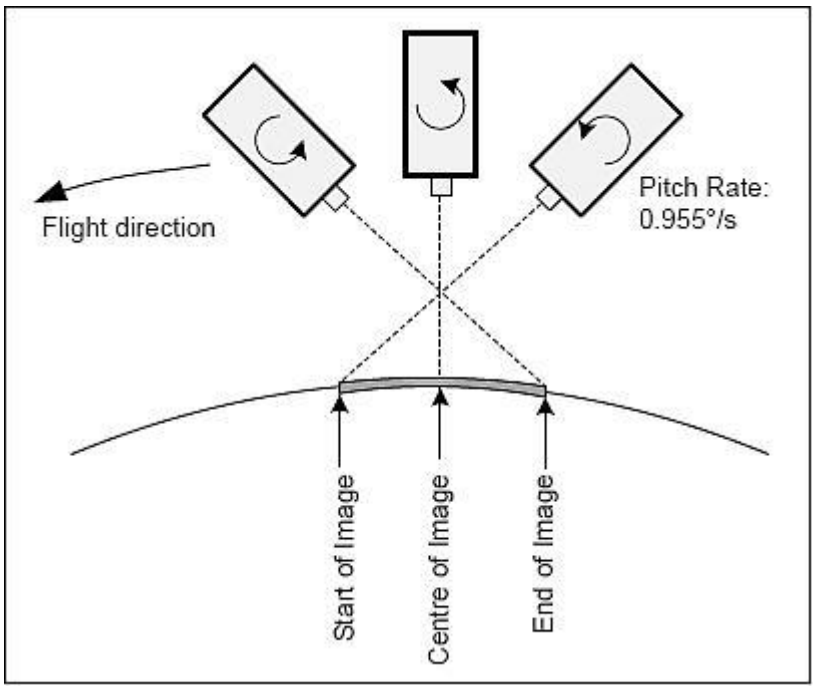

Figure 2.5 The Example of Pitch Axis Maneuvering

Z-axis

Z-direction indicates earth direction. Plus z-direction shows the position of the earth with respect to satellite and minus z- directions shows out of earth direction. Z-direction is named as *"Yaw"* in literature. If the rotation axis of satellites is z-axis, It is called "Yaw axis maneuvering". Thanks to yaw axis maneuvering agility, the orientation of satellites can be provided. Generally, satellites don't need rapid yaw maneuvering agility. In addition, minus z-direction is called *"Zenith "*and plus z-direction is called *"Nadir".*

Satellite coordinate system is shown in Figure 2.6 and Figure 2.7.

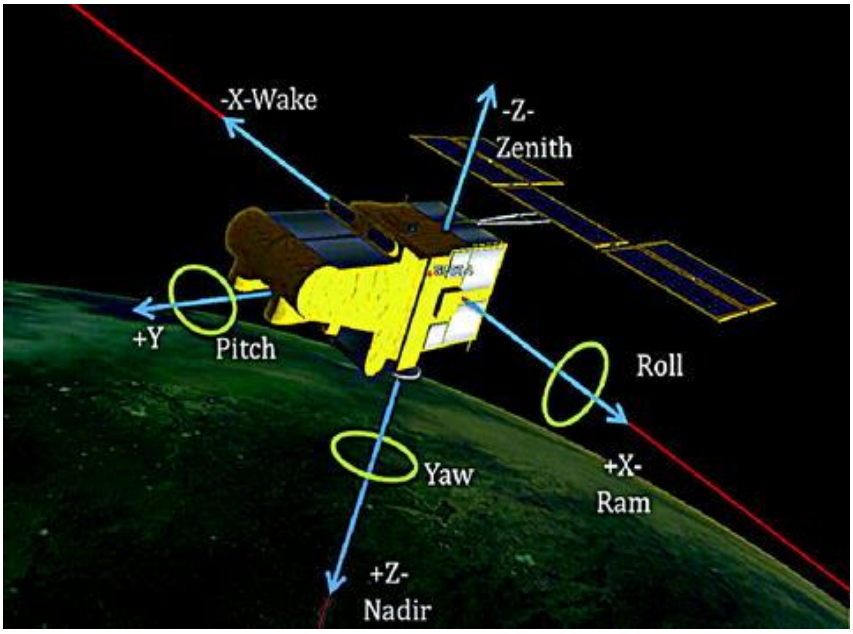

Figure 2.6 Satellite Coordinate System (1)

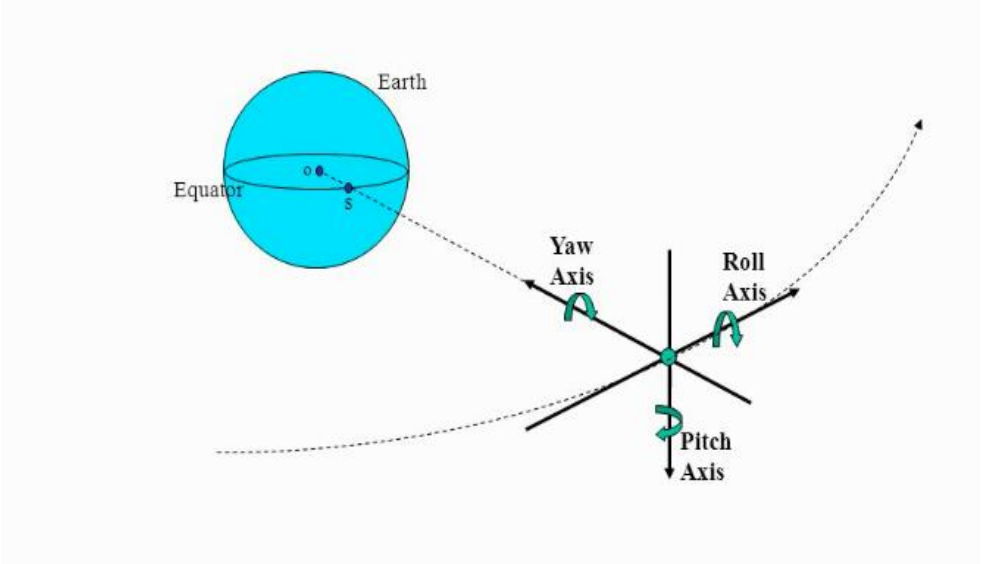

Figure 2.7 Satellite Coordinate System (2)

2.2.2. Classification of Control Moment Gyroscope

The first type of CMG is Single Gimbal Control Moment Gyroscope (SGCMG) shown in Figure 2.8. It has only one gimbal axis and one wheel. Gimbal axis orthogonal to the wheel axis and produced torque is orthogonal to both gimbal and wheel axis. Since the speed of the wheel is constant, the magnitude of angular momentum is constant. Due to gimbal axis rotation, the angular momentum direction changes continuously and torque is produced by changing angular momentum displacement.

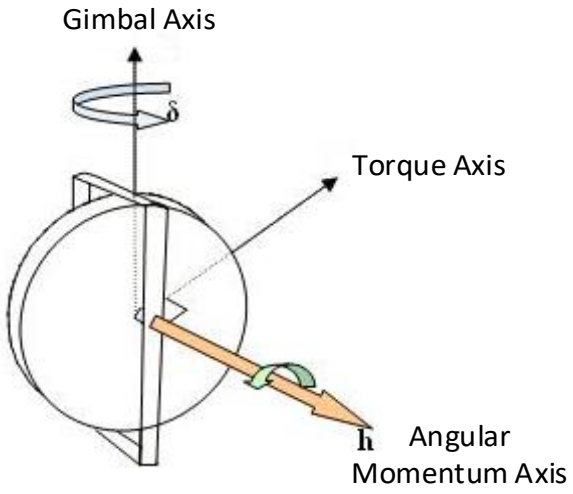

Figure 2.8 Single Gimbal CMG Configuration [9]

The second type of CMG is Double Gimbal Control Moment Gyroscope (DGCMG) shown in Figure 2.9 and Figure 2.10. It has two gimbal axes and one wheel. Gimbal axes are orthogonal to each other and the angular momentum axis is also orthogonal to both gimbal axes. Since the speed of the wheel is constant, the magnitude of angular momentum is constant. Since it has two gimbals, the ability of produced torque direction is wider than SGCMG. Therefore, output torque can be a sphere in 3D space and it is not limited to a plane as in SGCMG. However, the mechanical design of DGCMG is more complex than SGCMG and it has also higher volume and mass [9].

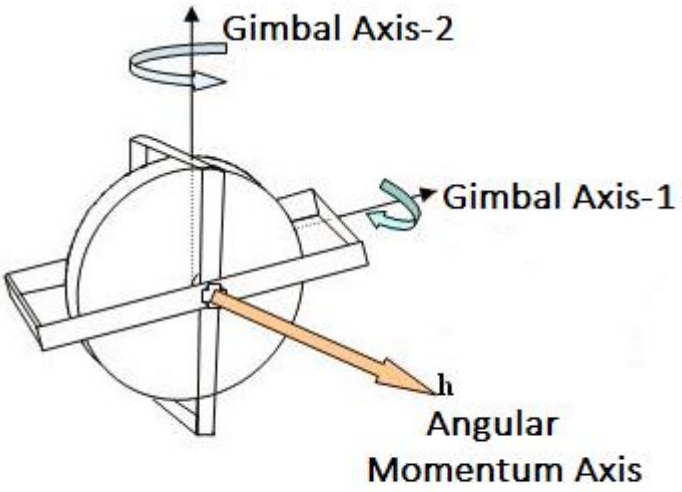

Figure 2.9 Double Gimbal CMG Configuration-1 [9]

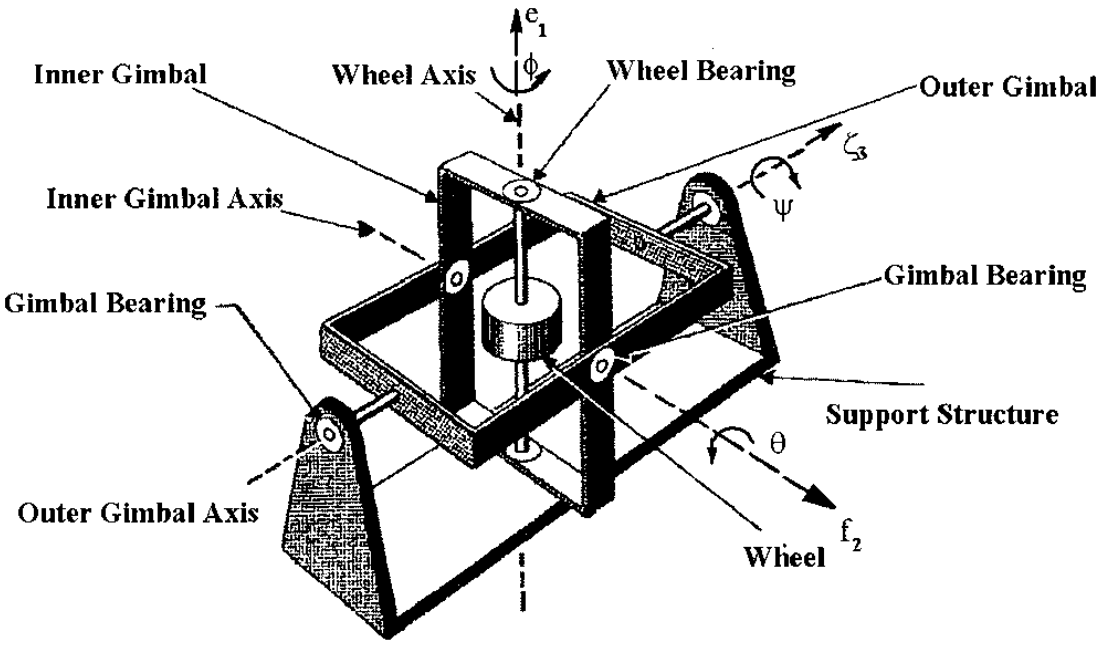

Figure 2.10 Double Gimbal CMG Configuration-2 [6]

The third type of CMG is Variable Speed Control Moment Gyroscope (VSCMG). It can have one or two gimbal axess and one wheel. Speed of wheel is also controlled in this type CMG like a reaction wheel. Therefore, the magnitude and direction of

angular momentum can change. Output torque is produced by both acceleration of wheel and rotation of gimbal. The control algorithm of VSCMG is complicated since two parts (wheel and gimbal) of the equipment are rotating instead of one part compared to other types of CMG and both of them have different control algorithm that needs to be combined. In addition, the mechanical design of wheel and electrical design of wheel motor should be optimized for different speed range and the motor driver should be compatible with different motor speed and torque ranges. Therefore, it has more difficult design than other types of CMG in terms of the control algorithm, mechanically and electrically. It causes reliability problems. Disadvantages and advantages of types of CMGs are summarized in Table 2.3.

Table 2.3 *Advantages and Disadvantages of Types of CMGs [3]*

CMG Type	**Advantage**	**Disadvantage**
SGCMG	Great torque amplification	Singularity
DGCMG	Torque amplification, extra degree of freedom	Cost, complexity, size
VSCMG	Extra degree of control	Reliability

As a result, the SGCMG is the most popular and widely used CMG type due to simple mechanical design and simple control algorithm. Furthermore, the cost of SGCMG is lower and the reserved volume and mass is smaller than other types of CMGs [3]. In this thesis, Single Gimbal Control Moment Gyroscope is selected to study and design because of the mentioned reasons above. The main drawback of SGCMGs is singularity problems. SGCMG does not produce any torque at certain gimbal angle and this condition is called a singularity. One of the solutions of singularity is using pyramidal configuration mentioned in Section 2.3.2.

2.3. Dynamic CMG Equations

The most important feature of CMG is the capacity of output torque and it is obtained from changing the direction of angular momentum with respect to time. Due to the rotation of the gimbal axis, the direction of angular momentum changes and it creates angular momentum and torque components in x, y, and z directions. In this section,

firstly, the derivation of general differential equations of CMG equations are discussed After that, dynamic CMG angular momentum and torque equations are obtained for pyramidal CMG configuration. Finally, simple satellite dynamic equations are shown.

2.3.1. General Differential Equations of CMG

Derivation of general equations is shown below:

Denotations:

H_{CMG} : $Total\ Angular\ Momentum\ of\ CMG$

H_{CMG}^{w} : $Angular\ Momentum\ of\ Wheel$

H_{CMG}^{g} : $Angular\ Momentum\ of\ Gimbal$

I_{CMG}^{w} : $Inertia\ of\ Wheel$

I_{CMG}^{g} : $Inertia\ of\ Gimbal$

ω_w : $Angular\ velocity\ of\ wheel$

$\dot{w}_w$: $Angılar\ acceleration\ of\ wheel$

ω_w : $Angılar\ velocity\ of\ wheel$

δ : $Displacement\ of\ angular\ momentum\ (displacement\ of\ gimbal\ angle)$

$\dot{\delta}$: $Angular\ velocity\ of\ gimbal$

$\ddot{\delta}$: $Angılar\ acceleration\ of\ gimbal$

τ_o : $Total\ output\ torque\ generated\ by\ CMG$

τ_c : $Total\ control\ torque\ generated\ by\ CMG$

τ_{wa} : $Torque\ due\ to\ wheel\ acceleration$

τ_{ga} : $Torque\ due\ to\ gimbal\ acceleration$

τ_f : $Torque\ due\ to\ friction$

Derivation:

Total angular momentum of CMG is equal to the sum of angular momentum of wheel and angular momentum of the gimbal. Total angular momentum equation is expressed in Equation (2.7) [4]

$$H_{CMG} = H_{CMG}^{w} + H_{CMG}^{g} \tag{2.7}$$

Total output torque generated by CMG consists of four components which are total control torque generated by CMG, the torque due to wheel acceleration, the torque due to gimbal acceleration and the torque due to friction. Total control torque generated by CMG is the main component and it is used for satellite maneuvering. Acceleration torques are unwanted disturbances torques of control torque. The torque due to friction includes wheel bearing friction, gimbal bearing friction and slip ring friction. Torque equation is given by [4]

$$\tau_o = \tau_c + \tau_{wa} + \tau_{ga} + \tau_f \tag{2.8}$$

Angular momentum of the rotating system is obtained by multiplying inertia and angular velocity of the system. Angular momentum of the wheel is calculated in Equation (2.9) and angular momentum of gimbal is calculated in Equation (2.10). Total angular momentum of CMG is expressed in Equation (2.11).

$$H_{CMG}^{w} = I_{CMG}^{w}\, \omega_w \tag{2.9}$$

$$H_{CMG}^{g} = I_{CMH}^{g}\, \dot{\delta} \tag{2.10}$$

$$H_{CMG} = I_{CMG}^{w}\, \omega_w + I_{CMG}^{g}\, \dot{\delta} \tag{2.11}$$

By using Euler law, total output torque equation is acquired. Rate of change of total angular momentum is equal to total output torque.

$$\frac{d}{dt}(H_{CMG}) = \frac{d}{dt}\,(I_{CMG}^{w}\, \omega^{w}) + \frac{d}{dt}\left(I_{CMG}^{g}\, \dot{\delta}\right) + \dot{\delta}\, x\, (I_{CMG}^{w}\, \omega^{w} + I_{CMG}^{g}\, \dot{\delta}) \tag{2.12}$$

Since the cross product of $\dot{\delta}\, x(\, I_{CMG}^{g}\, \dot{\delta})$ term is zero, simplified and the final equation is shown below:

$$\frac{d}{dt}(H_{CMG}) = \, (I_{CMG}^{w}\, \dot{\omega}^{w}) + \, \left(I_{CMG}^{g}\, \ddot{\delta}\right) + \dot{\delta}\, x\, (I_{CMG}^{w}\, \omega^{w}) = \tau_{o} \qquad (2.13)$$

$(I_{CMG}^{w}\, \dot{\omega}^{w})$ is corresponding to torque due to wheel acceleration (τ_{wa}).

$\left(I_{CMG}^{g}\, \ddot{\delta}\right)$ is corresponding to torque due to gimbal acceleration (τ_{ga})

$\left(\dot{\delta}\, x\, [I_{CMG}^{w}\, \omega^{w}]\right)$ is corresponding to total control torque (τ_{c})

Equation (2.13) represents a dynamic CMG torque equation. Acceleration torques $(\tau_{wa}\ and\ \tau_{ga})$ occur during generating output control torque. The torque due to wheel acceleration is created when wheel speed accelerates from 0 to nominal speed. At nominal CMG working conditions, since wheel speed is constant, this term is canceled. Both two acceleration torques are very small compared to output control torque in a CMG for large satellites. Therefore, they are not considerable effect for output control torque. For small satellites, these disturbances torques can directly affect the orientation of satellites. Equation (2.13) does not include friction torque components since angular momentum effects of friction torques are not mentioned in Equation (2.11). It can be also written in Equation (2.11) but the angular momentum equation would be more complex. It is already shown in Equation (2.8) that it has a negative impact on output control torque. In addition, friction torque causes small disturbance. However, it can be also ignored for large satellites,

Therefore; for large satellites, the dynamic torque equation can be written as below:

$$\tau_{o} = \tau_{c} = \frac{d}{dt}(H_{CMG}) = \, \dot{\delta}\, x\, (I_{CMG}^{w}\, \omega^{w}) = \dot{\delta}\, x\, H_{CMG}^{w} \qquad (2.14)$$

For n number CMG configuration, total angular momentum H_{CMG} is obtained from the vector sum of each angular momentum contribution individually by functions of $\delta_{i}\ where\ i = 0,1,2,3 \ldots \ldots n$

$$H_{CMG} = \sum_{i=1}^{n} H_{CMG_i}\ (\delta_i) \tag{2.15}$$

The output torque can be obtained by taking a derivative of Equation (2.15) with respect to time and the relationship between angular momentum vector and gimbal angle is expressed below.

$$\frac{d}{dt}\ H_{CMG} = \frac{d}{dt}\sum_{i=1}^{n} H_{CMG_i}\ (\delta_i) = \tau_o \tag{2.16}$$

$$\dot{\vec{H}}_{CMG} = \vec{J}(\delta)\dot{\vec{\delta}} = \vec{\tau}_o \tag{2.17}$$

$\vec{J}(\delta)$ is 3 x n Jacobian matrix. "3" represents x, y, and z directions and n represents the number of CMG used in the satellite. Therefore, the matrix form of Equation (2.17) is shown in Equation (2.19)

$$\vec{J}(\delta) = \frac{\partial \vec{H}_{CMG}}{\partial \delta} = \left[\frac{\partial H_{CMG_i}}{\partial \delta_j}\right] \tag{2.18}$$

$$\begin{bmatrix} \dot{H}_{CMG_x} \\ \dot{H}_{CMG_y} \\ \dot{H}_{CMG_z} \end{bmatrix} = \begin{bmatrix} \frac{\partial H_{CMG_x}}{\partial \delta_1} & \frac{\partial H_{CMG_x}}{\partial \delta_2} & \frac{\partial H_{CMG_x}}{\partial \delta_3} & \cdots & \frac{\partial H_{CMG_x}}{\partial \delta_n} \\ \frac{\partial H_{CMG_y}}{\partial \delta_1} & \frac{\partial H_{CMG_y}}{\partial \delta_2} & \frac{\partial H_{CMG_y}}{\partial \delta_3} & \cdots & \frac{\partial H_{CMG_y}}{\partial \delta_n} \\ \frac{\partial H_{CMG_z}}{\partial \delta_1} & \frac{\partial H_{CMG_z}}{\partial \delta_2} & \frac{\partial H_{CMG_z}}{\partial \delta_3} & \cdots & \frac{\partial H_{CMG_z}}{\partial \delta_n} \end{bmatrix} \begin{bmatrix} \dot{\delta}_1 \\ \dot{\delta}_2 \\ \dot{\delta}_3 \\ . \\ . \\ . \\ \dot{\delta}_n \end{bmatrix} = \begin{bmatrix} \tau_{o_x} \\ \tau_{o_y} \\ \tau_{o_z} \end{bmatrix} \tag{2.19}$$

2.3.2. Pyramidal Configuration of CMG

During space mission, actuators used in the satellite have two main features. Firstly, placed CMGs in the satellite should have one axis control capability. In other words, satellite should do maneuvering on x,y, and z axes independently. Therefore, CMG configuration does not have any torque components on the other two axes when one axis control command is received. Secondly, the control algorithm and CMG configuration should overcome the singularity problem. A singularity is encountered when there is some condition during space mission that CMG configuration is not

capable of producing torque. This occurs for a particular direction in the body frame when the spin axes of all CMGs in the cluster are either maximally or minimally projected in that direction [4]. In other words, there is some condition that all vector components of output torque remain on the same plane and no output torque is generated the direction of normal of this plane [9].

Total angular momentum and torque direction of one CMG does not have the capability to manage three-axis maneuvering due to spin axis limitation. In order to have three-axis maneuvering capability, at least three CMGs are required. However, three CMG configuration causes singularity problems [9]. In order to overcome the singularity problem, a lot of control algorithms such as steering law are developed but they are not scoped of this thesis. In addition, many CMG configurations are developed to have redundancy, three-axis maneuvering capability and to overcome singularity problem. Pyramidal CMG configuration is studied in this thesis since it is the most popular configuration that overcomes singularity problem and provide redundancy. There are four SGCMGs in this configuration. Angular momentum and torque envelope are nearly spherical and each axis has almost the same momentum capability [12]. Each face of the pyramid is inclined with the pyramid skew angle of $\beta=54.73^{o}$ to the horizontal. The pyramidal configuration is shown in Figure 2.11.

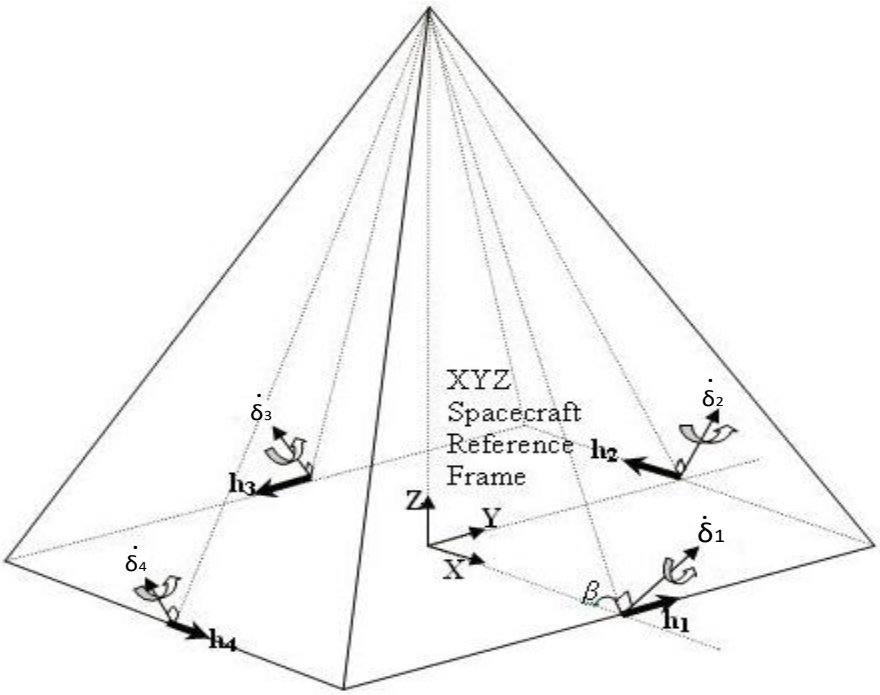

Figure 2.11 Pyramidal CMG Configuration [9]

Equivalent dynamic angular momentum matrix is written easily by analyzing pyramid geometry. Dynamic angular momentum matrix and Jacobian matrix are expressed in Equations (2.23) and (2.24)

H_0 : $Magnitude\ of\ Angular\ Momentum$

$$\vec{H}_{CMG_1}=\begin{bmatrix} H_{CMG_{1x}} \\ H_{CMG_{1y}} \\ HCMG_{1z} \end{bmatrix} = H_0 \begin{bmatrix} -cos\beta sin\delta_1 \\ cos\delta_1 \\ sin\beta sin\delta_1 \end{bmatrix}$$

$$\vec{H}_{CMG_2}=\begin{bmatrix} H_{CMG_{2x}} \\ H_{CMG_{2y}} \\ HCMG_{2z} \end{bmatrix} = H_0 \begin{bmatrix} -cos\delta_2 \\ -cos\beta sin\delta_2 \\ sin\beta sin\delta_2 \end{bmatrix}$$

$$\vec{H}_{CMG_3}=\begin{bmatrix} H_{CMG_{3x}} \\ H_{CMG_{3y}} \\ HCMG_{3z} \end{bmatrix} = H_0 \begin{bmatrix} cos\beta sin\delta_3 \\ -cos\delta_3 \\ sin\beta sin\delta_3 \end{bmatrix}$$

$$\vec{H}_{CMG_4}=\begin{bmatrix} H_{CMG_{4x}} \\ H_{CMG_{4y}} \\ HCMG_{4z} \end{bmatrix} = H_0 \begin{bmatrix} cos\delta_4 \\ cos\beta sin\delta_4 \\ sin\beta sin\delta_4 \end{bmatrix}$$

$$\vec{H}_{CMG} = \vec{H}_{CMG_1} + \vec{H}_{CMG_2} + \vec{H}_{CMG_3} + \vec{H}_{CMG_4} \tag{2.20}$$

$$\begin{bmatrix} H_{CMG_x} \\ H_{CMG_y} \\ H_{CMG_z} \end{bmatrix} = H_0 \begin{bmatrix} -cos\beta sin\delta_1 \\ cos\delta_1 \\ sin\beta sin\delta_1 \end{bmatrix} + H_0 \begin{bmatrix} -cos\delta_2 \\ -cos\beta sin\delta_2 \\ sin\beta sin\delta_2 \end{bmatrix} + H_0 \begin{bmatrix} cos\beta sin\delta_3 \\ -cos\delta_3 \\ sin\beta sin\delta_3 \end{bmatrix} + H_0 \begin{bmatrix} cos\delta_4 \\ cos\beta sin\delta_4 \\ sin\beta sin\delta_4 \end{bmatrix} \tag{2.21}$$

$$\begin{bmatrix} H_{CMG_x} \\ H_{CMG_y} \\ H_{CMG_z} \end{bmatrix} = H_0 \begin{bmatrix} -cos\beta sin\delta_1 - cos\delta_2 + cos\beta sin\delta_3 + cos\delta_4 \\ cos\delta_1 - cos\beta sin\delta_2 - cos\delta_3 + cos\beta sin\delta_4 \\ sin\beta sin\delta_1 + sin\beta sin\delta_2 + sin\beta sin\delta_3 + sin\beta sin\delta_4 \end{bmatrix} \tag{2.22}$$

$$\vec{J}(\delta) = H_0 \begin{bmatrix} -cos\beta cos\delta_1 & sin\delta_2 & cos\beta cos\delta_3 & -sin\delta_4 \\ -sin\delta_1 & -cos\beta cos\delta_2 & sin\delta_3 & cos\beta cos\delta_4 \\ sin\beta cos\delta_1 & sin\beta cos\delta_2 & sin\beta cos\delta_3 & sin\beta cos\delta_4 \end{bmatrix} \tag{2.23}$$

$$\begin{bmatrix} \dot{H}_{CMG_x} \\ \dot{H}_{CMG_y} \\ \dot{H}_{CMG_z} \end{bmatrix} = H_0 \begin{bmatrix} -cos\beta cos\delta_1 & sin\delta_2 & cos\beta cos\delta_3 & -sin\delta_4 \\ -sin\delta_1 & -cos\beta cos\delta_2 & sin\delta_3 & cos\beta cos\delta_4 \\ sin\beta cos\delta_1 & sin\beta cos\delta_2 & sin\beta cos\delta_3 & sin\beta cos\delta_4 \end{bmatrix} \begin{bmatrix} \dot{\delta}_1 \\ \dot{\delta}_2 \\ \dot{\delta}_3 \\ \dot{\delta}_4 \end{bmatrix} \tag{2.24}$$

The time derivative of the angular momentum vector is equal to the dynamic torque vector. Therefore, the dynamic torque equation for pyramidal configuration is shown in Equations (2.25), (2.26) and (2.27).

$$\begin{bmatrix} \dot{H}_{CMG_x} \\ \dot{H}_{CMG_y} \\ \dot{H}_{CMG_z} \end{bmatrix} = \begin{bmatrix} \tau_{o_x} \\ \tau_{o_y} \\ \tau_{o_z} \end{bmatrix}$$

$$T_{o_x} = H_0 \left(-\dot{\delta}_1 cos\beta cos\delta_1 + \dot{\delta}_2 sin\delta_2 + \dot{\delta}_3 cos\beta cos\delta_3 - \dot{\delta}_4 sin\delta_4\right) \tag{2.25}$$

$$T_{0_y} = H_o \left(-\dot{\delta}_1 sin\delta_1 - \dot{\delta}_2 cos\beta cos\delta_2 + \dot{\delta}_3 sin\delta_3 + \dot{\delta}_4 cos\beta cos\delta_4\right) \tag{2.26}$$

$$T_{o_z} = H_0 \left(\dot{\delta}_1 sin\beta cos\delta_1 + \dot{\delta}_2 sin\beta cos\delta_2 + \dot{\delta}_3 sin\beta cos\delta_3 + \dot{\delta}_4 sin\beta cos\delta_4\right) \tag{2.27}$$

In order to obtain only x-axis output torque, angular velocities of gimbals are taken $\dot{\delta}_2 = \dot{\delta}_4 = 0 \; and \; \dot{\delta}_3 = -\dot{\delta}_1 = \dot{\delta}$. As a result of this case, pyramidal CMG configuration does not have y and z-direction torque. Satellite is affected by only x-direction torque and it has only x-direction maneuvering capability.

Equivalent output torque of x-direction is expressed in Equation (2.28).

$$T_{O_x} = 2H_0\dot{\delta}cos\beta cos\delta \quad (2.28)$$

In order to obtain only y-axis output torque, angular velocities of gimbals are taken

$\dot{\delta}_1 = \dot{\delta}_3 = 0\ and\ \dot{\delta}_4 = -\dot{\delta}_2 = \dot{\delta}$. As a result of this case, pyramidal CMG configuration does not have x and z-direction torque. Satellite is affected by only y-direction torque and it has only y direction maneuvering capability.

Equivalent output torque of y-direction is expressed in Equation (2.29).

$$T_{O_y} = 2H_0\dot{\delta}cos\beta cos\delta \quad (2.29)$$

In order to obtain only z-axis output torque, angular velocities of gimbals are taken

$\dot{\delta}_1 = \dot{\delta}_3 = 0\ and\ \dot{\delta}_4 = \dot{\delta}_2 = \dot{\delta}$ or $\dot{\delta}_2 = \dot{\delta}_4 = 0\ and\ \dot{\delta}_3 = \dot{\delta}_1 = \dot{\delta}$. As a result of this case, pyramidal CMG configuration does not have x and y-direction torque. Satellite is affected by only z-direction torque and it has only z-direction maneuvering capability.

Equivalent output torque of z direction is expressed in Equation (2.30).

$$T_{O_z} = 2H_0\delta\ sin\beta cos\delta \quad (2.30)$$

2.3.3. Simple Satellite Dynamics Equations

To understand the effect of CMG torque on satellite, simple satellite dynamic equations are derived. Simple satellite equations are also the first significant issue to establish an attitude control algorithm. Total angular momentum vector of the satellite is equal to the sum of body angular momentum vector and CMG angular momentum vector.

Denotations:

H_{st}: $Total\ angular\ momentum\ of\ satellite\ with$

$respect\ to\ body\ fixed\ axis\ (x, y, z\ axis)$

I_{st}: $Total\ inertia\ of\ satellite$

ω_{st}: $Angular\ velocity\ of\ satellite$

$\dot{\omega}_{st}$: $Angular\ acceleration\ \ of\ satellite$

θ_{st}: $Displacement\ angle\ of\ satellite$

τ_{ext}: $\ External\ torque\ acting\ on\ satellite$

Angular momentum and torque relationship equation for the satellite system is given by [13].

$$\mathrm{H_{st}} = I_{st}\omega_{st} + H_{CMG} \tag{2.31}$$

$$\dot{\mathrm{H}}_{st} + \omega_{st}\ x\ H_{st} = \tau_{ext} \tag{2.32}$$

External torque acting on satellite consists of solar pressure, gravity gradient and aerodynamics torque.

Substituting Equation (2.31) into Equation (2.32) and the following equation is obtained.

$$\mathrm{I_{st}}\dot{\omega}_{st} + \dot{H}_{CMG} + \omega_{st}\ x\ (I_{st}\omega_{st} + H_{CMG}) = \tau_{ext} \tag{2.33}$$

Rearranging Equation (2.33) by expressing total output torque generated by CMG (τ_o) and the following equations are expressed.

$$\mathrm{I_{st}}\dot{\omega}_{st} + \ \omega_{st}\ x\ (I_{st}\omega_{st}) = \tau_{ext} - \dot{H}_{CMG} - \omega_{st}\ x\ H_{CMG} \tag{2.34}$$

$$-\dot{H}_{CMG} - \omega_{st}\ x\ H_{CMG} = \tau_o \tag{2.35}$$

$$\mathrm{I_{st}}\dot{\omega}_{st} + \ \omega_{st}\ x\ (I_{st}\omega_{st}) = \tau_{ext} + \tau_o \tag{2.36}$$

Equation (2.35) and Equation (2.36) are differential kinematic equations of the satellite. The relationship between satellite and CMG can be acquired by combining CMG equations which are mentioned in Section2.3.2 and these two equations.

Satellite attitude control algorithm starts with this relation after that control methods are applied to rotate satellite.

2.4. Conclusion

In this chapter, satellite actuators that are used for satellite maneuvering are defined and compared. The importance of using CMG is explained. It is obvious that the satellite which has CMG configuration is called agile satellite. The coordinate system is defined purely to understand the relationship between satellite and space. Types of CMGs are discussed in terms of advantages and disadvantages. SGCMG is selected to study in this thesis. General differential equations for one SGCMG are derived and it concluded that output torque capacity of CMG depends on gimbal speed and angular momentum of wheel. In order to get rid of singularity and obtain three axes control capability, pyramidal CMG configuration is selected. Equations of pyramidal configuration are explained and derived step by step. These equations will be used in CHAPTER 3 to determine the relationship between output torque and satellite maneuvering. In addition, calculation of required angular momentum, output torque of CMG, and determining wheel dimensions will be based on these equations in CHAPTER 5 and CHAPTER 6. Finally, the effect of output torque on satellite orientation is shown by simple satellite dynamic equations

CHAPTER 3

MATHEMATICAL MODEL RESULTS IN ORBIT APPLICATIONS

3.1. Problem Definition

The aim of this thesis is to design single gimbal control moment gyroscope (SGCMG) with outer rotor radial flux DC motor. Mathematical model simulation is created for three different size satellites (large, medium, and small) and two different CMG torque value (1Nm and 2Nm) to observe agility of satellite. Therefore, mathematical models are created for six cases. Mathematical models are evaluated in terms satellite maneuvering angle and maneuvering durations.

Same torque value of CMG is applied three different size satellite and agility of satellites is observed. Mathematical model results show that although the same torque value is applied to satellites, the agility of satellites is different from each other since mass and moment of inertia of satellite are different. In other words, a satellite that has higher mass and higher moment of inertia has lower agility.

If the higher CMG output torque is applied to satellite, maneuvering duration can be decreased and more agile satellite can be obtained. However, increasing output torque causes increasing size of the wheel. Increasing the size of the wheel means that CMG has higher volume and mass and higher volume and mass are critical disadvantage for space applications. Therefore, CMG design should be optimized in terms of mass, volume and maneuvering durations requirements

In order to optimize CMG volume and mass, required maneuvering capability should be determined. Following mathematical models are created to compare agility of satellites and to select optimum CMG for the proper satellite.

Mathematical models are created at the following conditions;

- Three different size satellites (large, medium, and small) represent previous satellite programs developed in Turkey. Large satellite is Gokturk-1, medium satellite is IMECE, and small satellite is Gokturk-2
- Maneuvering duration for 5, 10, 15, 20, 25, 30, 35, 40, 45, 50, 60, 70, 80, 90 degree maneuvering at x, y, z axes are calculated separately for two different torque capacity 1Nm and 2 Nm.
- 4 different CMGs are used, and they are placed at pyramidal configuration.
- Maneuvering duration is calculated at two different orientation error 0.01° and 0.02°. Orientation error shows the accuracy of the control system and the settling time of satellites.
- Satellite model is supposed to be rigid and non-rigid effects are neglected.
- External distortion torques and uncertainty inertia are neglected.
- Limitation of CMG is neglected.

3.2. Mathematical Model Results of Large Satellite for 1Nm CMG (>1000kg)

Satellite's moment of inertia matrix taken in this simulation model is given in the following expression for large satellite. Moment of inertia matrix is diagonal and it shows x,y, and z axes inertia separately.

$$I_{st} = \begin{bmatrix} I_{st_x} & 0 & 0 \\ 0 & I_{st_y} & 0 \\ 0 & 0 & I_{st_z} \end{bmatrix} = \begin{bmatrix} 560 & 0 & 0 \\ 0 & 1020 & 0 \\ 0 & 0 & 1000 \end{bmatrix} kgm^2$$

The maximum torque of one CMG is taken as 1 Nm in this model. The results of the mathematical model for this case is shown in Table 3.1.

Table 3.1 *Mathematical Model Results of Large Satellite for 1Nm Output Torque*

Roll (x-axis) (deg)	Pitch (y-axis) (deg)	Yaw (z-axis) (deg)	Maneuvering Duration (s) Error < 0,02°	Maneuvering Duration (s) Error < 0,01°
5	0	0	12,6	13,25
10	0	0	19	19,95
15	0	0	23,5	24,5
20	0	0	27,85	28,95
25	0	0	32	33,3
30	0	0	35,35	36,7
35	0	0	38,55	39,9
40	0	0	41,25	42,6
45	0	0	44,45	45,95
50	0	0	46,85	48,25
60	0	0	52	53,45
70	0	0	57	58,5
80	0	0	62,15	63,75
90	0	0	67,45	69,2
0	5	0	14,85	15,55
0	10	0	22,5	23,45
0	15	0	27,6	28,5
0	20	0	33,15	34,25
0	25	0	36,95	37,95
0	30	0	41,2	42,3
0	35	0	45,5	46,85
0	40	0	48,45	49,6
0	45	0	51,95	53,2
0	50	0	54,7	55,9
0	60	0	60,75	62
0	70	0	67,9	69,4
0	80	0	73,75	75,35
0	90	0	79,55	81,2
0	0	5	15,4	16,15
0	0	10	22,7	23,6
0	0	15	28,3	29,25
0	0	20	33,55	34,55
0	0	25	38	39,1
0	0	30	41,95	43,05
0	0	35	45,95	47,15
0	0	40	49,75	51
0	0	45	52,95	54,2
0	0	50	56,6	58
0	0	60	62,1	63,4
0	0	70	68,65	70,15
0	0	80	75,15	76,75
0	0	90	81,45	83,2

3.3. Mathematical Model Results of Large Satellite for 2Nm CMG (>1000kg)

Satellite's moment of inertia matrix taken in this simulation model is given in the following expression for large satellite. Moment of inertia matrix is diagonal and it shows x,y, and z axes inertia separately.

$$I_{st} = \begin{bmatrix} I_{st_x} & 0 & 0 \\ 0 & I_{st_y} & 0 \\ 0 & 0 & I_{st_z} \end{bmatrix} = \begin{bmatrix} 560 & 0 & 0 \\ 0 & 1020 & 0 \\ 0 & 0 & 1000 \end{bmatrix} kgm^2$$

The maximum torque of one CMG is taken as 2 Nm in this model. The results of the mathematical model for this case is shown in Table 3.2

Table 3.2 *Mathematical Model Results of Large Satellite for 2Nm Output Torque*

Roll (x-axis) (deg)	**Pitch (y-axis) (deg)**	**Yaw (z-axis) (deg)**	**Maneuvering Duration (s) Error < 0,02°**	**Maneuvering Duration (s) Error < 0,01°**
5	0	0	9,1	9,65
10	0	0	13,2	13,85
15	0	0	17,25	18,15
20	0	0	19,6	20,35
25	0	0	23,1	24,2
30	0	0	25,5	26,6
35	0	0	27,45	28,5
40	0	0	29,8	30,95
45	0	0	31,4	32,45
50	0	0	33,2	34,25
60	0	0	37,1	38,25
70	0	0	40,9	42,15
80	0	0	45,1	46,5
90	0	0	48,85	50,4
0	5	0	10,5	11
0	10	0	16,3	17,1
0	15	0	20,4	21,3
0	20	0	24,05	25,05
0	25	0	27,25	28,25
0	30	0	30,5	31,65
0	35	0	32,3	33,25
0	40	0	34,7	35,65
0	45	0	37,55	38,6
0	50	0	40,7	42
0	60	0	44,95	46,25
0	70	0	49,1	50,4
0	80	0	53,5	54,9
0	90	0	57,4	58,75
0	0	5	11,2	11,85
0	0	10	16,8	17,7
0	0	15	20,7	21,55
0	0	20	24,05	24,9
0	0	25	28	29,15
0	0	30	31,05	32,2
0	0	35	33,75	34,95
0	0	40	35,95	37,05
0	0	45	38,55	39,75
0	0	50	41,45	42,8
0	0	60	45,3	46,5
0	0	70	50,2	51,55
0	0	80	54,2	55,5
0	0	90	58,7	60,1

3.4. Mathematical Model Results of Medium Satellite for 1Nm CMG (500kg-1000kg)

Satellite's moment of inertia matrix taken in this simulation model is given in the following expression for medium satellite. Moment of inertia matrix is diagonal and it shows x,y, and z axes inertia separately.

$$I_{st} = \begin{bmatrix} I_{st_x} & 0 & 0 \\ 0 & I_{st_y} & 0 \\ 0 & 0 & I_{st_z} \end{bmatrix} = \begin{bmatrix} 598.94 & 0 & 0 \\ 0 & 481.98 & 0 \\ 0 & 0 & 374.43 \end{bmatrix} kgm^2$$

The maximum torque of one CMG is taken as 1 Nm in this model. The results of the mathematical model for this case is shown in Table 3.3.

Table 3.3 *Mathematical Model Results of Medium Satellite for 1Nm Output Torque*

Roll (x-axis) (deg)	Pitch (y-axis) (deg)	Yaw (z-axis) (deg)	Maneuvering Duration (s) Error < 0,02°	Maneuvering Duration (s) Error < 0,01°
5	0	0	12,65	13,25
10	0	0	19,15	19,95
15	0	0	23,85	24,7
20	0	0	28,55	29,65
25	0	0	32,15	33,25
30	0	0	36,05	37,3
35	0	0	39,85	41,25
40	0	0	42,05	43,3
45	0	0	45,95	47,45
50	0	0	47,8	49,1
60	0	0	53,2	54,6
70	0	0	58,5	59,95
80	0	0	62,75	64,1
90	0	0	67,4	68,85
0	5	0	10,1	10,5
0	10	0	15,5	16,15
0	15	0	19,1	19,75
0	20	0	22,05	22,7
0	25	0	25,55	26,35
0	30	0	28	28,8
0	35	0	31,25	32,25
0	40	0	32,85	33,75
0	45	0	36,05	37,1
0	50	0	38,3	39,45
0	60	0	42,1	43,3
0	70	0	47	48,4
0	80	0	50	60,5
0	90	0	53,8	66,75
0	0	5	9,65	10,2
0	0	10	14,3	15
0	0	15	17,45	18,05
0	0	20	20,7	21,4
0	0	25	23,35	24,05
0	0	30	25,9	26,7
0	0	35	28,1	28,85
0	0	40	30,8	31,75
0	0	45	32,75	33,65
0	0	50	34,95	35,9
0	0	60	38,55	39,45
0	0	70	43,2	44,4
0	0	80	45,95	47
0	0	90	50,6	51,85

3.5. Mathematical Model Results of Medium Satellite for 2Nm CMG (500kg-1000kg)

Satellite's moment of inertia matrix taken in this simulation model is given in the following expression for medium satellite. Moment of inertia matrix is diagonal and it shows x,y, and z axes inertia separately.

$$I_{st} = \begin{bmatrix} I_{st_x} & 0 & 0 \\ 0 & I_{st_y} & 0 \\ 0 & 0 & I_{st_z} \end{bmatrix} = \begin{bmatrix} 598.94 & 0 & 0 \\ 0 & 481.98 & 0 \\ 0 & 0 & 374.43 \end{bmatrix} kgm^2$$

The maximum torque of one CMG is taken as 2 Nm in this model. The results of the mathematical model for this case is shown in Table 3.4

Table 3.4 *Mathematical Model Results of Medium Satellite for 2Nm Output Torque*

Roll (x-axis) (deg)	Pitch (y-axis) (deg)	Yaw (z-axis) (deg)	Maneuvering Duration (s) Error < 0,02°	Maneuvering Duration (s) Error < 0,01°
5	0	0	9,45	10,05
10	0	0	13,95	14,7
15	0	0	17,7	18,55
20	0	0	20,55	21,45
25	0	0	23,7	24,8
30	0	0	25,75	26,7
35	0	0	28,4	29,5
40	0	0	30,45	31,55
45	0	0	32,85	34,05
50	0	0	34,3	35,35
60	0	0	38,75	40
70	0	0	41,85	43,05
80	0	0	45,45	46,65
90	0	0	47,75	48,8
0	5	0	7,45	7,9
0	10	0	10,5	10,85
0	15	0	13,8	14,35
0	20	0	15,9	16,45
0	25	0	18,05	18,65
0	30	0	19,95	20,55
0	35	0	22,4	23,2
0	40	0	24,15	25
0	45	0	25	25,8
0	50	0	27,25	28,15
0	60	0	30,9	31,95
0	70	0	32,15	39,75
0	80	0	35,2	43,35
0	90	0	38,25	46,95
0	0	5	6,85	7,25
0	0	10	10,15	10,65
0	0	15	12,65	13,15
0	0	20	14,65	15,15
0	0	25	16,6	17,15
0	0	30	19,35	20,2
0	0	35	20,35	21,05
0	0	40	21,75	22,35
0	0	45	23,35	24,05
0	0	50	25,2	26
0	0	60	27,95	28,75
0	0	70	30,55	31,4
0	0	80	33,85	34,8
0	0	90	36,05	36,95

3.6. Mathematical Model Results of Small Satellite for 1Nm CMG (100kg-500kg)

Satellite's moment of inertia matrix taken in this simulation model is given in the following expression for small satellite. Moment of inertia matrix is diagonal and it shows x,y, and z axes inertia separately.

$$I_{st} = \begin{bmatrix} I_{st_x} & 0 & 0 \\ 0 & I_{st_y} & 0 \\ 0 & 0 & I_{st_z} \end{bmatrix} = \begin{bmatrix} 139.6 & 0 & 0 \\ 0 & 140 & 0 \\ 0 & 0 & 158.1 \end{bmatrix} kgm^2$$

The maximum torque of one CMG is taken as 1 Nm in this model. The results of the mathematical model for this case is shown in Table 3.5.

Table 3.5 *Mathematical Model Results of Small Satellite for 1Nm Output Torque*

Roll (x-axis) (deg)	Pitch (y-axis) (deg)	Yaw (z-axis) (deg)	Maneuvering Duration (s) Error < 0,02°	Maneuvering Duration (s) Error < 0,01°
5	0	0	6,35	6,75
10	0	0	9,65	10,2
15	0	0	11,95	12,5
20	0	0	14,65	15,4
25	0	0	16,3	17,05
30	0	0	17,45	18,1
35	0	0	19,05	19,7
40	0	0	21,05	21,85
45	0	0	22,05	22,8
50	0	0	24,5	25,55
60	0	0	25,95	26,7
70	0	0	28,6	29,4
80	0	0	30,75	31,6
90	0	0	32,3	39,05
0	5	0	5,5	5,8
0	10	0	8,05	8,6
0	15	0	10,25	11,3
0	20	0	12,3	14,55
0	25	0	15,55	17,1
0	30	0	16,6	18,6
0	35	0	18,75	20,65
0	40	0	20,05	22,15
0	45	0	22,55	24,45
0	50	0	23,1	25,4
0	60	0	26,8	29
0	70	0	30	32,3
0	80	0	33,25	35,65
0	90	0	36,2	38,75
0	0	5	5,95	6,3
0	0	10	8,65	10,6
0	0	15	11,3	13,5
0	0	20	14,65	16,3
0	0	25	17	18,7
0	0	30	19,45	21,15
0	0	35	21,1	22,95
0	0	40	21,85	24,2
0	0	45	23,85	26,2
0	0	50	25,4	27,85
0	0	60	27,5	30,7
0	0	70	27,25	33,15
0	0	80	30,2	31,1
0	0	90	33,65	34,6

3.7. Mathematical Model Results of Small Satellite for 2 Nm CMG (100kg-500kg)

Satellite's moment of inertia matrix taken in this simulation model is given in the following expression for small satellite. Moment of inertia matrix is diagonal and it shows x,y, and z axes inertia separately.

$$I_{st} = \begin{bmatrix} I_{st_x} & 0 & 0 \\ 0 & I_{st_y} & 0 \\ 0 & 0 & I_{st_z} \end{bmatrix} = \begin{bmatrix} 139.6 & 0 & 0 \\ 0 & 140 & 0 \\ 0 & 0 & 158.1 \end{bmatrix} kgm^2$$

The maximum torque of one CMG is taken as 2 Nm in this model. The results of the mathematical model for this case is shown in Table 3.6.

Table 3.6 *Mathematical Model Results of Small Satellite for 2Nm Output Torque*

Roll (x-axis) (deg)	**Pitch (y-axis) (deg)**	**Yaw (z-axis) (deg)**	**Maneuvering Duration (s) Error < 0,02°**	**Maneuvering Duration (s) Error < 0,01°**
5	0	0	4,6	4,95
10	0	0	6,75	7,1
15	0	0	8,8	9,35
20	0	0	10	10,45
25	0	0	11,8	12,45
30	0	0	13,05	13,7
35	0	0	14,55	15,35
40	0	0	15,25	16
45	0	0	16,1	16,75
50	0	0	17	17,7
60	0	0	19,05	19,8
70	0	0	21,05	21,85
80	0	0	21,5	22,1
90	0	0	22,75	27,6
0	5	0	3,9	4,1
0	10	0	5,8	6,15
0	15	0	7,55	8
0	20	0	8,95	10,3
0	25	0	10,1	11,65
0	30	0	12,4	13,55
0	35	0	13,7	14,9
0	40	0	14,55	15,9
0	45	0	14,9	16,6
0	50	0	16,95	18,35
0	60	0	18,75	20,35
0	70	0	21,5	23,05
0	80	0	23,35	25,1
0	90	0	25,55	27,4
0	0	5	4,1	4,4
0	0	10	6,25	6,95
0	0	15	8,85	9,85
0	0	20	9,65	10,4
0	0	25	11,2	12,8
0	0	30	12,35	14,1
0	0	35	14,9	16,2
0	0	40	14,4	16,45
0	0	45	15,55	17,85
0	0	50	16,4	18,95
0	0	60	20,35	22,2
0	0	70	21,2	23,85
0	0	80	21,5	22,15
0	0	90	24,7	25,65

3.8. Conclusion

In order to understand the relationship between the satellite size and the output CMG torque, mathematical models are presented. Mathematical models are based on the satellite control algorithm of TUBITAK UZAY. The control algorithm is developed by AOCS (Attitude and Orbit Control System) team in TUBITAK UZAY for previous satellite programs. It was complicated and it is not scoped in this thesis. Results of the mathematical model are only taken into consideration to analyze satellite's maneuvering capability. Three different size satellites which are designed in this country are used in the mathematical model. Two different actuator torques (1 Nm and 2 Nm) are applied to these satellites. Maneuvering durations for x, y, and z-direction are calculated at different maneuvering angle of satellites (5º, 10 º, 15 º, 20º, 25 º, 30 º, 35 º, 40 º, 45 º, 50 º, 60º, 70 º, 80 º, 90 º) and they are shown in from Table 3.1 to Table 3.6.

Maneuvering duration is directly related to the moment of inertia of satellite. Moments of inertia of satellites are given for x,y, and z axes from Section 3.2 to Section 3.7. If the inertia of satellite is increased, maneuvering duration takes longer.

Although the mass of a large satellite is higher than medium satellite, the moment of inertia of the large satellite on x-axis is lower than medium satellites. Therefore, x-axis maneuvering time of large satellite is smaller than the medium satellite. However, the moment of inertia of large satellite on y-axis is bigger than medium satellite and small satellite. Therefore, y-axis maneuvering time of large satellite is more than medium satellite and small satellite. According to AOCS team, the most used maneuvering angle is 30º and 60º on x and y directions. Summary of maneuvering durations of these rotation angles for x and y-direction are shown in Table 3.7 when an error of the maneuvering angle is smaller than 0.01º.

Table 3.7 Summary of Maneuvering Duration for x and y Direction

Satellite	**Actuator Output Torque**	**Maneuvering Time (x-axis)**		**Maneuvering Time (y-axis)**	
		30º	60º	30º	60º
Large	1 Nm	36.7 s	53.45 s	42.3 s	62 s
Large	2 Nm	26.6 s	38.25 s	31.65 s	46.25 s
Medium	1 Nm	37.3 s	54.6 s	28.8 s	43.3 s
Medium	2 Nm	26.7 s	40 s	20.55 s	31.95 s
Small	1 Nm	18.1 s	26.7 s	18.6 s	29 s
Small	2 Nm	13.7 s	19.8 s	13.55 s	20.35 s

The requirement of maneuvering duration is specified by AOCS and it depends on satellite application. Proper actuator which satisfies maneuvering duration should be selected efficiently by considering mass, volume and torque constraints. In other words, although large CMG generates high output torque and it has a small maneuvering duration, it is not the best selection due to higher volume and higher mass. In conclusion, optimum CMG should be selected by considering mechanical constraints, maneuvering time limitation, and output torque capacity. Requirements of CMG which is designed in this thesis will be listed in CHAPTER 5.

CHAPTER 4

SPACECRAFT THERMAL CONTROL SYSTEM

Thermal issues are another significant point when equipment is designed. In order to understand the thermal relationship between space environment, satellite, and CMG, the thermal control process and fundamentals of heat transfer are explained in this part. Thermal control components and thermal qualification conditions of CMG are also covered in the chapter.

The aim of the thermal control system is to maintain all spacecraft and payload components within their required temperature limits over the entire mission. Each equipment in spacecraft has operating temperature range and non - operating temperature (Survival temperature) range. Operating and non-operating temperatures of some equipment are shown in Table 4.1.

Table 4.1 *Operating and Non-Operating Temperature of Some Equipment*

Equipment	**Operating Temperature (˚C)**	**Non-Operating Temperature ˚(C)**	**Source**
Analog Electronics	0 to 40	-20 to 70	[14]
Batteries	10 to 20	0 to 35	[14]
Digital Electronics	0 to 50	-20 to 70	[14]
IR Detectors	-269 to -173	-269 to 35	[14]
Momentum Wheel	0 to 50	-20 to 70	[14]
Reaction Wheel	-20 to 60	-20 to 60	[15]
CMG	-20 to 55	-20 to 55	[16]
Solid State Particle Detectors	-35 to 0	-35 to 35	[14]
Solar Panels	-100 to 125	-100 to 125	[14]

4.1. Heat Transfer Methods

There are three different heat transfer methods on the earth; convection, conduction and radiation. However, heat transfer is provided by conduction and radiation in space.

4.1.1. Convection

Thermal convection is defined as the transfer of thermal energy by the motion of particles. For instance, thermal energy is transferred by the motion of air on the earth due to density difference and gravity. The most common method to increase convection is using fans and it forces the air particles to mobilize. Space is a microgravity environment and there are no mass or particles in space. The temperature of space is 3K and it is very close to absolute zero. Therefore, there is no convectional thermal energy transfer between hot and cold particles in space [17]. As a result, convection heat transfer is only valid for launch after fairing operation. Heat transfer equation for convection method is shown in Equation (4.1) [14]. It shows that heat power transfer capability increases with temperature difference and convection surface area.

$$q = hA_{conv}\Delta T \tag{4.1}$$

where;

q: $Heat\ transfer\ rate\ (W)$

h: $Convection\ coefficient\ (W/mK)$

A_{conv}: $Convection\ surface\ area\ (m^2)$

ΔT: $Temperature\ difference\ (T_{surface} - T_{flow})$

4.1.2. Conduction

In conduction method, heat transfer is provided between two thermally conductive materials other than flowing fluids. Equipment which is in spacecraft body transfers heat to the base plate of satellite via conduction method. In order to increase conductive heat transfer, the heat pipe mechanism mentioned in Section 4.3.2.2 is

placed under the base plate. Experience and heritage in previous satellite programs show that heat transfer capability of conduction method without heat pipes in space is 0. 15 W/cm^2 and with heat pipes 1 W/ cm^2.

Conduction method heat transfer equation for rectangular shape is shown in Equation (4.2) [14]. It shows that heat power transfer capability increases with thermal conductivity which is directly related to the material itself, conduction area and derivative of temperature with respect to distance.

$$q = -kA_{cond}\frac{dT}{dx} \tag{4.2}$$

where;

q: $Heat\ transfer\ rate\ (W)$

k: $Thermal\ conductivity\ (W/mK)$

A_{cond}: $Conduction\ rea\ (m^2)$

T: $Temperature\ (K)$

x: $distance\ (m)$

4.1.3. Radiation

In radiation method, heat moves through places where there are no molecules. Radiation is actually a form of electromagnetic energy. Radiation is the most efficient energy transfer mechanism for spacecraft [18]. Most spacecraft have large radiators to rid themselves of heat.

Radiation method heat transfer equation is shown in Equation (4.3) when temperature of deep space is taken 4K[14]. It shows that heat flux increases with the fourth-order of temperature. In other words, for high temperatures, radiation heat transfer method is totally dominant. In addition, the black body is theoretically taken as a perfect radiator. However, in practice, real materials don't have perfect radiation efficiency which is called as emissivity.

$$q = \epsilon\sigma T^4 \qquad (4.3)$$

where;

q: $Heat\ flux\ (W\ /m^2)$

ϵ: $emissivity\ at\ the\ wavelength\ mixcorresponding\ to\ temperature\ T$

σ: $Stefan - Boltzmann's\ constant = 5.670\ x\ 10^{-8}\frac{W}{m^2K^4}$:

T: $Temperature\ (K)$

In radiation method, analyzing heat transfer is complex since each equipment or all materials in spacecraft which its temperature is above than absolute zero emits thermal radiation. Therefore, there are a lot of heat transfer components or equations for one equipment from other equipment to deep space. Because of this complexity, each equipment is qualified separately in specified thermal conditions during the design procedure and it is called as qualification temperatures of the equipment. Qualification temperatures consist of cycles of minimum and maximum temperature level. Designed equipment has to operate correctly at the maximum and the minimum temperatures. After that, satellite thermal control system analyzes all equipment together and it creates a satellite thermal model. This model satisfies the qualification temperature of each equipment placed in the satellite. Thermal qualification condition of the CMG is studied in Section 4.5 in more detail.

A view factor is the fraction of energy leaving one surface that strikes another surface. View factor is a function of the size, geometry, relative position, and orientation of two surfaces[14]. The view factor equation is given by [18].

$$F_{i-j} = \frac{\text{Radiation leaving } A_i \text{ and intercept by } A_j}{\text{Radiation leaving } A_i} \qquad (4.4)$$

The mathematical expression of the view factor is given by [19] in Equation (4.6) and the representation of the view factor is shown in Figure 4.1.

$$F_{i-j} = \frac{1}{Ai} \int_{A_i} \int_{A_j} \frac{cos\ \theta_i\ cos\ \theta_j}{\pi R^2}\ dA_i dA_j \tag{4.5}$$

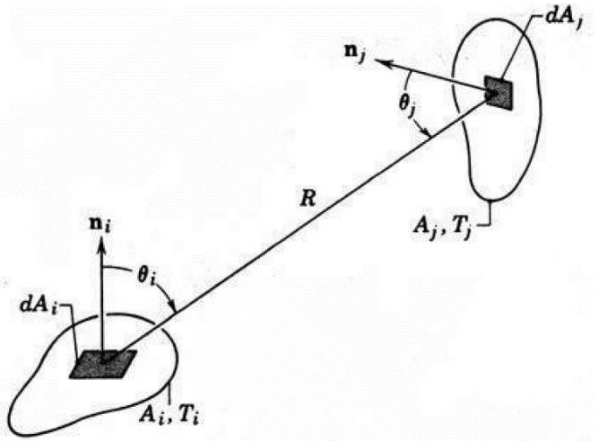

Figure 4.1 Representation of the View Factor between Two Surfaces [19]

Radiation heat transfer rate from surface 1 to surface 2 is shown in Equation (4.6).

$$\dot{Q}_{1-2} = \frac{\sigma A_1 (T_1^4 - T_2^4)}{\frac{1-\epsilon_1}{\epsilon_1} + \frac{1}{F_{1-2}} + \frac{A_1}{A_2}(\frac{1-\epsilon_2}{\epsilon_2})} \tag{4.6}$$

where;

$\dot{Q}_{1-2}$: $Heat\ transfer\ rate\ (W)$

ϵ_1: $Emissivity\ of\ surface - 1$

ϵ_2: $Emissivity\ of\ surface - 2$

A_1: $Area\ of\ surface - 1$

A_2: $Area\ of\ surface - 2$

F_{1-2}: $View\ factor\ of\ surface - 1\ with\ respect\ to\ surface - 2$

σ: $Stefan - Bolzmann's\ constant = 5.670\ x\ 10^{-8} \frac{W}{m^2 K^4}$:

T_1: $Temperature\ \ of\ surface - 1$

T_2: $Temperature\ \ of\ surface - 2$

4.2. Thermal Analysis

During spacecraft mission, there are three major heat loads coming from the satellite environment. The first and most effective heat load is obviously solar radiation. It depends on the distance between the sun and earth. The solar flux is 1414 W/m2 when the earth is the closest point to the sun (winter solstice) and it is 1322 W/m2 when the earth is the furthest away from the sun (summer solstice). A mean value of solar flux shown in Figure 4.2 can be taken as 1367 W/m2[10]. Second heat radiation is called as albedo radiation. Albedo radiation is defined as radiation that is reflected from the earth's atmosphere or ground before reaching the satellite. The coefficient of albedo radiation is taken as 0.3 (410 W /m2) but it depends on the position of the earth, reflected surface on the earth and seasons [19]. The reason for the last heat load is the planet's surface and the atmospheric gases and it is called as earth-emitted radiation. The value of the earth-emitted radiation at -18ºC is 240W /m2 [20]. Representation of heat load is shown in Figure 4.2

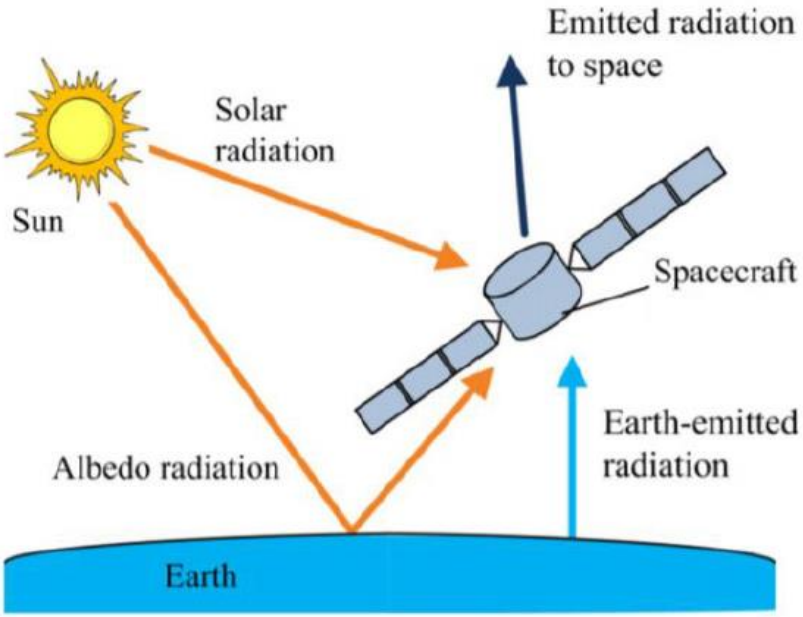

Figure 4.2 Representation of Heat Loads of The Satellite [19]

The total heat flux of the heat load is expressed as $q_{incident.}$ It has three components when it meets materials. The relationship between the total heat flux of heat load and components is shown in Figure 4.3 and Equation (4.7). If the material is opaque, $q_{transmitted}=0$.

$$q_{indicent} = q_{reflected} + q_{absorbed} + q_{transmitted} \qquad (4.7)$$

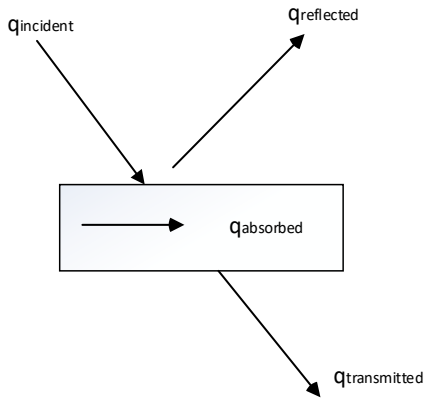

Figure 4.3 Components of Heat Flux of Total Heat Load

Absorbed heat flux from the heat loads is responsible for heating materials in spacecraft. ($q_{in}=q_{absorbed}$). Thermal balance equation in steady state is shown in Equation (4.8) [14].

Absorbed heat flux is represented by q_{in}, internal heat dissipation is represented by $q_{dissipated}$ and emitted heat energy from materials due to radiation is represented by $q_{out.}$. C represents the heat capacity (J/K).

$$q_{in} + q_{dissipated} - q_{out} = C\frac{dT}{dt} \qquad (4.8)$$

The components of q_{in} are shown in the following Equation (4.9). Mathematical representation of the components of q_{in} are derived based on Equation (4.10) [14] and they are shown in from Equation (4.10) to Equation (4.12).

$$q_{in} = q_{solar} + q_{albedo} + q_{earth-emitted} \quad (4.9)$$

$$q_{solar} = G_s A_{p1}\, \alpha\, cos\theta_{sun-inc} \quad (4.10)$$

$$q_{albedo} = 0.3 G_s A_{p2}\, \alpha\, cos\theta_{albedo-inc} \quad (4.11)$$

$$q_{earth-emitted} = G_{ee} A_{p3}\, \alpha\, cos\theta_{ee-inc} \quad (4.12)$$

where

G_S: $Solar\ flux = 1367 \frac{W}{m^2}$

G_{ee}: $Earth - emitted\ flux = 240 \frac{W}{m^2}$

A_{P1}: $Surface\ area\ with\ respect\ to\ solar\ flux$

A_{P2}: $Surface\ area\ with\ respect\ to\ albedo\ flux$

A_{P3}: $Surface\ area\ with\ respect\ to\ earth\ emitted\ flux$

α: Absorbtivity coefficient of the material

$\theta_{sun-inc}$: Incidence angle of solar *flux*

$\theta_{albedo-inc}$: Incidence angle of the albedo *flux*

θ_{ee-inc}: Incidence angle of the earth − emitted *flux*

Components of q_{out} are shown in the following Equation(4.13).

$$q_{out} = \epsilon \sigma A_R T^4 \quad (4.13)$$

Where $\epsilon, \sigma,$ and A_R represent emissivity, Stefan-Boltzmann's constant, and emitted surface area respectively.

Assume that internal dissipation of equipment or material is ignored. By using Equations (4.8), (4.9), (4.10), (4.11), (4.12) and (4.13) equilibrium of surface

temperature can be calculated as in Equation (4.14). It is seen that equilibrium temperature depends on the ratio of absorptivity to emissivity of materials.

$$T = \left(\frac{G_s A_{p1}\, \alpha\, cos\theta_{inc} + 0.3 G_s A_{p2}\, \alpha\, cos\theta_{albedo-inc} + G_{ee} A_{p3}\, \alpha\, cos\theta_{ee-inc}}{A_R \epsilon \sigma}\right)^{\frac{1}{4}} \quad (4.14)$$

4.3. Thermal Control Components

Thermal control components are classified two categories; passive control components and active control components. The main idea of passive control component is that heat flow is provided by conductive and radiative methods instead of electrical and mechanical input. On the other hand, active control components rely on thermostats, moving parts, heat pipes, heaters. Active thermal control components provide thermal control by using external mechanical parts or electrical input for cooling and heating.

4.3.1. Passive Thermal Control Components

Passive thermal control techniques involve coating, multi-layer insulator (MLI), radiators, thermal doubler, thermal strap, and thermal filler [20]. Since passive techniques are simple, more reliable, lower risk and lower cost, they are generally preferred in space applications. Mechanical and electrical tools are not used in this technique. They do not have electrical power, external moving parts and data handling from the system. Passive thermal components are installed once when designing satellite thermal subsystem and it does not change any property such as heat rejection capability in space [21].

4.3.1.1. Coating

Equation (4.14) shows that equilibrium temperature depends on the (α/ε) ratio of materials. Emissivity and absorptivity values of some coating materials using in space applications shown in Figure 4.4. Coated sphere equilibrium temperature in the sun is also shown in Figure 4.4. In order to increase equilibrium temperature, material that

has a higher ratio of absorptivity to emissivity (α/ε) is selected. On the other hand, material that has lower (α/ε) ratio is preferred for decreasing equilibrium temperature.

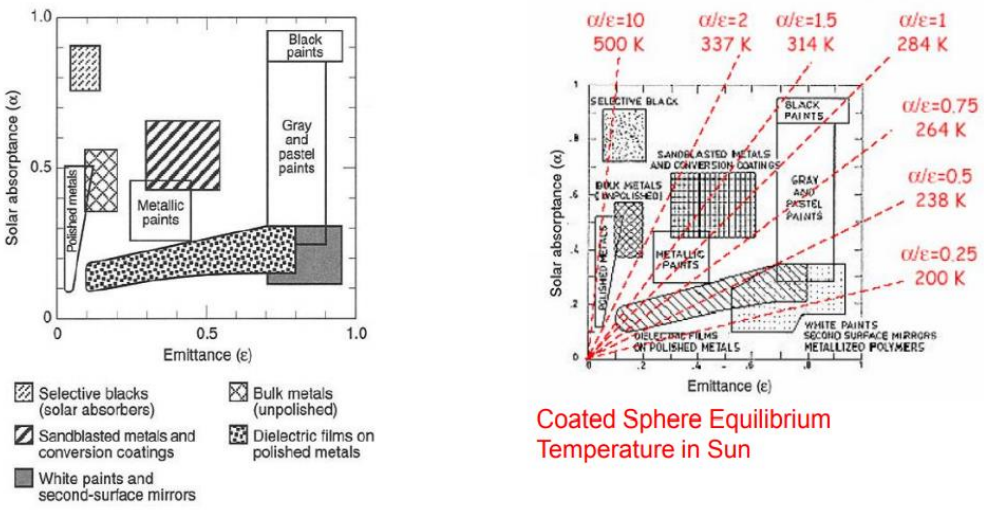

Figure 4.4 (α/ε) Ratio of Some Coating Materials [17] [19]

Thermal coating falls into four basic categories [10]:

- Solar absorber (α/ε > 1) [hot coatings]
- Solar reflector (α/ε << 1) [cold coatings]
- Flat absorber (α/ε ~ 1)
- Flat reflector (α/ε ~ 1)

In practice,

- Paints are generally used. All paints have high emissivity.
- Electronic boxes inside spacecraft and structural panels are usually painted to achieve a high emissivity (ε) (black paint is a conventional choice). Therefore one can dissipate heat from electronic components or make uniform the temperatures inside the spacecraft or payload [10].
- Internal temperature-sensitive components that do not dissipate much heat (propellant lines, tanks, etc.) often have low emissivity (ε) finish (bare or polished Aluminum, Gold) [10].

4.3.1.2. Multilayer Insulation (MLI)

The most popular single-layer radiation barrier among passive thermal control element is multilayer insulation. Multilayer insulation blankets provide thermal insulation between components and environment condition and there is no excessive heat transfer between environmental fluxes, launcher, other sources, and components. In addition, it also provides protection from micrometeorites, atomic oxygen, and electron charge accumulation [10].

MLI includes multiple layers of low-ε films (Mylar sheets). Several thin (1/4 mil thick) ribbed Mylar sheets that a vacuum-deposited aluminum finish constitutes the simplest MLI blanket constructions. As a result, due to ribbed Mylar sheets, conductive heat paths are minimized [10]. The example of MLI blanket is shown in Figure 4.5.

Figure 4.5 The Example of MLI Blanket [22]

4.3.1.3. Radiators

Radiators are primary passive thermal control components of spacecraft which are used for heat rejection on spacecraft. Typical usage of radiators is to cool detectors and electronics. Radiators with the large surface area are used to radiate heat into space. Structural panel radiators flat-panel radiators and deployable radiators are some types of radiators used in spacecraft. They reject heat by IR radiation which strongly depends on the temperature. Experiences show that radiator can waste between 100 W and 350W heats per m^2 [10]. In order to maximize heat rejection, IR emittance of

radiators are more than 0.8 ($\varepsilon > 0.8$) and they are less than 0.2 solar absorptances ($\alpha < 0.2$) to limit heat loads from the sun [10]. The example of radiators is given in Figure 4.6.

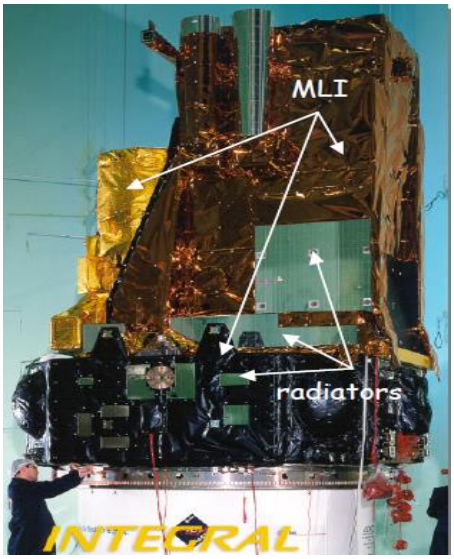

Figure 4.6 The Example of MLI and Radiators [20]

4.3.1.4. Thermal Doubler, Strap, and Filler

Thermal doubler provides heat flow by conduction method from materials. A thermal doubler is an aluminum alloy plate attached to a heat dissipater and a radiator. Aluminum alloy plate is chosen since it has a high conductive thermal capability as 120-170 W / m.K [20]. It is commonly used for controlling the temperature of electronic equipment in spacecraft. It is similar to heat pipe but it is not as efficient as heat pipe.

The thermal strap that provides a heat path between unit and radiators in the satellite consists of flexible strips, cable braid, and several braids shown in Figure 4.7 [10]. The thermal strap is essential and common to link a dissipative unit such as an electronic box to a radiator. It consists of Cu alloy and Al alloy. Length of the thermal strap should be smaller than 10cm [20].

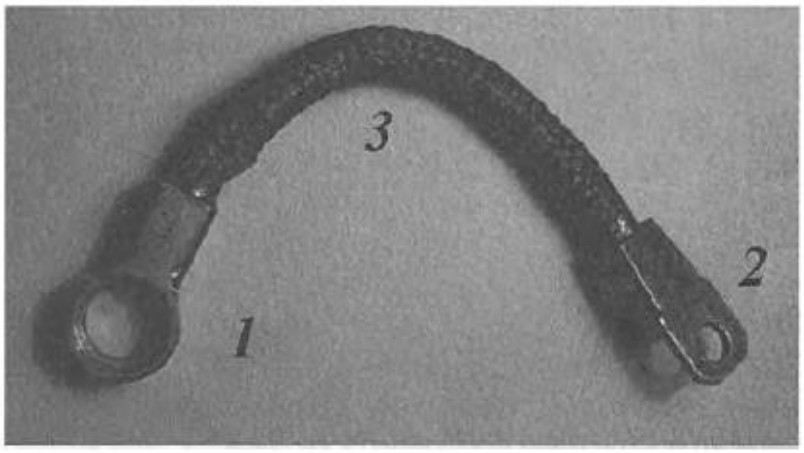

Figure 4.7 The Example of Thermal Strap, (1 and 2) Connectors; (3) Copper Braid [10]

The thermal filler is used under electronic equipment surface to increase heat conductivity. Generally, the thermal filler has high thermal conductivity and they are electrically isolated. Silicone elastomer and graphite can be used for thermal filler [20].

Thermal doubler, thermal strap, and thermal filler are shown in Figure 4.8.

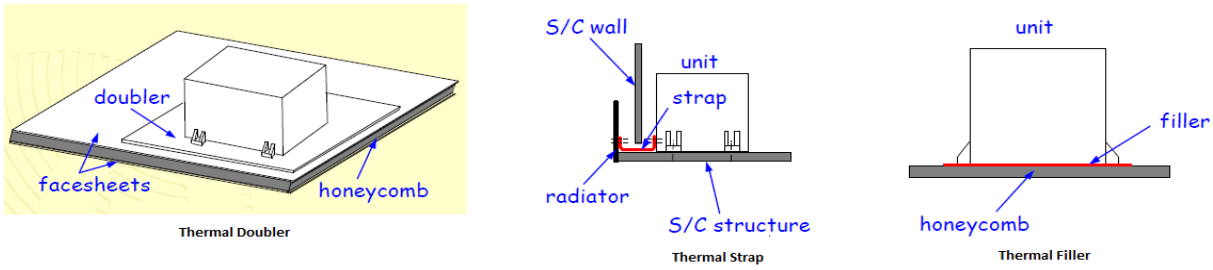

Figure 4.8 Thermal Doubler, Strap, and Filler [20]

4.3.2. Active Thermal Control Components

Active thermal control techniques involve heaters, heat pipes, and louver [20]. If passive control components cannot provide heat control, active components support to control heat transfer. Active thermal components are used for both cooling and heating in the spacecraft. Active control provides thermal transfer, variable rejection, and sensing devices. Spacecraft resources that electrical power, data handling and

control, sensing, and data storage are needed for active thermal control components. This technique requires more testing and has higher risk and cost [21].

4.3.2.1. Heaters

Heaters are used to heat cold region or equipment when equipment does not operate. Heaters are controlled by command of the satellite control unit and power distribution unit. If the base temperature is lower than the specified temperature, the switch of the heater is turned on. The heater includes resistors that generate heat. Resistor wires are embedded in Kapton. The example of heaters is given in Figure 4.9

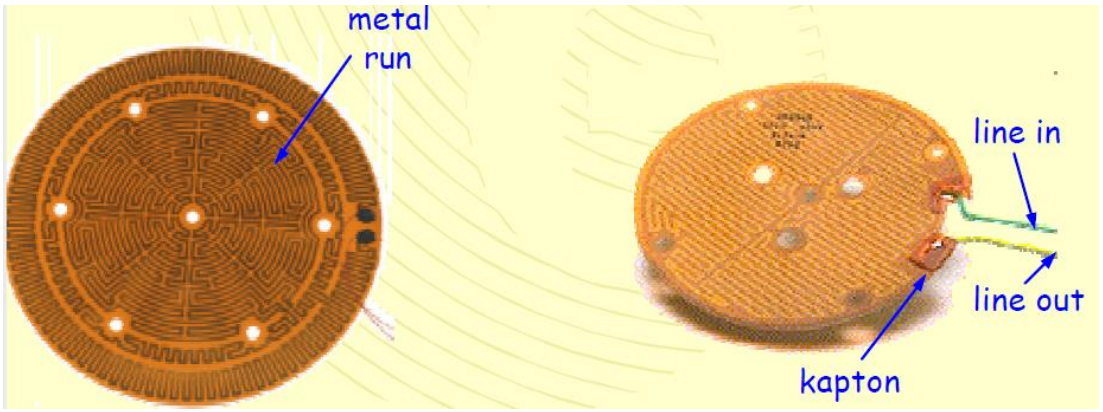

Figure 4.9 The Example of Heaters [20]

4.3.2.2. Heat Pipes

A heat pipe is a thermal transformer that transports large quantities of heat from one location to another location. Heat is transferred from equipment to radiators placed in the satellite [10].

The heat pipe is the most efficient mechanism to cool equipment. Heat pipe provides a low impedance path for heat. Thanks to the heat pipe, extremely high heat transfer rates can be obtained. There is a liquid inside of the heat pipe and thermal energy is absorbed by this liquid. The liquid is converted gas when it is heated and then this gas reaches the end of the heat pipe which is colder than the first part of heat pipe At the end of heat pipes, gas releases the energy to a radiator upon condensing back to a

liquid. Gas travels at the middle of the heat pipe and liquid travel at the edge of the heat pipe. The pipe is usually made of aluminum and the liquid is usually ammonia [22]. Heat pipes provide high heat transfer rates even with small temperature differences.

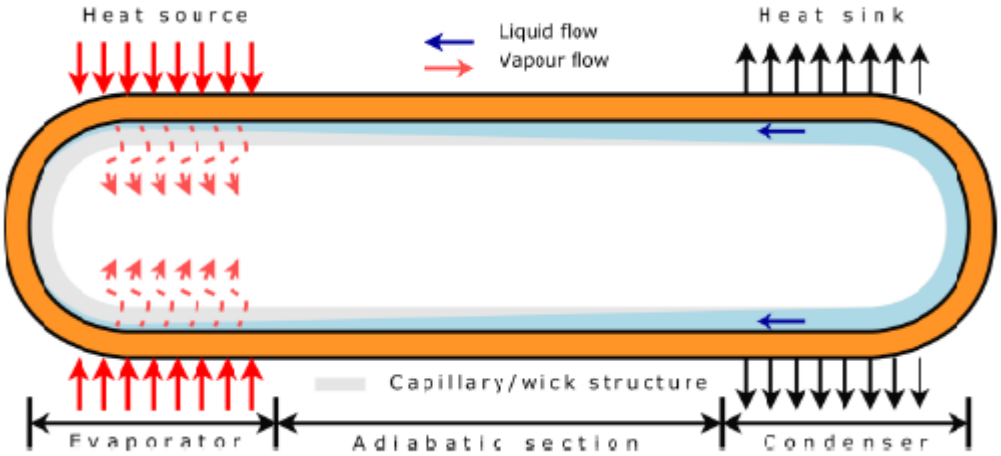

Figure 4.10 Heat Pipe Mechanism [22]

4.3.2.3. Louvers

Louvers are a device that changes equivalent radiators area and equivalent emissivity of radiators. They are mounted on radiators and they increase or decrease area between the radiator and deep space. Parallel blades that have a low emissivity (ε) can rotate and uncover a high emissivity (ε) radiator. As a result, equivalent emissivity (ε) can be adjustable. They can save heater power when the heater switch is off. The mechanism of louvers is shown in Figure 4.11.

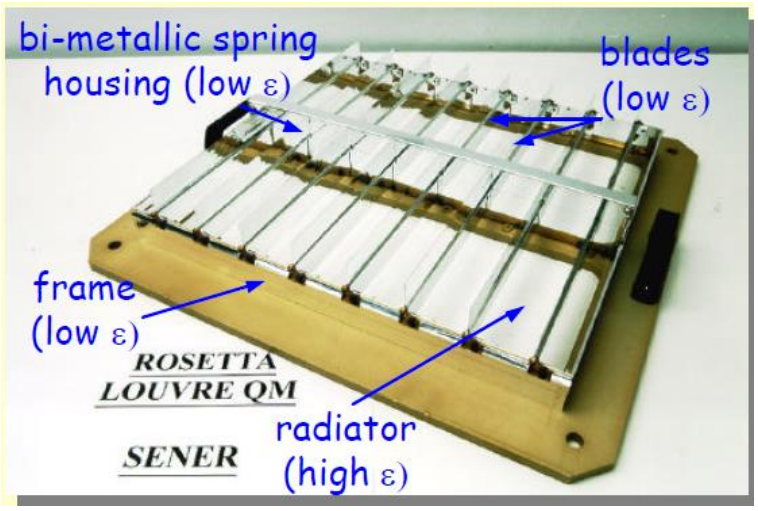

Figure 4.11 The Mechanism of Louvers [20]

4.4. CMG Thermal Specifications

Thermal specifications are other critical parameters for CMG design. Sample actuators thermal specifications are taken into account in this section. Operating temperature ranges of actuators are shared to understand system-level thermal specification and specify the operating temperature range of CMG. In addition, in order to compare operating temperature specification with experience results operating temperature data which are taken from satellite at orbit now are given. Heat dissipation of actuators is also shared to understand the efficiency of actuators. Finally, a simple thermal mathematical model is shown. Therefore, the operating temperature of the designed CMG should be between -20 ºC and 55 ºC. Operating temperature of some actuators is shown in Table 4.2.

Table 4.2 *Actuator Temperature Range Examples*

Actuator	**Temperature Range**
CMG 15-45S (Airbus) [16]	mechanism -20 to +55°C electronics -25 to +60°C
CMG [23]	Flywheel Motor −25 to +80 Slip Ring −20 to +60 Gimbal Motor −40 to +100 Encoder −40 to +100 Motion Controller −25 to +85
Reaction Wheel AMAZONIA-1 satellite [24]	-15°C to 55°C
Reaction Wheel (TURKSAT 6A)	Operation: -20 °C to 70°C Non-Operation: -40 °C to 70 °C
Reaction Wheel (Gokturk-1)	Operation: -10 °C to 60°C Non-Operation: -35 °C to 70 °C
Reaction Wheel (Gokturk-2)	Operation: -15 °C to 65°C Non-Operation: -40 °C to 80 °C

4.4.1. Operating Temperature [Obtained by previous satellite programs]

Experienced operating temperatures taken from four different actuators (reaction wheels) for Gokturk-2 satellite are shown in Figure 4.12 and Figure 4.13. A lot of temperature telemetries were taken 45 days after launch (December 2012) to ensure that actuators worked correctly in orbit and shown in Figure 4.12. After 45 days from launch, temperature telemetries are taken rarely to control actuators conditions shown in Figure 4.13 (December 2012 to March 2018). Although reaction wheels have acceleration or deceleration, temperature telemetries show that operating temperature is around 30 ˚C and it satisfies easefully operating temperature which are mentioned in Table 4.2. It is obvious that designed CMG will also satisfy thermal requirements if the efficient thermal design will be applied.

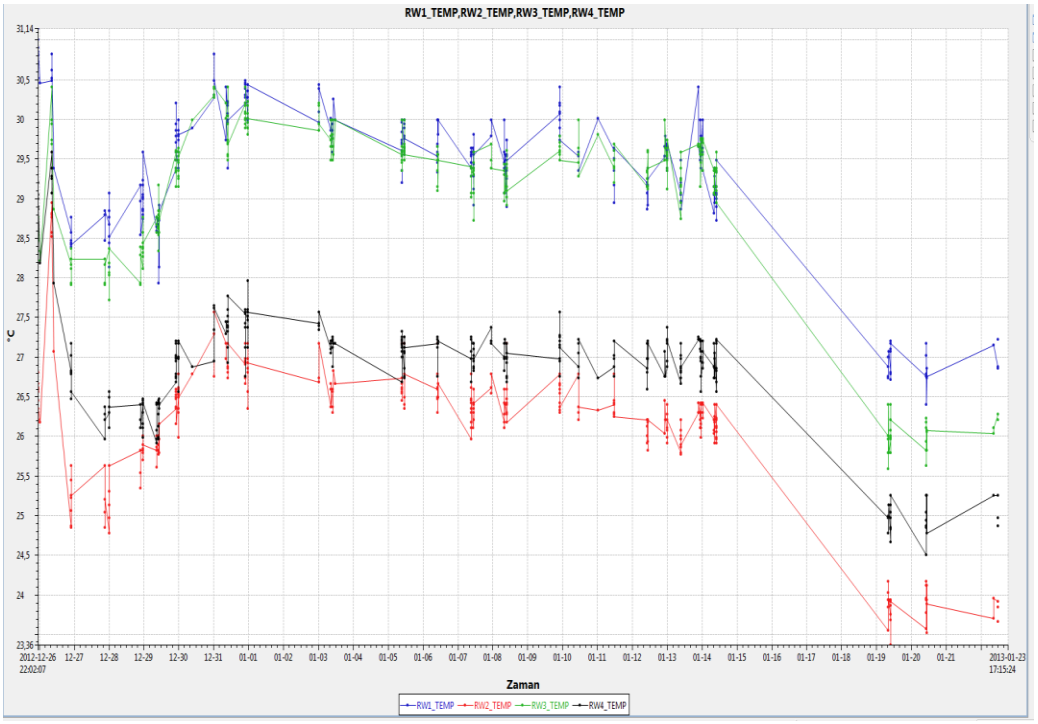

Figure 4.12 Operating Temperature Data 45 Days After Launch.

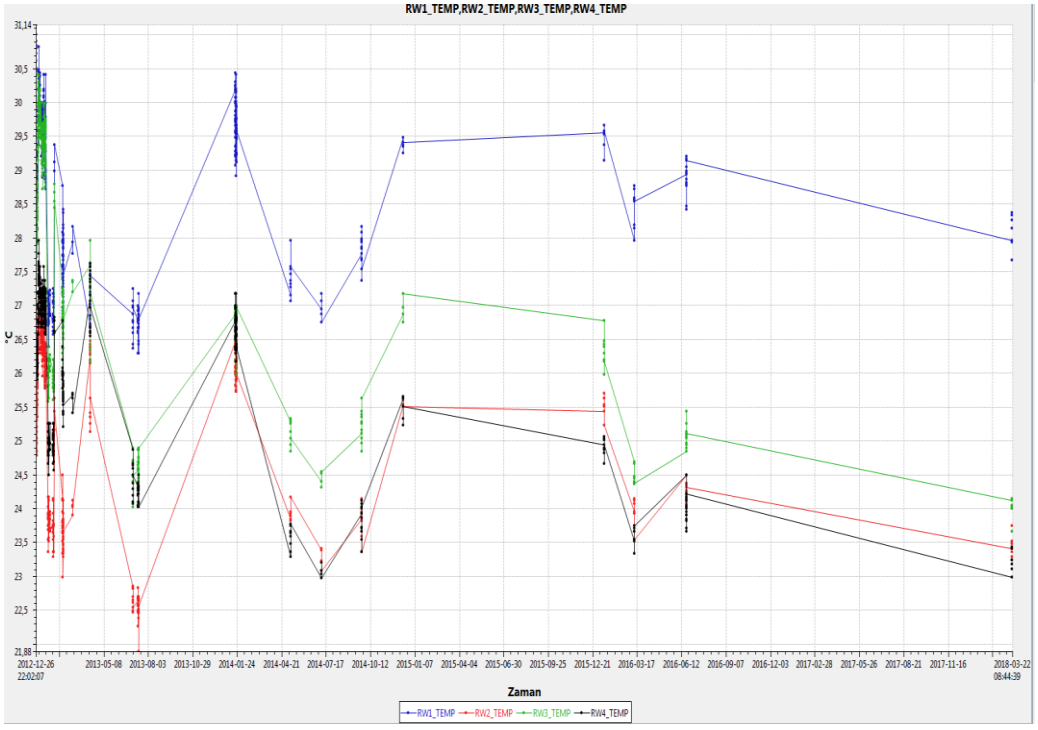

Figure 4.13 Operating Temperature Data from Launch to March 2018

4.4.2. Heat Dissipation of Actuators

The heat dissipations of some actuators used in different satellites programs are shown in Table 4.3. TURKSAT 6A is a geosynchronous satellite that the orbital period of this is same as the earth. Since geosynchronous satellite does not need rapid maneuvering capability the heat dissipation of actuator used in this satellite is smaller than actuator used in low earth orbit satellite called as GOKTURK-2. The maximum torque capability of these two actuators is 0.23 Nm. The main reason of the heat dissipation is the friction on bearing of the wheel when the wheel is rotating at high speed. Since there is no load in space condition at steady-state due to non-gravity, high ratio of power demand is spent for the friction on bearing. Low earth orbit satellites require rapid maneuvering capability and CMG is generally used for this type of satellites. Therefore, power demand and the heat dissipation value of designed CMG is specified based on GOKTURK-2. Designed CMG in this thesis is planned to have four times higher torque when it is compared to the reaction wheel of GOKTURK-2. Therefore, heat dissipation and power demand of designed CMG are assigned that it should be less than four times heat dissipation and power demand of GOKTURK-2 shown in Table 4.3.

Table 4.3 *Heat Dissipation of Sample Actuators*

Actuator	**Power Demand**	**Heat Dissipation**
T6A Reaction Wheel (0.23 Nm)	Max 150 W	Nominal 19 W , Max:33 W
GOKTURK-2 Reaction Wheel (0.23 Nm)	Max 95.2 W	Nominal 12 W Max 60 W
Designed CMG (1 Nm)	Max 380.8 W	Max 240 W

4.4.3. Thermal Model of Actuator

Simple mathematical model of actuators is shown in Figure 4.14. Thermal conduction of actuator is provided by conduction and radiation. In Figure 4.14, Node-1 and Node-5 show deep space. Node-2 represents the contact area between the satellite base plate and actuator. Node-3 represents the top side of actuator and Node-4 represents the bottom side of actuators. Heat transfer between Node-3 and Node-4 is provided by conduction. Conducted heat conductance G2 and G3 are directly related to contact area, actuator and base plate materials, and heat pipes capability. Analyzing radiated conductance G1 and G4 are very complex and it depends on several parameters such as the position of other equipment, coating, radiator areas, thermal doublers, etc. The purpose of this model is to give only an idea about thermal mathematical model of actuators. A real detailed mathematical model is so complex, and it is not the scope of this thesis. Thermal analysis results of CMG are shared in Section 9.6. The simple thermal model is shown in Figure 4.14.

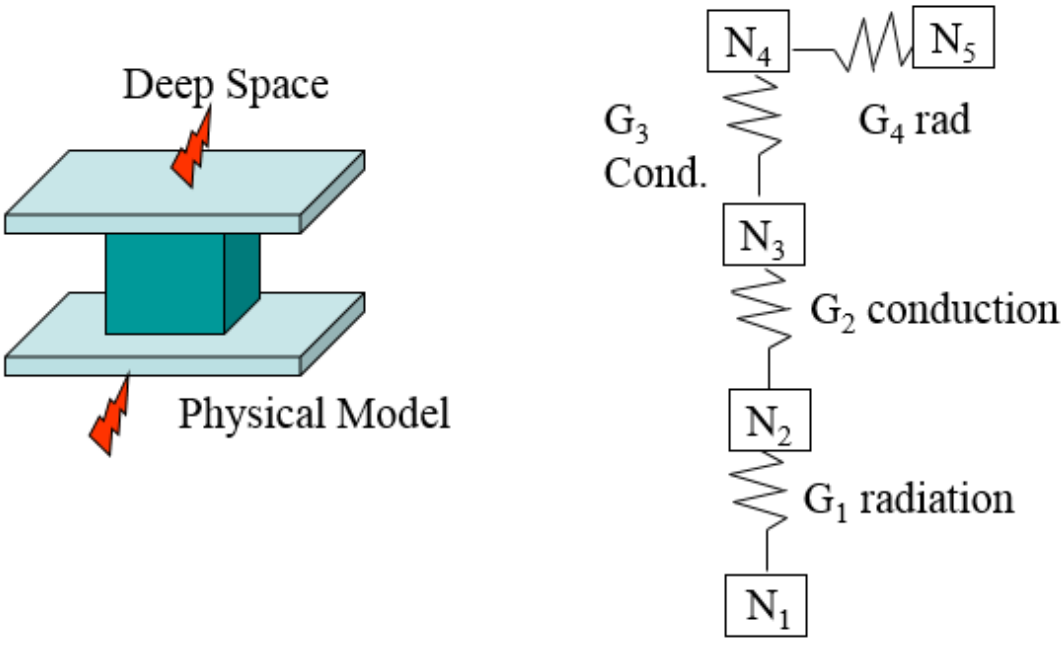

Figure 4.14 Simple Thermal Model of Actuator [25]

4.5. Thermal Qualification Conditions of CMG

Equipment that has space mission is subjected to extensive thermal tests at ground to prevent abnormal conditions during flight. Thermal tests demonstrate the operation of equipment at maximum temperature and minimum temperature. In order to qualify any equipment for a space mission, thermal cycles are applied to equipment at ground tests.

Acceptance test temperatures levels are higher than operating temperature and qualification test temperature levels are higher than acceptance test levels. In space applications, the temperature difference between qualification level and acceptance level is 10ºC shown in Figure 4.15 [10].

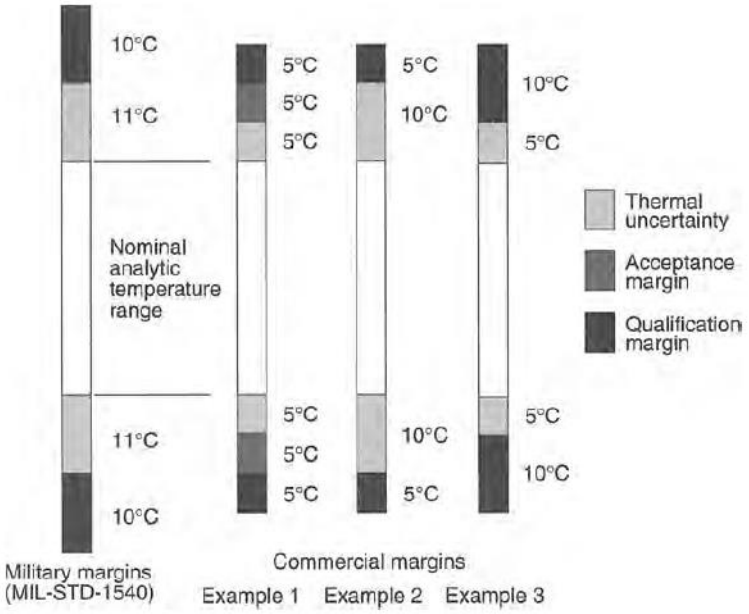

Figure 4.15 Thermal Margin of Thermal Test Conditions [10]

The operating temperature of the designed CMG should be selected between -20 ºC and 55 ºC with respect to actuators that designed before in Section 4.4. Operating temperatures are taken as same as acceptance test levels in this study. Therefore, designed CMG in this thesis is qualified between -30 ºC and 65 ºC. However, it is

noted that the temperature difference between acceptance level operating temperature is taken 11ºC to increase margin in some applications [10].

Thermal tests are applied under vacuum conditions and convection heat transfer method is not valid as space conditions. Equipment is placed in a thermal - vacum chamber and thermal cycles at minimum and maximum temperatures are applied many times to verify performance of the equipment. Thermal - vacuum chamber is a device that provides a stable temperature for hot and cold cases to perform equipment thermally in vacuum condition. The base plate inside of the thermal chamber is adjusted the qualification temperatures level. Therefore, only the radiation and conduction heat transfer method are active to cool equipment inside the thermal - vacuum chamber.

A number of thermal cycles are 24 for qualification level and 8 for acceptance level [10]. One thermal cycle involves one maximum temperature and one minimum temperature. At the first and last cycles, full functional test is performed and a reduced functional test is performed at intermediate cycles. During the reduced functional test, only some critical functional test is performed. The duration of the first and last thermal soaks is 6 hours and the duration of intermediate soaks is 1 hour. Transition rate from hot to the cold case or cold to the hot case is 3-5ºC / minute [10]. Thermal cycle profile of CMG qualification model is shown in Figure 4.16.

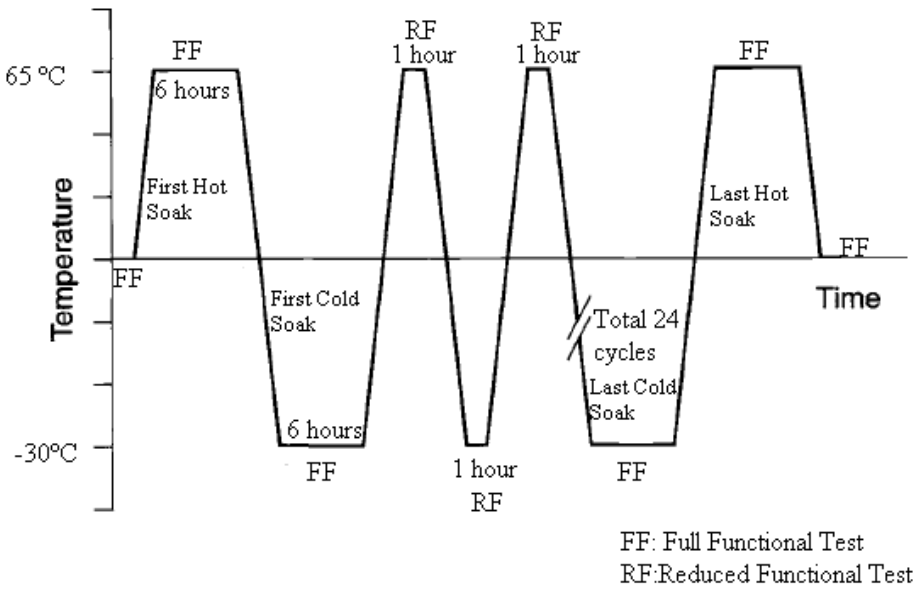

Figure 4.16 Thermal Cycle Profile of designed CMG [10]

In conclusion, materials or all electronic parts used in designed CMG must operate correctly under this maximum and minimum temperature conditions. After this test, designed CMG is qualified between -30 ºC and 65 ºC. It is noted that system-level thermal design satisfies operating temperature between -20 ºC and 55 ºC during a space mission and qualification level has covered the operating temperature with 10 ºC margin.

CHAPTER 5

CMG DESIGN PARAMETERS

5.1. Mechanical Constraint and Sizing of CMG

In aerospace applications, most significant properties for equipment are volume and mass since the satellite should be compact to fit launch vehicle and in order to decrease launch cost. Therefore, equipment mass and volume should be as low as possible. Reserved volume and mass of one actuator (reaction wheel) that was used in previous satellite's programs are shared in Table 5.1. The volume of the one actuator is assumed as a rectangular prism. Table 5.1 gives an idea between output torque capability and mechanical constraints. The aim of this thesis is to design actuator (CMG) that fits the same reserved volume and mass with higher torque capability than used actuators placed in the previous satellite. Therefore, the starting point of designed CMG is to specify mass, volume and torque capability.

Table 5.1 *Reserved Volume and Mass of One Actuator for Three Different Satellites*

Satellite Size	**Actuator Volume**	**Actuator Mass (Including Electronics)**	**Existing Torque**
Small	30,8 cm x 30,8 cm x12cm	8,1 kg	0,23Nm
Medium	35cm x 35cm x13 cm	10 kg	0,26 Nm
Large	40 cm x 40 cm x 18 cm	24 kg	2 Nm

5.2. Optimum CMG Selection for Medium Satellite

The purpose of the actuator is to provide rapid maneuvering capability to the satellite. The satellite that has shorter maneuvering duration is called an agile satellite. In order

to have agile satellite, actuators that have high output torque should be placed in the satellite.

Reserved volume and mass of actuator for medium-size satellite are chosen as mechanical constraints in this study since trend of earth observation satellites are medium satellites. According to system-level requirements coming from Attitude Orbit Control System (AOCS) team, the satellite has to rotate on x-direction less than 40 seconds for 30º rotation and 60 seconds for 60º rotation. Furthermore, It must rotate on y-direction less than 30 seconds for 30º rotation and 45 seconds for 60º rotation. Maneuvering duration for an actuator that has 1 Nm and 2Nm output torques has already revealed in Section 3.8. It is noted that both output torque values satisfy maneuvering duration requirements for x and y directions. However, since CMG that has 2 Nm output torque will have higher volume and mass, CMG that has 1 Nm output torque is a more suitable option in terms of volume and mass constraints. Therefore, CMG that has 1 Nm output torque is selected to design in this thesis.

Proposal of this thesis is that designed CMG will have same mass and same volume when it is compared with actuator that was used in previous medium satellite, but output torque capacity will be 4 times higher than previous actuator.

Reserved volume, reserved mass, the moment of inertia matrix of satellites are shown in Table 5.2 for previous satellite programs. It is seen that volume, mass, and inertia constraints of target CMG are selected based on volume, mass, and inertia constraints of the medium satellite. In addition, maneuvering duration of small, medium and large satellites are shown in Table 5.2 when target CMGs (1 Nm) are placed in the satellites. These maneuvering duration results are coming from mathematical results in Section 3.8. It is noted that maneuvering duration of medium satellite satisfy the maneuvering duration requirements of target CMG shown in Table 5.2.

Table 5.2 *Comparison of The Satellite Maneuvering Time with 1 Nm CMG*

Parameter	**Target CMG**	**Small Satellite**	**Medium Satellite**	**Large Satellite**
Reserved Volume (cm x cm x cm)	<35x35x13	30, 8 x30, 8 x 12	35 x35 x13	40 x 40 x 18
Reserved Mass (kg)	< 10	8,1	10	24
Moment of inertia ($kg.m^2$)	<D[600 500 500]	D[139.6, 140.0, 158.1]	D[598.94 ,481.98 , 376.43]	D[560 ,1020, 1000]
30°rotation on x-axis	<40s	17,05 s	37,3 s	36,7 s
60°rotation on x-axis	<60s	26,7 s	54,6 s	53,45 s
30° rotation on y-axis	<30s	18,6 s	28,8 s	42,3 s
60° rotation on y-axis	<45s	29 s	43,3 s	62 s

Reserved volume of the actuator for the medium satellite is close to small and large satellites shown in Table 5.2. Therefore, although target CMG is chosen for medium satellites, it is also used in small and large satellites. If target CMG is placed in a small satellite, the agility of satellite is extremely high. It is obvious that target CMG can be placed in the large satellite easily in terms of reserved volume and mass, but it does not satisfy maneuvering duration requirements. For instance, if CMG that has 1 Nm output torque is used in large satellite, maneuvering time will be 42.3 seconds for 30º rotation along the y-axis and 62 seconds for 60º rotation along the y-axis. These maneuvering durations are more than maneuvering duration requirements mentioned in Table 5.2. If these maneuvering durations are acceptable for system-level requirements of the satellite, target CMG is also placed in the large satellite.

In conclusion, although target CMG is a modular design that is used in all size of satellites, it is only analyzed for medium satellite. CMG used in small and large satellites is not scoped in this thesis.

5.3. CMG Design Specifications

Mechanical constraints and maneuvering time requirements are already studied in Section 5.2. In addition to these constraints and requirements, other specifications for designed CMG are listed in Table 5.3. These specifications come from system-level requirements. Designed CMG will have the same volume and mass but it has higher torque than used actuator in the previous medium satellite. Operating voltage is compatible with the bus voltage of earth observation satellites. Thermal specifications are studied in CHAPTER 4 and it is compatible with space environmental conditions. As a result, CMG will be designed based on these requirements.

Table 5.3 *CMG Design Specifications*

Parameter	**Value**
Volume	< 35 cm x 35cm x 13cm ± 20%
Mass	< 10 kg ± 20%
Moment of Inertia Matrix of Satellite	< diagonal [600 500 500] kgm^2
Nominal Torque	> 1Nm
30 ° rotation in x- axis (Roll axis)	≤ 40 seconds
30 ° rotation in y-axis (Pitch axis)	≤30 seconds
60 ° rotation in x- axis (Roll axis)	≤ 60 seconds
60 ° rotation in y-axis (Pitch axis)	≤45 seconds
Maximum Gimbal Excursions	≤ 45°
Wheel Required Time Reach to Maximum Speed (10000 rpm)	< 300 seconds ± 10%
Power Consumption	< 380 W
Operating Voltage	18V to 33 V
Operating Temperature	-20°C to 55°C
Heat Transfer Capability of Satellite Base Plate	1 W/ cm2 with heat pipes 0,15 W/ cm2 without heat pipes
Design Life	Not Applicable due to prototype model

5.4. Evaluation of Target CMG in Various Operating Conditions of Satellite

In this section, the required output torque that provides sufficient maneuvering agility to the satellite is calculated for four different cases that are corresponding to maneuvering duration requirements mentioned in Table 5.3. Maximum velocity of the satellite during maneuvering, required torque that satisfies maneuvering duration requirements, maximum gimbal angle during maneuvering and the position of the satellite during maneuvering are also calculated and shown separately for each case. Maximum gimbal excursions angle is taken 45° as mentioned in Table 5.3.

According to maneuvering duration specifications shown in Table 5.3:

- The satellite has to rotate on x-direction in less than 40 seconds for 30º rotation (Case-1)
- The satellite has to rotate on x-direction in less than 60 seconds for 60º rotation (Case-2)
- The satellite has to rotate on y-direction in less than 30 seconds for 60º rotation (Case-3)
- The satellite has to rotate on y-direction in less than 45 seconds for 60º rotation (Case-4)

The longest maneuvering duration among these constraints is assigned as 60 seconds for 60º rotation on the x-axis (Case-2). Therefore, maximum gimbal excursions angle (45º) must satisfy and provide sufficient output torque to the satellite during the longest maneuvering duration. At this case, gimbal angle reaches to maximum gimbal excursions angle (45°) in the first 30 seconds and then returns to 0 ° in the next 30 seconds period. As a result, gimbal speed is assumed to be constant during this maneuver and it is equal to 1.5 degrees/second (45º/30 seconds=1.5 deg/s) in this section.

5.4.1. Simple Torque Equations of Satellite

The relationship between satellite maneuvering angle (angular displacement of the satellite), required output torque that rotates satellite in a specified time, and the velocity of the satellite is shown in the following equations. Required output torque equation is derived step by step by using the following equations.

Denotations

I_{st}: $Total\ inertia\ of\ satellite$

I_{st_x}: $Total\ inertia\ of\ satellite\ on\ x\ axis$

I_{st_y}: $Total\ inertia\ of\ satellit\ on\ y\ axis$

I_{st_z}: $Total\ inertia\ of\ satellite\ on\ z\ axis$

$$I_{st} = \begin{bmatrix} I_{st_x} \\ I_{st_y} \\ I_{st_z} \end{bmatrix}$$

$\dot{\theta}_{st} = \omega_{st}$: $Angular\ velocity\ of\ satellite$

$\dot{\omega}_{st}$: $Angular\ acceleration\ \ of\ satellite$

θ_{st}: $Angular\ displacemnt\ of\ satellite$

τ_o: $Required\ output\ torque\ that\ rotates\ \ the\ satellite\ in\ specified\ time$

Derivation

Required output torque (τ_o) equation that rotates the satellite in a specified time in terms of the satellite inertia (I_{st}) and the angular acceleration ($\dot{\omega}_{st}$) of the satellite is given by Newton's first law and [11].

$$\tau_o = I_{st}\dot{\omega}_{st} \qquad (5.1)$$

$$\int \tau_o \, dt = \int I_{st} \dot{\omega}_{st} \, dt \tag{5.2}$$

By taking integral of Equation (5.1), the relationship between angular velocity (ω_{st}) of satellite and required output torque (τ_o) is obtained with respect to the time function in Equation (5.3).

$$\omega_{st} = \frac{\tau_0}{I_{st}} \, t \tag{5.3}$$

$$\int \omega_{st} \, dt = \int \frac{\tau_0}{I_{st}} \, t \, dt \tag{5.4}$$

$$\theta_{st} = \frac{\tau_o}{I_{st}} \frac{t^2}{2} \tag{5.5}$$

$$\tau_o = \frac{2 I_{st} \theta_{st}}{t^2} \tag{5.6}$$

By taking integral of Equation (5.4), the relationship between the angular displacement of the satellite (θ_{st}) and required output torque (τ_o) is obtained with respect to the time function in Equation (5.6). Required output torque is the average output torque that must be provided by the pyramidal configuration of CMG mentioned in Section 2.3.2.

Angular displacement is a known parameter for each case and it is taken as half of the required satellite maneuvering angle such as 15º for 30º rotation requirement that it is explained in next sections in detail. Satellite inertia has already been defined for medium satellite on x,y, and z directions in Table 5.3. Furthermore, the time is specified in maneuvering duration constraints and it is equal to half of the maneuvering duration constraints. In conclusion, the required output torque for four different cases is calculated in from Section 5.4.2 to Section 5.4.5 to satisfy maneuvering duration specifications mentioned in Table 5.3.

5.4.2. Case-1 30° rotation on x-axis should be less than 40s

The satellite should be rotated 30 º on x-axis in less than 40 seconds in this case.

Maximum satellite inertia on x-axis has already been given as 600 kgm^2 in Table 5.3. Required output torque that rotates the satellite 30º in 40 seconds and the velocity of the satellite is calculated by the following equations. Firstly, the satellite rotation angle should be converted to the angular displacement of the satellite in radian that is shown in Equation (5.8).

$$\theta_{\text{radian}} = \frac{\theta_{degre}\pi}{180} \tag{5.7}$$

$$\theta_{\text{radian}} = \frac{15°\pi}{180} = 0.2618\ rad \tag{5.8}$$

During half of the maneuvering time of this case ($\frac{40}{2} = 20\ seconds$), the velocity of the satellite increases with constant acceleration by applying positive output torque to the satellite and 15° angular displacement is achieved. After that, the velocity of the satellite decreases with constant deceleration and another 15° displacement is provided during deceleration by applying negative direction output torque to the satellite shown in Figure 5.1. At the end of the maneuvering, 30° rotation occurs within 40 seconds. During this rotation, the required output torque for x-axis is calculated in Equation (5.10) and maximum satellite velocity along the x-direction is calculated in Equation (5.11).

$$\tau_{\text{ox}} = \frac{2\ \theta_{st_x}\ I_{st_x}}{t^2} \tag{5.9}$$

$$\tau_{\text{ox}} = 2\ x\ 0.2618x\frac{600}{20^2} = 0.7854\ Nm \tag{5.10}$$

$$w_{st_x} = \frac{0.7854x}{600}\frac{20x180}{\pi} = 1.5\ deg/s \tag{5.11}$$

Required output torque, gimbal angle, satellite rotation angle (roll angle) and satellite angular velocity for case-1 are shown in Figure 5.1. It is noted that these results are analytical results that are calculated and drawn in Excel. Disturbances and losses during maneuvering are not taken into account in these calculations. Optimization and control of the satellite during maneuvering under these disturbances are in the charge

of Attitude Orbit Control System (AOCS) in the satellite and these are not scoped in this thesis.

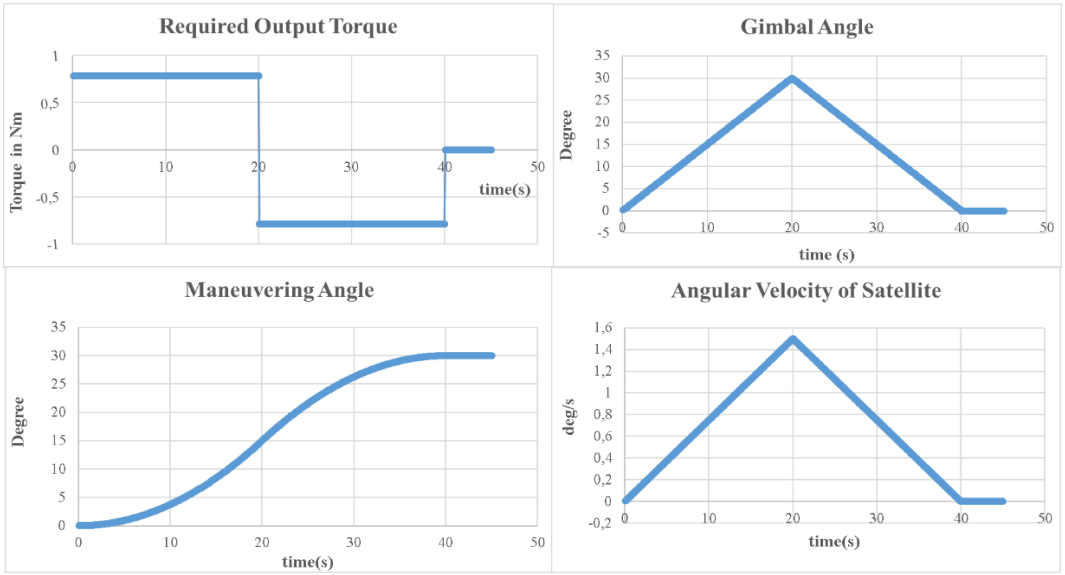

Figure 5.1 Output Torque, Gimbal Angle, Roll Angle and Satellite Angular Velocity for Case-1

5.4.3. Case-2 60° rotation on x-axis should be less than 60s

The satellite should be rotated 60 º on x-axis in less than 60 seconds in this case. Maximum satellite inertia on x-axis has already been given as 600 kgm2 in Table 5.3. Required output torque that rotates the satellite 60º in 60 seconds and the velocity of the satellite is calculated by the following equations. Firstly, the satellite rotation angle for this case should be converted to the angular displacement of the satellite in radian that is shown in Equation (5.13)

$$\theta_{\text{radian}} = \frac{\theta_{degre}\pi}{180} \tag{5.12}$$

$$\theta_{\text{radian}} = \frac{30°\pi}{180} = 0.5236\ rad \tag{5.13}$$

During half of the maneuvering time ($\frac{60}{2} = 30\ seconds$), the velocity of the satellite increases with constant acceleration by applying positive output torque to the satellite

and 30° displacement is achieved. After that, the velocity of the satellite decreases with constant deceleration and 30° displacement is provided during deceleration by applying negative direction output torque to the satellite shown in Figure 5.2. At the end of the maneuvering, 60° rotation occurs within 60 seconds. During this rotation, the required output torque for x-axis is calculated in Equation (5.15) and maximum satellite velocity along the x-direction is calculated in Equation (5.16).

$$\tau_{ox} = \frac{2\,\theta_{st_x}\,I_{st_x}}{t^2} \tag{5.14}$$

$$\tau_{ox} = 2\;x\;0.5236\;x\frac{600}{30^2} = 0.698\;Nm \tag{5.15}$$

$$w_{st_x} = \frac{0.698\;x}{600}\frac{30x180}{\pi} = 2\;deg/s \tag{5.16}$$

Required output torque, gimbal angle, satellite rotation angle (roll angle) and satellite angular velocity for case-2 are shown in Figure 5.2. It is noted that these results are analytical results that are calculated and drawn in Excel. Disturbances and losses during maneuvering are not taken into account in these calculations. Optimization and control of the satellite during maneuvering under these disturbances are in the charge of Attitude Orbit Control System (AOCS) in the satellite and these are not scoped in this thesis.

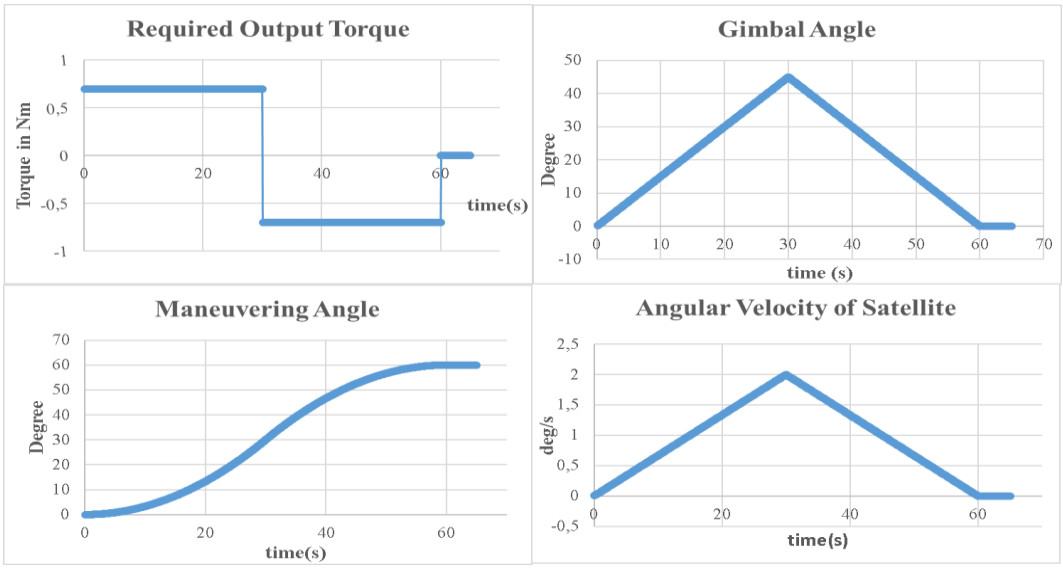

Figure 5.2 Output Torque, Gimbal Angle, Roll Angle and Satellite Angular Velocity for Case-2

5.4.4. Case-3 30° rotation on y-axis should be less than 30s

The satellite should be rotated 30 º on y-axis in less than 30 seconds in this case. Maximum satellite inertia on y-axis has already been given as 500 kgm2 in Table 5.3. Required output torque that rotates the satellite 30º in 30 seconds and the velocity of the satellite is calculated by the following equations. Firstly, the satellite rotation angle for this case should be converted to the angular displacement of the satellite in radian that is shown in Equation (5.18)

$$\theta_{\text{radian}} = \frac{\theta_{degre}\pi}{180} \tag{5.17}$$

$$\theta_{\text{radian}} = \frac{15°\pi}{180} = 0.2618\ rad \tag{5.18}$$

During half of the maneuvering time ($\frac{30}{2} = 15\ seconds$), the velocity of the satellite increases with constant acceleration by applying positive output torque to the satellite and 15° displacement is achieved. After that velocity of satellite decreases with constant deceleration and the second 15° displacement is provided during deceleration by applying negative direction output torque to the satellite shown in Figure 5.3. At the end of the maneuvering, 30° rotation occurs within 30 seconds. During this

rotation, the required output torque for y-axis is calculated in Equation (5.20) and maximum satellite velocity along y-direction is calculated in Equation (5.21).

$$\tau_{oy} = \frac{2\,\theta_{st_y}\,I_{st_y}}{t^2} \tag{5.19}$$

$$\tau_{oy} = 2\,x\,0.2618x\frac{500}{15^2} = 1.163\,Nm \tag{5.20}$$

$$w_{st_y} = \frac{1.163x}{500}\frac{15x180}{\pi} = 2\,deg/s \tag{5.21}$$

Required output torque, gimbal angle, satellite rotation angle (roll angle) and satellite angular velocity for case-3 are shown in Figure 5.3. It is noted that these results are analytical results that are calculated and drawn in Excel. Disturbances and losses during maneuvering are not taken into account in these calculations. Optimization and control of the satellite during maneuvering under these disturbances are in the charge of Attitude Orbit Control System (AOCS) in the satellite and these are not scoped in this thesis.

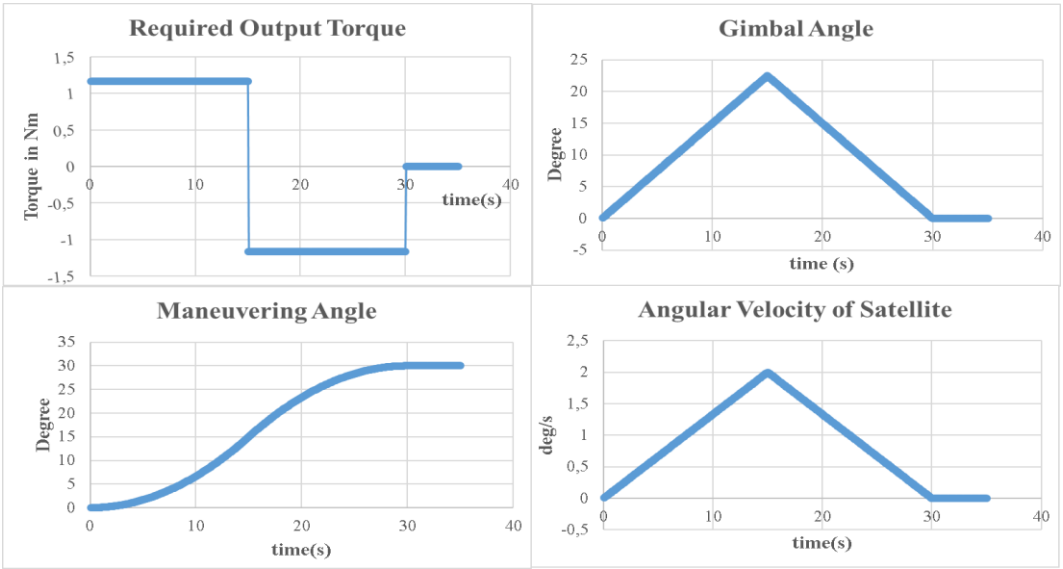

Figure 5.3 Output Torque, Gimbal Angle, Roll Angle and Satellite Angular Velocity for Case-3

5.4.5. Case-4 60° rotation on y-axis should be less than 45s

The satellite should be rotated 60 º on y-axis in less than 45 seconds in this case. Maximum satellite inertia on y-axis has already been given as 500 kgm2 in Table 5.3. Required output torque that rotates the satellite 60º in 45 seconds and the velocity of the satellite is calculated by the following equations. Firstly, the satellite rotation angle for this case should be converted to the angular displacement of the satellite in radian that is shown in Equation (5.23).

$$\theta_{\text{radian}} = \frac{\theta_{degre}\pi}{180} \tag{5.22}$$

$$\theta_{\text{radian}} = \frac{30°\pi}{180} = 0.5236\ rad \tag{5.23}$$

During half of the maneuvering time ($\frac{45}{2} = 22.5 seconds$), the velocity of the satellite increases with constant acceleration by applying positive output torque to the satellite and 30° displacement is achieved. After that velocity of satellite decreases with constant deceleration and the second 30° displacement is provided during deceleration by applying negative direction output torque to the satellite shown in Figure 5.4. At the end of the maneuvering, 60° rotation occurs within 45 seconds. During this rotation, the required output torque for y-axis is calculated in Equation (5.25) and maximum satellite velocity along y-direction is calculated in Equation (5.26).

$$\tau_{\text{oy}} = \frac{2\ \theta_{st_y}\ I_{st_y}}{t^2} \tag{5.24}$$

$$\tau_{\text{oy}} = 2\ x\ 0.5236 x \frac{500}{22.5^2} = 1.034 Nm \tag{5.25}$$

$$w_{\text{st}_y} = \frac{1.034}{500}\frac{22{,}5x180}{\pi} = 2.67\ deg/s \tag{5.26}$$

Required output torque, gimbal angle, satellite rotation angle (roll angle) and satellite angular velocity for case-4 are shown in Figure 5.4. It is noted that these results are analytical results that are calculated and drawn in Excel. Disturbances and losses

during maneuvering are not taken into account in these calculations. Optimization and control of the satellite during maneuvering under these disturbances are in the charge of Attitude Orbit Control System (AOCS) in the satellite and these are not scoped in this thesis.

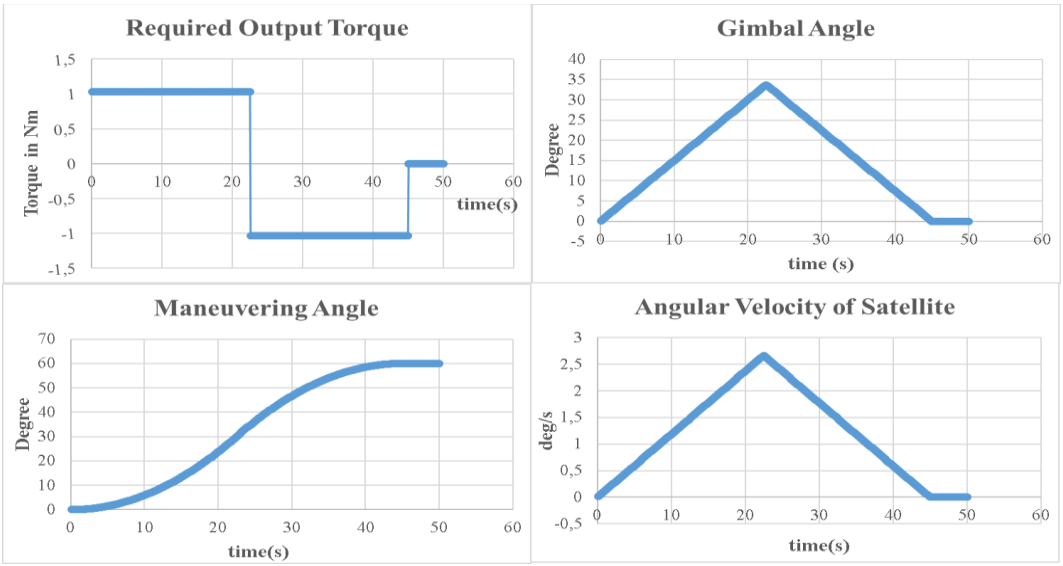

Figure 5.4 Output Torque, Gimbal Angle, Roll Angle and Satellite Angular Velocity for Case-4

5.4.6. Summary of Different Maneuvering Cases

Four different maneuverings based on maneuvering duration requirements mentioned in Table 5.3 are studied in from Section 5.4.2 to Section 5.4.5. The output torque that rotates satellite in specified angle and time, maximum gimbal angle during maneuvering and the velocity of the satellite are summarized in Table 5.4.

Table 5.4 *Summary of Four Different Maneuvering Conditions*

Case	Required Output Torque	Maximum Gimbal Angle	Rotation Angle and Rotation Time	Maximum Velocity of Satellite
Case-1	0,7854 Nm	30°	30°-40s (x-direction)	1.5 deg/s
Case-2	0,698 Nm	45°	60°-60s (x-direction)	2 deg/s
Case-3	1,163 Nm	22.5°	30°-30s (y-direction)	2 deg/s
Case-4	1,034 Nm	33.75°	60°-45s (y-direction)	2.67 deg/s

Case-3 has the maximum torque requirement that is equal to 1,163 Nm shown in Table 5.4. Therefore, this average torque requirement must be provided by CMGs that placed in the pyramidal configuration mentioned in Section 2.3.2. It is noted that if maximum required torque that is corresponding to Case-3 is provided to the satellite, torque requirement for other cases are also satisfied easily.

Since generated torque value depends on the gimbal angle during maneuvering, output torque value is not constant and it changes with varying gimbal angle. In other words, pyramidal configuration generates dynamic torque and it is not constant torque Therefore, required average torque value (1.163 Nm) is provided by total dynamic equivalent output torque on y-direction that is generated by the pyramidal configuration shown in Section 2.3.2 and expressed in Equation (2.29). This equality is also shown in Equation (5.27) for this condition. In this equation, there is a coefficient that represents the pyramid skew angle $[\cos(54.73°)]$ and it is constant. Another coefficient in this equation is "2" and it represents the number of operated CMGs during this maneuvering mentioned in Section 2.3.2.

$$1.163 = 2H_0\dot{\delta}\cos(54.73°)cos\delta \tag{5.27}$$

One CMG is designed in this thesis. Therefore, the output torque capacity of one CMG that satisfies the above conditions should be calculated. In order to calculate the output torque capacity of one CMG, firstly total dynamic equality for pyramidal configuration is modified and required dynamic torque equality for one CMG is obtained by simplifying Equation (5.27). Dynamic torque equality for one CMG that provides sufficient average torque to the satellite is shown in Equation (5.28).

$$H_0\dot{\delta}\cos\delta = 1\ \text{Nm} \tag{5.28}$$

According to Equation (5.28), one CMG has to produce 1Nm average output torque during maneuvering. However, it is obvious that generated output torque of one CMG depends on varying gimbal angle (δ) as a function of cosine and it is not constant since

the gimbal angle is changing during maneuvering. Therefore, the output torque capacity of one CMG that is equal to $H_0\dot{\delta}$ is calculated by taking integral of Equation (5.28). Since the gimbal angle (δ) is only one variable in dynamic torque equation, the interval of the integral equation is taken from 0 to $\frac{\pi}{4}$ (45º). The relationship between the average output torque of one CMG and output torque capability of one CMG is expressed in Equation (5.29).

$$1\ Nm = \frac{1}{\frac{\pi}{4}} \int_0^{\frac{\pi}{4}} H_0\dot{\delta}\cos\delta\ \mathrm{d}\delta = \frac{4}{\pi}\ H_0\dot{\delta}\left[\sin\left(\frac{\pi}{4}\right) - \sin(0)\right] = 0.9H_0\dot{\delta} \tag{5.29}$$

As a result, in order to generate 1 Nm average output torque, one CMG should have 1.11 Nm torque capability shown in Equation (5.30). It is noted that two CMGs are operated during this maneuvering and both of them have same output torque characteristics.

$$H_0\dot{\delta} = 1.11\ Nm \tag{5.30}$$

Dynamic output torque generated by one CMG with the effect of the pyramidal skew angle, dynamic output torque generated by one CMG without the effect of the pyramidal skew angle, dynamic output torque generated by pyramidal configuration, and required average output torque for 45º gimbal angle excursions is shown in Figure 5.5. Thanks to this dynamic torque characteristics, required average torque is provided to satellite and all rotation specifications can be satisfied.

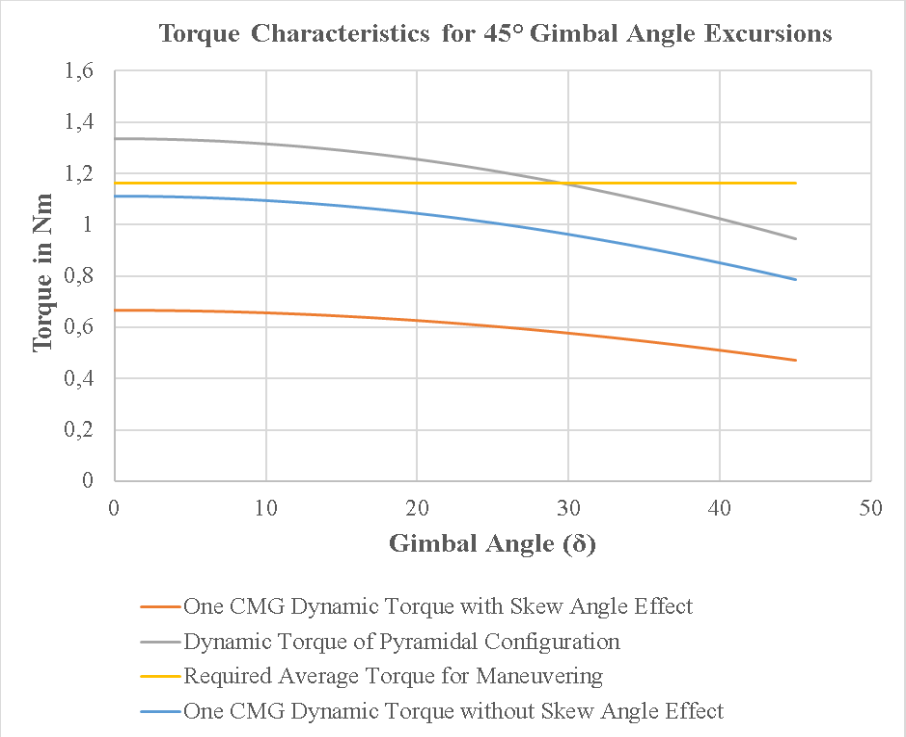

Figure 5.5 Torque Characteristics for 45º Gimbal Angle Excursions

In order to provide required torque calculated in Equation (5.30), wheel system should have sufficient angular momentum. Then, the required moment of inertia of the wheel system is calculated. There are two inertia contribution components of the wheel which are wheel motor and wheel. Since inertia of wheel motor is low compared to the wheel itself, it can be neglected. Torque equation in terms of wheel inertia is expressed in Equation (5.31).

$$I_{CMG}^{w}\,\omega_w\,\dot{\delta} = 1.11\,Nm \tag{5.31}$$

where;

$$\omega_w = 10000\,rpm = \frac{2\pi}{60}10000\,rpm = 1047.2\,rad/s$$

$$\dot{\delta} = 1.5\frac{deg}{s} = \frac{\pi}{180}\,1.5\frac{deg}{s} = 0.02618\,rad/s$$

Therefore, the required inertia of the wheel is equal to $\boldsymbol{I_{CMG}^{w} = 0.0405\,kg.m^2}$

5.5. The Effect of Maximum Gimbal Angle Excursion Choice on CMG Design

Maximum gimbal angle excursion is limited to 45 ° in CMG specifications. This limitation comes from previous experience of designed CMG. However, previously designed CMGs are old designs and the reason of gimbal angle limitation is mechanical considerations such as limitation of mechanical frame and cable tangle during gimbal rotation and stability parameters of control algorithm. In other words, new technology CMGs can have larger maximum gimbal angle excursion. As a result, the effect of larger maximum gimbal angle excursion selection on CMG design is investigated in this section. In fact, required inertia of wheel is decreased by selecting larger gimbal angle excursions and it directly affects the dimensions of the wheel.

5.5.1. 60° Gimbal Angle Analysis

Maximum gimbal angle is selected as 60° in this analysis. According to CMG design specifications, maximum maneuvering time is 60 seconds. At this case, gimbal angle reaches to maximum gimbal excursions angle (60°) in the first 30 seconds and then turns back to 0 ° in other 30 seconds period. As a result, gimbal speed is assumed constant and it is equal to 2 degrees/second (60º / 30 seconds=2 deg /s) in this part. In addition, required torque of satellite and the velocity of the satellite don't depend on gimbal angle. Therefore, only the maximum gimbal angle during different maneuvering is changed in this analysis. The results of 60° gimbal angle analysis are calculated by following the same procedure in Section 5.4. Summary of the results for four different maneuverings is shown in Table 5.5.

Table 5.5 *Summary of Four Different Maneuvering Conditions for 60° Gimbal Angle*

Case	**Required Output Torque**	**Maximum Gimbal Angle**	**Rotation Angle and Rotation Time**	**Maximum Velocity of Satellite**
Case-1	0.7854 Nm	40°	30°-40s	1.5 deg/s
Case-2	0.698 Nm	60°	60°-60s	2 deg/s
Case-3	1.163 Nm	30°	30°-30s	2 deg/s
Case-4	1.034 Nm	45°	60°-45s	2.67 deg/s

The relationship between the average output torque of one CMG and output torque capability of one CMG is expressed in Equation (5.32) for 60° maximum gimbal angle excursion. The interval of the integral equation is taken from 0 to $\frac{\pi}{3}$ (60º).

$$1\ Nm = \frac{1}{\frac{\pi}{3}} \int_{0}^{\frac{\pi}{3}} H_0 \dot{\delta} \cos\delta \, d\delta = \frac{3}{\pi} H_0 \dot{\delta} \left[\sin\left(\frac{\pi}{3}\right) - \sin(0) \right] = 0.827 H_0 \dot{\delta} \tag{5.32}$$

As a result, in order to generate 1 Nm average output torque, one CMG should have 1.21 Nm torque capability shown in Equation (5.33). It is noted that two CMGs are operated during this maneuvering and both of them have same output torque characteristics.

$$H_0 \dot{\delta} = 1.21\ Nm \tag{5.33}$$

Dynamic output torque generated by one CMG with the effect of the pyramidal skew angle, dynamic output torque generated by one CMG without the effect of the pyramidal skew angle, dynamic output torque generated by pyramidal configuration, and required average output torque for 60º gimbal angle excursion is shown in Figure 5.6. Thanks to this dynamic torque characteristics, required average torque is provided to satellite and all rotation specifications can be satisfied.

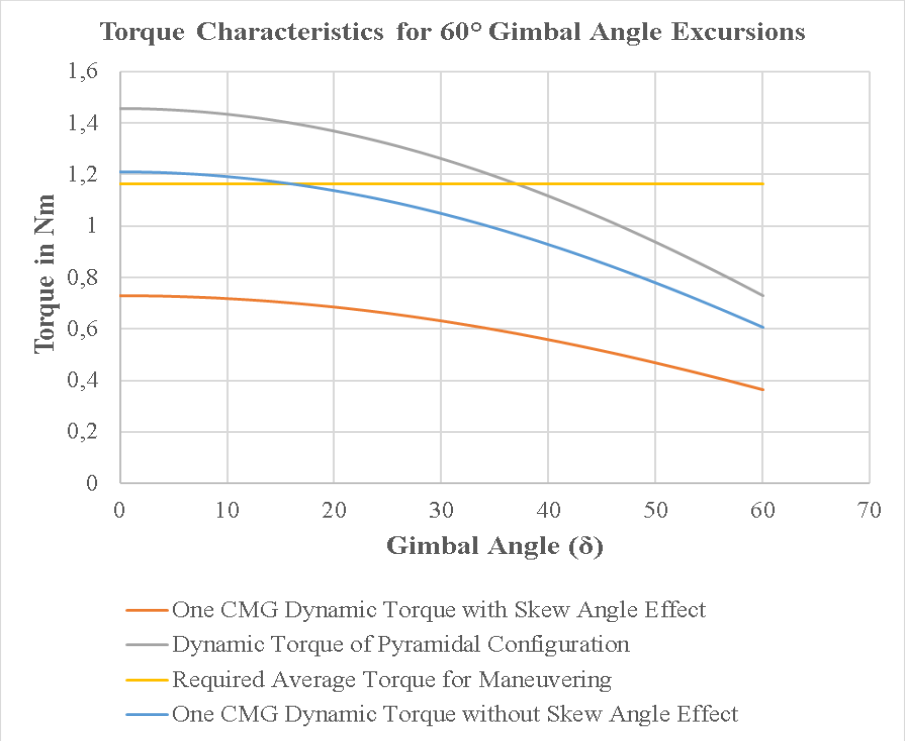

Figure 5.6 Torque Characteristics for 60º Gimbal Angle Excursion

In order to provide required torque calculated in Equation (5.33), wheel system should have sufficient angular momentum. Then, the required moment of inertia of the wheel system is calculated. Torque equation in terms of wheel inertia is expressed in Equation (5.34).

$$I_{CMG}^{w}\ \omega_w\ \dot{\delta} = 1.21\ Nm \tag{5.34}$$

where;

$$\omega_w = 10000\ rpm = \frac{2\pi}{60} 10000\ rpm = 1047.2\ rad/s$$

$$\dot{\delta} = 2\ \frac{deg}{s} = \frac{\pi}{180}\ 2\ \frac{deg}{s} = 0.0349\ rad/s$$

Therefore, the required inertia of the wheel is equal to $\boldsymbol{I_{CMG}^{w} = 0.0331\ kg.m^2}$

5.5.2. 75° Gimbal Angle Analysis

Maximum gimbal angle is selected as 75° in this analysis. According to CMG design specifications, maximum maneuvering time is 60 seconds. At this case, gimbal angle reaches to maximum gimbal excursions angle (75°) in the first 30 seconds and then turns back to 0 ° in other 30 seconds period. As a result, gimbal speed is assumed constant and it is equal to 2.5 degrees/second (75º / 30 seconds=2.5 deg /s) in this part. In addition, required torque of satellite and the velocity of the satellite do not depend on gimbal angle. Therefore, only the maximum gimbal angle during different maneuvering is changed in this analysis. The results of 75° gimbal angle analysis are calculated by following the same procedure in Section 5.4. Summary of the results for four different maneuverings is shown in Table 5.6.

Table 5.6 *Summary of Four Different Maneuvering Conditions for 75° Gimbal Angle*

Case	**Required Output Torque**	**Maximum Gimbal Angle**	**Rotation Angle and Rotation Time**	**Maximum Velocity of Satellite**
Case-1	0.7854 Nm	50°	30°-40s	1.5 deg/s
Case-2	0.698 Nm	75°	60°-60s	2 deg/s
Case-3	1.163 Nm	37.5°	30°-30s	2 deg/s
Case-4	1.034 Nm	56,25°	60°-45s	2.67 deg/s

The relationship between the average output torque of one CMG and output torque capability of one CMG is expressed in Equation (5.35) for 75° maximum gimbal angle excursion. The interval of the integral equation is taken from 0 to $\frac{\pi}{2.4}$ (75º).

$$1\ Nm = \frac{1}{\frac{\pi}{2.4}} \int_{0}^{\frac{\pi}{2.4}} H_0 \dot{\delta} \cos\delta \, d\delta = \frac{2.4}{\pi} H_0 \dot{\delta} \left[\sin\left(\frac{\pi}{2.4}\right) - \sin(0) \right] = 0.738 H_0 \dot{\delta} \tag{5.35}$$

As a result, in order to generate 1 Nm average output torque, one CMG should have 1.355 Nm torque capability shown in Equation (5.36). It is noted that two CMGs are operated during this maneuvering and both of them have same output torque characteristics.

$$H_0\dot{\delta} = 1.355\ Nm \tag{5.36}$$

Dynamic output torque generated by one CMG with the effect of the pyramidal skew angle, dynamic output torque generated by one CMG without the effect of the pyramidal skew angle, dynamic output torque generated by pyramidal configuration, and required average output torque for 75º gimbal angle excursions is shown in Figure 5.7. Thanks to this dynamic torque characteristics, required average torque is provided to satellite and all rotation specifications can be satisfied.

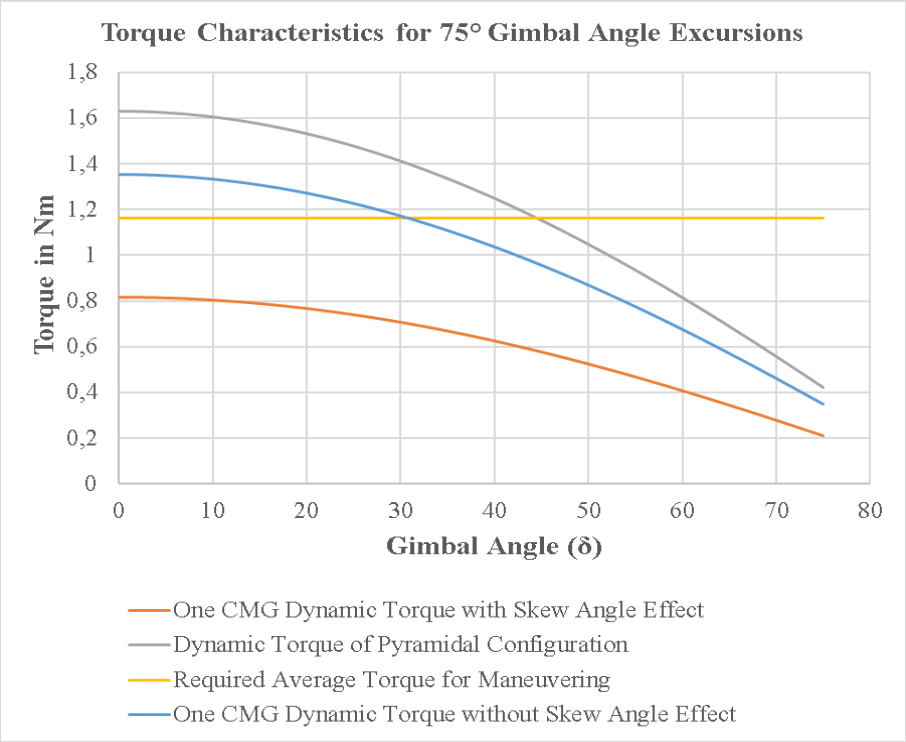

Figure 5.7 Torque Characteristics for 75º Gimbal Angle Excursion

In order to provide required torque calculated in Equation (5.36), wheel system should have sufficient angular momentum. Then, the required moment of inertia of the wheel system is calculated. Torque equation in terms of wheel inertia is expressed in Equation (5.37).

$$I_{CMG}^{w}\ \omega_w\ \dot{\delta} = 1.355\ Nm \tag{5.37}$$

where;

$$\omega_w = 10000\ rpm = \frac{2\pi}{60} 10000\ rpm = 1047.2\ rad/s$$

$$\dot{\delta} = 2.5\ \frac{deg}{s} = \frac{\pi}{180}\ 2.5\ \frac{deg}{s} = 0.0436\ rad/s$$

Therefore, the required inertia of the wheel is equal to $\boldsymbol{I_{CMG}^{w} = 0.0296\ kg.m^2}$

5.5.3. 90° Gimbal Angle Analysis

Maximum gimbal angle is selected as 90° in this analysis. According to CMG design specifications, maximum maneuvering time is 60 seconds. At this case, gimbal angle reaches to maximum gimbal excursions angle (90°) in the first 30 seconds and then turns back to 0 ° in other 30 seconds period. As a result, gimbal speed is assumed constant and it is equal to 3 degrees/second (90º / 30 seconds=3 deg /s) in this part. In addition, required torque of satellite and the velocity of the satellite do not depend on gimbal angle. Therefore, only the maximum gimbal angle during different maneuvering is changed in this analysis. The results of 90° gimbal angle analysis are calculated by following the same procedure in Section 5.4. Summary of the results for four different maneuverings is shown in Table 5.7.

Table 5.7 *Summary of Four Different Maneuvering Conditions for 90° Gimbal Angle*

Case	**Required Output Torque**	**Maximum Gimbal Angle**	**Rotation Angle and Rotation Time**	**Maximum Velocity of Satellite**
Case-1	0.7854 Nm	60°	30°-40s	1.5 deg/s
Case-2	0.698 Nm	90°	60°-60s	2 deg/s
Case-3	1.163 Nm	45°	30°-30s	2 deg/s
Case-4	1.034 Nm	67.5°	60°-45s	2.67 deg/s

The relationship between the average output torque of one CMG and output torque capability of one CMG is expressed in Equation (5.38) for 90° maximum gimbal angle excursion. The interval of the integral equation is taken from 0 to $\frac{\pi}{2}$ (90º).

$$1\ Nm = \frac{1}{\frac{\pi}{2}} \int_0^{\frac{\pi}{2}} H_0 \dot{\delta} \cos\delta \, d\delta = \frac{2}{\pi} H_0 \dot{\delta} \left[\sin\left(\frac{\pi}{2}\right) - \sin(0)\right] = 0.636 H_0 \dot{\delta} \tag{5.38}$$

As a result, in order to generate 1 Nm average output torque, one CMG should have 1.572 Nm torque capability shown in Equation (5.39). It is noted that two CMGs are operated during this maneuvering and both of them have same output torque characteristics.

$$H_0 \dot{\delta} = 1.572\ Nm \tag{5.39}$$

Dynamic output torque generated by one CMG with the effect of the pyramidal skew angle, dynamic output torque generated by one CMG without the effect of the pyramidal skew angle, dynamic output torque generated by pyramidal configuration, and required average output torque for 90º gimbal angle excursion is shown in Figure 5.8 Thanks to this dynamic torque characteristics, required average torque is provided to satellite and all rotation specifications can be satisfied. Thanks to this dynamic torque characteristics, required average torque is provided to satellite and all rotation specifications can be satisfied.

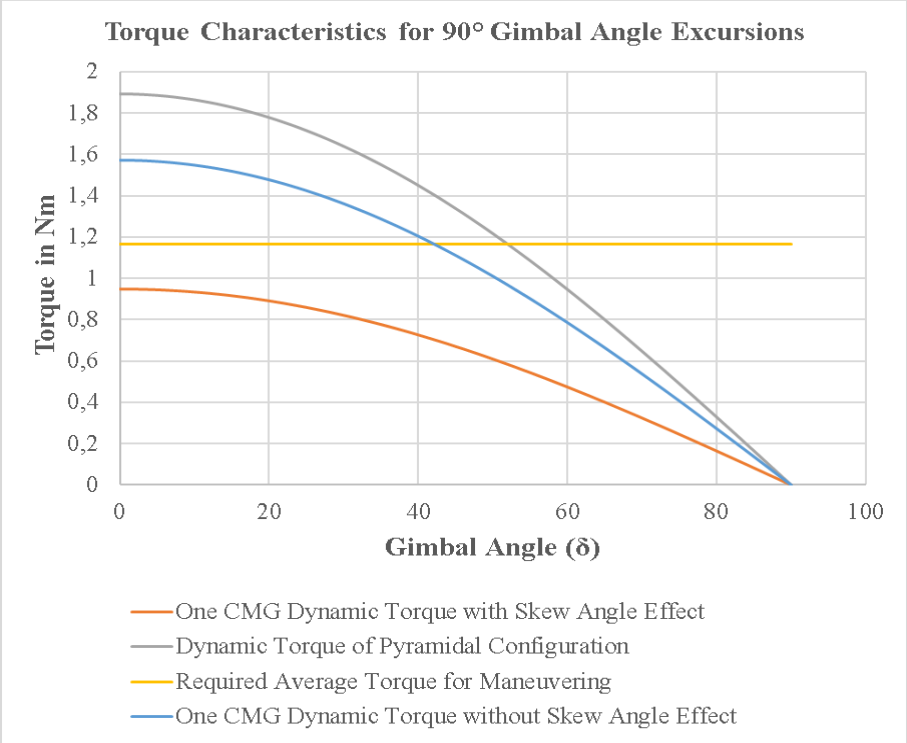

Figure 5.8 Torque Characteristics for 90º Gimbal Angle Excursion

In order to provide required torque calculated in Equation (5.39), wheel system should have sufficient angular momentum. Then, the required moment of inertia of the wheel system is calculated. Torque equation in terms of wheel inertia is expressed in Equation (5.40).

$$I_{CMG}^{w}\ \omega_w\ \dot{\delta} = 1.572\ Nm \tag{5.40}$$

where;

$$\omega_w = 10000\ rpm = \frac{2\pi}{60} 10000\ rpm = 1047.2\ rad/s$$

$$\dot{\delta} = 3\ \frac{deg}{s} = \frac{\pi}{180}\ 3\ \frac{deg}{s} = 0.0523\ rad/s$$

Therefore, the required inertia of the wheel is equal to $\boldsymbol{I_{CMG}^{w} = 0.0286\ kg.m^2}$

5.5.4. Comparison of Different Gimbal Angles Excursion on CMG Design

Maximum gimbal excursion is specified as 45° in CMG specifications. In order to understand the effect of the maximum gimbal angle excursion on CMG design, additional three cases that maximum gimbal angle is 60°, 75° and 90° are also taken into account in previous sections. Effects of a selection of different maximum gimbal angle excursion on CMG design are discussed in this section. Results and comparison of different maximum gimbal angle excursion are shown in Table 5.8.

Table 5.8 *Comparison of Different Maximum Gimbal Angle Excursion*

Maximum Gimbal Angle	**Average Torque of One CMG (Nm)**	**Maximum Torque (Nm)**	**Minimum Torque (Nm)**	**Angular Speed of Gimbal (deg/s)**	**Inertia ($kg.m^2$)**
45°	1	1.11	0.785	1.5	0.0405
60°	1	1.21	0.605	2.0	0.0331
75°	1	1.355	0.350	2.5	0.0296
90°	1	1.572	0	3.0	0.0286

According to Table 5.8, generated maximum output torque increases with increasing gimbal angle and generated minimum torque decreases with increasing gimbal angle. Since average output torque requirement is determined from maneuvering capability it does not depend on gimbal angle and it is the same for each maximum gimbal angle excursion. If the maximum gimbal angle excursion is increased, a difference of maximum and minimum torque generated by one CMG is increased and it causes oscillation on the satellite control system. The velocity of the satellite is not increased linearly and position control of the satellite during maneuvering is more difficult. In addition, the attitude control algorithm can be more complex to provide stability of satellite during maneuvering because of this difference.

Since maneuvering time limitation comes from system requirement and it is the same for each different gimbal angle, the angular speed of gimbal increases with increasing

gimbal angle. The main advantage of increasing gimbal angle is decreasing inertia. Required inertia is decreased since the angular speed of the gimbal directly affects the output torque equation of CMG shown in Equation (5.40). Thanks to low inertia, wheel dimensions, volume, and mass can be reduced. Therefore, since wheel volume is reduced, the total volume of CMG is also reduced. In addition, required motor dimensions which provide rotating energy to the wheel can be reduced since the required torque of the motor is lower if the inertia of the wheel is small. The summary of the comparison of different maximum gimbal angle excursion is shared Figure 5.9. In conclusion, although larger maximum gimbal angle excursion has many advantages in terms of mass and volume, shorter gimbal angle excursion is more suitable since the satellite is more stable during maneuvering and the effect of disturbances on the satellite is lower. Therefore, the satellite is more reliable if the shorter maximum gimbal angle excursion is selected.

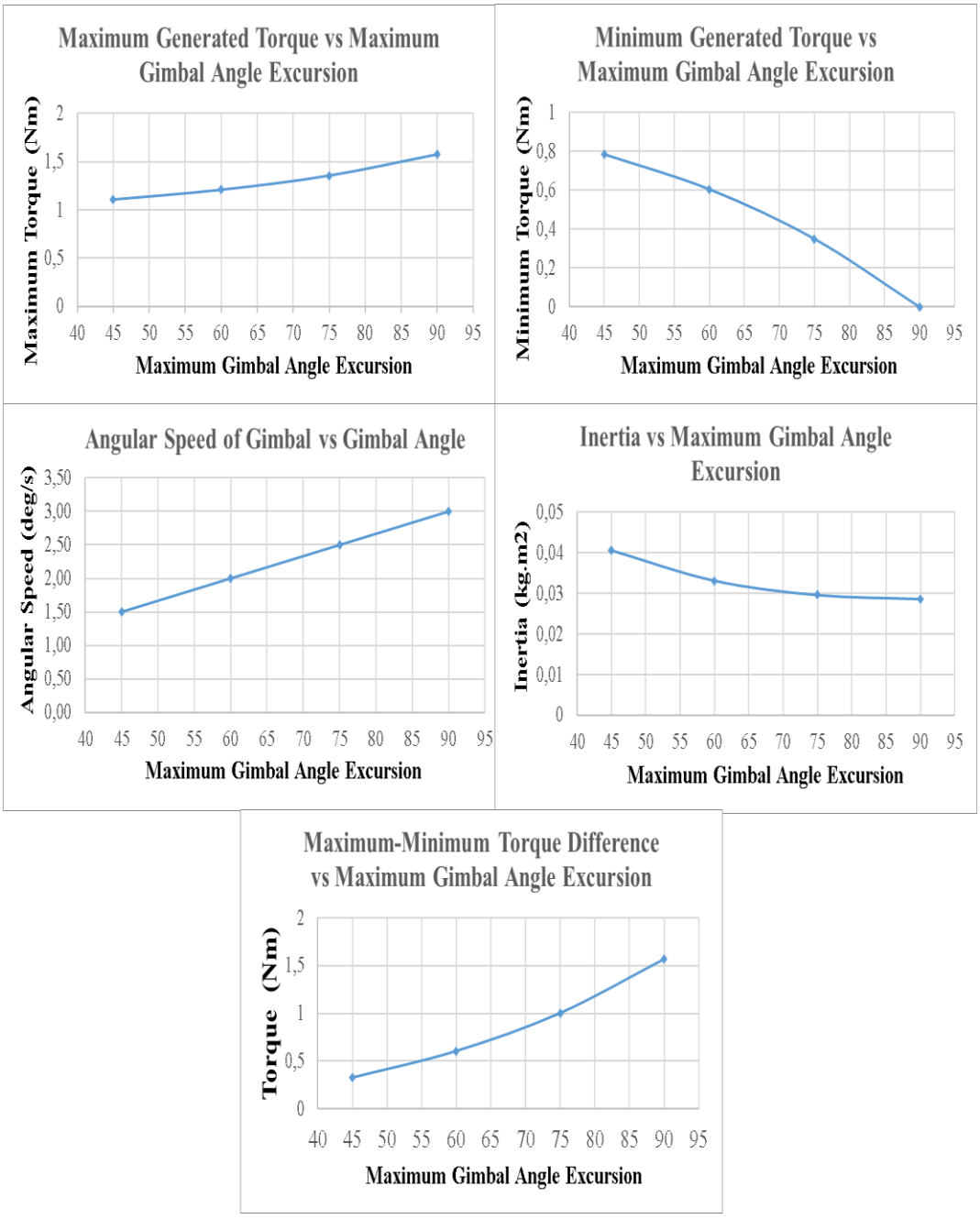

Figure 5.9 Comparison Summary of Different Maximum Gimbal Angle Excursion

CHAPTER 6

WHEEL DESIGN OF CMG

6.1. Introduction

CMG is a device based on conservation of the angular momentum. The angular momentum of CMG is provided by the wheel. The angular momentum has two components that are inertia and speed of the wheel. The target speed of the wheel is assigned as 10000 rpm (1047.2 rad/s) in Table 5.3. Therefore, the proper wheel should be designed to provide sufficient inertia calculated in Section 5.5. Inertia of the wheel depends on physical dimensions and mass of the wheel.

6.2. Inertia Calculations of the Wheel

The geometry of the wheel is taken as a disc. It consists of an outer radius (R2) and an inner radius (R1). The thickness of the wheel is described as “t”. The geometry of the wheel is shown in Figure 6.1. Contribution of spoke of the wheel is not considered in inertia calculations and they have also a positive effect on the inertia of the wheel. In addition, wheel is mounted on outer rotor of BLDC motor shown in Figure 6.2.

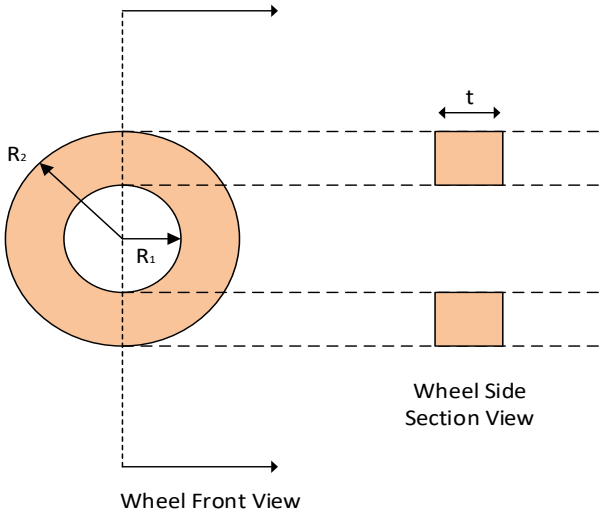

Figure 6.1 Wheel Geometry

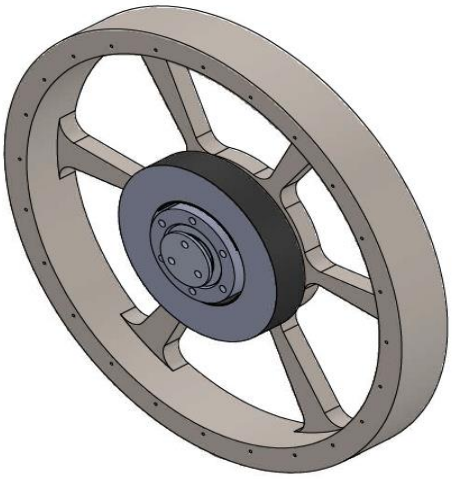

Figure 6.2 Representation of Wheel Mounted on Outer Rotor of BLDC Motor

The inertia of the wheel equation is derived in terms of the outer radius (R_2), inner radius (R_1), mass (m_{wheel}), density of wheel (d_{wheel}), and thickness of wheel (t) in Equation (6.1). Mass of wheel is calculated in Equation (6.2) and the volume of the wheel is calculated in Equation (6.3) [26].

$$I_{CMG}^{w} = \frac{m_{wheel}(R_2^2 + R_1^2)}{2} \tag{6.1}$$

$$m_{wheel} = \pi(R_2^2 - R_1^2)\, t\, d_{wheel} \tag{6.2}$$

$$V_{wheel} = \pi(R_2^2 - R_1^2)t \tag{6.3}$$

Substituting Equation (6.2) into Equation (6.1) and the inertia of the wheel is expressed in Equation (6.4) in terms of thickness of the wheel (t), outer radius of the wheel (R_2), inner radius of the wheel (R_1), and density of the wheel (d_{wheel}) material.

$$I_{CMG}^{w} = \pi\, t\, d_{wheel}\, \frac{(R_2^2 + R_1^2)(R_2^2 - R_1^2)}{2} \tag{6.4}$$

Rearranging Equation (6.4) and final expression of inertia of wheel is shown in Equation (6.5).

$$I_{CMG}^{w} = \frac{\pi\, t\, d_{wheel}}{2}\, (R_2^4 - R_1^4) \tag{6.5}$$

6.3. Design Constraints of the Wheel

There are three constraints while designing and choosing the dimensions of the wheel.

- The first constraint is the volume of CMG. Volume constraint has already specified in Section 5.3. The maximum volume of CMG shall be less than 35 cm x 35cm x 13cm. Thus, the outer diameter of the wheel should be less than 35 cm. Since CMG is placed to satellite within a box and the box has also the thickness, the outer radius of the wheel of CMG is decided to less than 15 cm.
- When the wheel is spinning at a high angular velocity, it can experience high stress. The wheel must withstand this stress during operation. There are two types of stress; these are tensile yield stress(σ_{yield}) and ultimate yield stress. ($\sigma_{ultimate}$). Yield stress is the maximum stress that a solid material can withstand when it is deformed within its elastic limit and ultimate stress is the maximum stress that a solid material can withstand before its failure. The material of the wheel is chosen as AISI Type 304 Stainless Steel since it is suitable for space applications and storage. It has also high ultimate and yield

stress and density. The density of selected stainless steel is $8000\ kg/m^3$. Ultimate stress is 505 MPa and yield stress is 215 MPa [27].

- According to European Cooperation for Space Standardization, factor of safety (FoS) must bigger than 1.1 for unmanned spacecraft and it must bigger than 1.25 for manned spacecraft [28].

6.4. The Effect of Maximum Gimbal Angle Excursion on Wheel Design

Required inertia that provided by the wheel is decreased by increasing maximum gimbal angle excursion studied in Section 5.5.4. Therefore, volume and mass of the wheel are also reduced by increasing maximum gimbal angle excursion.

6.5. Design Example of the Wheel When Maximum Gimbal Angle Excursion is 45°

$Thickness\ of\ wheel\ is\ taken\ as\ 3\ cm\ ;\ t = 3\ cm$

$Required\ inertia\ of\ the\ wheel\ ,\ I_{CMG}^{w} = 0.0405\ \text{kg.m}^2$

If the known parameters ($I_{CMG}^{w}, t, d_{wheel}$) are put into Equation (6.5), the relationship between the inner radius of the wheel and the outer radius of the wheel is obtained in Equation (6.6). The final numeric relationship between the inner radius of the wheel and the outer radius of the wheel is obtained in Equation (6.7) by simplifying Equation (6.6).

$$0{,}0405 = \frac{\pi\ 3x10^{-2}\ x8000}{2}\ (R_2^4 - R_1^4) \tag{6.6}$$

$$(R_2^4 - R_1^4) = 1{,}074\ x\ 10^{-4} \tag{6.7}$$

Selected outer radius should be smaller than 15 cm due to the volume limitation of the reserved CMG. The first step in the design procedure of the wheel is to assign an outer radius value and it is taken as $R_2 = 13\ cm$ for the first iteration. The inner radius of the wheel is calculated by putting selected outer radius into Equation (6.7) and it is calculated as $R_1 = 11{,}55\ cm$. The second step of the wheel design is to verify that

maximum tensile yield stress during operation should be smaller than the tensile stress of the used material. Tensile yield stress expression for the wheel is shown in Equation (6.8) [29].

$$\sigma_{yield} = \frac{d_{wheel}}{4}\ \omega_{wheel}^2\ [\ (3+v)R_2^2 + (1-v)R_1^2\ ] \tag{6.8}$$

Where v is Poisson ratio of AISI Type 304 Stainless Steel and it is equal to 0. 29 and the density of the AISI Type Stainless Steel ($d_{wheel} = 8000\,\frac{kg}{m^2}$) [27]. The speed of the wheel is expressed as ω_{wheel} and it is equal to 1047.2 rad/s (10000 rpm).

Maximum tensile yield stress during operation (σ_{op}) is calculated in Equation (6.9) numerical result is lower than the yield stress of selected material ($\sigma_{yield} = 215\ MPa$) it is shown in Equation (6.10).

$$\sigma_{op} = \frac{8000}{4}\ 1047{,}2^2\ [\ (3+0{,}29)\ 0{,}13^2 + (1-0{,}29)\ 0{,}1155^2\ ] \tag{6.9}$$

$$\sigma_{op} = 142720800{,}2\,\frac{N}{m^2} = 142{,}7\ MPa\ < 215\ MPa \tag{6.10}$$

The third step of the wheel design is to check factor of safety (FoS). Factor of safety must be bigger than 1.1 for unmanned spacecraft and 1.25 for manned spacecraft. Since designed CMG is planned to use earth observation satellites that are unmanned spacecraft, limitation of the factor of safety is taken as 1.1. FoS is calculated by dividing maximum yield speed by maximum operation speed [28]. Maximum yield speed ω_{yield} is calculated in Equation (6.12) by rearranging Equation (6.8) and factor of safety is calculated in Equation (6.13). It is seen that numeric result of FoS is 1.23 and it is bigger than 1.1.

$$\omega_{yield} = \sqrt{\frac{4\sigma_{yield}}{d_{wheel}\ [\ (3+v)R_2^2 + (1-v)R_1^2\ ]}} \tag{6.11}$$

$$\omega_{yield} = 1285{,}3\ rad/s \tag{6.12}$$

$$FoS = \frac{\omega_{yield}}{\omega_w} = \frac{1285,3}{1047,2} = 1,23 \ > 1,1 \qquad (6.13)$$

6.5.1. Design Outputs When Maximum Gimbal Angle is 45°:

The design of the wheel is explained step by step in Section 6.5. Design outputs are shown in the following expressions.

$Outer\ Radius\ of\ Wheel\ ;\ R_2 = 13\ cm$

$Inner\ Radius\ of\ Wheel\ ;\ R_1 = 11{,}55\ cm$

$Thickness\ of\ Wheel\ ; t = 3\ cm$

$Volume\ of\ Wheel\ ; V_{wheel} = 3{,}35\ x\ 10^{-4}\ m^3$

$Mass\ of\ Wheel\ ; m_{wheel} = 2.68\ kg$

$Inertia\ of\ Wheel\ ;\ I_{CMG}^{w} = 0.0405\ kg.m^2$

$Angular\ Momentum\ of\ Wheel:\ H_0 = 42{,}41\ Nms$

$Factor\ of\ Safety\ ; FoS = 1{,}23$

6.5.2. Design Outputs for Different Outer Radii and Different Gimbal Angles

According to the design example mentioned Section 6.5, different wheels are designed for different outer radius selected as 11cm, 12cm and 13 cm. Since the required inertia and angular momentum of CMG system is different for each maximum gimbal angle excursion case mentioned in Section 5.5.4, mass and volume of designed wheels are also different. The thickness of the wheel is taken as 3 cm for each design and required inertia and angular momentum for each case are provided by suitable wheel design. Results of the wheel design for different radii and maximum gimbal angle excursion are shown in Table 6.1.

Gimbal Angle(°)	45			60			75			90		
Outer Radius of Wheel (cm)	11	12	13	11	12	13	11	12	13	11	12	13
Inner Radius of Wheel (cm)	7,9	10	11,55	8,75	10,46	11,86	9,08	10,65	12	9,16	10,71	12,03
Volume of Wheel (m3)	5,50E-04	4,15E-04	3,35E-04	4,19E-04	3,26E-04	2,67E-04	3,64E-04	2,87E-04	2,36E-04	3,49E-04	2,76E-04	2,28E-04
Mass of Wheel (kg)	4,41	3,32	2,68	3,35	2,61	2,13	2,91	2,3	1,89	2,79	2,21	1,82
Inertia of Wheel (kg.m2)	0,0405	0,0405	0,0405	0,0331	0,0331	0,0331	0,0296	0,0296	0,0296	0,0286	0,0286	0,0286
Angular Momentum of Wheel (Nms)	42,41	42,41	42,41	34,66	34,66	34,66	31,00	31,00	31,00	29,95	29,95	29,95
Operating Tensile Yield Stress (MPa)	97,03	119,47	142,73	99,23	120,93	143,85	100,14	121,58	144,36	100,39	121,76	144,50
Maximum Yield Speed (rad/s)	1559	1405	1285	1541	1396	1280	1534	1392	1278	1532	1391	1277
Factor of Safety (FoS)	1,49	1,34	1,23	1,47	1,33	1,22	1,46	1,33	1,22	1,46	1,33	1,22

Table 6.1 *Results of Wheel Design for Different Case*

6.6. Conclusion

Firstly, the results of the wheel design are compared for one gimbal angle excursion itself.

If the outer radius is taken as larger

- Mass and volume of the wheel are lower.
- Operating tensile stress is higher and the maximum yield speed is reduced.
- Since maximum yield speed is reduced, factor of safety is also reduced.

Since factor of safety for all cases satisfy the requirement that it is 1.1 for unmanned spacecraft and operating tensile stress for all cases is also less than the requirement (215 MPa), the wheel that has a larger outer radius is a more suitable design in terms of mass and volume consideration.

Secondly, the results of the wheel design are compared for different maximum gimbal angle excursions. If the maximum gimbal angle excursion is increased and results are compared for the same outer radius selection:

- Mass and volume of the wheel are lower due to lower inertia requirement
- Operating tensile stress is a little bit higher and the maximum yield speed is reduced.
- Since maximum yield speed is reduced, factor of safety is also reduced.

In conclusion, the wheel has lower mass and volume if the outer radius is taken as larger and the maximum gimbal angle is increased. It is noted that if the wheel is used for manned space vehicles, outer radius of the wheel mustn't be selected as 13 cm since factor of safety of these wheels is less than 1.25.

Trendline and results of wheel design for three different outer radius and different maximum gimbal angle excursion cases are shown in from Figure 6.3 to Figure 6.6. In addition, the designed and selected wheel that used in this thesis is explained in detail in Section 9.3.

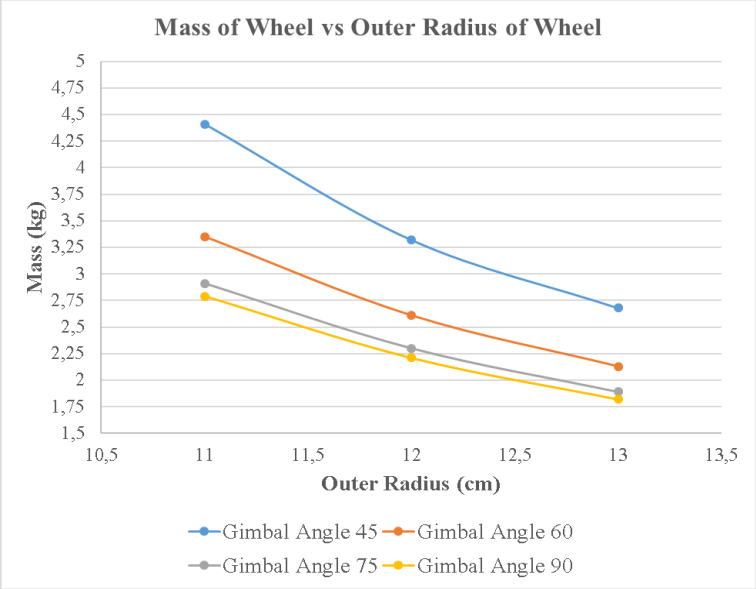

Figure 6.3 Trendline of Wheel Mass

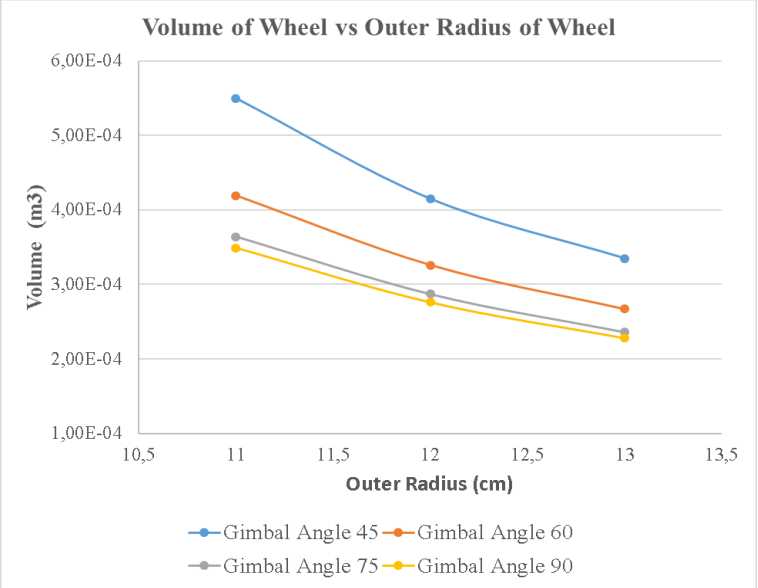

Figure 6.4 Trendline of Wheel Volume

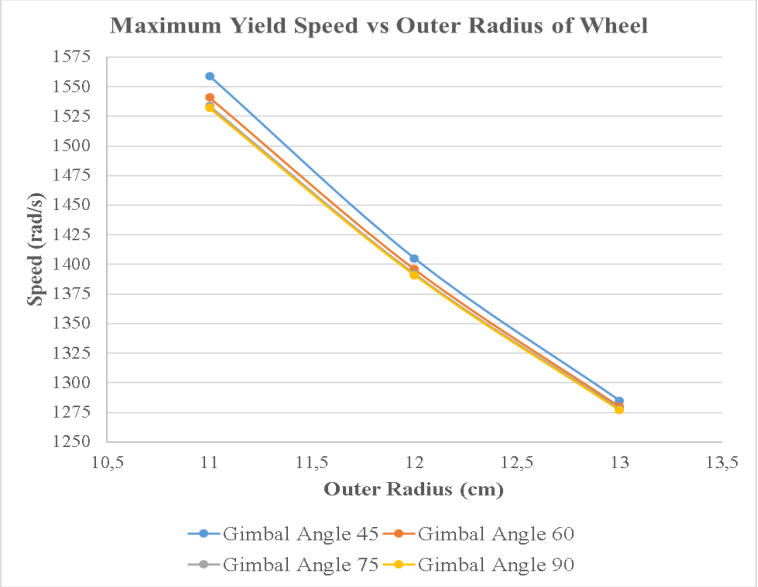

Figure 6.5 Trendline of Wheel Yield Speed

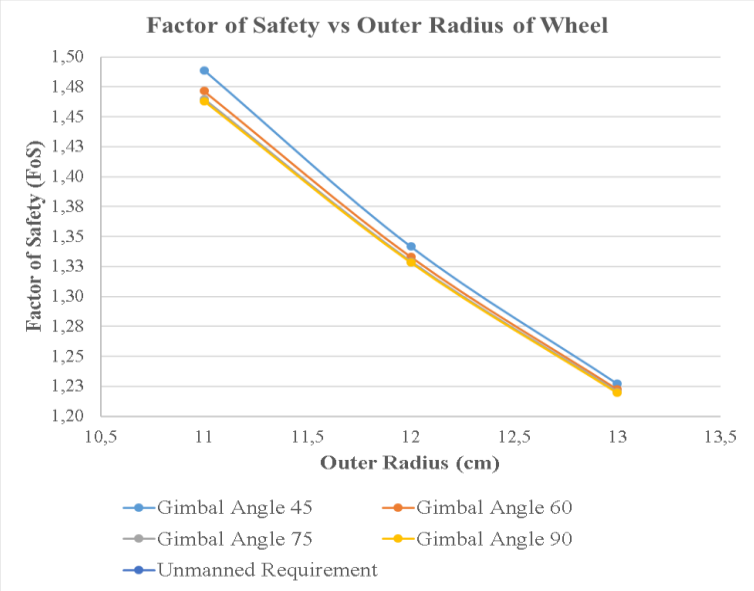

Figure 6.6 Trendline of FoS

CHAPTER 7

SELECTION AND DESIGN OF WHEEL MOTOR

7.1. Torque Requirement of Wheel Motor

In order to obtain angular momentum that creates output torque when the direction of the angular momentum vector is changed in CMG, the wheel should be rotated with specified speed. The force of the rotation is provided by an electric motor mounted on the wheel. According to CMG requirements mentioned in Table 5.3, the wheel has to reach maximum speed (10000 rpm) within 300 seconds. Therefore, there are two components of the motor torque due to acceleration torque and steady-state load (bearing friction). Torque capacity of the designed motor should satisfy the total of these torque components when CMG is operating. The mathematical expression of the dynamic torque equation of the wheel motor is shown in Equation (7.1).

$$\tau_m = \tau_{acc} + \tau_{load} = J_{wheel}\frac{d\omega_m}{dt} + \tau_{load} \tag{7.1}$$

Where;

τ_m: $required\ motor\ torque$

τ_{acc} : $acceleration\ torque\ component$

τ_{load}: $torque\ due\ to\ friction\ of\ the\ wheel$

J_{wheel} : $Inertia\ of\ \ the\ wheel$

ω_m: $Mechanical\ speed\ of\ the\ wheel\ \ (rad/s)$

The inertia of the wheel (J_{wheel}) is calculated for 4 different maximum gimbal angle excursions in Section 5.5. Required torque of the motor (τ_m) is obtained by sum of acceleration and load torque. Acceleration torque is directly related to the inertia of

the wheel and acceleration time. If the inertia of the wheel is higher and acceleration time is shorter, the motor must generate higher torque to satisfy speed and time requirements. Since the inertia of the wheel is different for each maximum gimbal angle excursion, the required acceleration torque is also different. Required acceleration torque is calculated by using Equation (7.2) and the required torque results of four different gimbal angle excursion are shown in Table 7.1

$$\tau_m = J_{wheel} \frac{d\omega_m}{dt} \tag{7.2}$$

dt is maximum acceleration time and it is specified as 300 seconds and ω_m is operating speed of the wheel and it is specified as 10000 rpm (1047,2 rad/s) in this study.

Table 7.1 *Required Acceleration Torque Results*

Maximum Gimbal Angle Excursion (°)	**Inertia (kg.m^2)**	**Acceleration Torque (Nm)**
45	0.0405	0.141
60	0.0331	0.116
75	0.0296	0.103
90	0.0286	0.100

The second component of the required torque of the motor is load torque (τ_{load}) . Load torque depends on wheel design and motor design. Since there is no gravity in space applications, the reason of the load torque is friction on the mechanical parts of the wheel and no-load torque of the motor. Therefore, the determination of load torque is not easy. In fact, although it can be estimated by analyzing mechanical parts of the wheel and no-load characteristics of the motor, it is complicated and it is generally obtained from test results. This load torque is taken as a target torque value of the existing satellite design and it is verified by tests. However, the maximum speeds of previous actuators and designed wheel in this thesis are non-compatible. Load torque of the previous actuator was calculated for maximum 4500 rpm and the speed of the

wheel is specified as 10000 rpm in this thesis. Hence, since wheel design of this study is not the same as previous design and test results of previous programs do not include higher speed results, some margin is added to estimated load torque and it is taken as 1.5 times of previous design. Results of load torque estimation based on previous experience are shown in Table 7.2.

Table 7.2 *Results of Friction Torque Calculations*

Speed (rpm)	**Load Torque (Nm)**	**Load Torque with Margin (Nm)**
10	0.003	0.0045
1000	0.008	0.012
2000	0.013	0.0195
3000	0.018	0.027
4500	0.025	0.0375
10000	0.053	0.0795

According to Table 7.2, load torque has initial load torque and it is equal to 3 mNm. For each 1000 rpm increment, 5 mNm frictional torque is added to initial torque. The results in Table 7.2 show that load torque increases with the increasing speed of the wheel. Therefore, load torque at 10000 rpm is calculated as 0.053 Nm nominal load torque and 0.0795 Nm load torque with 50% margin.

After estimation of load torque, required motor torque that provides acceleration and rotation on the wheel at 10000 rpm is calculated by summing acceleration torque and load torque. Required motor torque is calculated for different maximum gimbal angle excursion by using Equation (7.1) and the results are shown in Table 7.3. It is noted that although load torque depends on the speed of the wheel, load torque is assumed maximum and constant during acceleration.

Table 7.3 *Required Motor Torque for Different Maximum Gimbal Angle Excursion*

Gimbal Angle (°)	**Acceleration Torque (Nm)**	**Load Torque (Nm)**	**Required Motor Torque (Nm)**
45	0.141	0.0795	0.2205
60	0.116	0.0795	0.1955
75	0.103	0.0795	0.1825
90	0.100	0.0795	0.1795

7.2. Selection of Type of Wheel Motor

SGCMG design includes two different electric motors. One of them is used for gimbal motor. Gimbal motor provides the rotation of the wheel and the direction of angular momentum that is created by the rotation of the wheel is changed by gimbal motor. Low speed (1-20 rpm) [7] stepper motors are usually selected for gimbal motor since gimbal angle reaches maximum excursion angle at the half of specified maneuvering duration mentioned in Section 5.4. The detail of the gimbal motor is explained in CHAPTER 8. The second electric motor in CMG design is wheel motor. High-speed brushless DC motor is generally preferred as wheel motor in CMG applications. The required torque of the electric motor has already determined in Table 7.3 for different maximum gimbal excursion. The next step after determining required torque is to decide the type of the BLDC motor. Two previous studies [7] and [8] discuss the type of BLDC motors and design a new type of BLDC motors. Conventional radial flux BLDC motor and axial flux BLDC motor were compared in terms of power and torque density in [7]. Conventional Radial and axial flux motors for 2-pole and 6-pole were designed for CMG applications in [7]. Furthermore, although radial flux motor was designed for sinusoidal and square wave excitation, axial motor was only designed for square wave excitation in [7].

On the other hand, new type BLDC motor that is called as outer rotor radial flux BLDC motor was designed for same torque requirement as axial flux motor and the design results of outer rotor radial flux motor were compared with the results of the

axial flux motor in [8]. Sinusoidal and square wave excitations were also applied in this study.

The results of these two studies are summarized in this thesis in terms of mass, torque/mass, volume, torque/volume, efficiency, and inertia contribution of the motors. It is noted that all electric motors were designed for same torque value (32 mNm for steady-state operation and 50 mNm for acceleration). The comparison of the different types of wheel motor are shown in Table 7.4.

Table 7.4 *Comparison of Types of Wheel Motor*

Motor Type	**Mass (g)**	**Torque/mass (Nm/kg)**	**Volume (m^3)**	**Torque/volume (Nm/m^3)**	**Efficiency (%)**	**Inertia Contribution (%)**
Conventional RF-2 pole motor (square wave) [7]	270	0.18	4.20 E-05	1190	85	0.5
Conventional RF-6 pole motor (square wawe) [7]	145	0.345	2.45 E-05	2240	79	1
Axial flux-2pole (square wave) [7]	300	0.165	4.45 E-05	1125	91	15
Axial flux-6 pole (square wave) [7]	110	0.455	1.90 E-05	2630	92	6
Outer rotor radial flux- 2 pole (sinusoidal) [8]	210	0.24	3.05 E-05	1640	90	65
Outer rotor radial flux- 6 pole (sinusoidal) [8]	95	0.525	1.90 E-05	2630	93	2
Outer rotor radial flux- 2 pole (square wavel) [8]	185	0.27	2.70 E-05	1850	90	38
Outer rotor radial flux- 6 pole (square wave) [8]	110	0.455	2.05 E-05	2440	93	5

7.2.1. Discussion of the Results of Wheel Motors Types

The design results of three different motors studied in previous two studies are summarized in Table 7.4. The first motor is conventional radial flux motor and rotor is placed at inner side of motor and stator coils are placed at outer side of the motor. The flux path in this motor is designed radially. The second motor is an axial flux

motor. Rotor is placed at outer side of the motor and stator coils are placed at inner side of the motor. The flux path in axial flux motor is axially. The last type motor is outer rotor radial flux motor and it has the same configuration in terms of placement of stator and rotor. However, flux path is designed the same as conventional radial flux motor. Discussion and comparison of these three types of wheel motor are studied in this section by following statements.

- Since 6 poles motors share flux path, they have shorter stator back core thickness. Therefore, 6-poles motors have a lower mass. When we compare the mass of motors, outer rotor radial flux sine wave excited 6-pole motor, outer rotor radial flux square wave excited 6-pole motor and axial flux-6 pole motor have a lower mass. The most suitable motor in terms of mass is outer rotor radial flux sine wave excited 6-pole motor. Therefore, this type of motor has also higher torque/ mass performance.
- When volume and torque/volume are compared, outer rotor 6-pole motors and axial flux 6 pole motor should be chosen as wheel motors because these motors have lower volume and higher torque/volume performance.
- Outer rotor 6-poles motors have the highest efficiency. Outer rotor radial flux sine wave excited 6-pole motor or outer rotor radial flux square wave excited 6-pole motor should be chosen as wheel motor in terms of efficiency.
- Inertia contribution shows a positive effect of total inertia. Since 2-pole motors have longer stator back core length they have higher inertia contribution. The most suitable motor in terms of inertia contribution is outer rotor radial flux sine wave excited 2-pole motor. However, the wheel itself has already designed to provide sufficient inertia to CMG. Therefore, although higher inertia contribution is preferred specification, it is not critical for wheel motor design. It is noted that inertia contribution of designed motor is shared in Section 7.3.10.5
- As a result, outer rotor radial flux 6-pole motors have more advantages in terms of mass, torque/mass, volume, torque/volume, and efficiency.

These three motors were studied for smaller CMGs and small wheels where torque requirement of motors is 32 mNm for steady-state operation and 50 mNm for acceleration [7] [8]. The results of the two studies give an idea that outer rotor radial flux motors have a lot of advantage when they are compared with axial flux motor and conventional radial flux motors. However, since the wheel motor of this CMG study has higher torque requirement, motor design has to be updated to provide at least 0.2205 Nm for 45° gimbal angle, 0.1955 Nm for 60° gimbal angle, 0.1825 Nm for 75° gimbal angle and 0.1795 Nm for 90° gimbal angle and 0.0795 Nm for steady-state. In other words, the new motor design should be designed approximately 4 times higher torque than previous motor designs.

Since the manufacturing process of the outer rotor radial flux motor is easier than the outer rotor axial flux motors outer rotor radial flux motor is chosen as a wheel motor type in this thesis.

Although sine wave excitation motor has a little more advantage than square wave excitation in terms of torque density, square wave excitation is chosen in this thesis because the design of driving electronics of square wave excitation is easier than sine wave excitation. In addition, in order to obtain sinusoidal excitation for 10000 rpm motor, transistors of motor driver should have higher switching frequency and it causes higher switching loss and switching stress. (especially for 6-pole motor since fundamental frequency is 500 Hz). Therefore, implementation of sinusoidal excitation is not reasonable. As a result, the outer rotor radial flux motor with square wave excited motor is re-designed in this thesis for high torque requirement. Since the type of re-designed motor is an outer rotor radial flux motor, it is designed based on the study [8].

In conclusion, since mass and volume are the most significant criteria for space applications, the most suitable square-wave excited outer rotor motor design that satisfies electrical loading and magnetic loading conditions will be selected in terms of mass and volume.

7.3. Wheel Motor Design

Wheel motor design procedure has been already analyzed in [7] and [8]. Same design procedure is applied in this study in following sections. Design flowchart of wheel motor is shown in Figure 7.1.

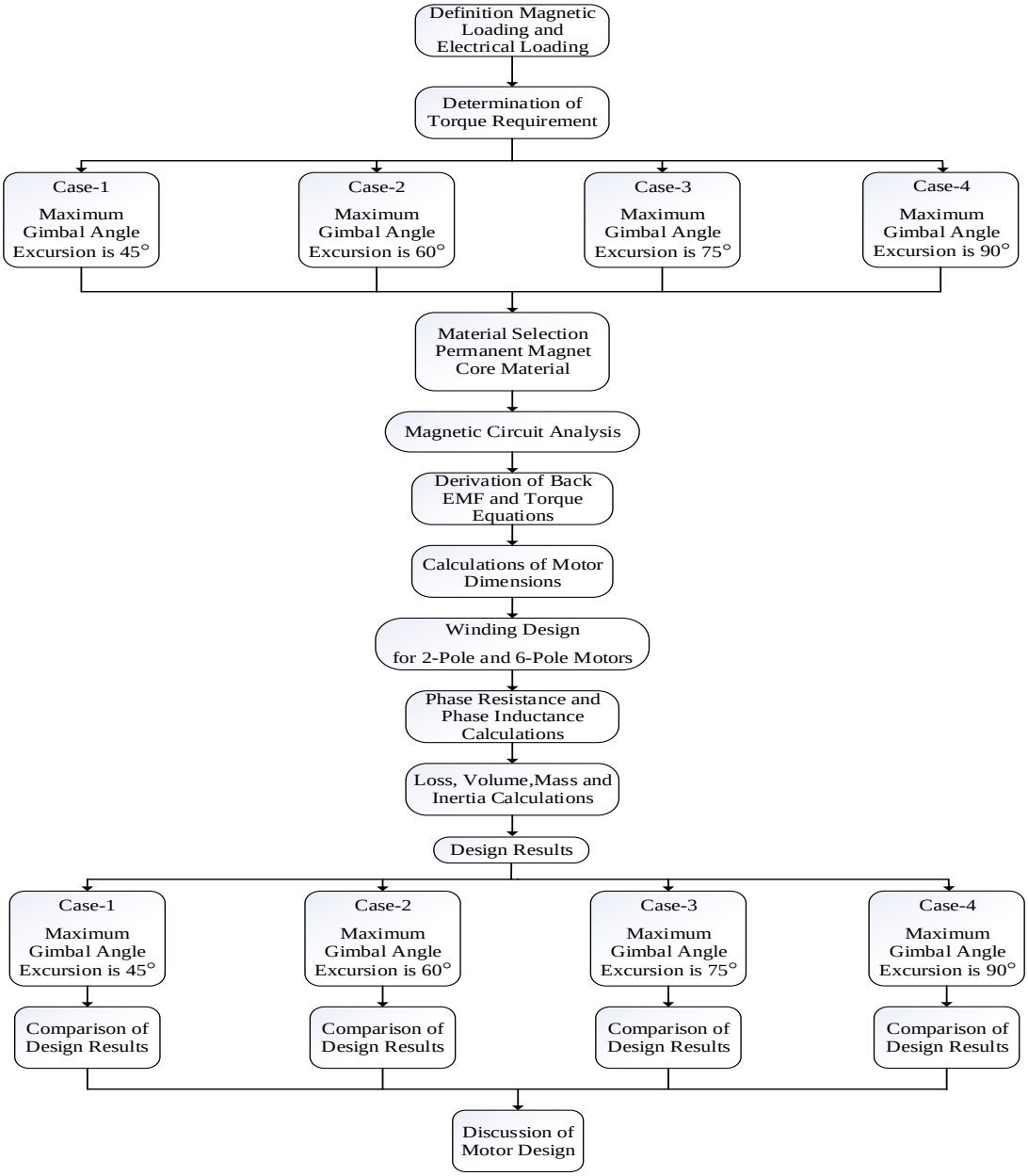

Figure 7.1 Design Flowchart of Wheel Motor

7.3.1. Material Selection

When designing PM brushless DC motor, selection of rotor core and permanent magnet are critical.

7.3.1.1. Selection of core material

Ferromagnetic materials are most preferred magnetic materials used in rotor and stator of the motor. A high percentage of stator and rotor consists of ferromagnetic materials.

Cogent Power No 12 ferromagnetic material is chosen as core material in this thesis and specifications of this material is shown in Table 7.5

Table 7.5 Specification s of Selected Core Material [8]

Parameter	**Value**
Hysteresis Coefficient (k_h)	0.0314
Eddy Current Coefficient (k_e)	2.18 E-05
Density (kg/m^3)	7650
Relative Permeability (μ_r)	4000
Maximum Service Temperature (˚C)	230
Curie Temperature (˚C)	800

Losses are the most important criteria to select core material. Manufacturers usually give core loss values in W/kg. Core losses for Cognet Power No 12 are shown in Table 7.6.

Table 7.6 *Core Loss Data for Cognet Power No 12 [7]*

Magnetic Flux Density in T	**Cogent power No 12 (0.2mm)**		
	50 Hz	400 Hz	2.5 kHz
0.1	0.02	0.16	1,65
0.2	0.08	0.71	6.83
0.3	0.16	1.55	15.2
0.4	0.26	2.57	25.4
0.5	0.37	3.75	37.7
0.6	0.48	5.05	52
0.7	0.62	6.49	66.1
0.8	0.76	8.09	83.1
0.9	0.92	9.84	103
1	1.09	11.8	156
1.1	1.31	14.1	
1.2	1.56	16.7	
1.3	1.89	19.9	
1.4	2.29	24	
1.5	2.74	28,5	
1.6	3.14		
1.7	3.49		
1.8	3.78		
1.9			
2			

In this thesis, the wheel motor is operated at 10000 rpm and the motor design is investigated for 2-pole or 6-pole. This means that the frequency of motor 166 Hz for 2-pole and 500 Hz for 6-pole motor. For high frequency motor applications, cogent power material is suitable since it can operate at higher frequency with lower power loss.

7.3.1.2. Permanent Magnet

Radiation-hardened and corrosion resistant permanent magnet is necessary for space applications. VACOMAX 225 HR type samarium cobalt magnet (Sm_2Co_{17}) has suitable properties and is selected. Also as seen in the table it can operate high temperature. Properties of the selected magnet are given in Table 7.7.

Table 7.7 Properties of VACOMAX 225 HR [7]

Property	**Value**
B_r	1.03-1.1 T
H_c	720-820 kA/m
μ_r (Relative permeability)	1.06-1.34
Temperature coefficient for B_r	-0.03% to 0.045%
T_{curie}	800 °C
$T_{service}$	350 °C
Thermal conductivity	12 W/(m.°C)

7.3.2. Magnetic Circuit of Outer Rotor BLDC Motor

The performance of permanent magnet BLDC motor is directly related to the magnetic circuit design of the electric motor. Permanent magnets are mounted on the surface of the rotor in BLDC motors. The geometry and B-H curve of permanent magnets determine the magnetic circuit of electric motors. Therefore, the thickness of required magnetic material in the BLDC motor is calculated by solving the equations of magnetic circuits. Symbol list of design parameters for magnetic circuit are given in Table 7.8.

Table 7.8 *Symbol List of Design Parameters for Magnetic Circuit*

Parameter	**Denotation**
Generated constant flux of PM per pole	ϕ_r
Magnetic flux in air gap per pole	ϕ_g
Fundamental magneti flux per pole	ϕ_m
Permeance of PM due to internal leakage magnetic flux	P_{m0}
Permeance of PM due to leakage magnetic flux between rotor and airgap	P_{rl}
Equivalent permeance of magnet.	P_m
Reluctance of air gap	R_g
Reluctance of core	R_{core}
Remenant flux density of PM	B_r
Average flux density of magnet	B_m
Average flux density of air gap	B_{gav}
Permeability of vacuum condition	μ_0
Relative permeability of PM	μ_{rec}
Magnet thickness	l_m
Area of the magnet	A_m
Area of air gap	A_g
Area of core	A_c
Air gap distance	g
Equivalent air gap distance	g'
Carter Coefficient	K_c
Mean length of the core	l_{core}
Magnet span	β
Pole pair	pp
Inner radius of the motor	R_i
Length of the motor	L
Magnetomotive force (m.m.f)	F_m
Average flux density	B_g
Flux concentration factor	$C = \frac{A_m}{A_g}$
Magnetic field strength at operating condition	H_m

Equivalent magnetic circuit of the outer rotor BLDC motor is shown in Figure 7.2.

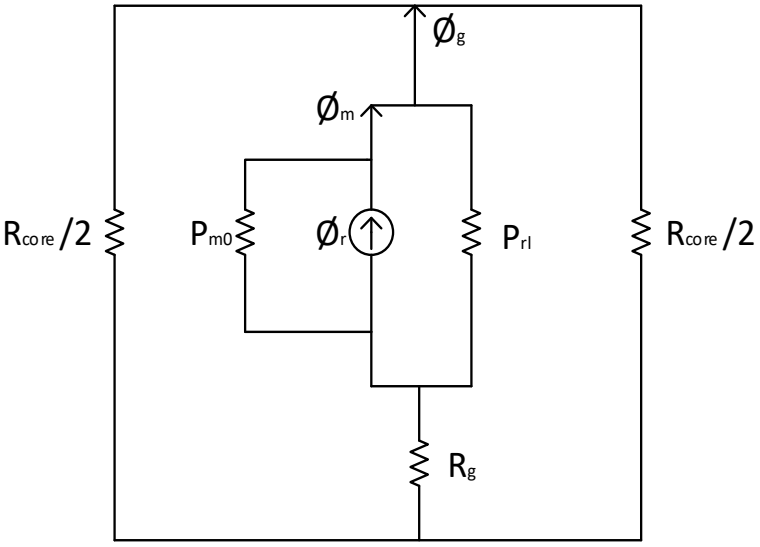

Figure 7.2 Equivalent Magnetic Circuit Branch of Outer Rotor BLDC Motor

Magnetic circuits equations based on [7] and [8] are summarized in Table 7.9

Table 7.9 *Equations of Magnetic Circuit*

$\phi_r = B_r A_m$
$P_{mo} = \frac{u_o u_{rec} A_m}{l_m}$
$P_{rl} = 0.1 P_{mo}$ [30]
$P_m = 1.1\ P_{mo}$
$g' = K_c\ g = 1.05\ g$[30]
$R_g = \frac{g'}{\mu_0 A_g}$
$R_{core} = \frac{l_{core}}{\mu_o u_r A_{core}}$
$A_m = \frac{\beta}{pp}\left(R_i + g + \frac{l_m}{2}\right)L;\ where\ \beta = \frac{2}{3}\pi$
$A_g = \left(\beta\frac{\left(R_i + \frac{g}{2}\right)}{pp} + 2g\right)(L + 2g)$
$F_m = \frac{\phi_r - \phi_g}{P_m} = \phi_g R_g$

Table 7.10 *Equations of Magnetic Circuit (cont'd)*

$\frac{\phi_r}{P_m} = \phi_g R_g + \frac{\phi_g}{P_m}$
$\phi_r = \phi_g (P_m R_g + 1)$
$\phi_g = \frac{\phi_r}{P_m R_g + 1}$
$B_{gav} A_g = \frac{B_r A_m}{P_m R_g + 1}$
$B_{gav} = \frac{B_r A_m}{A_g (P_m R_g + 1)}$
$B_{gav} = \frac{B_r}{(P_m R_g + 1)} C$
$F_m = \frac{\phi_r - \phi_m}{P_{m0}} + \frac{\phi_m - \phi_g}{P_{rl}} = \phi_g R_g$
$B_m = \frac{1 + P_{rl} R_g}{1 + P_m R_g} B_r$
$-H_m = \frac{B_r - B_m}{\mu_0 \mu_{rec}}$

Magnetic circuit equations for air gap flux density and magnetic flux density are solved in the above equations. According to these equations, magnetic loading of various motor parts and air gap flux density will be determined for given magnet properties shown in Table 7.7 and for selected dimensions of the motor in next parts of this study.

7.3.3. Back emf and Torque Derivations Under Square Wave Excited Motor

The torque requirement of electrical motors is directly related to both magnetic loading and electrical loading. Derivation of back emf and torque derivation under square wave excitation is investigated in this section. Symbol list of design parameters back emf are listed Table 7.11 and derivation of back emf for one phase are summarized in Table 7.12.

Table 7.11 *Symbol List of Design Parameters for Back EMF Calculations*

Parameter	**Denotation**
Flux linkage of air gap	λ
Maximum magnetic flux in air gap per pole	ϕ_{g_max}
Flat top value of air gap flux density	B_g
Mechanical angle of the motor	θ_{mech}
Mechanical speed of motor	ω_{mech}
Back emf of one phase	E_{ph}
Inner diameter of the motor	D_i
Length of the motor	L

Table 7.12 *Derivation of Back EMF*

$\lambda = N_{ph}\phi_g$
$\phi_{g\_max} = B_g\ A_g = B_g \pi\ R_i\ L$
$\lambda\ (\theta_{mech}) = \phi_{g\_max}(1 - \frac{\theta_{mech}}{2/\pi}$
$e = -\frac{d\lambda}{dt} = -\frac{d\lambda}{d\theta_{mech}} x \frac{d\theta_{mech}}{dt} = -\omega_{mech}\ \frac{d\lambda}{d\theta_{mech}}$
$E_{ph} = \omega_{mech}\ N_{ph} \frac{2}{\pi} B_g \pi\ R_i\ L = N_{ph} B_g\ L\ \ D_i\ \omega_{mech}$ [30]

In order to calculate the average flux density in the air gap, the fundamental component of the air gap magnetic flux density should be calculated by using Equation (7.3) [7]. After that, average air gap flux density is expressed in terms of the fundamental component of the air gap magnetic flux density in Equation (7.4).

$$B_{g1} = \frac{4}{\pi}\ B_g \sin(\frac{\theta_m}{2}) \qquad (7.3)$$

$$B_{gav} = \frac{2}{\pi}\ B_{g1} \qquad (7.4)$$

Since magnet span is selected 120º, $\theta_m = 120^{\circ}$. By substituting Equation (7.3) into Equation (7.4), the expression of average air gap flux density in terms of flat-top air gap flux density is shown in Equation (7.5). It is noted that relationship between flat-top magnetic flux density, flux linkage, and back emf are shown in Figure 7.3

$$B_{gav} = 0.7\, B_g \qquad (7.5)$$

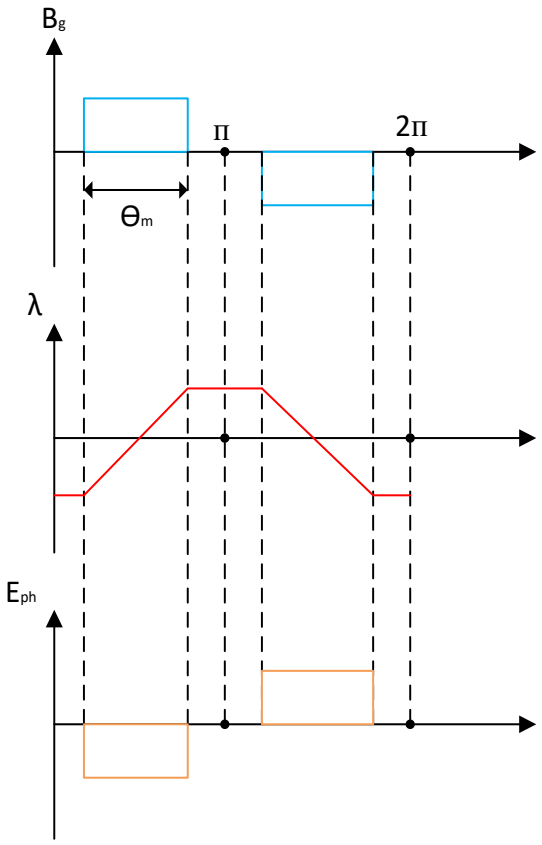

Figure 7.3 Air Gap Flux Density, Flux Linkage, and Back emf

Symbols used for design parameters in torque derivation under square wave excited motor are listed in Table 7.13. Equations used in calculation of torque for one phase are summarized in Table 7.14.

Table 7.13 *Symbol List of Design Parameters for Torque Calculations*

Parameter	**Denotation**
Electrical loading	q
RMS current per phase	I_{rms}
DC link current	I_{DC}
Electromechanical motor torque power	$\mathrm{P_{em}}$
Electromechanical motor torque	τ_{em}
Back emf of one phase	E_{ph}
Inner diameter of the motor	D_i
Length of the motor	L

Table 7.14 *Derivation of Torque Equation*

$q = \frac{6N_{ph}I_{rms}}{\pi D_i}$
$I_{rms} = \frac{\sqrt{2}}{\sqrt{3}} I_{DC}$
$P_{em} = 2E_{ph}I_{DC} = \tau_{em}\omega_{mech}$
$\tau_{em} = \frac{2E_{ph}I_{DC}}{\omega_{mech}}$
$I_{DC} = \frac{qD_i}{6N_{ph}} \frac{\sqrt{2}}{\sqrt{3}}$
$\tau_{em} = \frac{\pi B_g q D_i^2 L}{\sqrt{6}}$

7.3.4. Motor Dimension Calculations

The purpose of the investigation is to design an outer rotor PM brushless DC motor, with respect to new torque requirements, which are mentioned in Section 7.2.1. A similar type of motor has been designed for low torque requirement in [8]. However, the new motor design should be analyzed and checked in terms of electrical loading, efficiency, volume, and mass.

During the design procedure, the following requirements are considered.

- Since the same motor core selected in [7] and [8] are also used in this study, the average air gap magnetic flux density is $B_{gav} = 0.43\ T$. Therefore, Flat-top value of air gap magnetic flux density is $B_g = 0.62\ T$.
- According to [7], maximum current loading is to up 6000 A-t/m and maximum current density is to up 7 A/mm^2. Maximum values for electrical loading characteristics are only valid for acceleration. In steady-state, current loading is up to 3000 A-t/m and maximum current density is to up 3 A/mm^2.
- Produced torque of motor during acceleration shall be at least 0.2205 Nm for 45° gimbal angle, 0.1955 Nm for 60° gimbal angle, 0.1825 Nm for 75° gimbal angle and 0.1795 Nm for 90° gimbal angle. Therefore, four different motors will be designed to understand the effect of motor torque on motor dimensions.
- Produced torque of motor during steady-state shall be at least 0.0795 Nm (at 10000 rpm).
- Maximum flux density at any parts of the motor core shall be less than 1.4T due to characteristics of core material [8].

After the description of requirements, basic dimensions of the motor such as slot area, slot depth, back core length, inner diameter, motor length and the outer diameter of the motor should be determined The symbols used during calculations are listed in Table 7.15. Representation of outer rotor BLDC motor dimension is shown in Figure 7.4. Back core of stator and rotor are taken as equal to ensure that maximum allowed flux density in core to the same value. The slot width and the tooth width are also taken as equal to decrease the unknown number and to ease calculations. During the whole design procedure, D_{shaft} is selected as 22 mm due to consideration of cable area of phases in this study.

Table 7.15 *Symbol List of Design Parameters for Motor Dimensions Calculations*

Parameter	**Denotation**
Total Slot Area	$\mathrm{A_{slot}}$
Pole Area	A_{pole}
Back Core Area	A_{bc}
Slot Depth	h_s
Back Core Depth	h_{bc}
Inner Diameter	D_i
Inner Radius	R_i
Outer Diameter	D_o
Outer Radius	R_o
Motor Length	L
Ratio between inner diameter and length of the motor	$\mathrm{R_{DL}} = \frac{\mathrm{D_i}}{\mathrm{L}}$
Shaft Diameter	D_{shaft}
Inner Diameter / Core Length Ratio	R_{DL}
Air gap distance	g
Magnet thickness	l_m
Tooth Lip-1	h_1
Tooth Lip-2	h_2
Lip Opening	w_1
Slot Thickness	w_2
Tooth Width at Airgap	t_1
Tooth Width	t_2
Magnetic flux in back core	ϕ_{bc}
Magnetic flux for one pole	ϕ_{pole}
Average magnetic flux density of back core	B_{bc}
Peak value of magnetic flux density of back core	$\mathrm{B_{bcp}}$
Pole number	p
Current density of copper wire	J_{cu}
Slot fill factor	K_{cu}

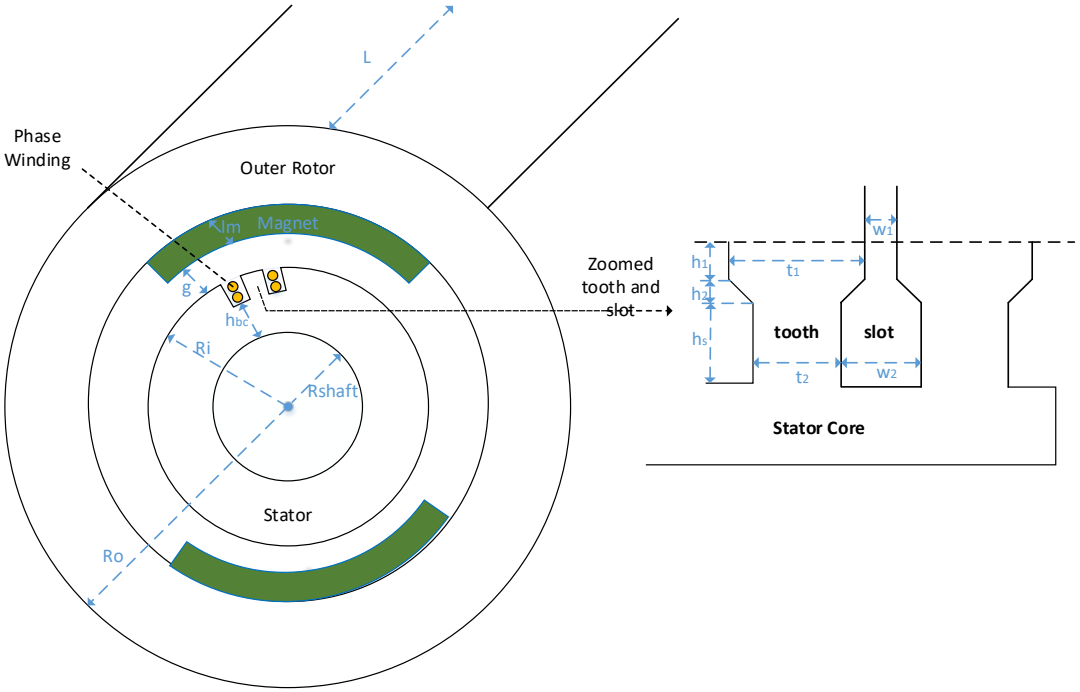

Figure 7.4 Representation of Outer Rotor BLDC Motor Dimensions

Equations used in the design in terms of motor dimensions are summarized in Table 7.16.

Table 7.16 Equations of Motor Dimension Calculations

$D_{shaft=}\ 22\ mm$
$\phi_{bc} = \frac{\phi_{pole}}{2}$
$\phi_{pole} = B_{gav}\ A_{pole}$
$\phi_{bc} = B_{bc}\ A_{bc}$
$A_{pole} = \frac{\pi D_i L}{p}$
$A_{bc} = h_{bc} L$
$\frac{B_{gav}}{2}\frac{\pi D_i L}{p} = B_{bc}\ h_{bc}\ L$
$h_{bc} = \frac{1}{2}\frac{B_{gav}}{B_{bc}}\pi\frac{D_i}{p}$
B_{bcp} = 1.4T [7] and [8]

Table 7.17 Equations of Motor Dimension Calculations (cont'd)

$B_{bc} = \frac{2}{\pi} B_{bcp} = 0.89\ T$
$h_{bc} = \frac{D_i - 2h_s - D_{shaft}}{2}$
$h_s = \frac{1}{2} [D_i \left(1 - \frac{B_g \pi}{B_{bc} p}\right) - D_{shaft}$
$q = \frac{J_{cu} K_{cu} A_{slot}}{\pi D_i}$ *where* $K_{cu} = 0.4$
$A_{slot} = \frac{\pi}{2}[\left(\frac{D_i}{2}\right)^2 - \left(\frac{D_i}{2} - h_s\right)^2]$
$q = \frac{J_{cu} K_{cu}}{2D_i} \left(\frac{D_i}{2}\right)^2 - \left(\frac{D_i}{2} - h_s\right)^2$
$q = \frac{\tau_{em} \sqrt{6} R_{DL}}{\pi B_g D_i^3}$
$D_o = D_i + 2g + 2l_m + 2h_{bc}$

7.3.5. Winding Design

After the main dimensions of the motor are calculated, the problem is in this section to design winding. Operation voltage of satellite is changed between 18V-33V. If back emf is satisfied for minimum operating voltage, it is also satisfied for higher than minimum operating voltage. Therefore, minimum operating voltage is taken for back emf calculations. Number of turns per phase are calculated for 2-pole and 6-pole motor design that is same as previous motor design in [7] and [8] and it should be divided by 3 and the result should be an integer. Winding design parameters and equations are summarized in Table 7.18.

Table 7.18 *Winding Design Parameters and Equations*

Minimum bus voltage=18 V
Voltage drop across the one semiconductor =1 V [8]
Slot number=18 [8]
$E_{ph} = 8V$

Table 7.19 *Winding Design Parameters and Equations (cont')*

$Number\ of\ turns\ per\ phase;\ N_{ph} = \frac{E_{ph}}{B_g L D_i w_{mech}}$
$I_{rms} = \frac{q\ \pi\ D_i}{6\ N_{ph}}$

Winding design for 2-pole and 6-pole motor are shown in Figure 7.5 and Figure 7.6

Slot Number	1	2	3	4	5	6	7	8	9	10	11	12	13	14	15	16	17	18
Phase Winding	A	A	A	-C	-C	-C	B	B	B	-A	-A	-A	C	C	C	-B	-B	-B
Number of Turns per Phase	Nph/3	Nph/3	Nph/3	Nph/3	Nph/3	Nph/3	Nph/3	Nph/3	Nph/3	Nph/3	Nph/3	Nph/3	Nph/3	Nph/3	Nph/3	Nph/3	Nph/3	Nph/3
Poles	Pole 1									Pole 2								

Figure 7.5 Winding Design of 2-pole Motor

Slot Number	1	2	3	4	5	6	7	8	9	10	11	12	13	14	15	16	17	18
Phase Winding	A	-C	B	-A	C	-B	A	-C	B	-A	C	-B	A	-C	B	-A	C	-B
Number of Turns per Phase	Nph/3	Nph/3	Nph/3	Nph/3	Nph/3	Nph/3	Nph/3	Nph/3	Nph/3	Nph/3	Nph/3	Nph/3	Nph/3	Nph/3	Nph/3	Nph/3	Nph/3	Nph/3
Poles	Pole 1			Pole 2			Pole 3			Pole 4			Pole 5			Pole 6		

Figure 7.6 Winding Design of 6-pole Motor

7.3.6. Phase Resistance Calculation

Design parameters and equations for phase resistance calculations are shown in Table 7.20.

Table 7.20 *Design Parameters and Equations for Phase Resistance Calculations*

$Conductor\ (Copper)\ resistivity\ ;\sigma_{co} = 1.72\ x\ 10^{-8}\ \Omega m$
$Conductor\ area A_{co} = A_{cu}$
Mean length of conductor; MLC

Table 7.21 *Design Parameters and Equations for Phase Resistance Calculations (cont'd)*

$Phase\ resistance;\ R_{ph} = \frac{\sigma_{co} l_{co}}{A_{co}} = \frac{\sigma_{cu}(MLC)N_{ph}}{A_{cu}}$
$MLC = \left[\frac{\pi\left(D_i - \frac{h_s}{2}\right)}{p} + 2L\right] + 2(0.007)$ *[7] and [8]*
$A_{co} = A_{cu} = \frac{q\pi D_i}{6N_{ph}J_{cu}}$

7.3.7. Phase Inductance Calculation

Design parameters and equations for phase inductance calculations are shown in Table 7.22.

Table 7.22 *Design Parameters and Equations for Phase Resistance Calculations*

$Flux\ linkage\ of\ baack\ core;\ \lambda_{bc} = N_{ph}\ \phi_{bc}$
$Magnetic\ flux\ of\ back\ core;\ \phi_{bc} = \frac{N_{ph} I}{2R_g + 2R_m}$
$L = \frac{\lambda_{bc}}{I} = \frac{N_{ph}^2}{2R_g + 2R_m}$
$Air\ gap\ inductance\ per\ phase;\ L_g = \frac{pp}{2} L$
Slot leakage inductance per phase; $L_{sl} = n_c(2N_c^2)[\frac{\mu_o h_s L}{3w_2} + \frac{\mu_o h_2 L}{\frac{w_1+w_2}{2}} + \frac{\mu_o h_1 L}{w_1}$ *[7] and [8]*
n_c *is the total number of slots per phase*
N_c *is the total number of conductors in the slot*
$End\ turn\ inductance\ per\ phase;\ L_e = \frac{n_c \mu_0 T_{cp} N_c^2}{8}\ ln(\frac{T_{cp}\sqrt{\pi}}{\sqrt{2}A_{slot}})$ *[7] and [8]*
$A_{slot} = w_2 h_s + \frac{w_1+w_2}{2}\ h_2 + h_1 w_1.$
$T_{cp} = D_i$ *[7]*
$Phase\ inductance;\ L_{ph} = L_g + L_{sl} + L_e$

In order to understand slot leakage inductance and end-turn inductance, slot geometry and end-turn geometry are shown in Figure 7.7 and Figure 7.8.

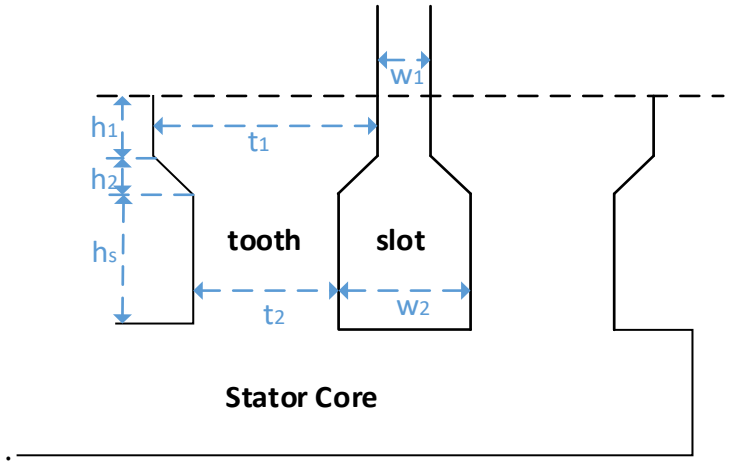

Figure 7.7 Slot Geometry

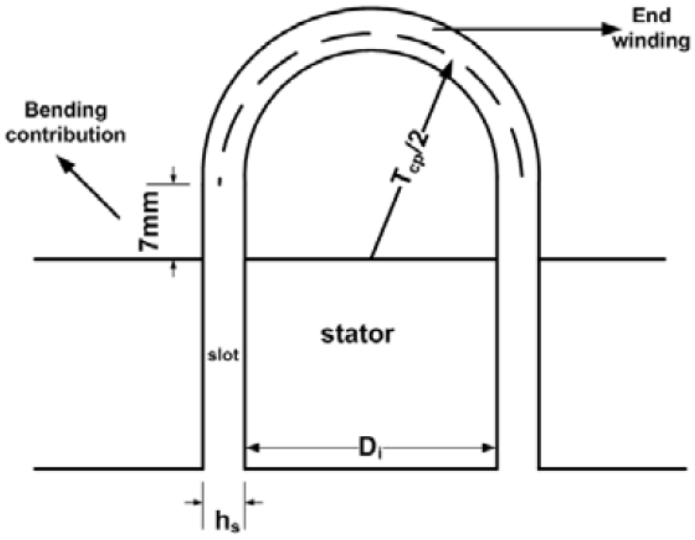

Figure 7.8 Geometry of End Turn [7]

7.3.8. Loss Calculation

Symbols used for loss calculation are listed in Table 7.23.

Table 7.23 *Symbol List of Loss Calculations*

Parameter	**Denotation**
Hysteresis losses	P_h
Eddy current losses	P_e
Core losses	P_c
Hysteresis coefficient	k_h
Eddy current coefficient	k_e
Steinmetz exponent	n
Magnetic flux density of tooth	B_{tooth}
Maximum magnetic flux density of tooth	$B_{tooth-max}$
RMS current of phase	I_{ph-rms}
DC-link voltage	V_{DC}
Copper losses	P_{co}

Loss calculations of the motor are summarized in Table 7.24.

Table 7.24 *Loss Calculation of the Motor*

$P_h = k_h\, f\, B^n$
$P_e = k_e f^2 B^2$
$P_c = P_h + P_e$
$k_e = 2.18\, E-05$ *(see Table 7.5)*
n=2 [8]
B=1.4 T [7]
$B_{tooth} = \frac{B_{gav}(t_2 + w_2)}{t_2};\ where\ t_2 = w_2$
$B_{tooth} = 2\, B_{gav} = 0.86\, T$
$B_{tooth-max} = \frac{\pi}{2} 0.86 = 1.35\, T$ *[7]*
$I_{ph-rms} = I_{rms} + \frac{P_c}{3V_{DC}\sqrt{\frac{2}{3}}}$
$V_{DC} = 2\, I_{rms}\, R_{ph} + E_{ph}$

Table 7.25 *Loss Calculation of the Motor (cont'd)*

$I_{DC} = \sqrt{\frac{3}{2}}\, I_{ph-rms}$
$P_{co} = 2I_{DC}^2\, R_{ph}$
$P_{total-loss} = P_c\, x\, (mass\ of\ stator) + P_{co}$

7.3.9. Mass, Volume, Inertia and Efficiency Calculations

Design parameters and equations are shown in Table 7.26.

Table 7.26 *Mass, Volume, Inertia, and Efficiency Calculations of Motor*

Rotor mass; $M_{rotor} = \pi \left[\left(\frac{D_o}{2}^2\right) - (D_o - 2h_{bc})^2\right] L\, d_{core}$
d_{core} =7650 kg/m3 (see Table 7.5)
Magnet mass; $M_{magnet} = p\frac{\alpha}{2}\left(D_i + 2g + \frac{l_m}{2}\right)\frac{l_m}{2}\, Ld_{magnet}$ Where p=pole number, α =120 degree, d_{magnet} =8400kg/m3[7]
Mass of stator hallow; $M_{hallow} = \pi\,(D_{shaft} + h_{bc})h_{bc}\, L\, d_{core}$
Mass of teeht; $M_{teeth} = n_{tooth}\, A_{tooth}\, L\, d_{core}$ where $n_{tooth} = 18$
Tooth area; $A_{tooth} = h_s w_s$
Mass of stator; $M_{stator} = M_{hollow} + M_{teeth}$
Volume of motor; $V_{motor} = \pi\,(R_o^2)L$
Inertia of motor; $J_{motor} = \frac{1}{2}\, M_{rotor}\, [R_o^2 + (R_o - h_{bc})^2]$
$\eta = \frac{P_{out}}{P_{in}} = \frac{P_{out}}{P_{out} + P_{total-loss}} = \frac{P_{out}}{P_{out} + P_c + P_{co}}$ where P_{out}: Output Power and P_{in}: Input Power

7.3.10. Design Results

Design results are obtained by changing RDL (ratio of inner diameter to length of motor) from 0.7 to 20 based on [8]. The purpose of changing RDL is to decrease

number of unknown parameters in motor equations. Thanks to definition of RDL, motor torque equation can be expressed in terms of only D_i (inner diameter of motor) shown in Table 7.16. In addition, several motor designs are obtained by changing RDL and the most suitable motor design result that electrical loading is less than 6000 A-t/m is selected in terms of low mass and volume. It is also noted that inertia contribution of motor is investigated.

Design results are shown and discussed regarding the 2-pole and 6-pole for square-wave excited motor in this section. There are four different cases for motor design results since required motor torque is different for different gimbal angles.

7.3.10.1. Design Results for Gimbal Angle 45 °

Required motor torque is taken 0.2205 Nm mentioned before in Section 7.1. Detail design results are shown in Table 7.27.

Mass, volume and inertia contribution and comparison of 2-pole and 6-pole motors with respect to different RDL values shown in from Figure 7.9 to Figure 7.11. Base values of mass, volume, and inertia are taken from wheel design result that outer radius is 13 cm for 45º maximum gimbal angle for contribution calculations.

Base Values

Mass: 2.68 kg Volume: 335 cm^3 Inertia: 40.5 $g.m^2$

Table 7.27 *Detailed Motor Design Results for Gimbal Angle 45 °*

Parameter	2-pole square wave excited motor						6-pole square wave excited motor					
	Value						Value					
RDL	0,7	1	1,3	3	10	20	0,7	1	1,3	3	10	20
Di (mm)	95,38	95,93	96,47	99,24	107,75	116,12	37,31	39,24	40,85	47,19	59,96	69,64
L (mm)	136,26	95,93	74,21	33,08	10,77	5,81	53,30	39,24	31,42	15,73	6,00	3,48
g (mm)	0,75	0,75	0,75	0,75	0,75	0,75	0,75	0,75	0,75	0,75	0,75	0,75
Do (mm)	172,83	173,83	174,80	179,80	195,35	211,11	51,60	54,06	56,13	64,34	81,66	96,88
hs (mm)	0,16	0,22	0,29	0,61	1,61	2,59	2,89	3,61	4,21	6,57	11,33	14,93
lm (mm)	1,45	1,46	1,47	1,52	1,78	2,27	1,63	1,65	1,67	1,80	2,44	3,98
h1 (mm)	1,00	1,00	1,00	1,00	1,00	1,00	1,00	1,00	1,00	1,00	1,00	1,00
h2 (mm)	1,00	1,00	1,00	1,00	1,00	1,00	1,00	1,00	1,00	1,00	1,00	1,00
w1 (mm)	0,75	0,75	0,75	0,75	0,75	0,75	0,75	0,75	0,75	0,75	0,75	0,75
w2 (mm)	7,96	8,00	8,04	8,26	8,91	9,56	2,65	2,76	2,85	3,20	3,90	4,43
hsbc (mm)	36,53	36,74	36,95	38,01	41,27	44,47	4,76	5,01	5,22	6,02	7,66	8,89
t1 (mm)	15,90	15,99	16,09	16,57	18,06	19,52	5,76	6,10	6,38	7,49	9,72	11,40
t2 (mm)	7,96	8,00	8,04	8,26	8,91	9,56	2,65	2,76	2,85	3,20	3,90	4,43
J (g.m2)	81,17	58,48	46,25	23,08	10,47	7,69	0,16	0,14	0,13	0,11	0,11	0,13
V (cm3)	3197	2277	1781	840	323	203	111	90	78	51	31	26
Mtotal (kg)	24,19	17,22	13,47	6,34	2,43	1,52	0,76	0,61	0,53	0,34	0,21	0,18
Rph (mOhm)	97,69	51,83	33,07	35,74	32,87	53,81	47,44	27,67	33,59	24,57	26,09	29,20
Lph (uH)	22,46	15,96	12,45	23,20	34,13	61,95	20,26	15,55	22,91	29,60	61,45	93,69
Nph	3,00	3,00	3,00	6,00	12,00	21,00	9,00	9,00	12,00	18,00	36,00	51,00
Irms (A) @SS	4,25	4,25	4,25	4,25	4,25	4,25	4,25	4,25	4,25	4,25	4,25	4,25
Irms(A) @Acc	11,78	11,78	11,78	11,78	11,78	11,78	11,78	11,78	11,78	11,78	11,78	11,78
q (A.t/m)	223,71	314,09	401,53	851	2217	3542	3736	4589	5287	7917	12862	16421
Ploss @Acc(copper + iron)(W)	98,44	69,55	54,86	29,54	19,78	22,76	22,39	19,55	18,04	14,68	13,47	14,90
Ploss @SS(copper + iron)(W)	91,51	63,86	49,63	23,77	10,12	7,67	13,71	11,28	9,93	6,93	4,78	4,29
Efficiency (%) @ Acc	70,11	76,85	80,80	88,66	92,11	91,03	91,16	92,20	92,75	94,02	94,49	93,94
Efficiency (%)@ SS	47,64	56,59	62,65	77,79	89,16	91,56	85,86	88,07	89,34	92,32	94,57	95,10

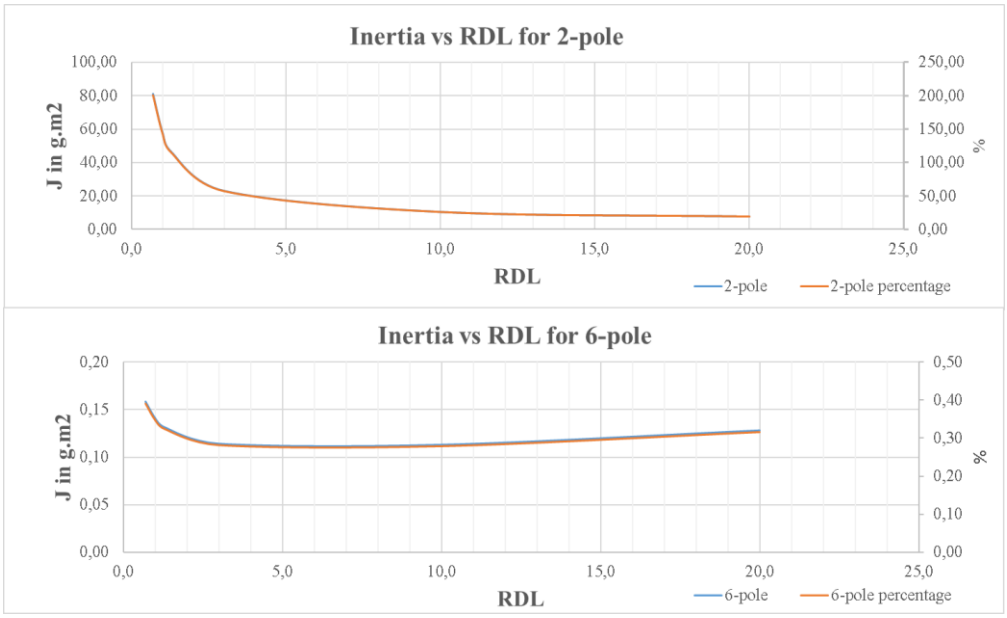

Figure 7.9 Inertia Comparison and Contribution for Gimbal Angle 45º

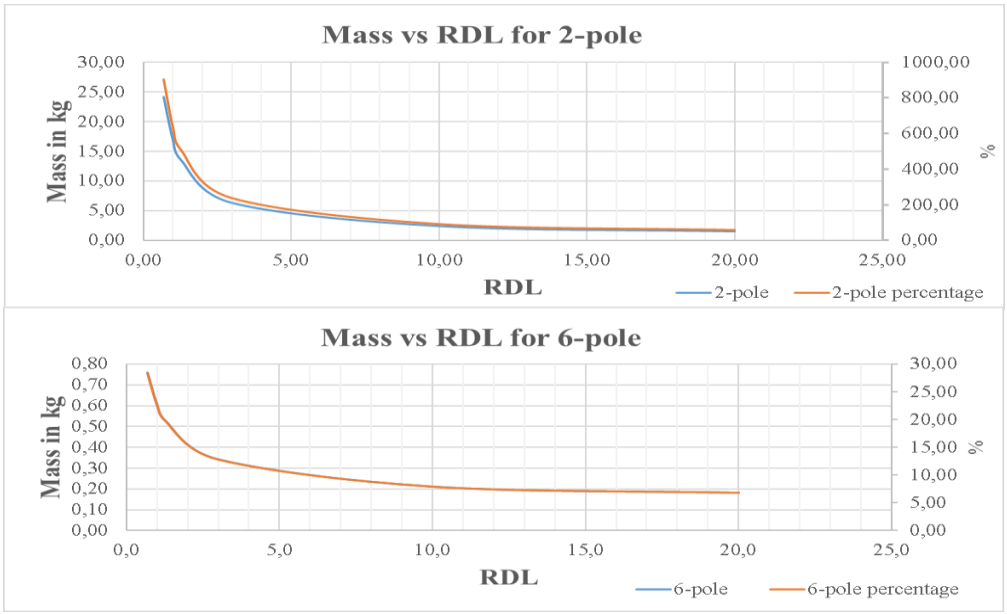

Figure 7.10 Mass Comparison and Contribution for Gimbal Angle 45º

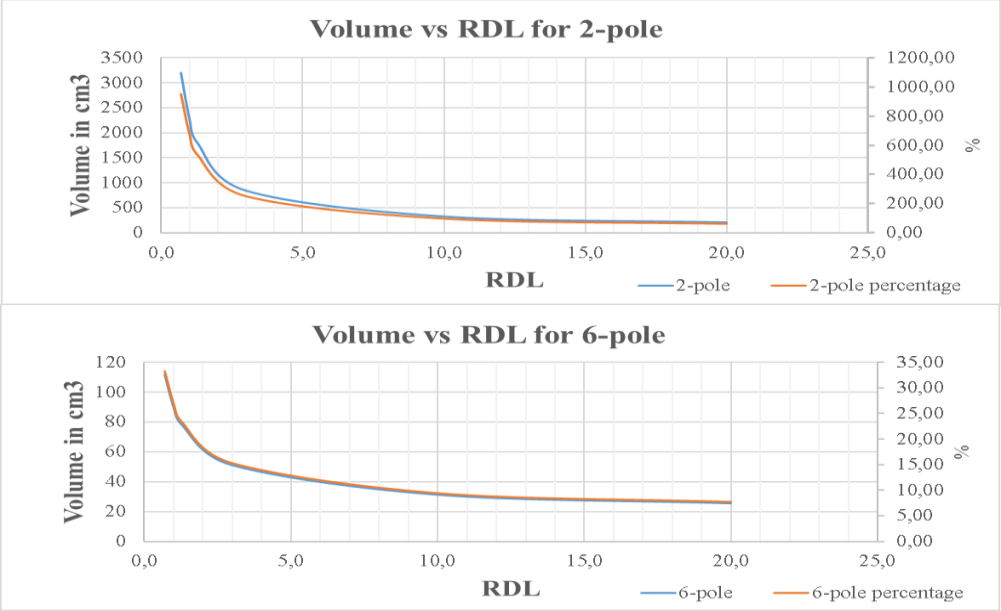

Figure 7.11 Volume Comparison and Contribution for Gimbal Angle 45º

7.3.10.2. Design Results for Gimbal Angle 60°

Required motor torque is taken 0.1955 Nm mentioned before in Section 7.1. Detail design results are shown in Table 7.28.

Mass, volume and inertia contribution and comparison of 2-pole and 6-pole motors with respect to different RDL values shown in from Figure 7.12 to Figure 7.14 Base values of mass, volume, and inertia are taken from wheel design result that outer radius is 13 cm for 60º maximum gimbal angle for contribution calculations.

Base Values

Mass: 2.13 kg Volume: 267 cm^3 Inertia: 33.1 $g.m^2$

Table 7.28 *Detailed Motor Design Results for Gimbal Angle 60°*

Parameter	2-pole square wave excited motor						6-pole square wave excited motor					
	Value						Value					
RDL	0,7	1	1,3	3	10	20	0,7	1	1,3	3	10	20
Di (mm)	95,229	95,73	96,2	98,72	106,58	114,46	36,73	38,56	40,09	46,16	58,47	67,82
L (mm)	136,04	95,73	74	32,91	10,66	5,72	52,47	38,56	30,84	15,39	5,85	3,39
g (mm)	0,75	0,75	0,75	0,75	0,75	0,75	0,75	0,75	0,75	0,75	0,75	0,75
Do (mm)	172,57	173,5	174	178,88	193,30	208,20	50,87	53,21	55,18	63,07	79,86	94,89
hs (mm)	0,1426	0,201	0,26	0,55	1,47	2,39	2,68	3,36	3,93	6,19	10,77	14,25
lm (mm)	1,4468	1,457	1,47	1,53	1,79	2,29	1,63	1,66	1,68	1,81	2,48	4,13
h1 (mm)	1	1	1	1,00	1,00	1,00	1,00	1,00	1,00	1,00	1,00	1,00
h2 (mm)	1	1	1	1,00	1,00	1,00	1,00	1,00	1,00	1,00	1,00	1,00
w1 (mm)	0,75	0,75	0,75	0,75	0,75	0,75	0,75	0,75	0,75	0,75	0,75	0,75
w2 (mm)	7,9488	7,987	8,02	8,22	8,82	9,43	2,62	2,72	2,81	3,14	3,81	4,33
hsbc (mm)	36,472	36,66	36,8	37,81	40,82	43,84	4,69	4,92	5,12	5,89	7,46	8,66
t1 (mm)	15,871	15,96	16	16,48	17,85	19,23	5,66	5,98	6,25	7,31	9,45	11,09
t2 (mm)	7,9488	7,987	8,02	8,22	8,82	9,43	2,62	2,72	2,81	3,14	3,81	4,33
J (g.m2)	80,542	57,86	45,6	22,49	9,93	7,17	0,15	0,13	0,12	0,10	0,10	0,11
V (cm3)	3181,8	2262	1767	827	313	195	107	86	74	48	29	24
Mtotal (kg)	24,08	17,12	13,4	6,25	2,35	1,46	0,73	0,58	0,50	0,32	0,20	0,17
Rph (mOhm)	109,67	58,09	37	39,68	35,90	58,16	51,05	29,62	35,82	25,96	32,06	34,18
Lph (uH)	22,401	15,9	12,4	22,99	33,51	60,47	19,78	15,14	22,29	28,70	69,85	101,79
Nph	3	3	3	6,00	12,00	21,00	9,00	9,00	12,00	18,00	39,00	54,00
Irms (A) @SS	4,25	4,25	4,25	4,25	4,25	4,25	4,25	4,25	4,25	4,25	4,25	4,25
Irms(A) @Acc	10,45	10,45	10,45	10,45	10,45	10,45	10,45	10,45	10,45	10,45	10,45	10,45
q (A.t/m)	199	280	359	767	2031	3279	3473	4289	4960	7500	12300	15761
Ploss @Acc(copper + iron)(W)	97,815	68,73	54	28,56	18,40	20,83	20,85	18,12	16,68	13,49	12,34	13,63
Ploss @SS(copper + iron)(W)	91,71	63,76	49,5	23,59	10,08	7,80	13,35	10,96	9,65	6,75	4,75	4,35
Efficiency (%) @ Acc	67,669	74,86	79,1	87,76	91,75	90,77	90,76	91,87	92,47	93,82	94,31	93,76
Efficiency (%)@ SS	47,583	56,63	62,7	77,92	89,20	91,44	86,18	88,37	89,61	92,50	94,60	95,04

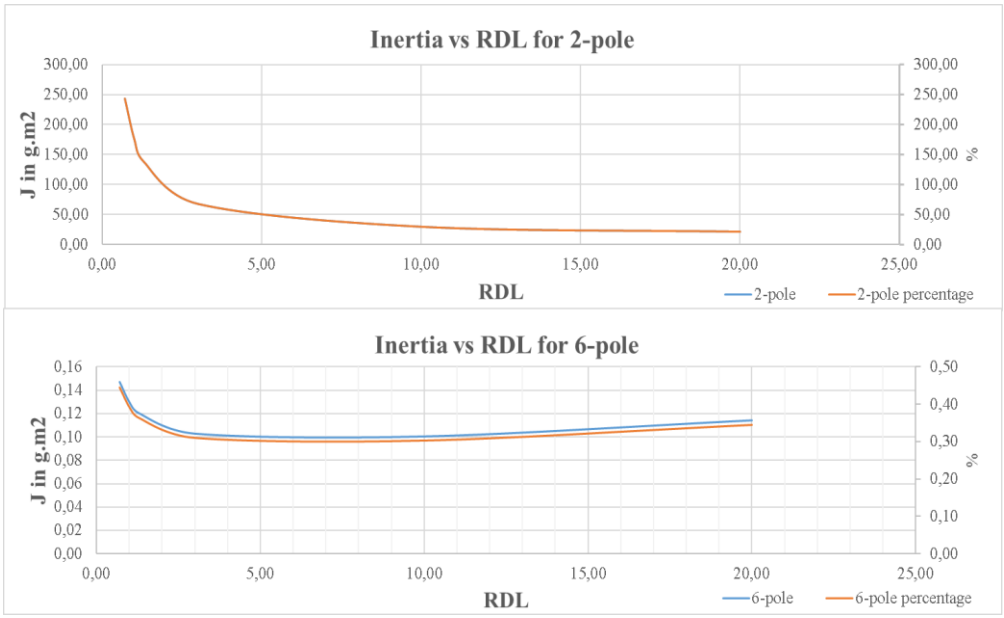

Figure 7.12 Inertia Comparison and Contribution for Gimbal Angle 60º

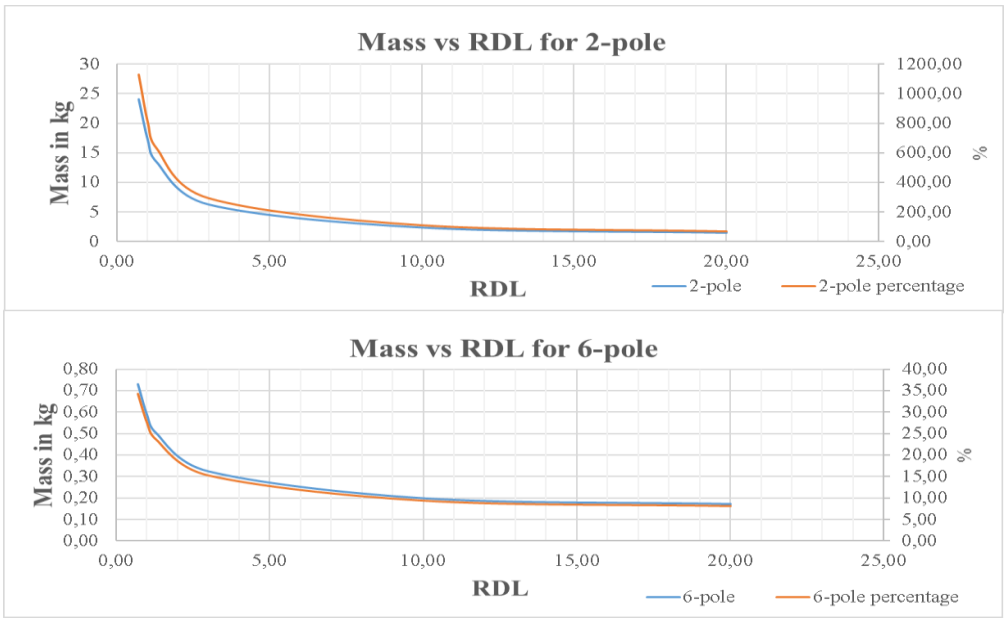

Figure 7.13 Mass Comparison and Contribution for Gimbal Angle º60

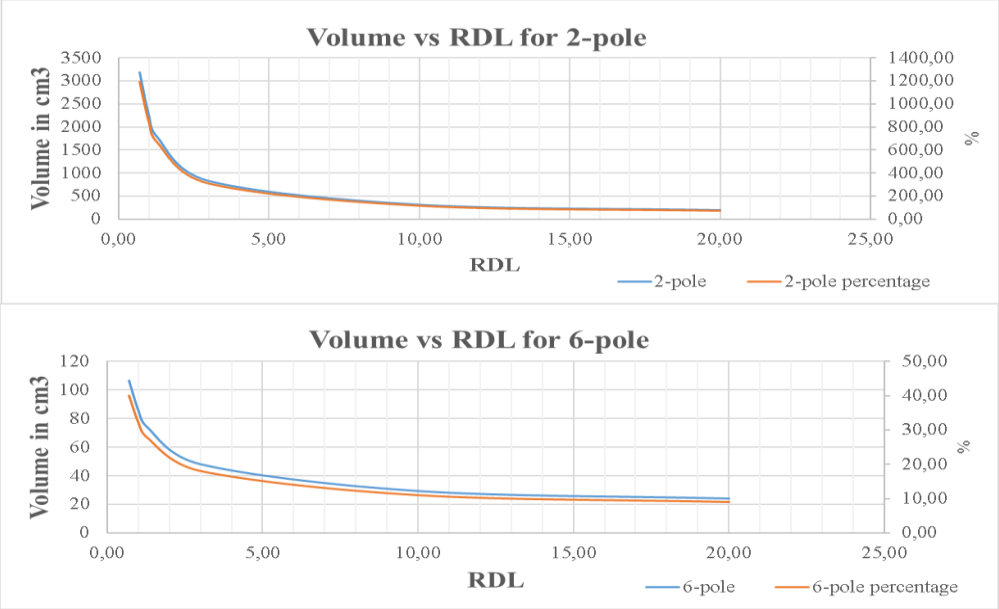

Figure 7.14 Volume Comparison and Contribution for Gimbal Angle 60º

7.3.10.3. Design Results for Gimbal Angle 75°

Required motor torque is taken 0.1825 Nm mentioned before in Section 7.1. Detail design results are shown in Table 7.24.

Mass, volume and inertia contribution and comparison of 2-pole and 6-pole motors with respect to different RDL values shown in from Figure 7.15 to Figure 7.17. Base values of mass, volume, and inertia are taken from wheel design result that outer radius is 13 cm for 75º maximum gimbal angle for contribution calculations.

Base Values

Mass: 1.89 kg Volume: 236 cm^3 Inertia: 29.6 $g.m^2$

Table 7.29 *Detailed Motor Design Results for Gimbal Angle 75°*

Parameter	2-pole square wave excited motor						6-pole square wave excited motor					
	Value						Value					
RDL	0,7	1	1,3	3	10	20	0,7	1	1,3	3	10	20
Di (mm)	95,15	95,62	96,07	98,44	105,95	113,55	36,41	38,18	39,67	45,59	57,64	66,81
L (mm)	135,93	95,62	73,90	32,81	10,59	5,68	52,01	38,18	30,52	15,20	5,76	3,34
g (mm)	0,75	0,75	0,75	0,75	0,75	0,75	0,75	0,75	0,75	0,75	0,75	0,75
Do (mm)	172,43	173,27	174,09	178,39	192,19	206,61	50,47	52,74	54,66	62,36	78,86	93,79
hs (mm)	0,13	0,19	0,24	0,52	1,40	2,29	2,56	3,22	3,77	5,97	10,46	13,88
lm (mm)	1,45	1,46	1,47	1,53	1,79	2,30	1,63	1,66	1,68	1,82	2,51	4,21
h1 (mm)	1,00	1,00	1,00	1,00	1,00	1,00	1,00	1,00	1,00	1,00	1,00	1,00
h2 (mm)	1,00	1,00	1,00	1,00	1,00	1,00	1,00	1,00	1,00	1,00	1,00	1,00
w1 (mm)	0,75	0,75	0,75	0,75	0,75	0,75	0,75	0,75	0,75	0,75	0,75	0,75
w2 (mm)	7,94	7,98	8,01	8,20	8,77	9,36	2,61	2,70	2,78	3,11	3,77	4,27
hsbc (mm)	36,44	36,62	36,79	37,70	40,58	43,49	4,65	4,87	5,06	5,82	7,36	8,53
t1 (mm)	15,86	15,94	16,02	16,43	17,74	19,07	5,60	5,91	6,17	7,21	9,31	10,91
t2 (mm)	7,94	7,98	8,01	8,20	8,77	9,36	2,61	2,70	2,78	3,11	3,77	4,27
J (g.m2)	80,22	57,54	45,32	22,19	9,65	6,90	0,14	0,12	0,11	0,10	0,09	0,11
V (cm3)	3174	2255	1759	820	307	190	104	83	72	46	28	23
Mtotal (kg)	24,02	17,06	13,31	6,20	2,31	1,43	0,71	0,57	0,49	0,31	0,19	0,17
Rph (mOhm)	117,19	62,01	39,46	42,15	37,78	60,85	53,27	30,81	37,19	26,80	32,93	39,04
Lph (uH)	22,37	15,87	12,36	22,87	33,18	59,67	19,52	14,92	21,94	28,21	68,60	111,41
Nph	3,00	3,00	3,00	6,00	12,00	21,00	9,00	9,00	12,00	18,00	39,00	57,00
Irms (A) @SS	4,25	4,25	4,25	4,25	4,25	4,25	4,25	4,25	4,25	4,25	4,25	4,25
Irms(A) @Acc	9,75	9,75	9,75	9,75	9,75	9,75	9,75	9,75	9,75	9,75	9,75	9,75
q (A.t/m)	186	263	336	722	1930	3136	3328	4123	4778	7267	11987	15392
Ploss @Acc(copper + iron)(W)	97,51	68,32	53,55	28,05	17,67	19,80	20,03	17,36	15,95	12,86	11,74	12,96
Ploss @SS(copper + iron)(W)	91,87	63,74	49,39	23,51	10,08	7,89	13,17	10,81	9,52	6,67	4,75	4,41
Efficiency (%) @ Acc	66,21	73,67	78,11	87,20	91,54	90,61	90,51	91,67	92,30	93,70	94,21	93,65
Efficiency (%)@ SS	47,54	56,64	62,77	77,98	89,20	91,34	86,34	88,51	89,74	92,58	94,60	94,97

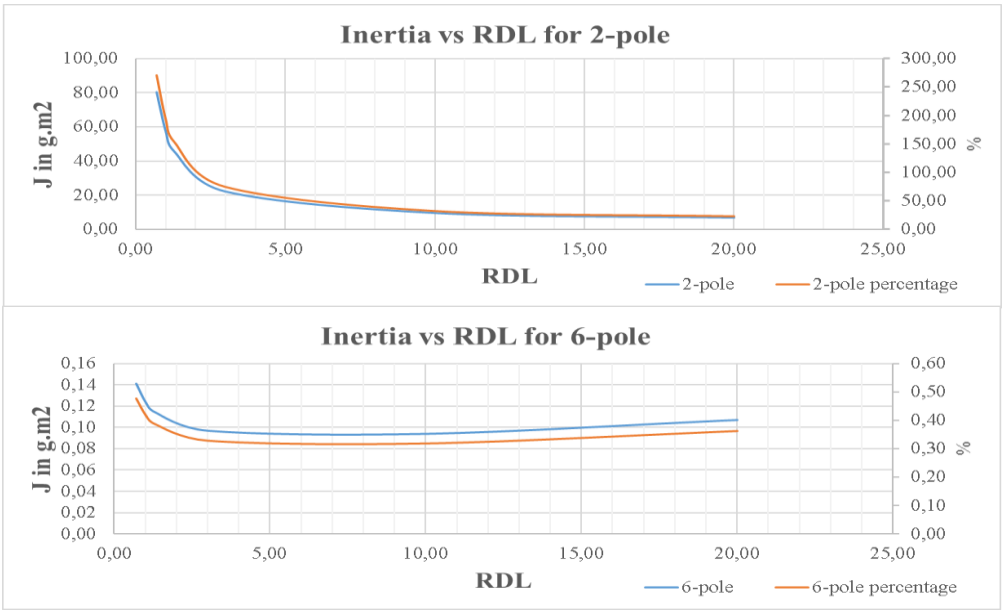

Figure 7.15 Inertia Comparison and Contribution for Gimbal Angle 75º

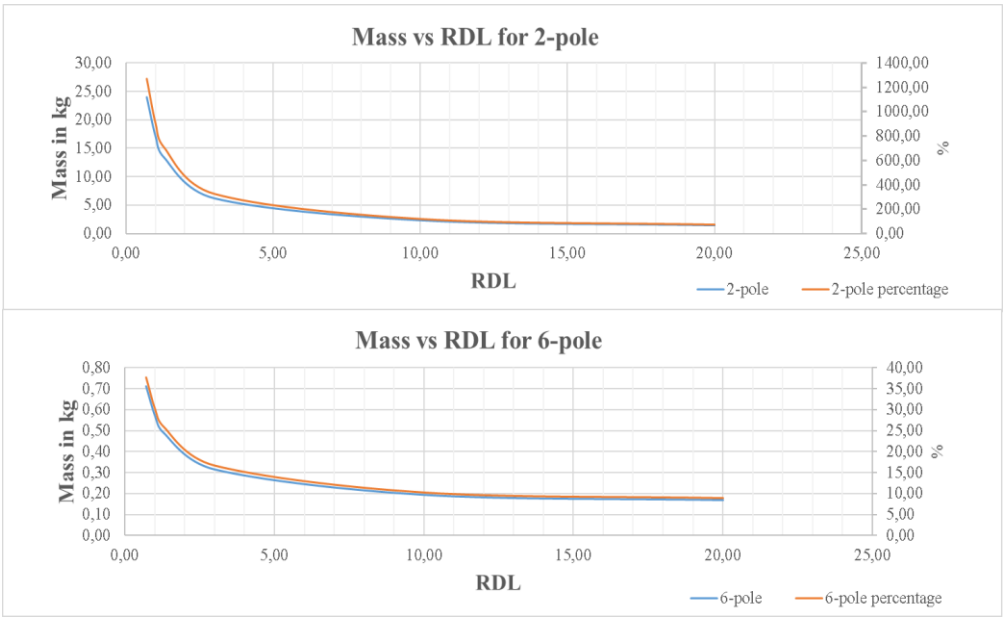

Figure 7.16 Mass Comparison and Contribution for Gimbal Angle 75º

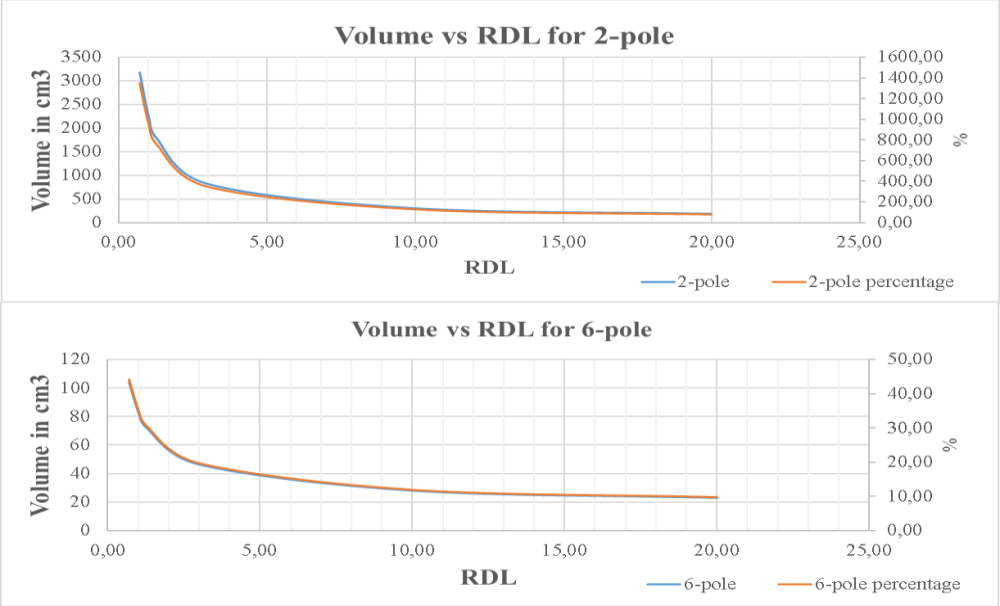

Figure 7.17 Volume Comparison and Contribution for Gimbal Angle 75º

7.3.10.4. Design Results for Gimbal Angle 90°

Required motor torque is taken 0.1795 Nm mentioned before in Section 7.1. Detail design results are shown in Table 7.30.

Mass, volume and inertia contribution and comparison of 2-pole and 6-pole motors with respect to different RDL values shown in from Figure 7.18 to Figure 7.20. Base values of mass, volume, and inertia are taken from wheel design result that outer radius is 13 cm for 90º maximum gimbal angle for contribution calculations.

Base Values

Mass: 1.82 kg Volume: 228 cm^3 Inertia: 28.6 $g.m^2$

Table 7.30 *Detailed Motor Design Results for Gimbal Angle 90°*

Parameter	2-pole square wave excited motor						6-pole square wave excited motor					
	Value						Value					
RDL	0,7	1	1,3	3	10	20	0,7	1	1,3	3	10	20
Di (mm)	95,13	95,59	96,04	98,38	105,80	113,33	36,34	38,09	39,6	45,45	57,44	66,57
L (mm)	135,90	95,59	73,88	32,79	10,58	5,67	51,91	38,09	30,44	15,15	5,74	3,33
g (mm)	0,75	0,75	0,75	0,75	0,75	0,75	0,75	0,75	0,75	0,75	0,75	0,75
Do (mm)	172,40	173,23	174,04	178,28	191,93	206,24	50,38	52,63	54,54	62,20	78,63	93,53
hs (mm)	0,13	0,18	0,24	0,51	1,38	2,26	2,53	3,18	3,73	5,92	10,39	13,79
lm (mm)	1,45	1,46	1,47	1,53	1,79	2,30	1,63	1,66	1,68	1,82	2,51	4,23
h1 (mm)	1,00	1,00	1,00	1,00	1,00	1,00	1,00	1,00	1,00	1,00	1,00	1,00
h2 (mm)	1,00	1,00	1,00	1,00	1,00	1,00	1,00	1,00	1,00	1,00	1,00	1,00
w1 (mm)	0,75	0,75	0,75	0,75	0,75	0,75	0,75	0,75	0,75	0,75	0,75	0,75
w2 (mm)	7,94	7,98	8,01	8,19	8,76	9,34	2,60	2,70	2,78	3,10	3,76	4,26
hsbc (mm)	36,43	36,61	36,78	37,68	40,52	43,40	4,64	4,86	5,05	5,80	7,33	8,50
t1 (mm)	15,85	15,93	16,01	16,42	17,72	19,03	5,59	5,90	6,16	7,18	9,28	10,87
t2 (mm)	7,94	7,98	8,01	8,19	9	9,34	2,60	2,70	2,78	3,10	3,76	4,26
J (g.m2)	80,14	57,46	45,25	22,12	10	6,83	0,14	0,12	0,11	0,10	0,09	0,11
V (cm3)	3172	2253	1757	819	306	189	103	83	71	46	28	23
Mtotal (kg)	24,01	17,05	13,29	6,18	2,30	1,42	0,71	0,57	0,48	0,31	0,19	0,17
Rph (mOhm)	119,08	63,00	40,08	42,77	38,25	61,52	53,83	31,11	37,53	27,01	33,15	39,28
Lph (uH)	22,36	15,86	12,35	22,85	33,10	59,48	19,46	14,87	21,86	28,09	68,30	110,93
Nph	3,00	3,00	3,00	6,00	12,00	21,00	9,00	9,00	12,00	18,00	39,00	57,00
Irms (A) @SS	1,35	1,91	2,46	2,70	3,90	3,88	3,08	4,01	3,62	4,22	4,07	4,14
Irms(A) @Acc	9,59	9,59	9,59	9,59	9,59	9,59	9,59	9,59	9,59	9,59	9,59	9,59
q (A.t/m)	184	258	331	711	1906	3102	3294	4084	4735	7212	11912	15304
Ploss @Acc(copper + iron)(W)	97,45	68,22	53,44	27,93	17,50	19,57	19,84	17,18	15,78	12,71	11,59	12,80
Ploss @SS(copper + iron)(W)	91,91	63,74	49,37	23,49	10,08	7,92	13,13	10,77	9,49	6,65	4,76	4,42
Efficiency (%) @ Acc	65,86	73,37	77,86	87,06	91,48	90,57	90,45	91,63	92,25	93,67	94,19	93,62
Efficiency (%)@ SS	47,53	56,64	62,77	77,99	89,20	91,31	86,38	88,54	89,77	92,60	94,60	94,95

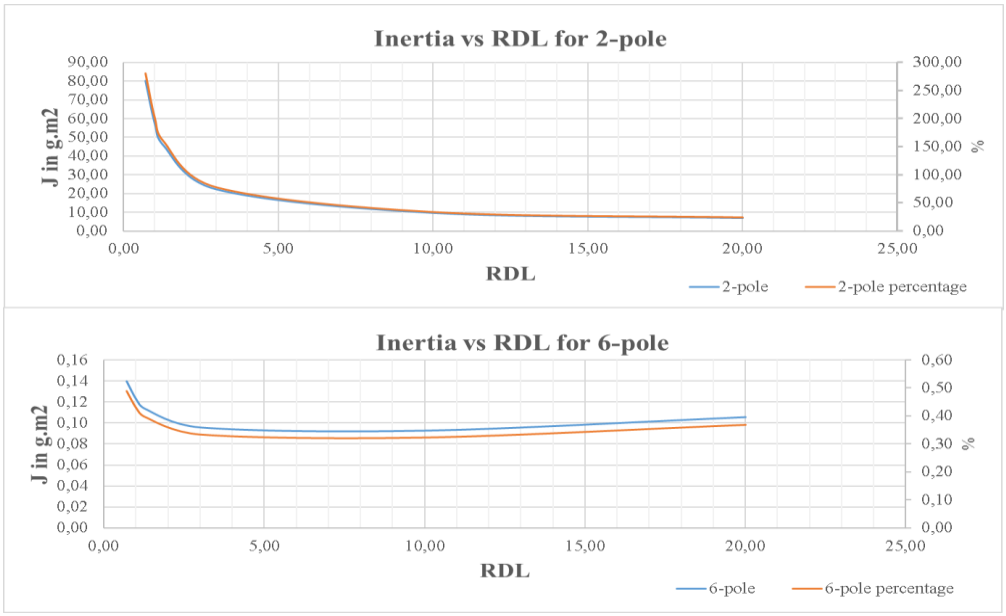

Figure 7.18 Inertia Comparison and Contribution for Gimbal Angle 90º

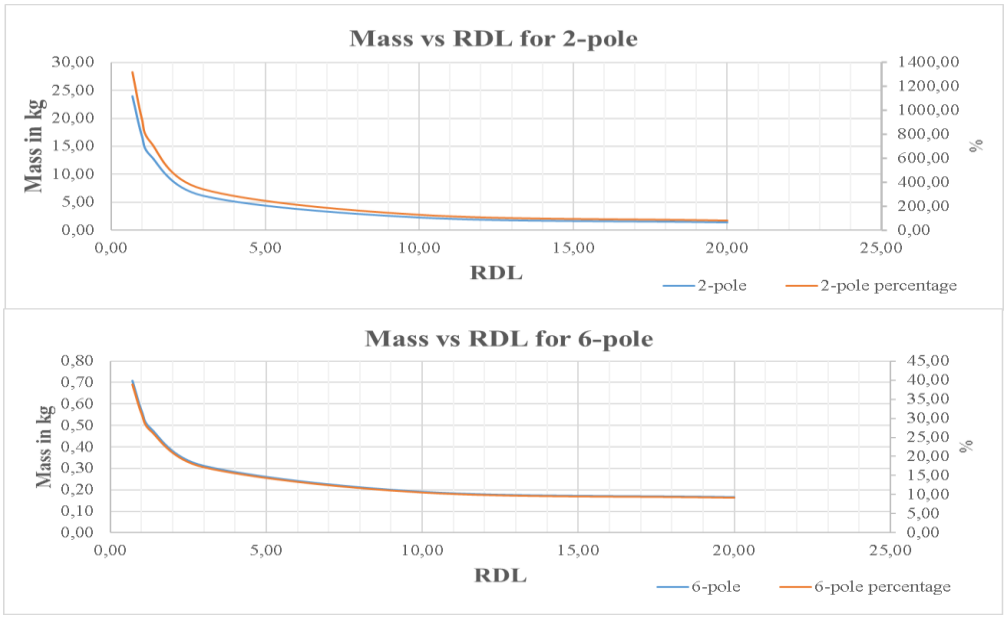

Figure 7.19 Mass Comparison and Contribution for Gimbal Angle 90º

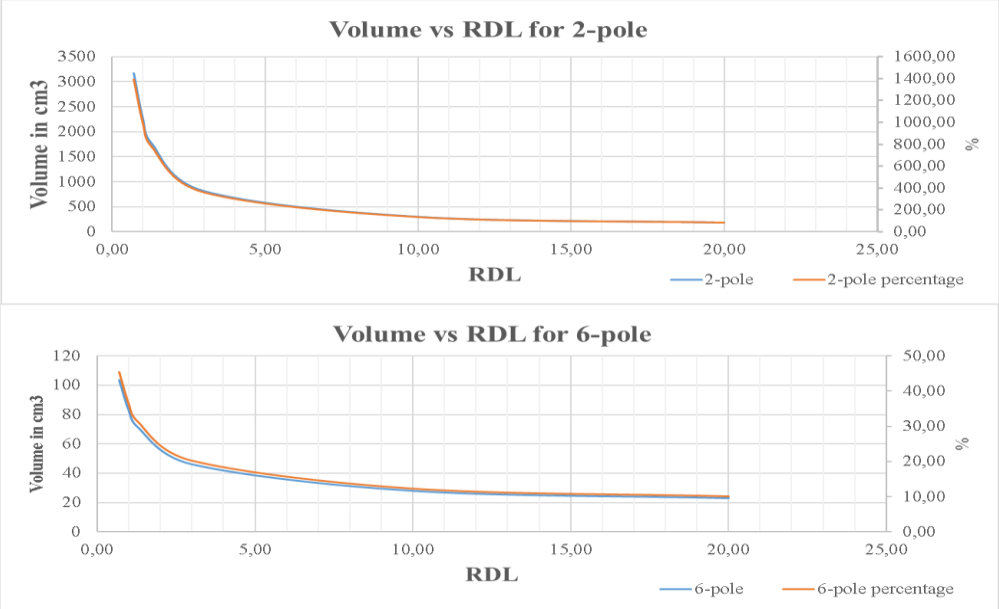

Figure 7.20 Volume Comparison and Contribution for Gimbal Angle 90º

7.3.10.5. Discussion of Motor Design Results

In this section, motor design results are discussed in terms of mass, volume, inertia, and manufacturability. Two unknowns slot depth (h_s) and an inner diameter of the motor (D_i) is the starting point of the motor calculations. The purpose of this calculation is to optimize motor dimensions and obtain a minimum inner diameter in order to decrease mass and volume.

The average air gap magnetic flux density is taken 0.43 T and this constraint is satisfied for each design. In addition to this, electrical loading (q) of the designed motor has to be less than 6000 A.t/m.

When the results of 2-pole motors and the 6-pole motors are compared for each different gimbal angle individually;

- Since magnetic loading is directly related stator back core depth, back core depth of 2-pole motors is longer than 6-pole motors. For this reason, mass and volume of 2-pole motors are higher than 6-pole motors. Therefore, 2-pole

motors are not suitable for space applications in terms of mass and volume efficiency.

- Since mass and dimensions of 2-pole motor are bigger than 6-pole motor, inertia contribution of 2 pole motor is more than 6-pole motor. However, inertia contribution is not critical since the required inertia has been already provided by the wheel. It is noted that inertia contributions of 6-pole motors are lower than 1% and it can be ignored.
- Manufacturability constraints are also taken into account when a suitable motor is selected. The stack length of the motor is designed to be longer than 15 mm due to mechanical consideration. Therefore, it is obvious that designed motors that have bigger RDL values such as 10 and 20 are not suitable.

When the results of 2-pole and 6-pole motors are evaluated, 6-pole motors are more suitable in terms of mass and volume consideration. On the other hand, there are several 6-pole motor designs with respect to different RDL values. Therefore, 6-pole motor design results are also compared with respect to different RDL values. This comparison is summarized in the following statements.

- Mass and volume of the motor decreases by increasing RDL.
- Inertia contribution of motor decreases by increasing RDL.
- The length of the motor is longer than 15mm when RDL is smaller 3.
- Electrical loading is higher than 6000 A.t/m when RDL is bigger than 1.3.

In conclusion, the designed motor that has bigger RDL is a more proper choice for motor design in terms of mass and volume. However, after RDL=1.3, electrical loading and manufacturability constraints are not satisfied. For these reasons, 6-pole motor design that RDL=1.3 is the most suitable motor design in this study for each different maximum gimbal angle excursions. It is also noted that design results are almost the same for different gimbal angle cases. It is obvious that mass and volume of motor are a little bit decreased by increasing gimbal angle because of the lower inertia requirement.

7.4. Motor Driver - STEVAL-SPIN3202 Evaluation Board

In space applications, the first and common method to verify motor driver for prototype models is to use motor driver evaluation board. The aim of the evaluation board is to check the designed motor and CMG functionally. After verification, motor driver for flight model equipment will be designed by using radiation-hardened components. However, it is not studied in this thesis since the cost of radiation-hardened components is expensive and designing motor driver for flight model equipment is complicated in terms of redundancy, reliability, selecting radiation-hardened components, coding of controller and hardware. The verification of prototype CMG designed in this study is planned with the help of STEVAL-SPIN3202 evaluation board.

The STEVAL-SPIN3202 three-phase brushless DC motor driver board [31] is an evaluation board based on the STSPIN32F0A and STD140N6F7 MOSFETs. It provides up to 45 V and 15 A_{rms} motor driving applications. It is a user-friendly board and this board is designed for both sensored and sensorless vector control and six-step algorithms with single shunt resistor sensing. Six-step algorithm with a digital hall sensor is selected driving method in this study and this evaluation board satisfies driving method and specifications of the designed motor.

The evaluation board is supplied voltage range from 7V to 45 V and it satisfies requirement about input voltage range from 18V to 33V. The output current of the evaluation board is 15 A_{rms} and it also satisfies requirement that the maximum acceleration rms current is 11.78 A for 45º gimbal angle motor design. Six N channel STD140N6F7 MOSFETs are placed in three half-bridge systems for high side and low side switches. The capability of this MOSFET is 60 V drain-source voltage, 80 A continuous drain-source current and 3.1 mΩ drain-source resistance when the switch is ON [32]. Internal buck converter generates 3.3 V to supply internal logic circuits and linear regulator converts supply voltage to 12 V for gate drivers. Two 20 mΩ resistances are connected in parallel to sense motor current. Internal operational

amplifier performs current monitoring by using voltage difference between sense resistors. An internal comparator in STSPIN32F0A compares maximum selected current reference and current monitoring value and then if it is higher than the selected reference value, the integrated comparator is triggered and all the high side power switches are disabled. Three overcurrent threshold levels that are 20 A, 65 A and 140 A are defined for evaluation board. In addition, the bus voltage is sensed by the voltage divider. The evaluation board is compatible with quadrature encoder and digital hall sensors for motor position feedback. Therefore, the evaluation board supports field-oriented control (FOC) and 6-step sensorless or sensored trapezoidal control. Thanks to ST-LINK-V2, users can load new firmware and debug without any external hardware. There are three buttons on the evaluation board. Reset button provides resetting STSPIN32F0A MCU and ST-LINK V2. User 1 button starts the motor movement and speed of the motor can be adjusted by trimmer from 1200 rpm to 12000 rpm. In order to stop the motor, user 1 button should be pushed one more time. If any error occurs when the motor is operating, the LED of user 2 button is ON. Fault can be cleared by pushing user 1 button. Features of the evaluation board are shown in Table 7.31 and evaluation board is shared in Figure 7.21.

Table 7.31 *Features of STEVAL-SPIN3202 Evaluation Board* [31]

Parameter	**Value and Feature**
Input Voltage	7V to 45 V
Output Current	Up to 15 Arms
Power Stage	Based on STD140N6F7 MOSFETs
Embedded Regulators	3.3V buck regulator
	12 V LDO regulator
Current Sensing	Single Shunt Resistor
External Speed Sensing	Digital Hall Sensors or Encoder
Protection	Over Current Sensing
	Bus Voltage Sensing
Software	Fully compatible with STM32 PMSM FOC software development kit
	6-step sensorless and sensored firmware supported
Others	Embedded ST-LINK / V2-1
	Easy user interface with buttons and trimmer
	STM32 FW boot loader supported
	RoHS compliant

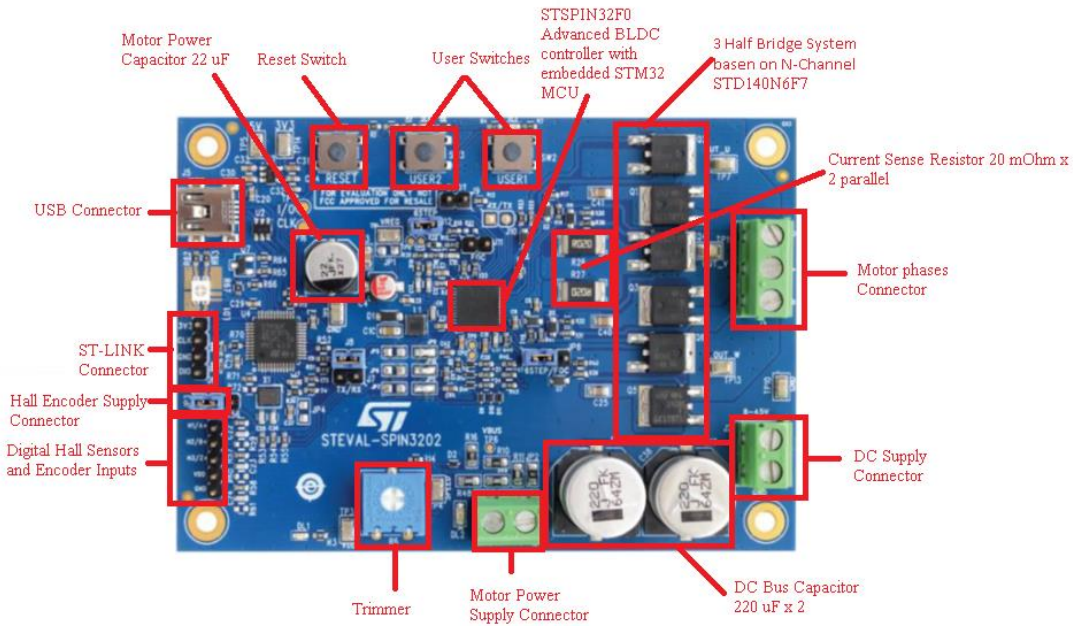

Figure 7.21 STEVAL-SPIN3202 Evaluation Board [31]

STSPIN32F0 [33] is an advanced BLDC controller with embedded STM32 MCU. It has 3.3V DC/DC buck converter with overcurrent, short-circuit, and thermal protection and 12 V LDO linear regulator with thermal protection. Three-phase gate drivers that have 600 mA sink/source capacity are placed in the controller. In order to

drive high side MOSFETs, a circuit of bootstrap gate drivers are used in the controller. It has 32-bit ARM® Cortex®-M0 core that has up to 48 MHz clock frequency, 4-kByte SRAM with HW parity, 32-kByte Flash memory with option bytes used for write/readout protection. There are 16 general-purpose input and output ports, 5 general-purpose timers and 12-bit ADC converter. It is compatible with I^2C, USART, and SPI communication interfaces. Moreover, it includes three rail-to-rail operational amplifiers to use signal conditioning such as motor current sense. The block diagram of STSPIN32F0 is shown in Figure 7.22.

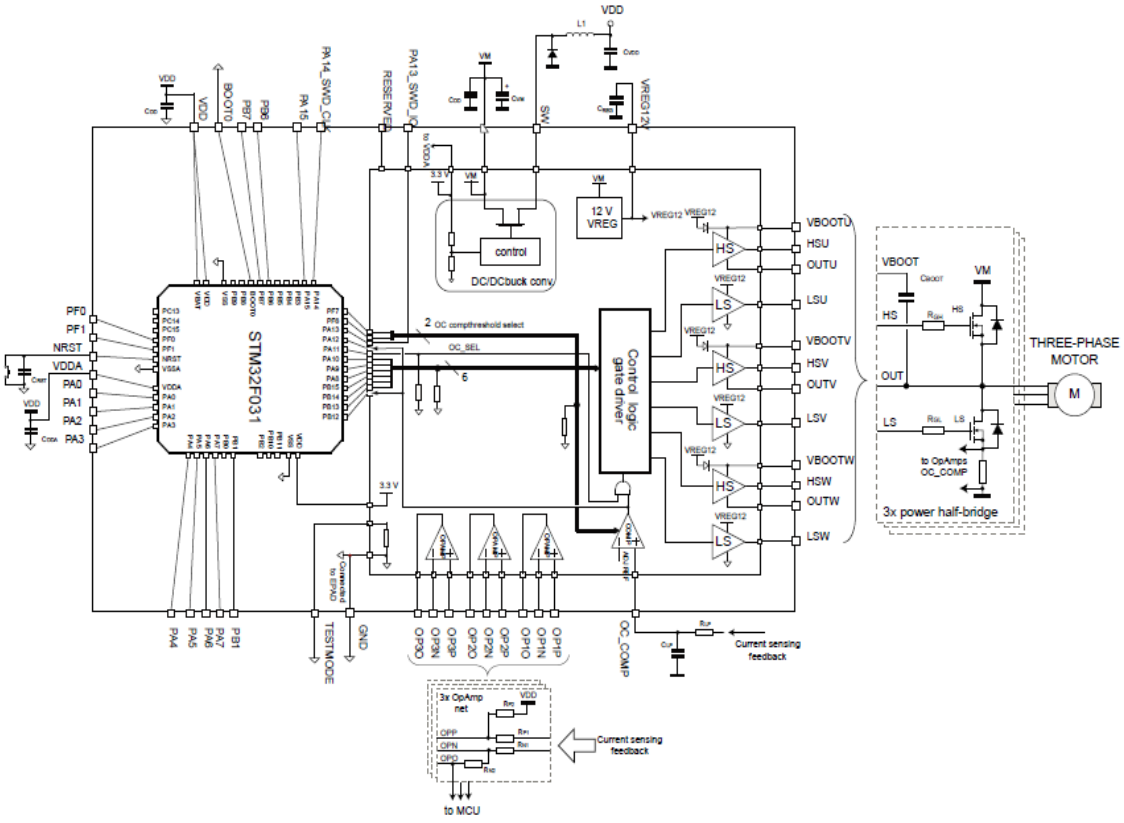

Figure 7.22 Block Diagram of STSPIN32F0 [33]

CHAPTER 8

SELECTION OF STEPPER MOTOR AND DRIVER

8.1. Stepper Motor

CMG creates the output torque when the direction of the angular momentum vector is changed. The wheel designed in CHAPTER 6 provides angular momentum of the system but the direction of this angular momentum is changed by gimbal structure in CMG. In order to change the direction of the angular momentum, stepper motor and stepper motor driver are selected and placed under the wheel construction. In conclusion, the gimbal of CMG consists of stepper motor, stepper motor driver and gear system to increase output torque of the stepper motor.

The maximum required output speed of the stepper motor depends on the maximum permissible gimbal angle. In this study, four different maximum gimbal angle excursions are analyzed and the output speed of gimbal is calculated 1.5 deg/s for 45-degree gimbal angle, 2 deg/s for 60-degree gimbal angle, 2.5 deg/s for 75-degree gimbal angle and 3 deg/s for 90-degree gimbal angle in Section 5.5.4 to satisfy maneuvering duration specifications. In other words, the output speed of the selected stepper motor shouldn't be less than 3 deg/s. Since Faulhaber motors are generally used in space applications, AM 1524 V6 2 -phase stepper motor with anti-backlash (zero-backlash) gearhead (15/8 series) is chosen in this study. The usage of anti-backlash is significant since backlash can cause an irrevocable error in space applications. The nominal voltage of the stepper motor when two phases are on is 6 volts and the step angle of the motor is 15 degrees. The continuous output torque of motor with spur gearheads (zero-backlash 15/8 series) is 0.1 Nm.

The most important consideration during designing stepper motor calculation is "gyro torque" acting back to the gimbal system. If satellite inertial body rate is in the same

direction of CMG output torque, gimbal gears and the stepper motor are directly affected by gyro torque. Therefore, the total torque capability of stepper motor and gear should be higher than the gyro torque [11].

In order to prevent damage of stepper motor from gyro torque, external gear system should be designed. The gyro torque can be calculated as in Equation (8.1) [11] and maximum gyro torque is shown in Equation (8.2).

$$\tau_{\text{Gyro}} = \omega_{\text{st}} \text{ x } h_{\text{wheel}} \tag{8.1}$$

$$\tau_{Gyro\_max} = \omega_{st}\, h_{wheel} \cos\delta \tag{8.2}$$

ω_{st} is satellite inertial body rate and it is equal to the angular velocity of the satellite in rad/s, h_{wheel} is the angular momentum of the wheel and δ is gimbal angle during rotation Detailed representation of gimbal structure is shown in Figure 8.1.

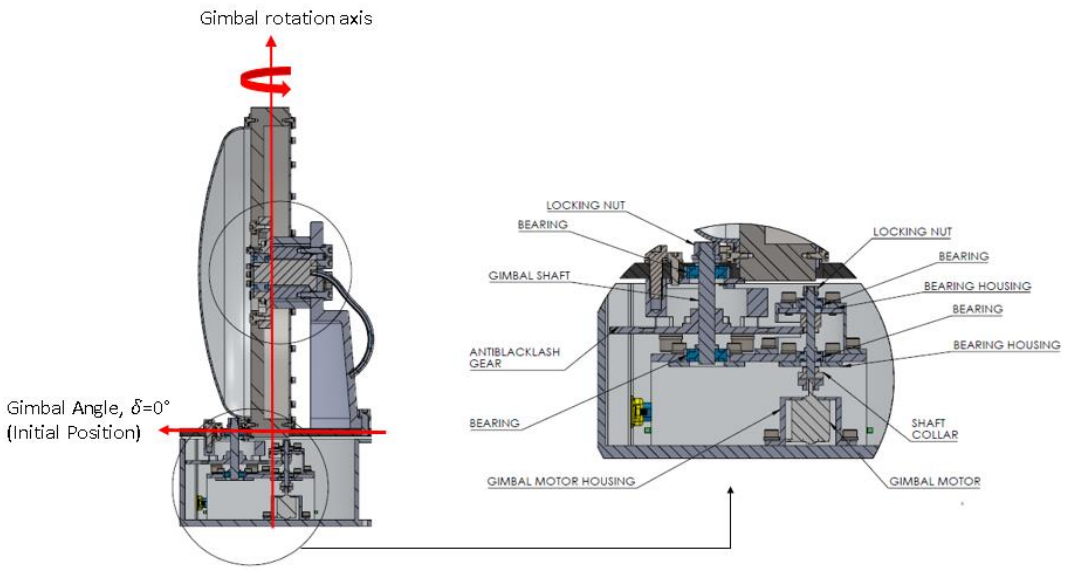

Figure 8.1 Detailed Representation of Gimbal Structure

In Section 5.5, four different cases that are related to maneuvering specifications are studied in detail and the same cases are also applied for four different maximum gimbal angle excursions (Totally 16 cases). Equation (8.2) shows that gyro torque acting back to system (τ_{Gyro}) depends on the angular velocity of the satellite and

gimbal angle during satellite maneuvering. Therefore, maximum gyro torque acting back to the gimbal system occurs when the angular velocity of the satellite reaches the maximum during maneuvering. Maximum gyro torques acting back to the gimbal system are calculated in Table 8.1 for each maneuvering case. Required top values of gyro torques are shown with a yellow row for each maximum gimbal angle excursions case.

Table 8.1 *Maximum Gyro Torque Acting Back to Gimbal System*

Maximum Gimbal Angle Case	Case	Case Specification	Maximum Satellite Angular Velocity (wst) (deg/s- rad/s)	Maximum Gimbal Angle During Maneuvering (δ)	Angular Momentum (hwheel) (Nms)	Maximum Gyro Torque (τGyro) (Nm)
45	1	30° rotation on x-axis < 40s	1.5 - 0.0262	30°	42.41	0.962
	2	60° rotation on x-axis < 60s	2 - 0.0349	45°	42.41	1.046
	3	30° rotation on y-axis < 30s	2 - 0.0349	22.5°	42.41	1.367
	4	60° rotation on y-axis < 45s	2.67 - 0.0466	33.75°	42.41	1.643
60	1	30° rotation on x-axis < 40s	1.5 - 0.0262	40°	34.66	0.695
	2	60° rotation on x-axis < 60s	2 - 0.0349	60°	34.66	0.604
	3	30° rotation on y-axis < 30s	2 - 0.0349	30°	34.66	1.047
	4	60° rotation on y-axis < 45s	2.67 - 0.0466	45°	34.66	1.142
75	1	30° rotation on x-axis < 40s	1.5 - 0.0262	50°	31	0.522
	2	60° rotation on x-axis < 60s	2 - 0.0349	75°	31	0.280
	3	30° rotation on y-axis < 30s	2 - 0.0349	37.5°	31	0.858
	4	60° rotation on y-axis < 45s	2.67 - 0.0466	56.25°	31	0.802
90	1	30° rotation on x-axis < 40s	1.5 - 0.0262	60°	29.95	0.392
	2	60° rotation on x-axis < 60s	2 - 0.0349	90°	29.95	0
	3	30° rotation on y-axis < 30s	2 - 0.0349	45°	29.95	0.739
	4	60° rotation on y-axis < 45s	2.67 - 0.0466	67.5°	29.95	0.534

Since the gimbal angle and the angular velocity of the satellites are changing during satellite maneuvering, gyro torque acting back to the gimbal system is a function of gimbal angle and the angular velocity of the satellite. Gimbal angle affects the function as a cosine function and angular velocity of the satellite affects the function as a linear. In conclusion gyro torques acting back to the gimbal system with respect to time during medium satellite maneuvering are shown in from Figure 8.2 to Figure 8.5 for four different maximum gimbal angle excursions.

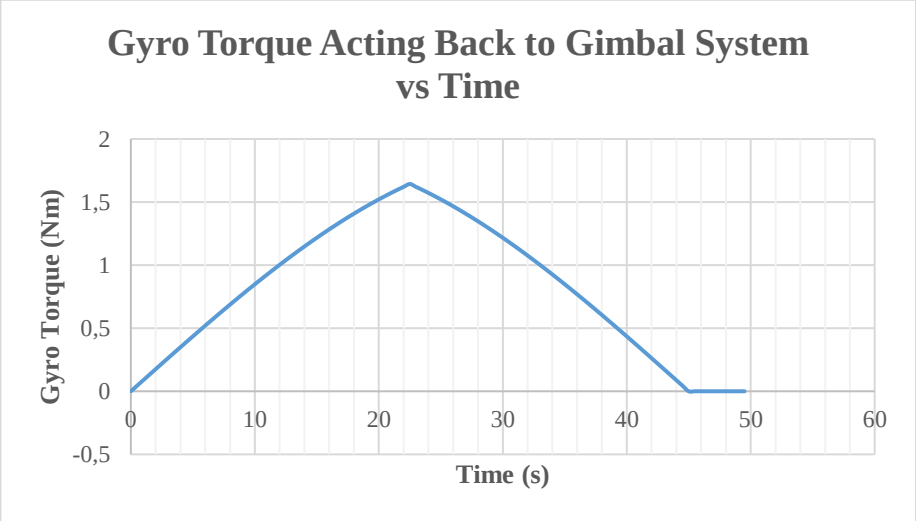

Figure 8.2 Gyro Torque Acting Back to Gimbal System for 45° Gimbal Angle Excursion- Case 4

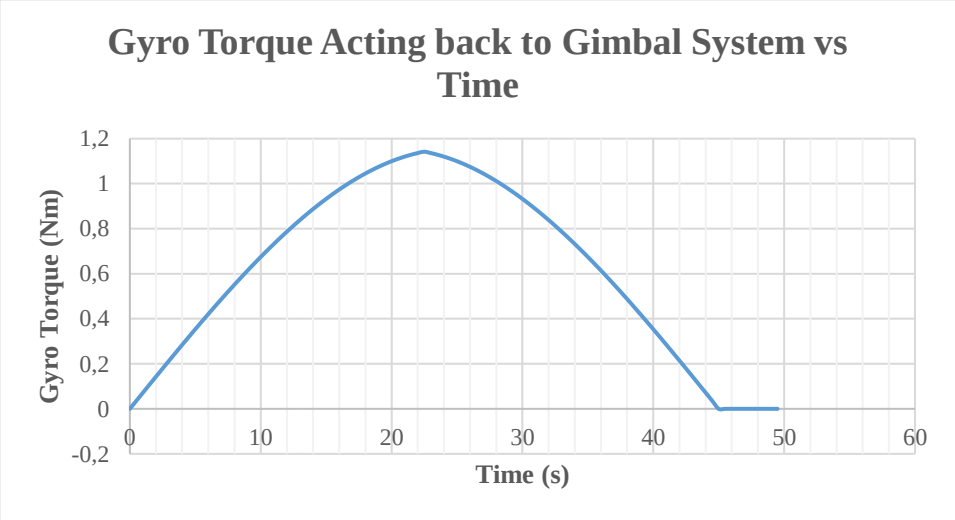

Figure 8.3 Gyro Torque Acting Back to Gimbal System for 60° Gimbal Angle Excursion - Case 4

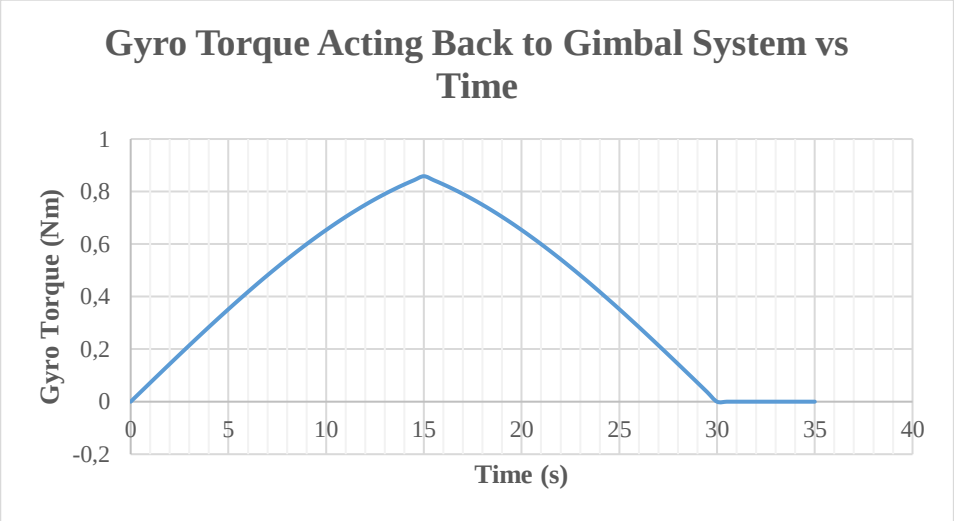

Figure 8.4 Gyro Torque Acting Back to Gimbal System for 75° Gimbal Angle Excursion - Case 3

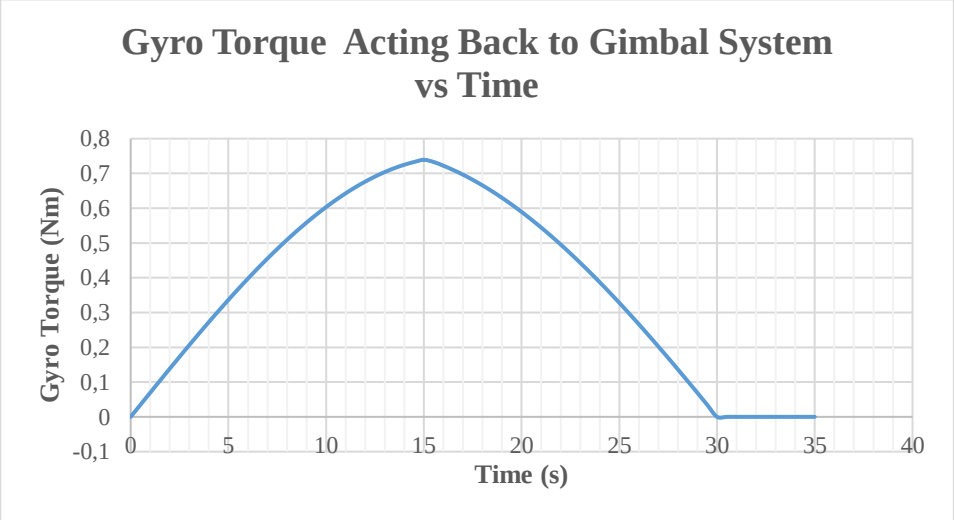

Figure 8.5 Gyro Torque Acting Back to Gimbal System for 90° Gimbal Angle Excursion - Case 3

Total torque of the gimbal system should overcome gyro torque acting back to the system in order to stabilize the position of the gimbal and to rotate the wheel with respect to gimbal axis. Therefore, external gear should be placed at the output of the stepper motor to increase torque capability. The efficiency of the gimbal gear system is taken as 0.8 [11]. The relationship between total required torque of gimbal system (τ_{gear}) and gyro torque (τ_{Gyro}) is expressed in Equation (8.3) and the gear ratio is

calculated in Equation (8.4) in terms of required torque of the gimbal system and stepper motor output (τ_{motor}) that already defined as 0.1 Nm.

$$\tau_{\text{gear}} = 0.8\,\tau_{\text{Gyro}} \tag{8.3}$$

$$Gear\ Ratio = \frac{\tau_{gear}}{\tau_{motor}} \tag{8.4}$$

The total required torque of gimbal system for four different maximum gimbal angle excursions is calculated by multiplying the maximum value of gyro torque acting back to the gimbal system mentioned in Table 8.1 and 0.8. Required gear ratio for different maximum gimbal angle excursion is calculated by dividing total required torque of gimbal system with 0.1 Nm. The results of gear ratio calculations are shown in Table 8.2.

Table 8.2 *The Results of Gimbal System Gear Ratio Calculations*

Gimbal Angle - Case	**Maximum Gyro Torque (τ_{Gyro})**	**Gimbal System Torque (τ_{gear})**	**Calculated Gear Ratio**	**Selected Gear Ratio**
45° - Case 4	1.643 Nm	1.314 Nm	13.14 : 1	14:1
60° - Case 4	1.142 Nm	0.913 Nm	9.13 : 1	10:1
75° - Case 3	0.858 Nm	0.686 Nm	6.86 : 1	7:1
90° - Case 3	0.739 Nm	0.591 Nm	5.91 : 1	6:1

The reduction ratio of the step motor spur gearheads is 141:1. Step resolution of gimbal system for different maximum gimbal angle excursion can be calculated by using Equation (8.5). The maximum step number is calculated in Equation (8.6).

$$\text{Step resolution} = \frac{\text{Motor Step Angle}}{\text{Total Gear Ratio}} \tag{8.5}$$

$$\text{Maximum Step Number} = \text{Gimbal Speed}\ \frac{\text{Total Gear Ratio}}{\text{Motor Step Angle}} \tag{8.6}$$

Step angle of the motor has been already defined as 15 degrees. The total gear ratio is calculated by multiplying the selected gear ratio of the gimbal system mentioned in Table 8.2 and gear ratio of spur gearheads (141:1). Gimbal speed for four different maximum gimbal angle excursions has been already calculated in Section 5.5. Step

resolution and the maximum step number calculations for different maximum gimbal angle excursions are calculated in Table 8.3

Table 8.3 *Step Resolution and Maximum Step Number Calculations for Different Maximum Gimbal Angle Excursion*

Maximum Gimbal Angle Excursion	**Total Gear Ratio**	**Step Resolution**	**Maximum Step Number**
45°	1974	0.0076 degree	197.4 steps/second
60°	1410	0.0106 degree	188 steps/second
75°	987	0.0152 degree	164.5 steps/second
90°	846	0.0177 degree	169.2 steps/second

When torque-step characteristics of AM 1524 V6 2 -phase stepper motor with anti-backlash (zero-backlash) gearhead (15/8 series) is considered, 0.1 Nm output torque is provided until 2000 steps/ seconds. Therefore, maximum step number of each case shown in Table 8.3 is satisfied easily.

8.2. Stepper Motor Driver

The AD-VM-M1 stepper motor driver [34] is selected to control 2-phase stepper motor. Motor driver has two modes which are half step mode and full-step mode. Full-step mode is used to utilize 15 degrees motor step angle. There are three inputs namely as CW (CCW), clock pulse and inhibit in the stepper motor driver. CW (CCW) determines the rotating direction. Clock pulse is directly related to step change. If one clock is received, the motor rotates one step. İnhibit is used to save energy when this pin is activated motor phases are not energized. Operating voltage is between 6V-24V and the maximum current is 0.5 A per phase [34]. Stepper motor driver technical specification is shown in Table 8.4.

Table 8.4 *Stepper Motor Driver Technical Specification* [34]

			AD VL M_S	AD VM M_S
Power supply voltage	Min Max	V	3 14	6 24
Power supply current		mA	16	16
Motor Output current	max.	mA	400	500
Auxiliary on-board supply	Voltage Current	V mA	5 50	5 50
Logic input level Conventional Info.	Low high	V	0 to 0.6 1.6 to 24	0 to 0.6 1.6 to 24
Direction of rotation			cw/ccw	cw/ccw
Step mode			full step (two phase ON full-step (one phase ON (wave) half step	

Stepper motor driver consists of two parts namely as power stage and translator. There are two full bridges motor driver per phase in the power stage. The translator is a type of 8-Bit CMOS ROM with one-time programmable microcontroller. Block diagram of the stepper motor driver is shown in Figure 8.6.

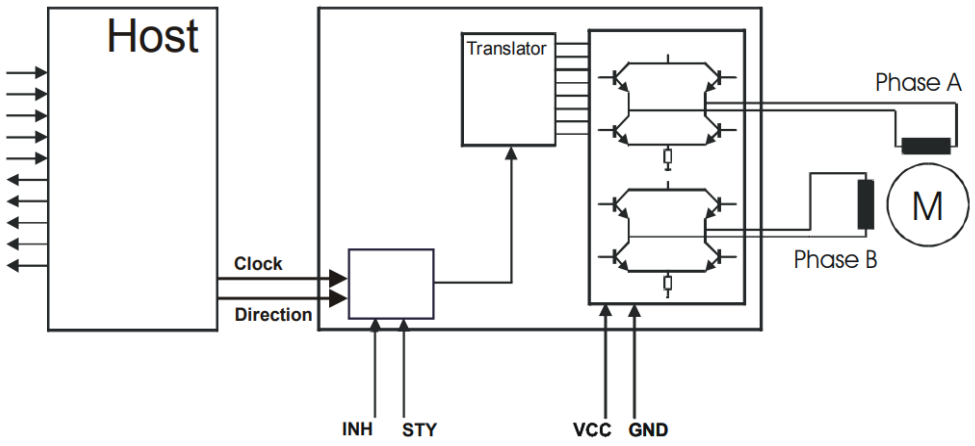

Figure 8.6 Block Diagram of Stepper Motor Driver [34]

8.3. Stepper Motor Position Measurement

Angle sensors namely as hall effect device sensor and potentiometer are used to understand the position of the stepper motor. Hall effect device sensor indicates the nominal or zero condition of gimbal angle. When the gimbal angle reaches 0 degree, the output state of hall effect device sensor is changed from high to zero. A

potentiometer is used for measuring angle of the gimbal. Potentiometer is chosen since it is cheaper and simple. Since the measured value of potentiometer is not generally accurate, it is only used for information. The output of the potentiometer only gives an idea about the position of the gimbal basic circuit diagram and characteristics of angle sensors are shown in Figure 8.7. It is also noted that a similar position measurement method is applied for controlling the position of solar array in the telecommunication satellites.

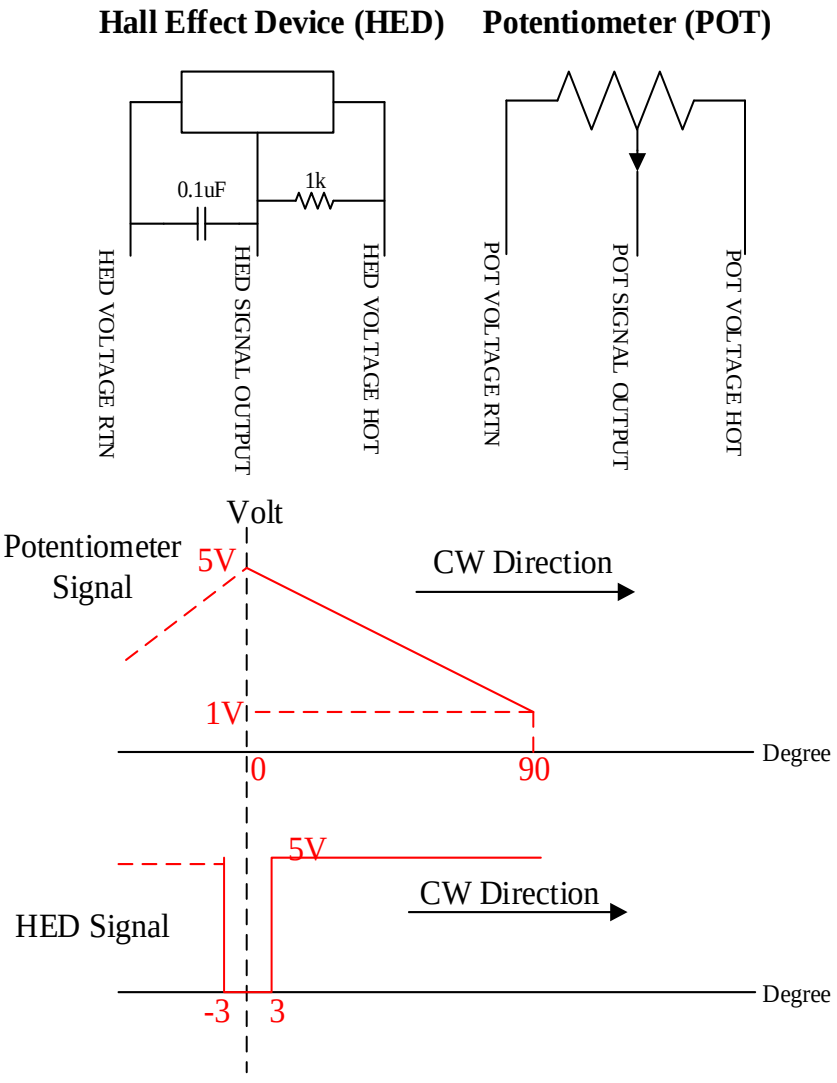

Figure 8.7 Basic Circuit Diagram and Characteristics of Angle Sensors

Potentiometer has generally dead-band in its range. The output of the potentiometer in dead-band is floating and there is no meaningless output. In order to not operate at dead-band, potentiometer is not used in the whole range. Therefore, the output of potentiometer is not reached to 0V and it is operated between 5V and 1V.

As seen in Figure 8.7, there is one capacitor and one resistance to obtain stable output from HED sensor. If the direction of the gimbal is CW, the state of the HED sensor output is changed at -3 degree and if the direction of the gimbal is CCW, it is changed at 3 degrees. It is noted that both potentiometer and hall effect devices are powered by 5V.

CHAPTER 9

DESIGN RESULTS AND CONCLUSION

9.1. Introduction

In this section, the results of the investigation in previous chapters will be summarized and the choice for manufacturing prototype CMG will be made.

9.2. Determination of Maximum Gimbal Angle Excursions

The effect of four different gimbal angles (45°, 60°, 75°, and 90°) on CMG design are studied in Section 5.5. The maximum gimbal angle excursion is defined as the maximum rotation angle of the wheel during operation. Although larger gimbal angle is more efficient in terms of mass and volume reduction of CMG, it is selected as 45° since output ripple of CMG is the lowest and stability is the primary concern for Attitude Orbit Control System. Therefore, satellite control algorithm is easier, and system is more reliable. In addition, the same gimbal angle was used in the previous satellite program. It means that AOCS has heritage and risk is low.

After the determination of maximum gimbal angle excursion, the parts of the control moment gyroscopes are selected. Mass and volume of the parts are minimized as low as possible. Parts of the designed CMG are shown in Figure 9.1

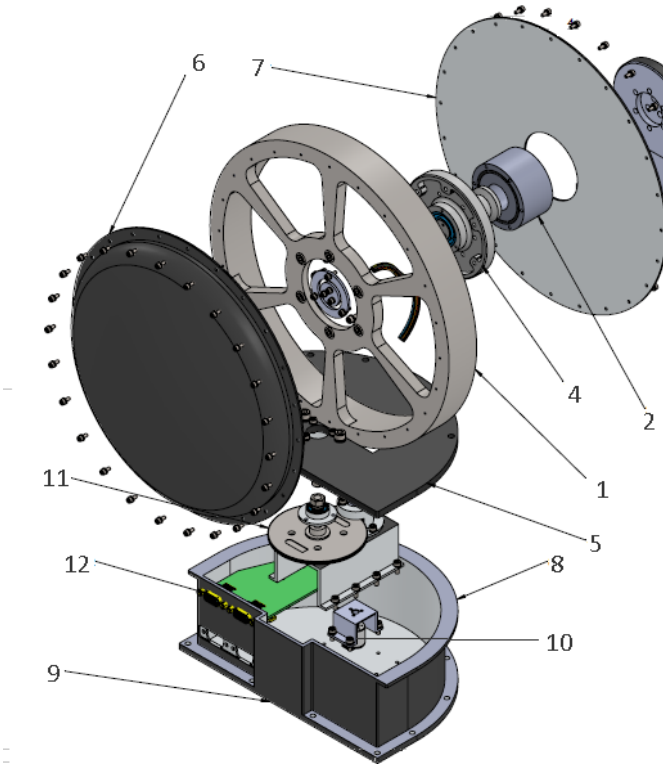

No	Part Name
1	Flywheel
2	Flywheel BLDC Motor
3	Flywheel Motor Mounting Part
4	Flywheel Bearing Assembly
5	Flywheel Mounting Plate
6	Front Cover
7	Back Cover
8	Gimbal Cover
9	Bottom Plate
10	Gimbal Motor (Step Motor)
11	Gimbal Gear Assembly
12	Drive Electronics

Figure 9.1 Parts of Designed CMG Model

9.3. Design Results of the Wheel

Design results of the wheel for different gimbal angles and different outer radii are shown in Table 6.1. The wheel that has the lowest mass and volume is selected for 45° gimbal angle. Safety factor of the selected wheel is 1.23 and it is bigger than 1.1 (safety factor of unmanned spacecraft) but it is smaller than 1.25 (safety factor of manned spacecraft). In conclusion, the designed wheel should be placed in unmanned spacecraft.

Design results of selected wheel parameters are shown in Table 9.1 and mechanical drawing is shared in Figure 9.2.

Table 9.1 *Design Results of Selected Wheel*

Parameter	**Value**
Selected Gimbal Angle	45°
Thickness of Wheel	3 cm
Outer Radius	13 cm
Inner Radius	11.55 cm
Volume of Wheel	335 cm^3
Mass of Wheel	2.68 kg (2.98 kg with spokes)
Inertia of Wheel	0.0405 $kg.m^2$
Operating Tensile Yield Stress	99.23 MPa
Operating Speed	1047,2 rad/s (10000rpm)
Maximum Yield Speed	1285 rad/s
Factor of Safety	1.23

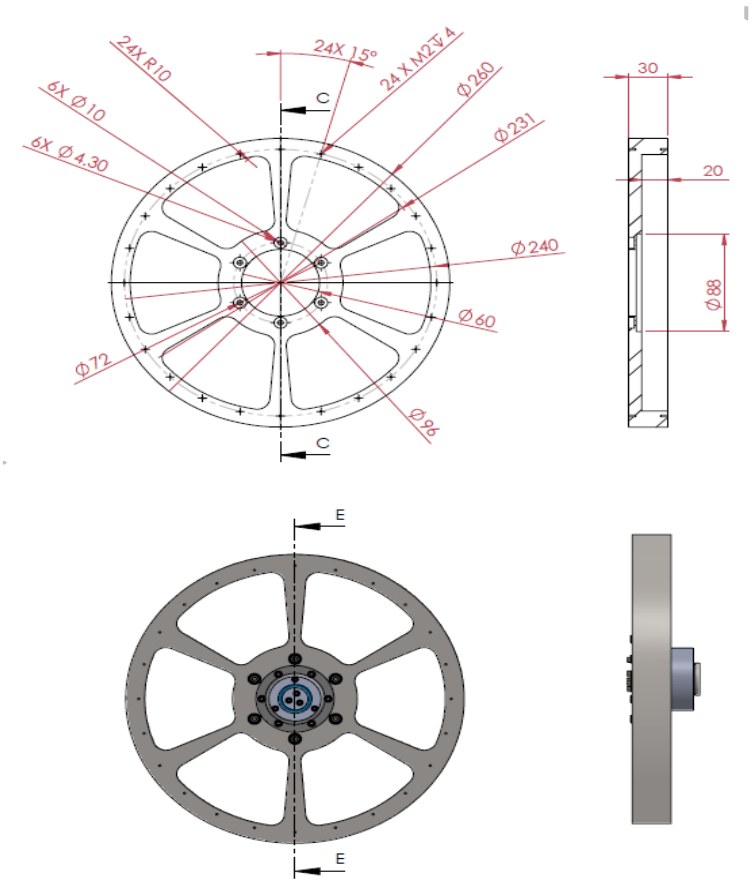

Figure 9.2 Mechanical Drawing of Designed Wheel

9.4. Design Results of BLDC Motor of The Wheel

BLDC Motor that rotates the wheel at 10000 rpm is designed in CHAPTER 7. Motor torque values are 0.2205 Nm for acceleration and 0.0795 Nm for steady-state in case of 45° gimbal angle.

6-pole motor is chosen in this thesis since it has lower mass and volume when it is compared with 2-pole motor. The motor that has bigger RDL is a more proper choice for motor design in terms of mass and volume. However, after RDL=1.3, electrical loading and manufacturability constraints are not satisfied. For these reasons, RDL is chosen 1.3. Design results of motor parameters are shown in Table 9.2. Representation of motor dimensions is shown in Figure 9.3.

Table 9.2 *Design Results of BLDC Motor*

Tabl**Parameter**	**Design Results**
Motor Torque Capacity	0.2205 Nm
Type	Outer Rotor Radial Flux
Excitation	Trapezoidal
Core Material	Cogent Power No 12
Stator Lamination	0.2mm
Permanent Magnet	VACOMAX 225 HR type samarium cobalt magnet (Sm2Co17)
Average Air gap Flux Density	0.43 T
Maximum Electrical Loading During Acceleration	6000 A-t/m
Maximum Electrical Loading at Steady State	3000 A-t/m
Pole Number	6
Total Slot Number	18
Back EMF per Phase	8V
RDL	1.3
Shaft of Motor, Dshaft	22 mm
Inner Diameter, Di	40.85 mm
Length, L	31.42 mm
Air Gap, g	0.75mm
Outer Diameter, Do	56.13 mm
Slot Depth, hs	4.21 mm
Magnet Thickness, lm	1.67 mm
Tooth Lip-1, h1	1 mm
Tooth Lip-2, h2	1 mm
Lip Opening, w1	0.75 mm
Slot Thickness, w2	2.85 mm
Back Core Depth, hbc	5.22 mm
Tooth Width at Airgap, t1	6.38 mm
Tooth Width, t2	2.85 mm
Motor Inertia	0.13 g.m2
Motor Volume	78 cm3
Motor Mass	0.53 kg
Phase Resistance	33.59 mΩ
Phase Inductance	22.91 μH
Turn Number per Phase	12
RMS Current at Steady-State	4.25 A
RMS Current During Acceleration	11.78 A
Electrical Loading During Acceleration	5995 A-t/m
Copper and Iron loss During Acceleration	18.04 W
Copper and Iron loss at Steady State	9.93 W
Maximum Power Demand During Acceleration	248.9 W
Maximum Power Demand at Steady State	88.4 W
Efficiency During Acceleration	92.75 %
Efficiency at Steady State	89.34 %

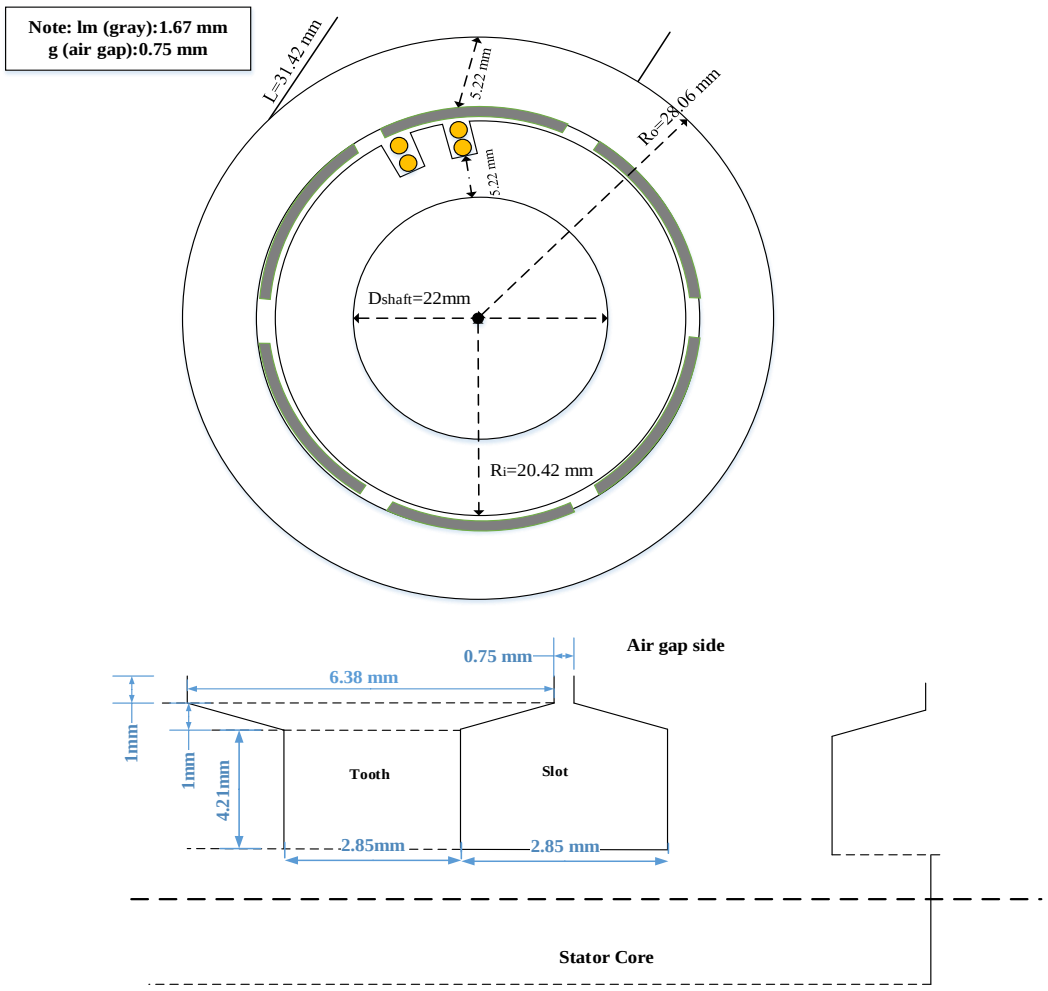

Figure 9.3 Representation of Designed Motor Dimensions

9.5. Design Results of Stepper Motor and Driver (Gimbal Structure)

AM 1524 V6 2-phase stepper Faulhaber motor with anti-backlash (zero-backlash) gearhead (15/8 series) is selected for gimbal motor in this study. The continuous output torque of stepper motor with spur gearheads (zero-backlash 15/8 series) is 0.1 Nm.

The AD-VM-M1 stepper motor driver is selected to control 2-phase stepper motor. Supply voltage of the driver is changed from 6V to 24V. The maximum current capability of the driver per phase is 0.5 A. It is compatible with the chosen step motor.

External gear ratio (14:1) is added to output of the step motor in order to increase equivalent torque of the gimbal structure.

Position measurement of gimbal structure is provided by potentiometer and hall effect. The exact positions of these sensors have not determined yet. It will be decided before manufacturing process.

9.6. Thermal Analysis Results

Thermal analysis of CMG is run at ANSYS workbench steady-state thermal analysis module. Thermal analysis of the designed CMG is performed for two different environmental conditions that are thermal vacuum chamber (TVAC) and clean room. Firstly, designed CMG is simulated in TVAC conditions and after that designed CMG is simulated in clean room conditions to verify main functions of CMG. The assumptions of the simulation model are listed below for these conditions.

- The operating temperature of CMG is between -20ºC and 55ºC. The qualification condition in TVAC is between -30ºC and 65ºC. Therefore, ambient temperature is taken 65ºC in the simulation model for TVAC conditions.
- The average temperature of clean room is 22ºC. Therefore, ambient temperature is taken 22ºC in the simulation model for clean room conditions.
- There is no convectional heat transfer for TVAC conditions due to vacuum. On the other hand, convectional heat transfer is valid for clean room conditions. Heat transfer coefficient of convectional method is taken $10 W/m^2$ in clean room for exterior surface of the model. (see Figure D.3 in Appendix D)
- Material types used in the simulation are listed in Appendix D Table D.2 as well as their isotropic thermal conductivity. Thermal conductance between each part is taken 2000. $W/m^2 \cdot °C$.

- The emissivity of the materials is taken 0.84 and it is equal to the emissivity of black painted materials. It is also noted that parts of the designed CMG are painted black to increase the radiation heat transfer rate.
- Transient effects are not considered in this simulation model.
- Heat loads are given as volumetric heat generation.

9.6.1. Thermal Analysis by Using The Same Bearings as Previous Actuator

Initially it is assumed that the same bearings, used in a similar satellite reaction wheel are used for the designed CMG. The main heat loads of the designed CMG are two bearings on the wheel and wheel BLDC motor. Steady-state loss of BLDC motor is calculated 9.93 W as mentioned in Table 9.2. The friction of two bearings is calculated 0.053 Nm at 10000 rpm (1047,2 rad/s) in Table 7.2. The total loss of these two bearings are expressed in Equation (9.1) and the loss of one bearing is calculated by using Equation (9.2).

$$P_{total\ bearing\ loss} = \omega_{wheel}\ \tau_{friction} = 1047{,}2\ x\ 0.053 = 55.5\ W \quad (9.1)$$

$$P_{one\ bearing\ loss} = \frac{55.5}{2} W = 27.75\ W \quad (9.2)$$

The summary of CMG heat loads is shown in Table 9.3.

Table 9.3 *Summary of CMG Heat Loads*

Part	**Heat Load**
Bearing 1	27.75 W
Bearing 2	27.75 W
BLDC Motor	9.93 W

Thermal analysis results of the designed CMG are shown in Figure 9.4 and Figure 9.5 for TVAC conditions and clean room conditions respectively.

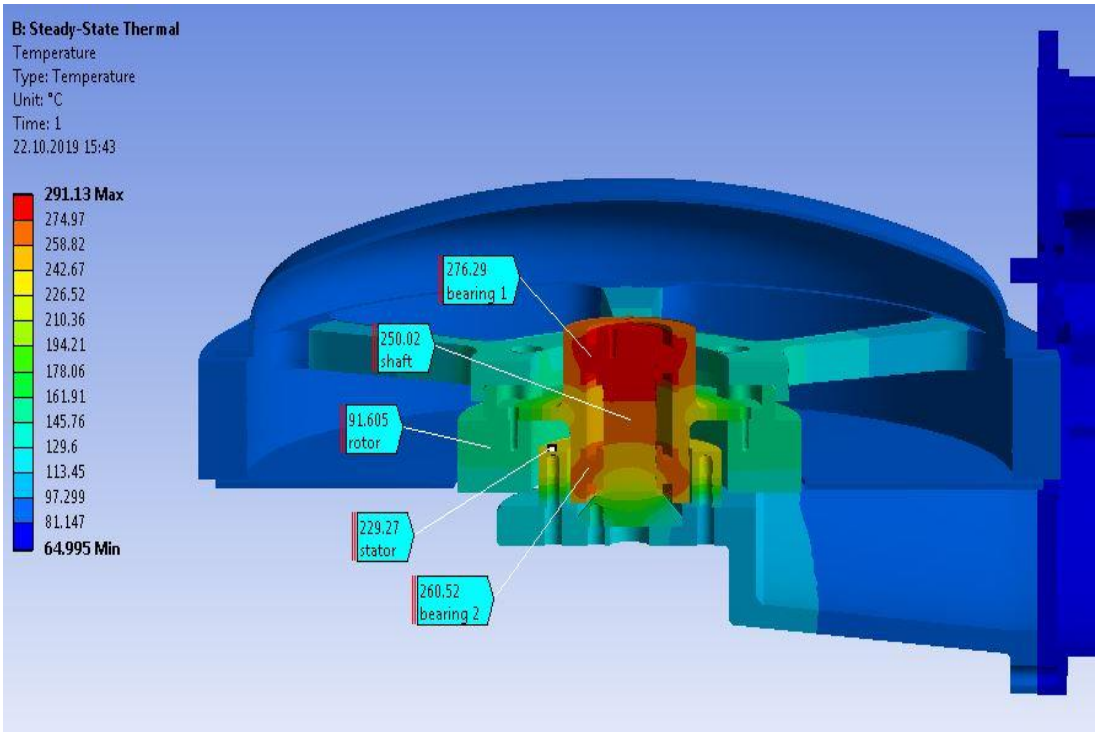

Figure 9.4 Thermal Analysis Results of CMG for TVAC Conditions

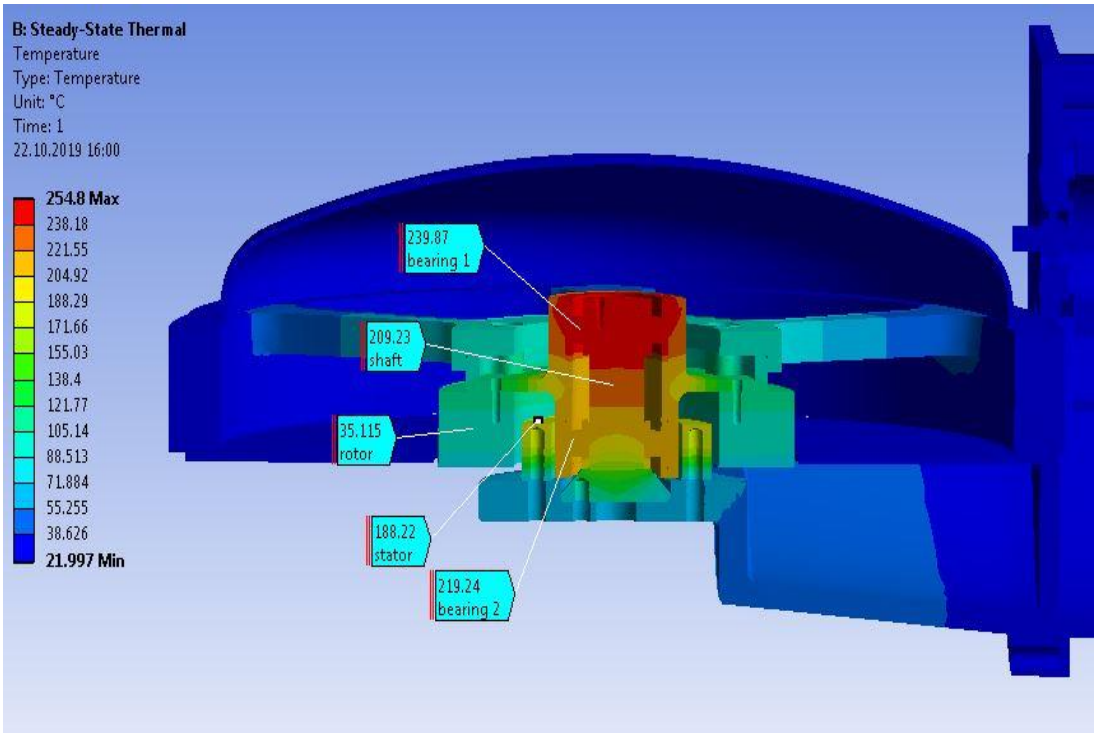

Figure 9.5 Thermal Analysis Results of CMG for Clean Room Conditions

9.6.2. Thermal Analysis by Using SKF 2200 ETN9 Bearings

Thermal analyses in Section 9.6.1 show that thermal performance of the designed CMG by using previous actuator bearings is not sufficient since all parts of the designed CMG is out of the temperature limits. Normally, previous actuator bearings are optimized for 4500 rpm, but they are operated at 10000 rpm in this study. Therefore, thermal analyses in Section 9.6.1 show that these bearings are not suitable at 10000 rpm. For these reasons, types of bearings which have lower friction commercially available are sought. It is found that SKF 2200 ETN9 [35] has low loss coefficient and it is suitable for the application here. This bearing is used in thermal analysis. The friction of one bearing is calculated 0.00891 Nm at 10000rpm by following steps of calculation given in [36]. The loss of the one bearing is calculated by using Equation (9.3).

$$P_{one\ bearing\ loss} = \omega_{wheel}\, \tau_{friction} = 1047{,}2\ x\ 0.00891 = 9.3\ W \qquad (9.3)$$

Summary of CMG heat loads with SKF 2200 ETN9 bearings is shown in Table 9.4.

Table 9.4 *Summary of CMG Heat Loads with SKF 2200 ETN9 Bearings*

Part	**Heat Load**
Bearing 1	9.3 W
Bearing 2	9.3 W
BLDC Motor	9.93 W

Thermal analysis results of the designed CMG with SKF 2200 ETN9 bearings are presented in Figure 9.6 and Figure 9.7 for TVAC conditions and clean room conditions respectively.

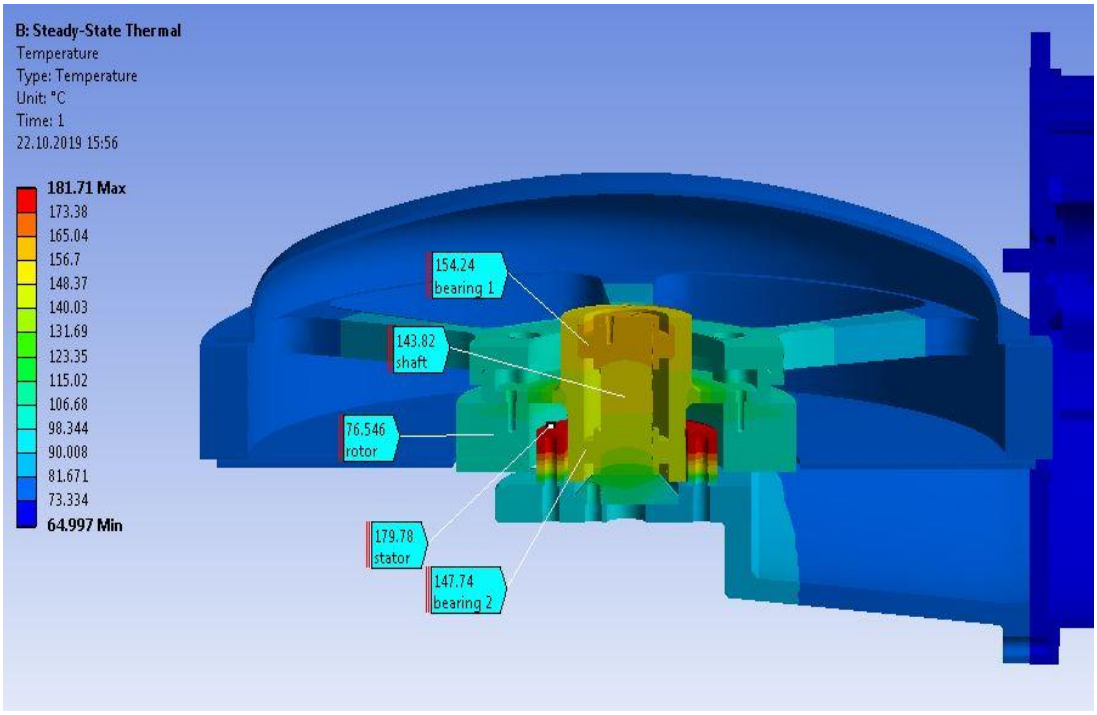

Figure 9.6 Thermal Analysis Results of CMG with SKF 2200 ETN9 Bearings for TVAC Conditions

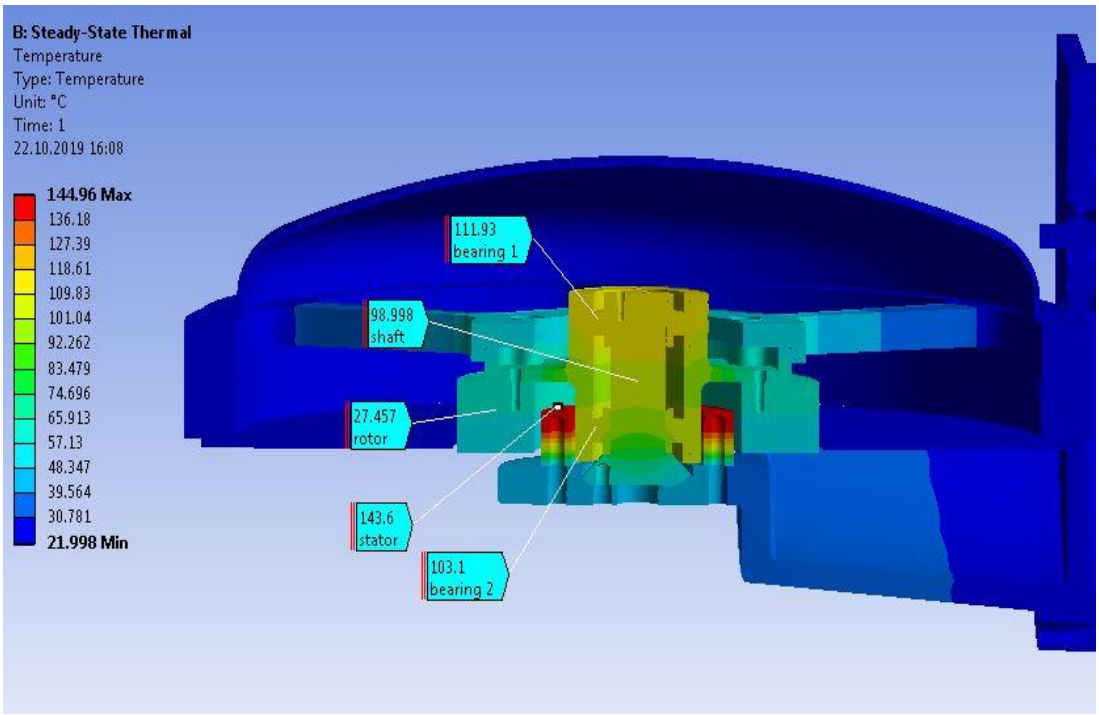

Figure 9.7 Thermal Analysis Results of CMG with SKF 2200 ETN9 Bearings for Clean Room Conditions

9.6.3. Summary and Discussion of Thermal Analysis

The summary of the thermal analysis results is shown in Table 9.5. The maximum temperature of bearings should be less than 120º C [35] and the maximum service temperature of the motor should be 230 º C as mentioned in Table 7.5 for this designed prototype model of CMG.

Table 9.5 *Summary of the Thermal Analysis Results*

Case	Bearing Type	Condition	Bearing 1 Temperature	Bearing 2 Temperature	Shaft Temperature	Motor Stator Temperature	Motor Rotor Temperature
1	Same with previous actuator	TVAC	276ºC	260ºC	250ºC	229ºC	91ºC
2		Clean Room	240ºC	219ºC	209ºC	188ºC	35ºC
3	SKF 2200 ETN9	TVAC	154ºC	148ºC	144ºC	180ºC	76ºC
4		Clean Room	112ºC	103ºC	99ºC	144ºC	27ºC

When the results in Table 9.5 are investigated, the following observations are made Bearing - 1 and bearing - 2 have the highest temperature in Case - 1 since the heat loads on bearings are dominant when they are compared with the stator of the motor in these cases. Therefore, since bearings and shaft contact each other and maximum temperature occurs in this area. In Case-1 i.e. in the vacuum chamber, both bearings are well above the allowable temperature limit. The stator temperature is also very high and exceeds even class C insulation temperature limit. In Case-2 i.e. in the clean room conditions, the bearing temperatures still remain high. The stator temperature also remains high, but it is within class C insulation temperature limit.

Case - 3 and Case - 4 present the temperatures of various parts of the designed CMG with lower loss bearings. Since motor stator loss is more dominant than bearing loss for this case, maximum temperature occurs on the stator of the motor in Case - 3 and Case – 4. Results in Table 9.5 show that temperatures of the parts are greatly reduced due to low friction loss on bearings. In Case-3 where CMG operates in vacuum, bearing temperatures appear to be above allowable limits. The motor temperature both on the stator and rotor are within class C insulation temperature limit. In Case-4 i.e. in the clean room conditions, both motor and the bearings remain within allowable

temperature limits. In other words, although the functions of designed CMG can be verified in the clean room conditions with SKF 2200 ETN9 bearings, this design is not acceptable for flight configuration.

The following conclusions are drawn from this evaluation; although motor and bearing temperatures are lower with the low friction bearings, they are still high. Therefore, new solutions to decrease the temperature need to be considered below.

- The first one is to use high precision space compatible “custom design“ bearings. Thanks to these bearings, the friction of bearings is decreased dramatically, and temperatures of the parts are also decreased. However, this type of bearing is not cost efficient.
- Secondly, bearing friction depends on the speed of the wheel. If the speed of the wheel is decreased, heat dissipation is also decreased but sufficient CMG output torque cannot be produced. In order to compensate output torque capacity, gimbal speed can be increased but this time it can cause the satellite instability during maneuvering. Therefore, trade-off between these factors should be optimized if the wheel speed is decreased.
- The third one is to change mechanical design of CMG. In this design, conduction heat transfer is not effective since the parts that have high temperature are far from the mounting base plate of the CMG. If the distance of these parts is made closer to base plate, conduction heat transfer can be more efficient, and the equilibrium temperature of these parts can be reduced.
- The last one is to apply the hermetic sealing to the wheel side (high temperature area). Hermetic sealing means that there is no air transfer between environment and inside of the equipment. Normally, there is no air in the space and convectional heat transfer is not valid. However, if some air (such as 0.1 atm) is enclosed inside the CMG before applying hermetic sealing, convectional heat transfer occurs inside the CMG. In other words, since wheel is rotated at 10000 rpm, heat transfer coefficient of convectional method can

be increased dramatically for enclosed area. Thus, there is no hot spot in the enclosed area and the heat is homogeneously distributed.

The results here indicate that the motor design can be made to operate within the required temperature levels by employing several measures in mechanical design of the CMG. This matter, however, is not the focus of this study.

9.7. CMG Design Results

The prototype model of the designed CMG is shown in .

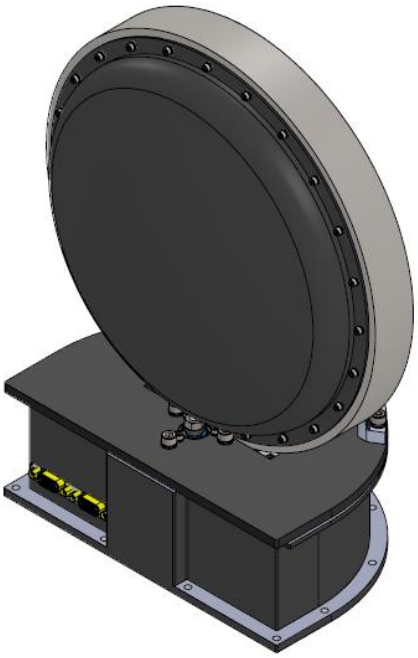

Figure 9.8 Prototype Model of the Designed CMG

Comparison of CMG design specifications determined in Section 5.3 and prototype CMG design results are shown in Table 9.6.

Table 9.6 *Comparison of Design Specification and Design Results*

Parameter	**Design Specification**	**Design Result**
Volume	< 35 cm x 35cm x 13cm ± 20%	33 cm x 26cm x 15.1cm
Mass	< 10 kg ± 20%	8.696 kg
Nominal Torque	> 1Nm	1.11 Nm
30 ° rotation in x- axis (Roll axis)	≤ 40 seconds	40 seconds
30 ° rotation in y-axis (Pitch axis)	≤30 seconds	30 seconds
60 ° rotation in x- axis (Roll axis)	≤ 60 seconds	60 seconds
60 ° rotation in y-axis (Pitch axis)	≤45 seconds	45 seconds
Maximum Gimbal Excursions	≤ 45°	45°
Wheel Required Time Reach to Maximum Speed (10000 rpm)	< 300 seconds ± 10%	300 seconds
Power Consumption	< 380 W	248.95 W
Operating Voltage	18V to 33 V	18V to 33 V
Operating Temperature	-20°C to 55°C	X (Not satisfied)

All design specifications are satisfied except for operating temperature. This thermal problem can be solved by methods that are listed in Section 9.6.3.

9.8. Conclusion

In this study, proof of concept CMG prototype model is studied in detail. Specifications of CMG for medium satellites are revealed and CMG is designed with respect to these specifications. Maneuvering calculations of the satellite on x and y axes are covered for four different maneuvering cases to determine the required CMG output torque capacity. Dynamic CMG equations are derived for pyramidal configuration in Section 2.3.2 and it is concluded that the output torque capacity of the one CMG depends on the angular momentum of the wheel, the speed of the gimbal, maximum gimbal angle excursion, and the skew angle of the pyramid.

The effect of the four different maximum gimbal angle excursions (45°, 60°, 75°, and 90°) is investigated in Section 5.5. It is shown that if the maximum gimbal angle

excursion is increased required inertia of the wheel is reduced. As a result, the mass and volume of the wheel and CMG could be decreased. However, increasing the gimbal angle causes oscillation on the satellite control algorithm due to the higher output ripple torque of CMG. Since stability and reliability are the primary concerns of the satellite system, the lowest angle (45°) is selected in this study.

Wheels that have different dimensions are designed in CHAPTER 6 for different gimbal angle excursions. The design aim of the wheel is to provide the required inertia to create CMG output torque. During the design procedure, the first constraint is to obtain the lowest mass and volume wheel in order to satisfy CMG design specifications and decrease the launch cost of the satellite. The second constraint is the yield stress limitation (215 MPa) of the wheel at 10000 rpm. The last constraint is that the safety factor of the wheel must be lower than 1.1 for unmanned spacecraft. As a result, the designed wheel in this study satisfies all design constraints and the results are shared in Table 9.1.

To drive the wheel of CMG, the outer rotor BLDC motors are shown to be advantageous in previous studies [7] and [8]. Therefore, an outer rotor BLDC motor is designed to drive the chosen wheel in CHAPTER 7. Magnetic loading of the designed motor is taken as about 0.43 T for air-gap and the maximum flux density for any part of the motor is limited to 1.4 T as in previous studies [7] and [8]. Electrical loading is taken as lower than 6000 A.t/m for acceleration and 3000 A.t/m for steady-state. The stack length of the motor is designed to be longer than 15 mm due to mechanical consideration. The designed outer rotor BLDC motor satisfies the design constraints mentioned above. Another constraint is that the mass of the outer rotor BLDC motor must be as low as possible. In conclusion, different motors are designed by changing RDL (ratio of inner diameter to length of the motor) and the most efficient motor in terms of mass and volume is selected in this study. The resulting motor data is presented in Table 9.2.

Step motor, step motor driver and gear system are selected for gimbal structure in CHAPTER 8. Space compatible step motor and step motor driver are chosen as commercial off-the-shelf (COTS) products. The most critical design constraint of the

gimbal structure is the required torque to drive the gimbal system. In order to provide enough torque (1.314 Nm), a step motor that has 0.1 Nm output torque is found and an external gear system is placed with a gear ratio of 14:1.

Thermal analysis of the designed CMG is performed for two different bearing types that are the same bearings used in the similar satellite actuator and SKF 2200 ETN9. The first bearing type is optimized for 4500 rpm. This bearing is used in this study at 10000 rpm and heat dissipation of this bearing is excessive at 10000rpm. For this reason, a new bearing SKF 2200 ETN9 bearing that has lower friction loss is sought. Temperatures of the CMG parts are greatly reduced by using SKF 2200 ETN9 bearings, but they are still not sufficient to satisfy thermal constraints especially for TVAC conditions. In order to decrease the temperature, new solutions such as using high precision space compatible custom design bearings, decreasing the wheel operating speed, changing the mechanical design and trapping some air in hermetic sealing are offered in Section 9.6.3. Thermal analysis results are shared in Section 9.6.

In conclusion, it is shown that the designed CMG with outer rotor BLDC motor satisfies all CMG design specifications. However, extra measures are found to be necessary to facilitate CMG to operate in the space environment. It is also shown that the designed CMG can be tested in clean room conditions to verify the working principle and output torque capacity of the prototype model CMG. Once, if the CMG performance is verified in clean room, further measures to improve the design for flight condition temperature range can be easily developed.

CMG is a trade restricted equipment between the countries because of the International Traffic in Arms Regulations. In Turkey, a project that develops a reaction wheel is still in progress. However, there is no study or project to develop a CMG for space applications. It can be said that proof of concept CMG prototype model in this study can be the first step to develop CMG for medium satellite space applications in Turkey.

Designed CMG has almost the same mass and the same volume when it is compared with the reaction wheel placed in the previous medium satellite, but the output torque

of the designed CMG is four times higher than the reaction wheel. This advantage is very critical for space applications.

Comparison of the reaction wheel and the designed prototype CMG are shown in Table 9.7 in terms of mass/ torque and mass/volume.

Table 9.7 *Comparison of Reaction Wheel and Designed CMG*

Parameter	**Reaction Wheel**	**Designed CMG**
Output Torque	0.26 Nm	1.11 Nm
Mass	10 kg	8.696 kg
Volume	35 cm x 35cm x 13cm (including electronics)	33cm x 26cm x15.1cm (including electronics)
Torque/ Mass	0.026 Nm/kg	0.128 Nm/kg
Torque/ Volume	16.32 Nm/m^3	85.68 Nm/m^3

9.9. Future Work

CMG model studied in this thesis is a proof of concept prototype model. There are two open items in this model:

- The exact positions of positions sensors in the gimbal structure needs to be determined before the manufacturing process.
- The designed CMG must be reviewed in terms of thermal design to reduce operating temperature within acceptable limits for TVAC conditions.

The mechanical structure of the prototype model also needs to be reviewed in order to further decrease the weight of the CMG. Mechanical parts can be chosen lower density materials if they are compatible with space applications.

Methods for increasing torque/mass ratio can be also investigated. If the speed of gimbal is increased, CMG can have higher output torque since the output torque equation of CMG directly depends on the gimbal speed. Therefore, the effect of choosing high speed gimbal angle on satellite control algorithm should be studied in detail.

The required inertia is provided by the wheel in CMG. The designed wheel provides sufficient inertia to the system but wheel design is not totally optimized in terms of

inertia/mass and inertia/volume of the wheel in this thesis. Therefore, a better wheel design should be studied by comparing and analyzing different wheel geometries.

The prototype model will be built to verify the main functions of CMG. The manufacturing cost of the prototype CMG will be afforded by TUBITAK UZAY. Functional tests of CMG will be performed in TUBITAK UZAY clean room. During test activities, torque capability of CMG, thermal condition of CMG, electrical interfaces and motor driver evaluation board will be verified and compared with the conceptual design results.

A project proposal was submitted to the ministry of development to design the qualification model of CMG. The cost of the qualification model is expected to be very high when it is compared with the prototype model due to using space-qualified materials. If the project proposal is accepted, the following items will be taken into account for the qualification model of CMG.

- All components and materials will be compatible with space environment conditions.
- In the prototype model, motor driver for BLDC motor is chosen as STEVAL-SPIN3202 evaluation board. However, it is not compatible with space conditions. Used material in this evaluation board is not radiation-hardened. Therefore, motor driver circuit that has redundancy circuits and radiation-hardened electronic components will be designed and tested. In addition, driver software algorithm will be developed, and it will be compatible with the satellite control unit.
- Qualification tests (functional tests, mechanical tests, thermal vacuum tests, and EMI/EMC test) will be performed. 24 cycles will be performed in the thermal vacuum test. Mechanical tests that needs to be done include sine vibration tests, random vibration tests, and shock tests. The aim of the mechanical tests is to confirm functions of the designed CMG that there is no hazardous condition under launch configuration. EMI/EMC tests will be performed for the qualification model to verify CMG performance under noisy

conditions. The test sequence for the qualification model of CMG is shown in Figure 9.9.

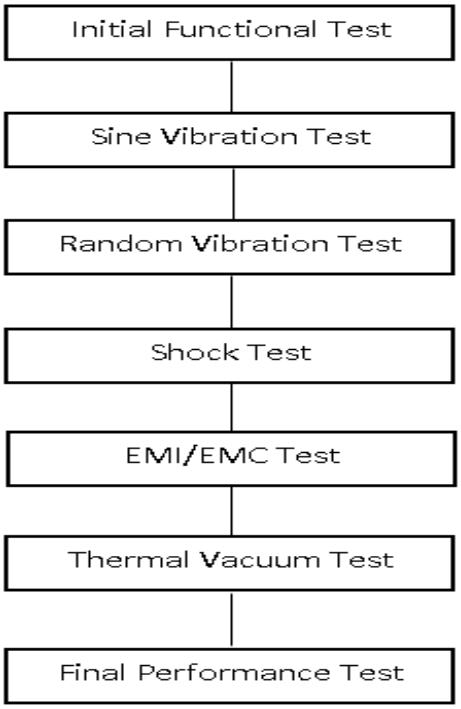

Figure 9.9 Test Sequence for Qualification Model

REFERENCES

[1] B. Wie, D. Bailey, and C. Heiberg, "Rapid Multitarget Acquisition and Pointing Control of Agile Spacecraft," *J. Guid. Control. Dyn.*, vol. 25, no. 1, pp. 96–104, 2008.

[2] V. J. Lappas, "Control Techniques for Aerospace Systems," 2003.

[3] V. J. Lappas, "CMG Based AOCS for Agile Small Satellites," *Univ. Surrey*, no. October, 2002.

[4] V. Nagabhusan, "Development of Control Moment Gyroscopes for Attitude Control of Small Satellites," Master's Thesis, University of Florida, 2009.

[5] R. Votel and D. Sinclair, "Comparison of Control Moment Gyros and Reaction Wheels for Small Earth-Observing Satellites," *26th Annual AIAA/USU Conference on Small Satellite*. 26th Annual AIAA/USU Conference on Small Satellite, pp. 1–7, 2012.

[6] J. Ahmed and D. S. Bernstein, "Adaptive Control of Double-Gimbal Control-Moment Gyro with Unbalanced Rotor," *J. Guid. Control. Dyn.*, vol. 25, no. 1, pp. 105–115, 2008.

[7] K. Yılmaz, "Comparison of Axial Flux and Radial Flux Brushless DC Motor Topologies for Control Moment Gyroscope Wheel," Master's Thesis, Middle East Technical University, 2009.

[8] N. Çağan, "Design of An Outer-Rotor Brushless DC Motor for Control Moment Gyroscope Applications," Master's Thesis, Middle East Technical University, 2015.

[9] E. Yavuzoğlu, "Steering Laws for Control Moment Gyroscope Systems Used in Spacecrafts Attitude Control," Master's Thesis, Middle East Technical University, 2003.

[10] D. G. Gilmore, *Spacecraft Thermal Control Handbook Volume I: Fundamental Technologie*, 2nd ed. 2002.

[11] R. Berner, "Control Moment Gyro Actuator for Small Satellite Applications," Master's Thesis, University of Stellenbosch, 2005.

[12] J. A. Paradiso, "Global steering of single gimballed control moment gyroscopes using a directed search," *J. Guid. Control. Dyn.*, vol. 15, no. 5, pp. 1236–1244, 2008.

[13] C. J. Heiberg, D. Bailey, and B. Wie, "Precision Spacecraft Pointing Using Single-Gimbal Control Moment Gyroscopes with Disturbance," *J. Guid.*

Control. Dyn., vol. 23, no. 1, pp. 77–85, 2008.

[14] C. J. E. Keesee, “Spacecraft Thermal Control Systems,” pp. 1–40.

[15] NewSpace Systems, “10Nms Reaction Wheel.” datasheet.

[16] Airbus Defense & Space, “CMG 15-45S A Compact, Cost-Effective, High Performance Control Momentum Gyroscope Solution for Small Satellites.” datasheet, 2014.

[17] S. Czernik, “Design of the Thermal Control System for Compass-1,” Diploma Thesis, University of Applied Sciences Aachen Germany, 2004.

[18] L. Klobu and I. Tiselj, “Thermal Radiation Heat Transfer Between Surfaces,” 2016.

[19] A. Promoteur and G. Facult, “Thermal Design of the OUFTI-Next mission,” University of LiègeMaster’s Thesis, Faculty of Applied Sciences Centre Spatial de Liège, 2018.

[20] Philippe Poinas, “Satellite Thermal Control Engineering.” ESA, prepared for SME 2004, pp. 1–66, 2004.

[21] R. N. Miyake, “Spacecraft Design Thermal Control Subsystem,” no. January, 2003.

[22] L. Jacques, “Spacecraft Thermal Control,” Liege Universite, 2017.

[23] N. Baker, “Feasibility and Design of Miniaturized Control Moment Gyroscope for A 3-Axis Stabilized Micro Satellite,” Master’s Thesis, Luleå University of Technology, 2016.

[24] D. F. da Silva, I. Muraoka, and E. C. Garcia, “Thermal Control Design Conception of The Amazonia-1 Satellite,” 2014.

[25] A. Ketsdever, “Structures and Thermal Control,” Lecture Notes MAE 5595 Lesson 12 University of Colorado, 2008.

[26] A. M. C. Garza, “Reaction Wheels for Picosatellites,” Master’s Thesis, Lulea University of Technology, 2009.

[27] Glemco Inc, “AISI Type 304 Stainless Steel.” datasheet, 2010.

[28] European Cooperation for Space Standardization, “Space Engineering Structural Factors of Safety for Spaceflight Hardware, ECSS-E-ST-32-10C Rev.1.” 2009.

[29] EMFFORCE OPS MANUAL Space Systems Product Development, “E Reaction Wheel Design (LW, WF),” *Massachusetts Institute of Technology , Dept of Aeronautics and Astronautics*, 2003. [Online]. Available: https://ocw.mit.edu/courses/aeronautics-and-astronautics/16-83x-space-

systems-engineering-spring-2002-spring-2003/projects/design_final_e.pdf. [Accessed: 15-Jul-2019].

[30] T. J. E. Miller, *Brushless Permanent-Magnet and Reluctance Motor Drives Oxford Sciene Publications*. 1989.

[31] STMicroelectronics, "STSPIN32F0A advanced 3-phase BLDC driver with embedded STM32 MCU single shunt evaluation board," *databrief*, 2017. [Online]. Available: https://www.st.com/resource/en/data_brief/steval-spin3202.pdf. [Accessed: 02-Aug-2019].

[32] STMicroelectronics, "STD140N6F7 N-channel 60 V, 3.1 mΩ typ., 80 A STripFET F7 Power MOSFET in a DPAK Package, datasheet," 2019. [Online]. Available: https://www.st.com/resource/en/datasheet/std140n6f7.pdf. [Accessed: 03-Aug-2019].

[33] STMicroeletronics, "STSPIN32F0 - Advanced BLDC controller with embedded STM32 MCU, datasheet," 2017. [Online]. Available: https://www.st.com/resource/en/datasheet/stspin32f0.pdf. [Accessed: 03-Aug-2019].

[34] ARSAPE, "Constant Voltage Step Motor Driver User Manual," 2005. [Online]. Available: http://www.microprivod.ru/files/IM/AD_VL.pdf. [Accessed: 05-Aug-2019].

[35] SKF, "Self-Aligning Ball Bearings 2200 ETN9." [Online]. Available: https://www.skf.com/in/products/bearings-units-housings/ball-bearings/self-alg-ball. [Accessed: 21-Oct-2019].

[36] SKF, "The SKF model for calculating the frictional moment," *Skf*, 2017. [Online]. Available: https://www.skf.com/binary/21-299767/0901d1968065e9e7-The-SKF-model-for-calculating-the-frictional-movement_tcm_12-299767.pdf. [Accessed: 21-Oct-2019].

APPENDICES

A. Stepper Motor and Stepper Motor Gearhead

FAULHABER

Stepper Motors 6,0 mNm

Two phase, 24 steps per revolution
PRECIstep® Technology

Series AM1524

	AM1524 ...	0450		0250		0150		0075		
		Current	Voltage	Current	Voltage	Current	Voltage	Current	Voltage	Drive mode
1	Nominal current per phase (both phases ON) [1]	0,45	–	0,25	–	0,15	–	0,075	–	A
2	Nominal voltage per phase (both phases ON) [1]	–	2	–	3,5	–	6	–	12	V DC
3	Phase resistance (at 20°C)	3,6		12,5		35		138		Ω
4	Phase inductance (1kHz)	1,9		6,3		16,5		70,6		mH
5	Back-EMF amplitude	2,4		4,4		7,2		14,7		V/k step/s
6	Holding torque (at nominal current in both phases)	6,0								mNm
7	Holding torque (at twice the nominal current)	10								mNm
8	Step angle (full step)	15								degree
9	Angular accuracy [1]	± 10								% of full step
10	Residual torque, max.	0,9								mNm
11	Rotor inertia	45								$\cdot 10^{-9}$ kgm²
12	Resonance frequency (at no load)	120								Hz
13	Electrical time constant	0,5								ms
14	Ambient temperature range	–35 ... +70								°C
15	Winding temperature tolerated, max.	130								°C
16	Thermal resistance R_{th1} / R_{th2}	12,9 / 31,6								°C/W
17	Thermal time constant τ_{w1} / τ_{w2}	6 / 350								s
18	Shaft bearings	sintered sleeve bearings (standard)				ball bearings, preloaded (optional)				
19	Shaft load, max.:									
	– radial (3 mm from bearing)	0,5				6,0				N
	– axial	0,5				2,0				N
20	Shaft play, max.:									
	– radial (0,2N)	15				12				µm
	– axial (0,2N)	150				~0				µm
21	Mass	12								g

[1] Relevant for 2 phases ON only. On PWM drivers or chopper (current mode), the current is set to the nominal value and the supply voltage is typically 3 to 5x higher than the nominal voltage.
[2] Curves measured with a load inertia of 50 $\cdot 10^{-9}$ kgm², in half-step mode for the "1 x nominal voltage" curve, in 1/4 micro-stepping mode for the other curves.

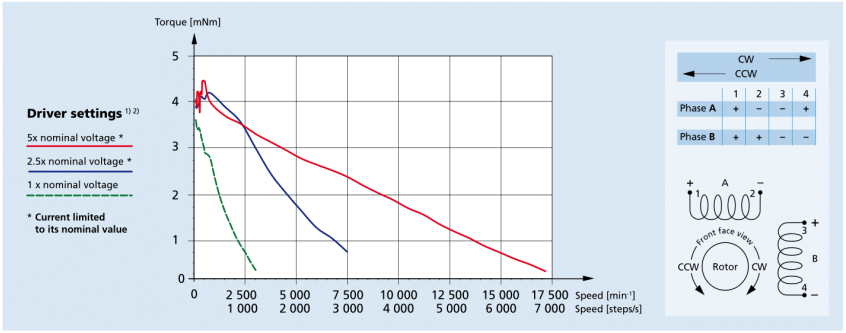

For notes on technical data and lifetime performance refer to "Technical Information".
Edition 2019

Dimensional drawing

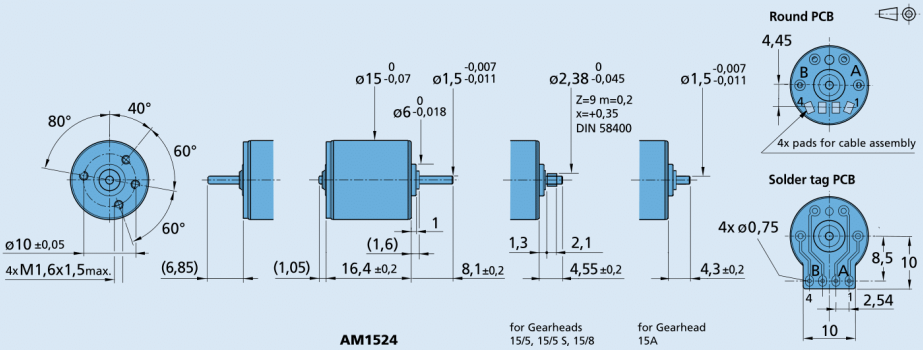

Combinations

Drive Electronics	Encoders	Cables	Gearheads / Lead screws
MCST3601	Available on request	List available on request	**15A**
			15/5(S)
			15/8*
			15/10
			16/7
			17/1
			Lead screws **M2 - M3**

* Zero Backlash Gearheads

Ordering information

Example: **AM15242R015057**

Motor type AM = Motor design 15 = Motor diameter (mm) 24 = Steps per revolution	Bearings Special lubricant options available	Winding	Motor execution Only front output shaft		With double output shaft		Front output shaft
AM1524	**SB** (sleeve bearings)	**0150**	**55**	(Round PCB)	**54**	(Round PCB)	Plain shaft, L=8,1 mm for 15/10,16/7, 17/1, M3
	2R (2 ball bearings)	**0075**	**57**	(Round PCB)	**56**	(Round PCB)	Pinion 15/5(S), 15/8
	RC (2 ball bearings,	**0250**	**70**	(Round PCB)	**71**	(Round PCB)	Plain shaft, L=4,3 mm for gearhead 15A
	vacuum/low temp.)	**0450**	**83**	(Round PCB)	**82**	(Round PCB)	Plain shaft for lead screw M2
			05	(Solder tag PCB)	**04**	(Solder tag PCB)	Plain shaft, L=8,1 mm for 15/10,16/7, 17/1, M3
			07	(Solder tag PCB)	**06**	(Solder tag PCB)	Pinion 15/5(S), 15/8
			72	(Solder tag PCB)	**73**	(Solder tag PCB)	Plain shaft, L=4,3 mm for gearhead 15A
			23	(Solder tag PCB)	**22**	(Solder tag PCB)	Plain shaft for lead screw M2
					94		Idem -04 & for encoder
					96		Idem -06 & for encoder
					97		Idem -73 & for encoder

Spur Gearheads

Zero Backlash

0,1 Nm

For combination with
DC-Micromotors
Stepper Motors

Series 15/8

	15/8
Housing material	metal
Geartrain material	steel
Recommended max. input speed for:	
– continuous operation	5 000 min⁻¹
Backlash, at no-load	0 °
Bearings on output shaft	ball bearings, preloaded
Shaft load, max.:	
– radial (6,5 mm from mounting face)	≤ 25 N
– axial	≤ 5 N
Shaft press fit force, max.	≤ 5 N
Shaft play	
– radial (6,5 mm from mounting face)	≤ 0,03 mm
– axial	= 0 mm
Operating temperature range	- 30 ... + 100 °C

Technical data							
Number of gear stages		4	4	5	5	6	6
Continuous torque	mNm	100	100	100	100	100	100
Intermittent torque	mNm	300	150	300	150	300	150
Mass without motor, ca.	g	24	24	26	26	28	28
Efficiency, max.		-	-	-	-	-	-
Direction of rotation, drive to output		=	=	≠	≠	=	=
Reduction ratio [1] (rounded)		**76:1**	**141:1**	**262:1**	**485:1**	**900:1**	**1 670:1**
L2 [mm] = length without motor		32,0	32,0	34,1	34,1	36,2	36,2
L1 [mm] = length with motor	1516E...SR	34,9	34,9	37,0	37,0	39,1	39,1
	1524E...SR	42,9	42,9	45,0	45,0	47,1	47,1
	AM1524...57	35,5	35,5	37,6	37,6	39,7	39,7

[1] The reduction ratios are rounded, the exact values are available on request or at www.faulhaber.com.

Note: These gearheads are available only with motors mounted.

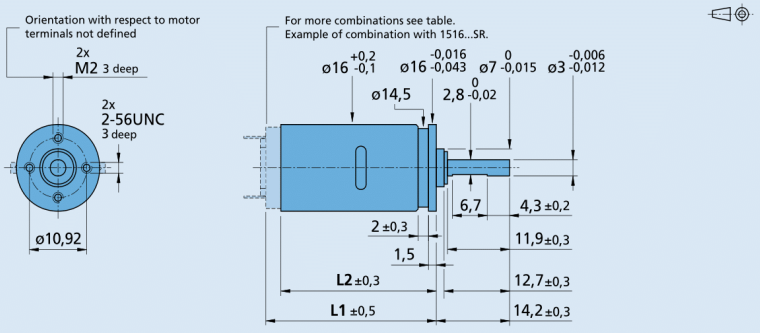

15/8

For notes on technical data and lifetime performance refer to "Technical Information".

Edition 2019

www.faulhaber.com

B. CMG Mechanical Drawings

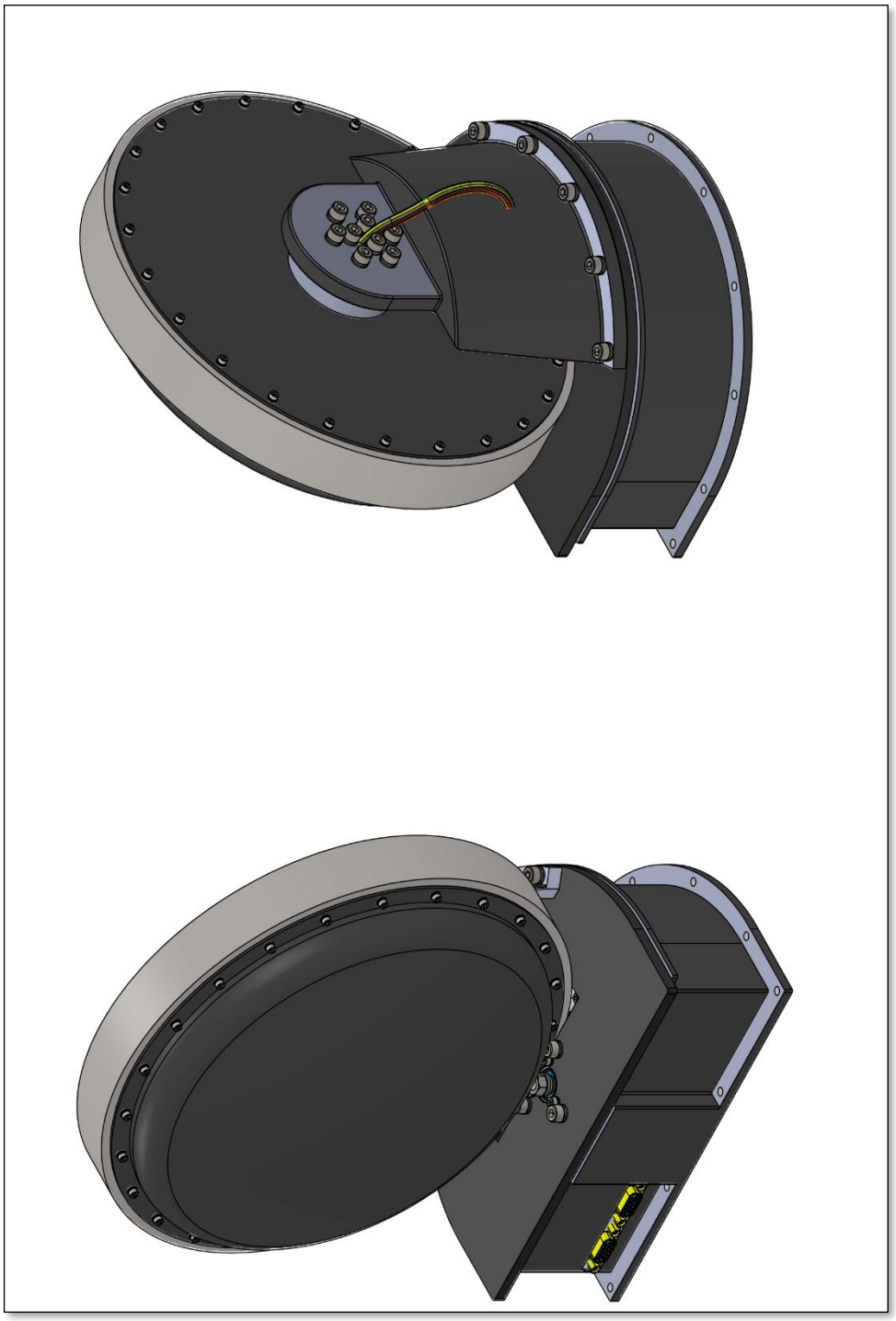

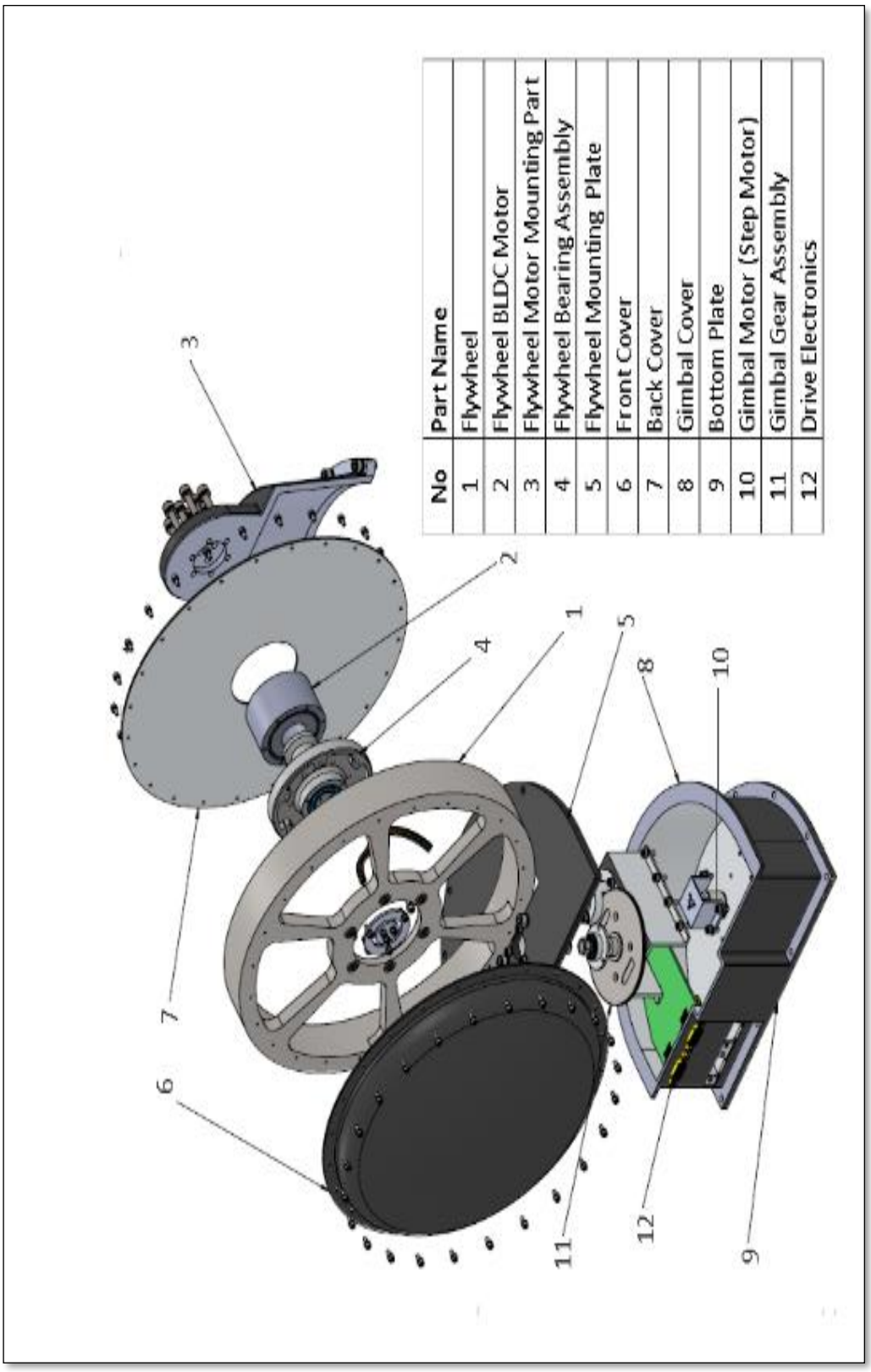

No	Part Name
1	Flywheel
2	Flywheel BLDC Motor
3	Flywheel Motor Mounting Part
4	Flywheel Bearing Assembly
5	Flywheel Mounting Plate
6	Front Cover
7	Back Cover
8	Gimbal Cover
9	Bottom Plate
10	Gimbal Motor (Step Motor)
11	Gimbal Gear Assembly
12	Drive Electronics

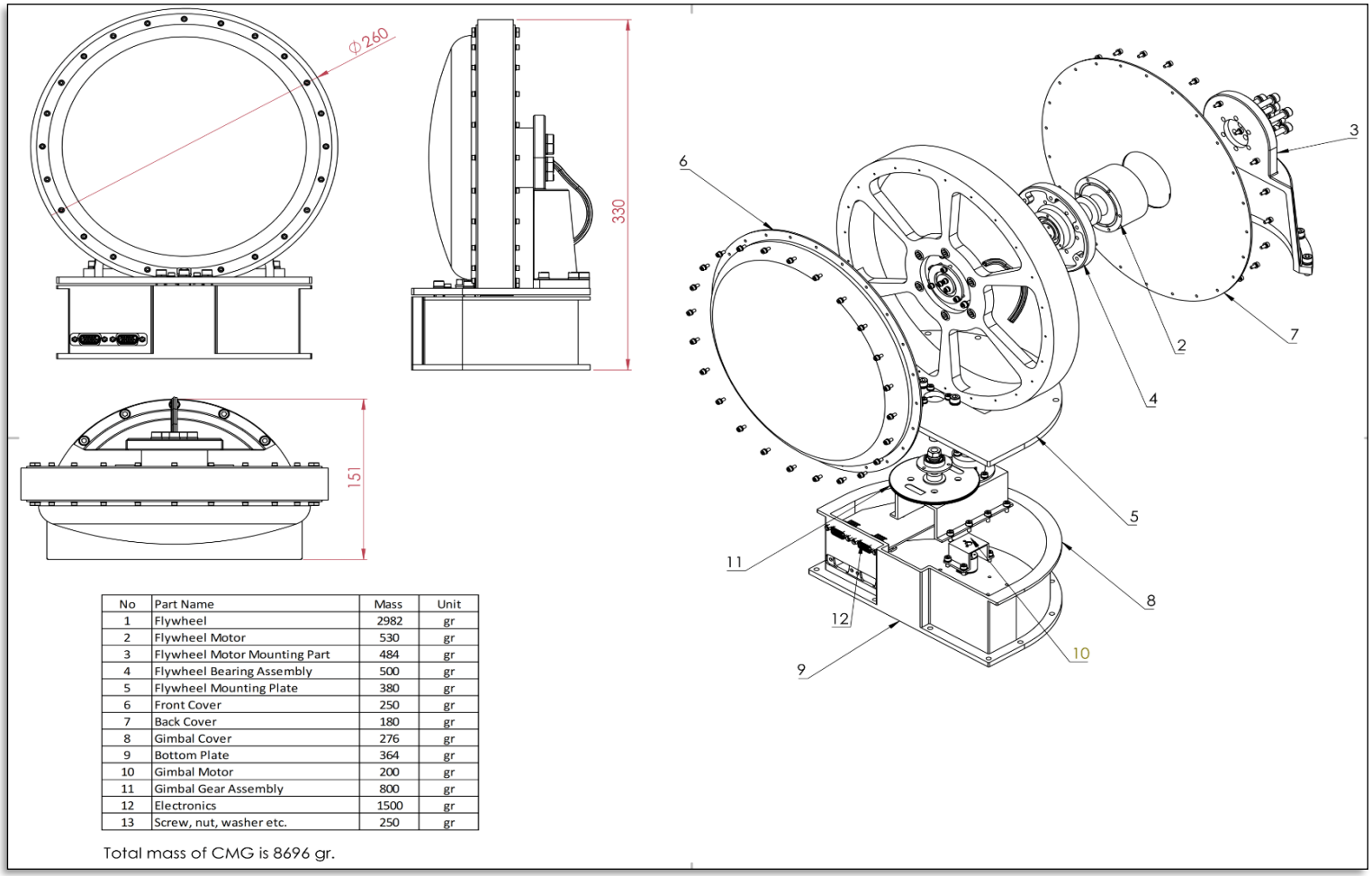

No	Part Name	Mass	Unit
1	Flywheel	2982	gr
2	Flywheel Motor	530	gr
3	Flywheel Motor Mounting Part	484	gr
4	Flywheel Bearing Assembly	500	gr
5	Flywheel Mounting Plate	380	gr
6	Front Cover	250	gr
7	Back Cover	180	gr
8	Gimbal Cover	276	gr
9	Bottom Plate	364	gr
10	Gimbal Motor	200	gr
11	Gimbal Gear Assembly	800	gr
12	Electronics	1500	gr
13	Screw, nut, washer etc.	250	gr

Total mass of CMG is 8696 gr.

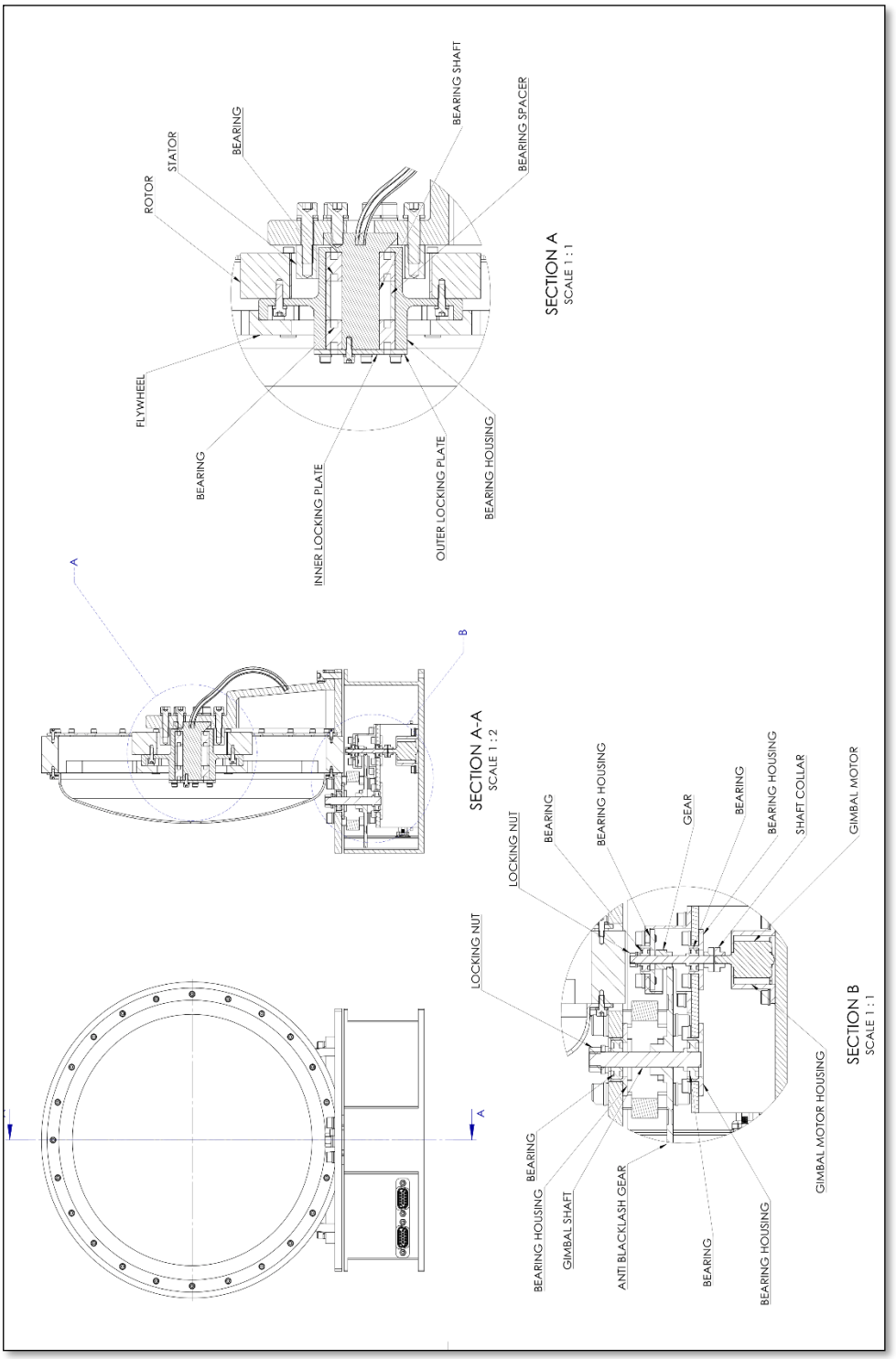
ROTOR
STATOR
BEARING
BEARING SHAFT
BEARING SPACER
FLYWHEEL
BEARING
INNER LOCKING PLATE
OUTER LOCKING PLATE
BEARING HOUSING
SECTION A
SCALE 1 : 1
A
B
SECTION A-A
SCALE 1 : 2
LOCKING NUT
BEARING
BEARING HOUSING
GEAR
BEARING
BEARING HOUSING
SHAFT COLLAR
GIMBAL MOTOR
LOCKING NUT
BEARING
BEARING HOUSING
GIMBAL SHAFT
ANTI BLACKLASH GEAR
BEARING
BEARING HOUSING
GIMBAL MOTOR HOUSING
SECTION B
SCALE 1 : 1

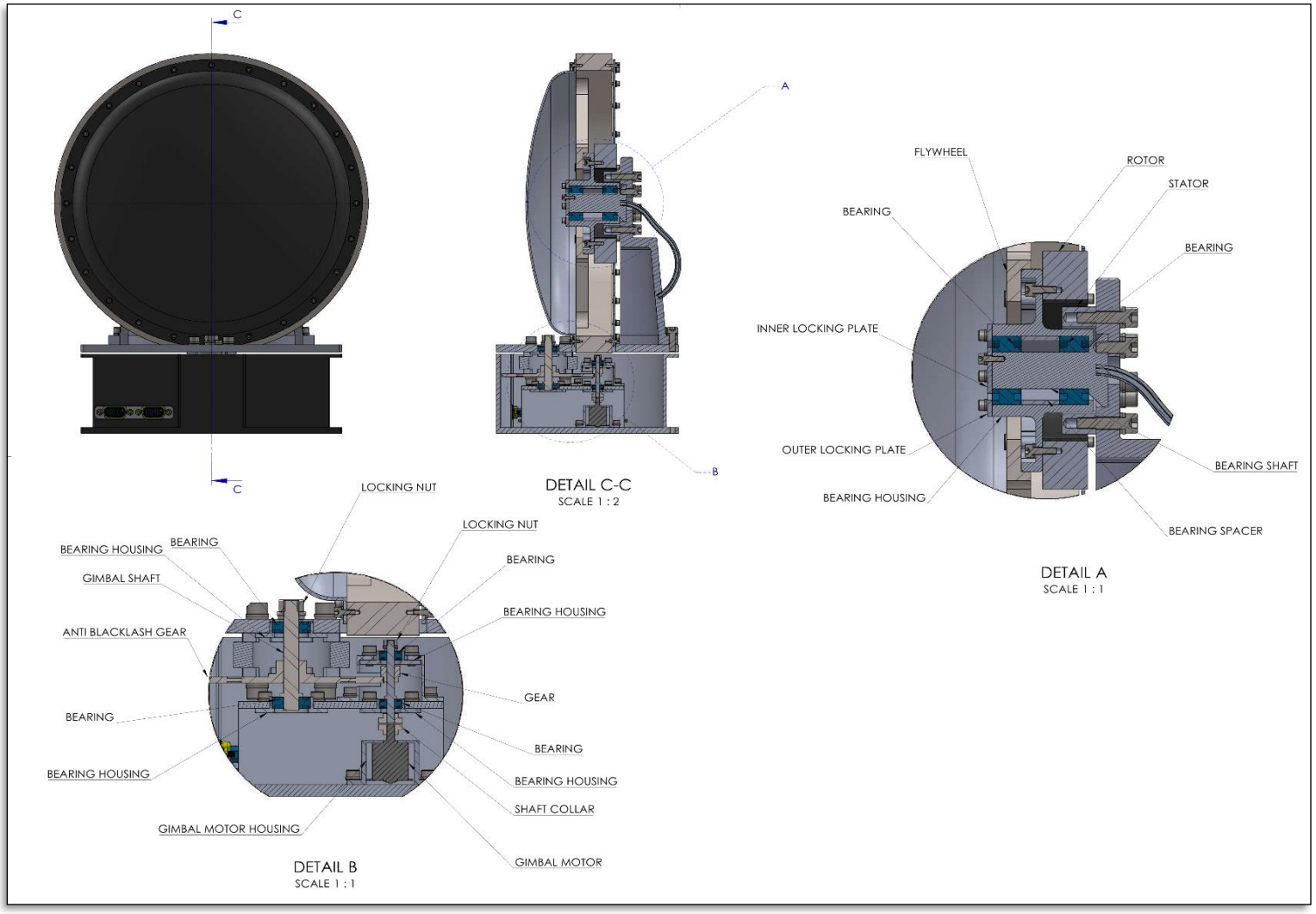
C
C
A
B
DETAIL C-C
SCALE 1 : 2
FLYWHEEL
ROTOR
STATOR
BEARING
BEARING
INNER LOCKING PLATE
OUTER LOCKING PLATE
BEARING SHAFT
BEARING HOUSING
BEARING SPACER
DETAIL A
SCALE 1 : 1
LOCKING NUT
LOCKING NUT
BEARING HOUSING
BEARING
BEARING
GIMBAL SHAFT
BEARING HOUSING
ANTI BLACKLASH GEAR
GEAR
BEARING
BEARING
BEARING HOUSING
BEARING HOUSING
SHAFT COLLAR
GIMBAL MOTOR HOUSING
GIMBAL MOTOR
DETAIL B
SCALE 1 : 1

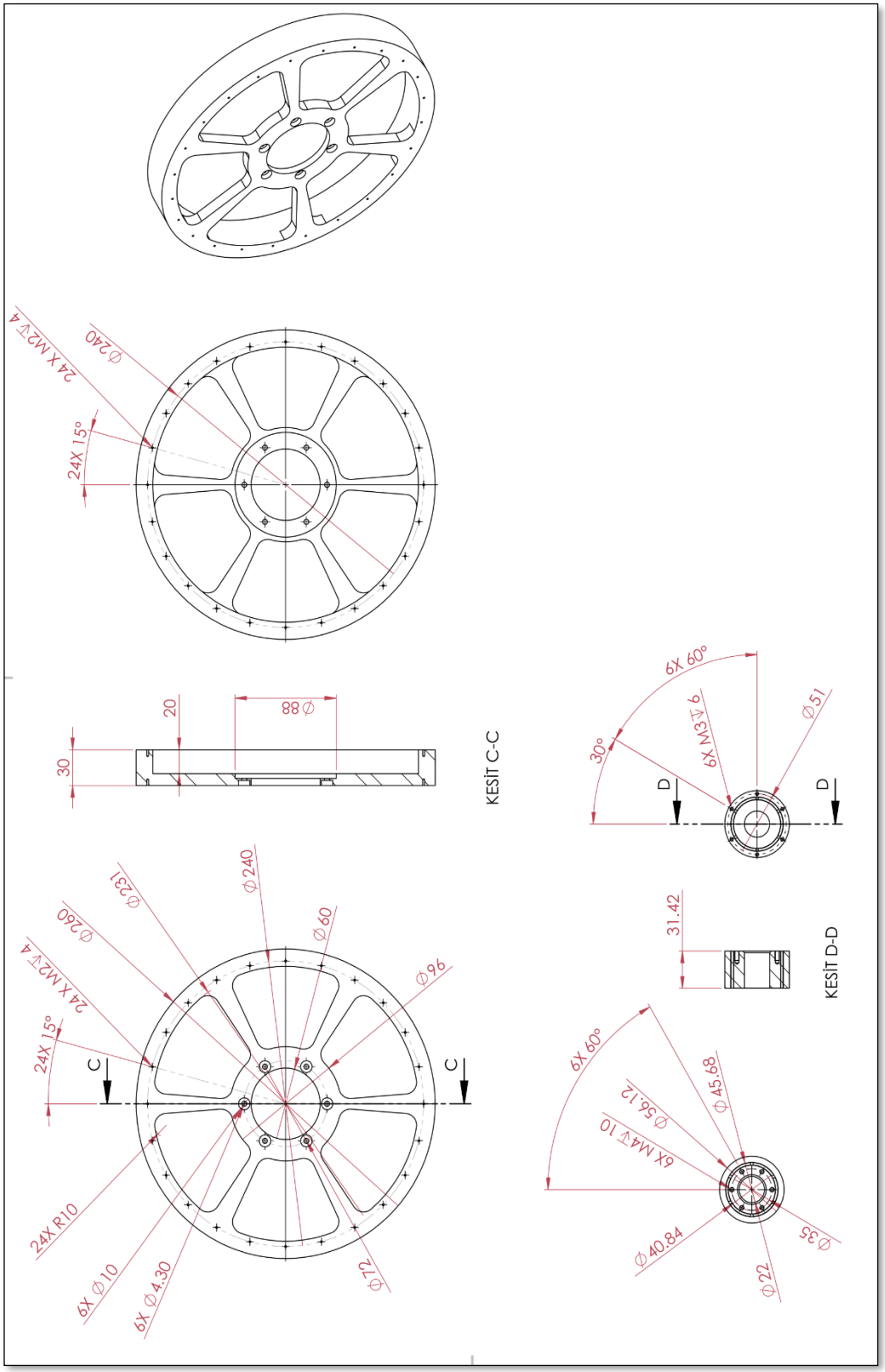
24 X M2▽4
Ø240
24X 15°
20
Ø88
30
KESİT C-C
6X 60°
30°
6X M3▽6
Ø51
D
D
31.42
KESİT D-D
Ø231
Ø240
Ø260
Ø60
Ø96
24 X M2▽4
24X 15°
C
C
24X R10
6X Ø10
6X Ø4.30
Ø72
6X 60°
Ø45.68
Ø56.12
6X M4▽10
Ø40.84
Ø35
Ø22

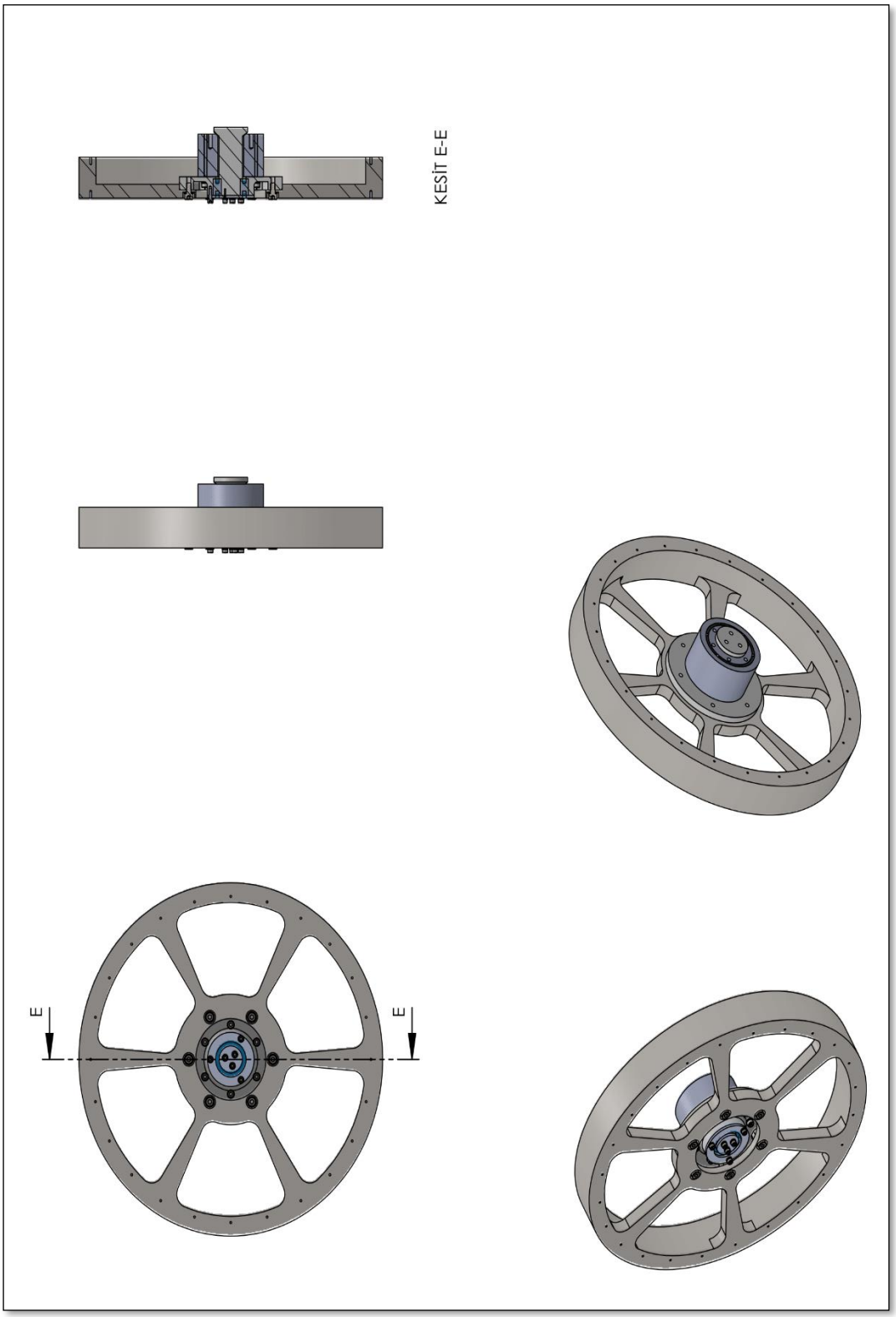
KESİT E-E
E
E

C. Investigation and Discussion of Different Pole Number BLDC Motors

2-pole and 6-pole outer rotor BLDC motors are designed for different RDL values in this CMG application based on previous studies. 6 - pole motor (RDL=1.3) is selected for 45° gimbal angle due to mass, volume and manufacturing constraints mentioned in Section 7.3.10.5. In this part, 4 - pole, 8 - pole, 10 - pole and 12 - pole outer rotor BLDC motors are also investigated for 45° gimbal angle and performance of different pole number motors are compared and discussed in terms of efficiency and losses for same required motor torque mentioned in Section 7.1. 4 - pole and 8 - pole motor results are shown in Table C.1 and 10 - pole and 12 - pole motor results are shown in Table C.2.

Table C.1 *4-Pole and 8-Pole Outer Rotor BLDC Motor Design Results*

Parameter	4-pole square wave excited motor						8-pole square wave excited motor					
	Value						Value					
RDL	0,7	1	1,3	3	10	20	0,7	1	1,3	3	10	20
Di (mm)	42,01	43,77	45,28	51,36	64,01	73,74	35,61	37,59	39,24	45,66	58,47	68,13
L (mm)	60,02	43,77	34,83	17,12	6,40	3,69	50,87	37,59	30,19	15,22	5,85	3,41
g (mm)	0,75	0,75	0,75	0,75	0,75	0,75	0,75	0,75	0,75	0,75	0,75	0,75
Do (mm)	62,66	65,14	67,26	75,90	94,46	110,33	47,41	49,82	51,83	59,76	76,48	91,66
hs (mm)	1,96	2,50	2,97	4,84	8,75	11,75	3,39	4,20	4,86	7,46	12,64	16,54
lm (mm)	1,53	1,55	1,57	1,68	2,22	3,42	1,74	1,76	1,79	1,93	2,66	4,49
h1 (mm)	1,00	1,00	1,00	1,00	1,00	1,00	1,00	1,00	1,00	1,00	1,00	1,00
h2 (mm)	1,00	1,00	1,00	1,00	1,00	1,00	1,00	1,00	1,00	1,00	1,00	1,00
w1 (mm)	0,75	0,75	0,75	0,75	0,75	0,75	0,75	0,75	0,75	0,75	0,75	0,75
w2 (mm)	3,15	3,25	3,34	3,71	4,47	5,06	2,46	2,57	2,65	2,98	3,65	4,15
hsbc (mm)	8,05	8,38	8,67	9,83	12,26	14,12	3,41	3,60	3,76	4,37	5,60	6,52
t1 (mm)	6,58	6,89	7,15	8,21	10,42	12,12	5,46	5,81	6,10	7,22	9,46	11,14
t2 (mm)	3,15	3,25	3,34	3,71	4,47	5,06	2,46	2,57	2,65	2,98	3,65	4,15
J (g.m2)	0,48	0,41	0,37	0,30	0,27	0,28	0,09	0,08	0,08	0,07	0,07	0,08
V (cm3)	185	146	124	77	45	35	90	73	64	43	27	22
Mtotal (kg)	1,27	1,00	0,85	0,53	0,30	0,24	0,65	0,53	0,46	0,30	0,19	0,18
Rph (mOhm)	30,92	39,88	26,97	24,18	32,73	40,45	40,68	23,88	29,07	21,20	25,28	25,99
Lph (uH)	11,62	19,78	16,24	25,19	60,60	93,50	18,90	14,59	21,58	28,16	69,50	102,40
Nph	6,00	9,00	9,00	15,00	33,00	48,00	9,00	9,00	12,00	18,00	39,00	54,00
Irms (A) @SS	4,25	4,25	4,25	4,25	4,25	4,25	4,25	4,25	4,25	4,25	4,25	4,25
Irms(A) @Acc	11,78	11,78	11,78	11,78	11,78	11,78	11,78	11,78	11,78	11,78	11,78	11,78
q (A.t/m)	2618	3306	3883	6142	10573	13829	4299	5220	5965	8737	13869	17536
Ploss @Acc(copper + iron)(W)	26,23	27,30	20,07	15,52	16,74	19,21	32,01	22,02	22,81	16,04	15,08	14,40
Ploss @SS(copper + iron)(W)	14,50	12,33	9,98	6,59	4,75	4,43	16,53	12,98	11,87	8,16	5,77	4,86
Efficiency (%) @ Acc	89,80	89,43	92,00	93,70	93,24	92,32	87,83	91,29	91,01	93,50	93,87	94,13
Efficiency (%)@ SS	85,17	87,10	89,29	92,67	94,60	94,94	83,43	86,51	87,52	91,08	93,52	94,48
Pcore (W)	12,49	9,83	8,33	5,17	2,90	2,17	13,83	11,45	10,04	6,88	4,31	3,38
Pcu_acceleration (W)	13,74	17,47	11,74	10,35	13,84	17,04	18,17	10,57	12,77	9,16	10,78	11,02
Pcu_ss (W)	2,01	2,50	1,66	1,42	1,85	2,26	2,70	1,53	1,83	1,27	1,46	1,48

Table C.2 *10-Pole and 12-Pole Outer Rotor BLDC Motor Design Results*

Parameter	10-pole square wave excited motor						12-pole square wave excited motor					
	Value						Value					
RDL	0,7	1	1,3	3	10	20	0,7	1	1,3	3	10	20
Di (mm)	34,73	36,74	38,41	44,88	57,71	67,36	34,20	36,23	37,91	44,40	57,24	66,89
L (mm)	49,61	36,74	29,55	14,96	5,77	3,37	48,85	36,23	29,16	14,80	5,72	3,34
g (mm)	0,75	0,75	0,75	0,75	0,75	0,75	0,75	0,75	0,75	0,75	0,75	0,75
Do (mm)	45,30	47,66	49,62	57,37	73,82	89,23	44,10	46,42	48,36	55,98	72,32	88,15
hs (mm)	3,70	4,56	5,26	8,00	13,43	17,52	3,92	4,80	5,53	8,37	13,97	18,18
lm (mm)	1,87	1,89	1,91	2,06	2,88	5,03	2,02	2,03	2,06	2,21	3,14	5,61
h1 (mm)	1,00	1,00	1,00	1,00	1,00	1,00	1,00	1,00	1,00	1,00	1,00	1,00
h2 (mm)	1,00	1,00	1,00	1,00	1,00	1,00	1,00	1,00	1,00	1,00	1,00	1,00
w1 (mm)	0,75	0,75	0,75	0,75	0,75	0,75	0,75	0,75	0,75	0,75	0,75	0,75
w2 (mm)	2,36	2,46	2,54	2,87	3,51	4,00	2,29	2,39	2,48	2,80	3,43	3,90
hsbc (mm)	2,66	2,81	2,94	3,44	4,42	5,16	2,18	2,31	2,42	2,83	3,65	4,27
t1 (mm)	5,31	5,66	5,95	7,08	9,32	11,01	5,22	5,57	5,87	7,00	9,24	10,92
t2 (mm)	2,36	2,46	2,54	2,87	3,51	4,00	2,29	2,39	2,48	2,80	3,43	3,90
J (g.m2)	0,06	0,06	0,05	0,05	0,05	0,06	0,05	0,04	0,04	0,04	0,04	0,05
V (cm3)	80	66	57	39	25	21	75	61	54	36	24	20
Mtotal (kg)	0,64	0,52	0,45	0,30	0,20	0,19	0,67	0,54	0,47	0,31	0,21	0,22
Rph (mOhm)	37,44	39,19	26,88	26,57	22,55	25,04	35,55	37,28	25,58	25,21	20,88	22,63
Lph (uH)	18,44	25,39	21,17	37,78	68,84	113,48	18,26	25,18	21,03	37,65	68,75	113,49
Nph	9,00	12,00	12,00	21,00	39,00	57,00	9,00	12,00	12,00	21,00	39,00	57,00
Irms (A) @SS	4,25	4,25	4,25	4,25	4,25	4,25	4,25	4,25	4,25	4,25	4,25	4,25
Irms(A) @Acc	11,78	11,78	11,78	11,78	11,78	11,78	11,78	11,78	11,78	11,78	11,78	11,78
q (A.t/m)	4634	5589	6360	9204	14429	18148	4854	5832	6617	9505	14783	18531
Ploss @Acc(copper + iron)(W)	33,16	31,06	23,92	19,95	15,03	14,91	35,37	32,91	25,75	21,19	15,57	14,92
Ploss @SS(copper + iron)(W)	18,79	16,16	13,73	10,02	6,69	5,69	21,59	18,60	15,97	11,70	7,81	6,55
Efficiency (%) @ Acc	87,44	88,14	90,61	92,05	93,89	93,93	86,72	87,53	89,97	91,60	93,68	93,93
Efficiency (%)@ SS	81,59	83,75	85,84	89,26	92,57	93,60	79,41	81,74	83,91	87,68	91,42	92,70
Pcore (W)	16,23	13,57	11,99	8,38	5,36	4,24	19,06	16,05	14,26	10,11	6,56	5,23
Pcu_acceleration (W)	16,94	17,49	11,93	11,57	9,67	10,67	16,32	16,86	11,49	11,08	9,01	9,70
Pcu_ss (W)	2,57	2,59	1,74	1,63	1,33	1,45	2,53	2,55	1,71	1,59	1,25	1,33

Trends of motor core loss, motor copper loss at steady state, motor total loss at steady state and motor efficiency at steady state are shown in Figure C.1, Figure C.2, Figure C.3, and Figure C.4 respectively for different pole number motors.

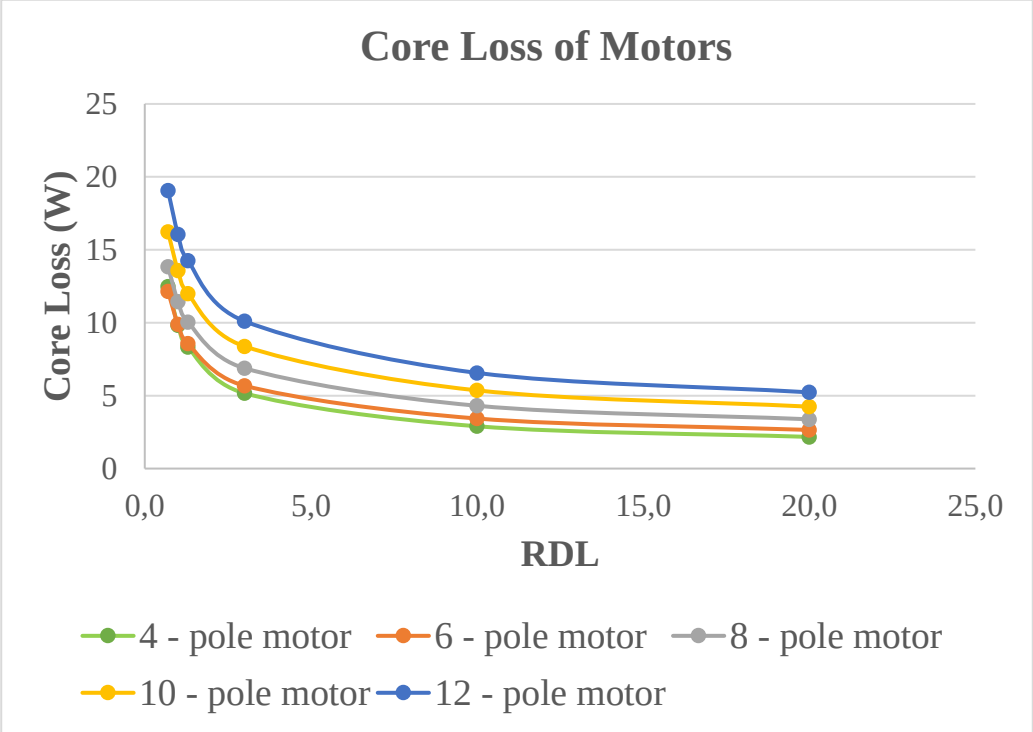

Figure C.1 Core Losses vs Different Pole Number Motors

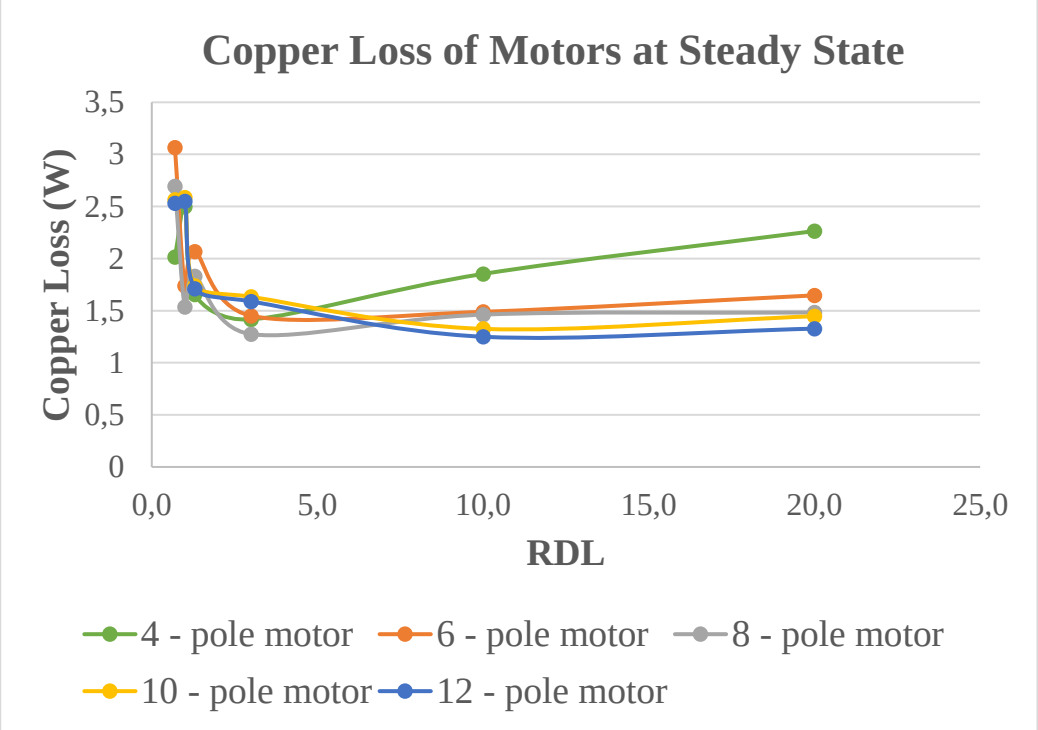

Figure C.2 Copper Losses vs Different Pole Number Motors at Steady State

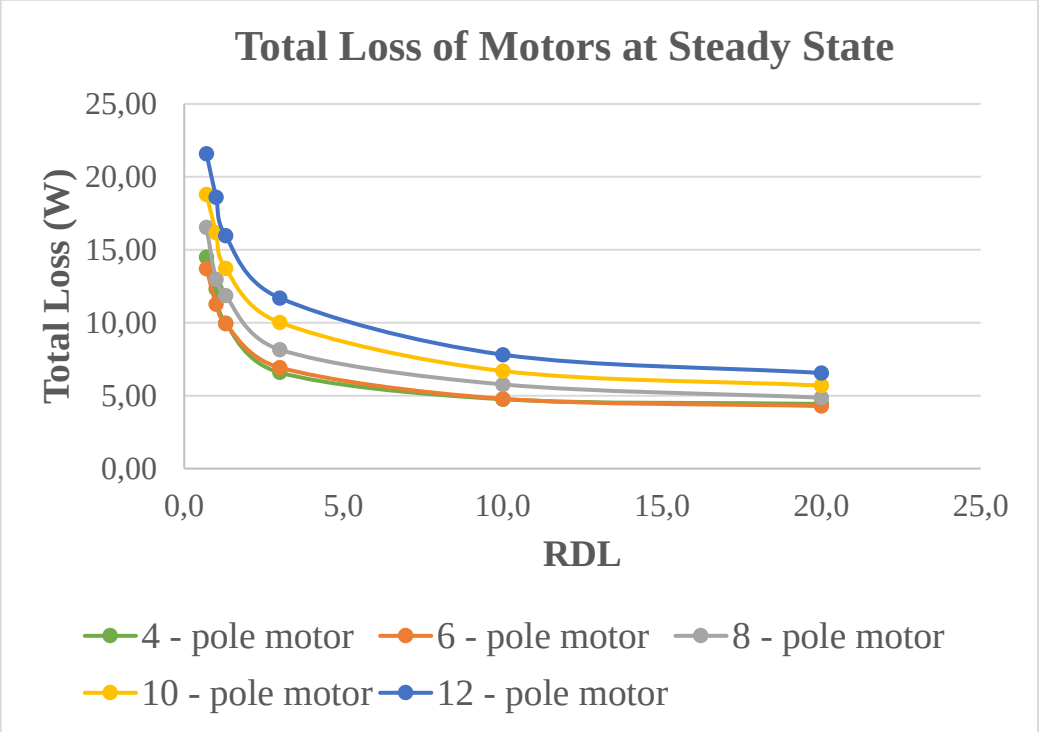

Figure C.3 Total Loss vs Different Pole Number Motors at Steady State

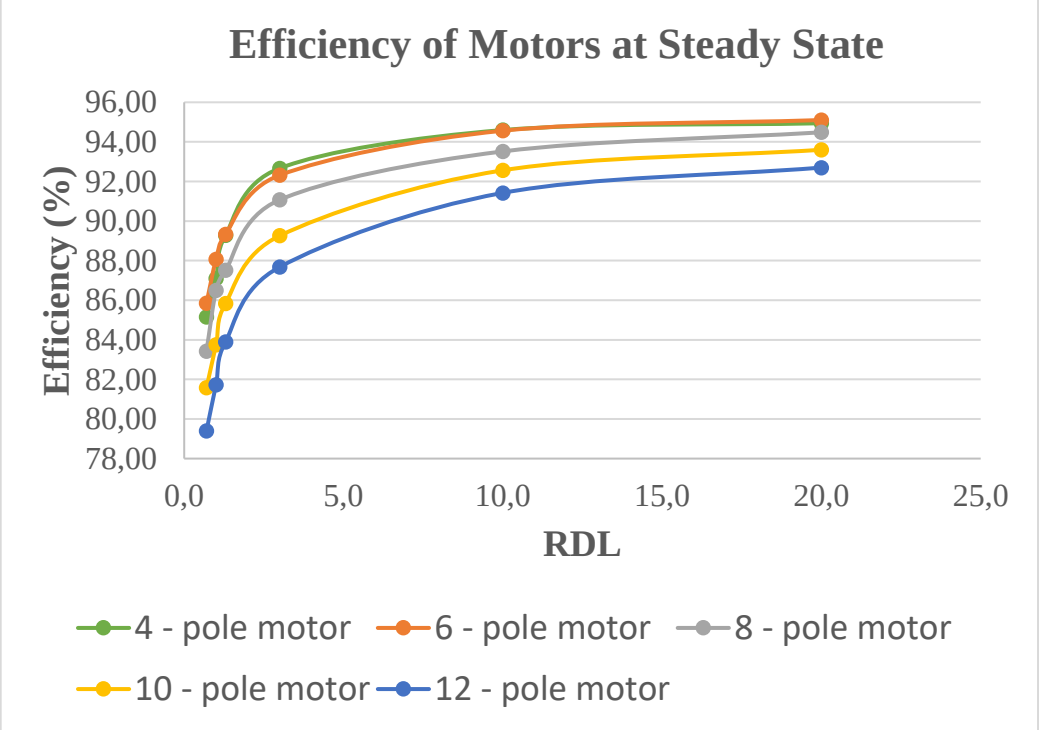

Figure C.4 Efficiency vs Different Pole Number Motors at Steady State

Discussion of Motor Losses Results

Core loss of the motor depends on mass of the motor, fundamental frequency of the motor and flux density of the motor. During core loss calculations, flux density of the motor is taken same for different pole numbers. The fundamental frequency of the motor is dominant in the core loss calculations since eddy current losses that cause core loss depend on f^2. Figure C.1 shows that if the pole number is increased core loss is also increased since fundamental drive frequency is higher. It is also noted that if the RDL (ratio of inner diameter to length of motor) is increased, core loss is decreased since the total mass of the motor is decreased by increasing RDL.

Copper loss of the motor depends on DC- link current of the motor (I_{DC}) and phase resistance of the motor. Phase resistance depends on "Mean Length of Conductor " (MLC), phase turn number and copper area of the conductor as mentioned in Section 7.3.6. Phase resistance of the motors are calculated in Table C.1 and Table C.2. MLC is smaller if the pole number is increased since motor dimensions get smaller. In addition, although phase resistance depends on the phase turn number and it is increased by increasing pole number, general trend is that if the pole number is increased phase resistance is decreased and copper losses are also decreased as shown in Figure C.2. It is also noted that there is oscillation in copper loss calculation especially for small RDL values since phase turn number is an integer number and multiple of 3 because of this fact, dramatic change in phase resistance occurs in some cases.

Total loss of the motor is calculated by summing core loss and copper loss. Figure C.1 and Figure C.2 show that core loss is more dominant than copper loss for outer rotor BLDC motor in this study. Therefore, if the pole number is increased total loss is also increased. Figure C.3 shows that total losses of 4- pole and 6-pole number motors are very close each other. In conclusion, if the pole number is increased, efficiency of the motor is decreased. Since efficiencies of 4-pole and 6-pole motors are very close to

each other as shown in Figure C.4 and 6- pole motor has lower mass and volume, it is more suitable for this CMG application.

The summary of the discussion in this section is given in Table C.3 for different pole number BLDC motors in terms of loss and efficiency.

Table C.3 *Summary of Different Pole Number BLDC Motors*

If the pole number of the motor is increased	Fundamental frequency is increased Core losses are increased Mean length of conductor is decreased Copper losses are decreased Total loss is increased Efficiency is decreased

D. Boundary Conditions of Thermal Analysis

The boundary conditions of CMG for thermal analysis are summarized in Figure D.1. Thermal analysis is performed at two different environmental conditions (TVAC and clean room) for two different bearing types. Boundary conditions of TVAC are shown in Figure D.2 and boundary conditions of the clean room are shown in Figure D.3 and Figure D.4. Two different types of bearing are considered in thermal analysis. The first bearing type is bearing that was used in the previous satellite actuator. The second bearing type is SKF 2200 ETN9. Heat loads of these bearings are different at operating speed. Heat loads are shown in Table D.1.

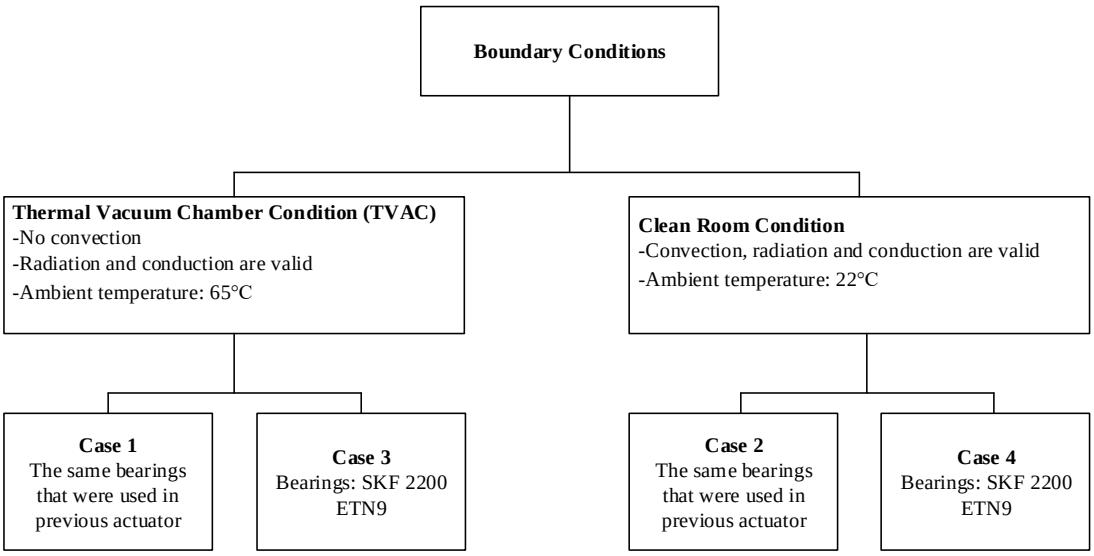

Figure D.1 Boundary Conditions of Different Cases

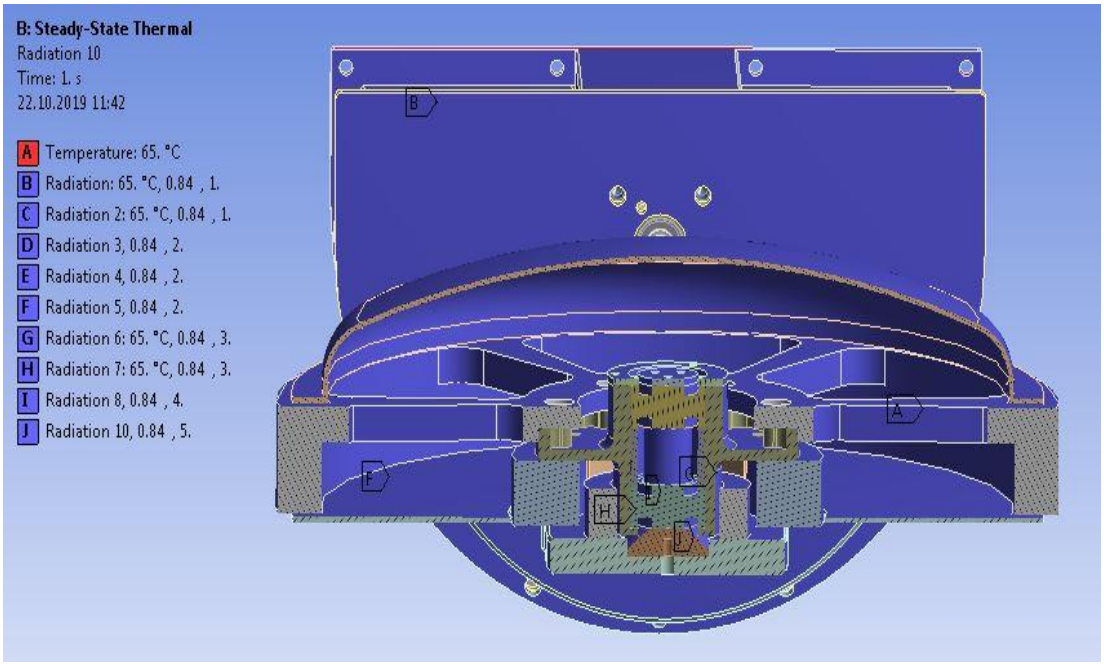

Figure D.2 Boundary Conditions of TVAC

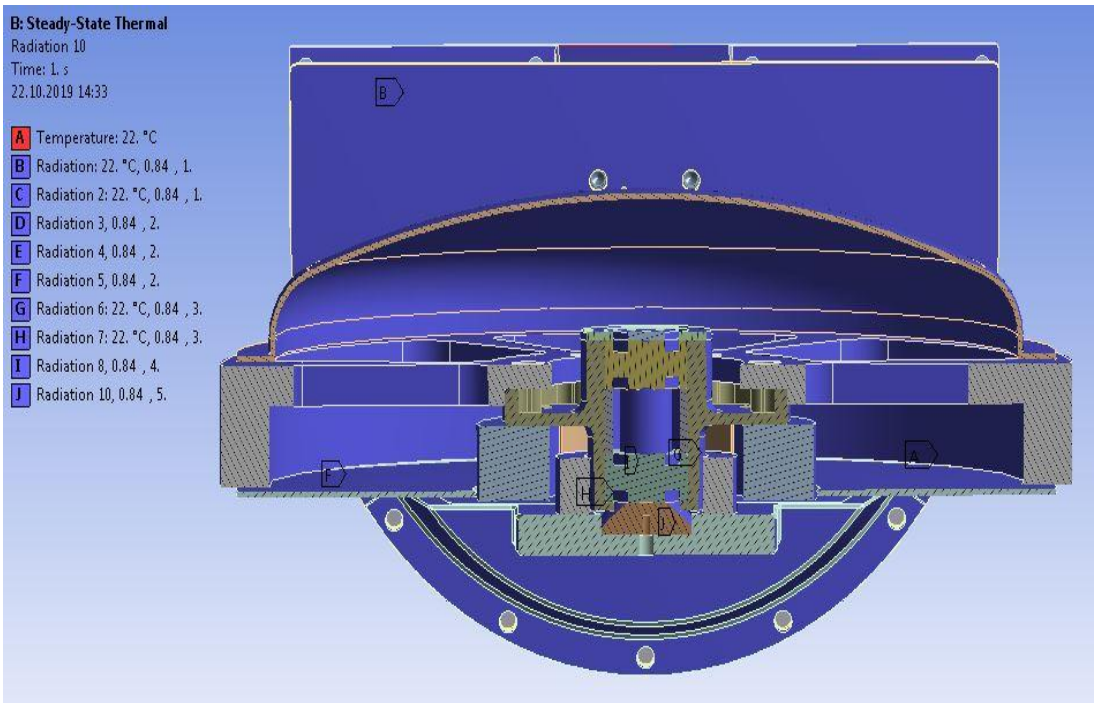

Figure D.3 Boundary Conditions of Clean Room-1

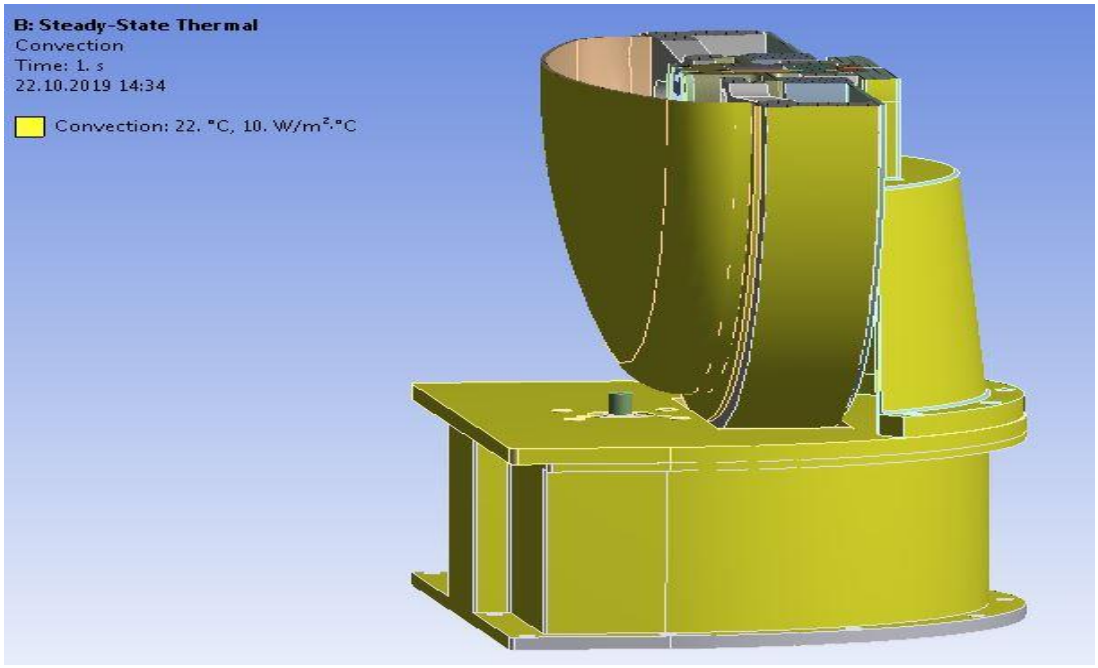

Figure D.4 Boundary Conditions of Clean Room-2

Heat loads are shown in Table D.1 for two different types of bearing. Case - 1 and Case - 2 include bearings that were used in previous satellite programs and Case - 3 and Case - 4 include bearings that are SKF 2200 ETN9. The volumes of these bearings are assumed the same in order to use same step file in thermal analysis. Heat loads of Case - 1 and Case – 2 are shown in Figure D.5 and heat loads of Case - 3 and Case – 4 are shown in Figure D.6 as a volumetric heat generation.

Table D.1 *Heat Loads of Cases*

Case	**Parts of CMG**	**Volume (m^3)**	**Heat Load (W/m^3)**	**Heat Load (W)**
Case-1 Case-2	Bearing 1	4.733 E-06	5.8631 E+06	27.75 W
	Bearing 2	4.733 E-06	5.8631 E+06	27.75 W
	Motor Stator	1.6621 E-05	5.974 E+05	9.93 W
Case-3 Case-4	Bearing 1	4.733 E-06	1.965 E+06	9.3 W
	Bearing 2	4.733 E-06	1.965 E+06	9.3 W
	Motor Stator	1.6621 E-05	5.974 E+05	9.93 W

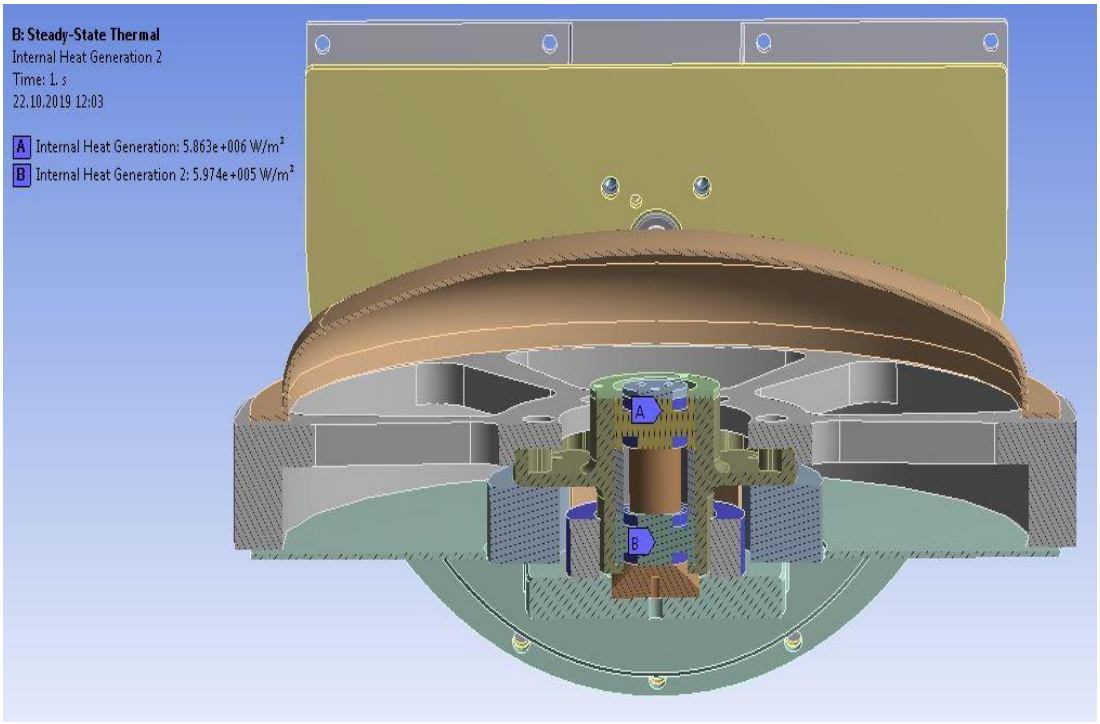

Figure D.5 Heat Loads of Case -1 and Case-2

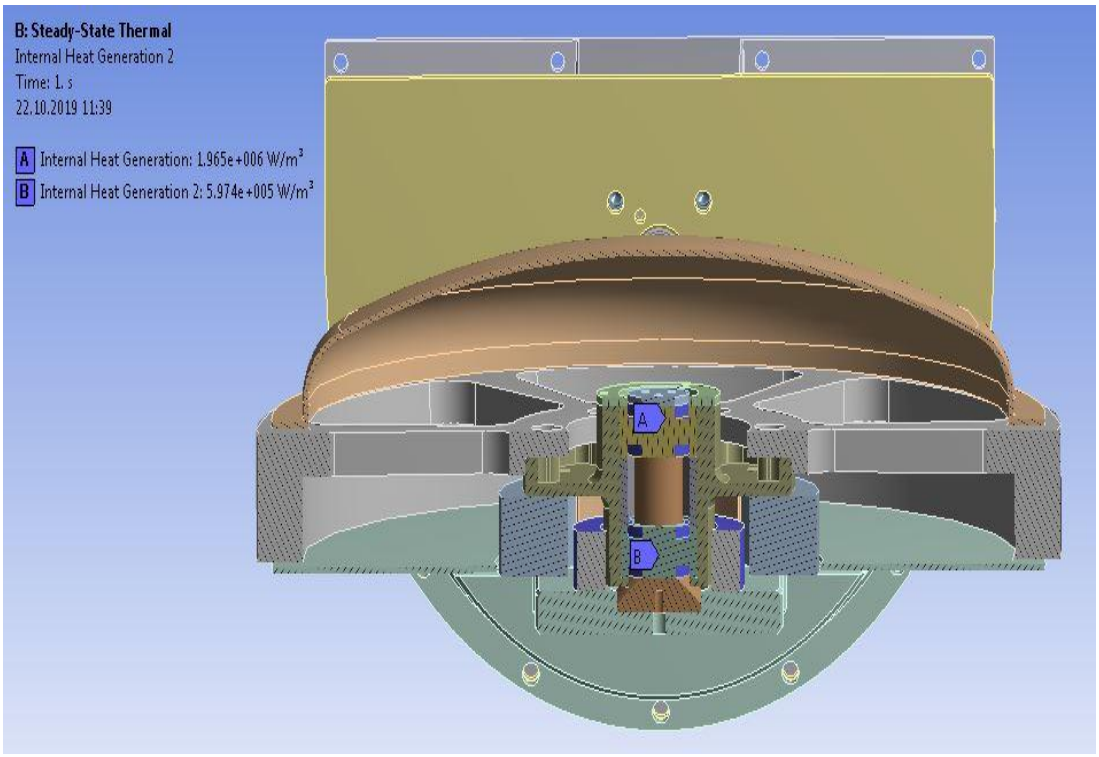

Figure D.6 Heat Loads of Case -3 and Case-4

Table D.2 *Materials Types of CMG Parts*

Part	**Material**	**Isotropic Thermal Conductivity (W/mK)**
Flywheel	AISI 304 (stainless steel)	16.2
Front Cover	Al 6061 (aluminum)	167
Back Cover	Al 6061 (aluminum)	167
Flywheel Motor Mount Plate	Al 7075 (aluminum)	130
Flywheel Bearing Fix	Al 6061 (aluminum)	167
Flywheel BLDC Motor Stator	Cognet Power No 12 Electrical Steel	X direction: 28 Y direction:28 Z direction:0.37
Flywheel BLDC Motor Rotor	Cognet Power No 12 Electrical Steel	
Flywheel BLDC Motor Permanent Magnets	VACOMAX 225 HR Type Samarium Cobalt Magnet (Sm2Co17)	10
Flywheel Bearings	AISI 316 (stainless steel)	16.3
Flywheel Shaft Support Parts	Ti6Al4V (titanium, aluminum and vanadium alloy)	6.7
Flywheel Shaft		
Bottom Plate	Al 6061 (aluminum)	167
Gimbal Gears Fix	Al 6061 (aluminum)	167
Gimbal Bearings	AISI 316 (stainless steel)	16.3
Gimbal Gears	AISI 316 (stainless steel)	16.3
Gimbal Shaft	AISI 316 (stainless steel)	16.3
Gimbal Shaft Coupling	AISI 316 (stainless steel)	16.3
Gimbal Gear Shafts	AISI 316 (stainless steel)	16.3
Gimbal Rotater	AISI 316 (stainless steel)	16.3
Gimbal Motor Mount Plate	Al 6061 (aluminum)	167